Experimental and constitutive modelling of microstructural-hydro-mechanical coupled behaviour of saturated and unsaturated soils

Tianchi Wu

Geoenvironmental Research Centre
School of Engineering
Cardiff University

Thesis submitted in candidature for the degree of Doctor of Philosophy at Cardiff University

December 2024

Declaration

This work has not been submitted in substance for any other degree or award at this or any other university or place of learning, nor is being submitted concurrently in candidature for any degree or other award.

Signed …….Tianchi Wu……. Date

STATEMENT 1
This thesis is being submitted in partial fulfilment of the requirements for the degree of Doctor of Philosophy (PhD).
Signed …….Tianchi Wu……. Date

STATEMENT 2
This thesis is the result of my own independent work/investigation, except where otherwise stated, and the thesis has not been edited by a third party beyond what is permitted by Cardiff University's Policy on the Use of Third Party Editors by Research Degree Students. Other sources are acknowledged by explicit references. The views expressed are my own.
Signed …… .Tianchi Wu……. Date

STATEMENT 3
I hereby give consent for my thesis, if accepted, to be available online in the University's Open Access repository and for inter-library loan, and for the title and summary to be made available to outside organisations.
Signed ……....Tianchi Wu……..... Date

STATEMENT 4
I hereby give consent for my thesis, if accepted, to be available online in the University's Open Access repository and for inter-library loans after expiry of a bar on access previously approved by the Academic Standards & Quality Committee.
Signed …..…..Tianchi Wu……. Date

Acknowledgements

I would like to express my deepest and greatest gratitude to my dearest supervisors Professor Peter Cleall and Professor Snehasis Tripathy for their warmest and unceasing support and encouragement for my research and personal life. To Professor Peter Cleall, I will always remember it all too well that how fast you replied to my email when I contacted you for the first time to ask for a PhD position under your supervision. I was at one of the hardest and stressful stages of my life, but your instant and positive reply gave me a lot of confidence and I am so grateful to your patient and step-to-step guidance for helping me with my PhD application and scholarship. After I enrolled, you always met me regularly to give me useful advice for my research and sincere concern to my personal life. I love the way you helped me develop as much as the way you asked me 'how is your weekend?' and 'Did you go anywhere to have fun?'. I feel lucky that I can keep a balance between work and life under your supervision. Without you, I would have never had the chance to explore the world while keeping making good progress in my research.

To Professor Snehasis Tripathy, I always admire your experienced knowledge in laboratory soil mechanics and your rigorous attitude to research. I always received the most comments on my papers and thesis from you. I must confess that I often felt overwhelmed by your insightful questions but I also have to admit that it is your abundant experience and to-the-point comments helping me gradually become a qualified and independent researcher. I especially would like to give my sincere gratitude to your hands-on instruction on how to do laboratory experiments. As a student without previous experiences in this field, you always patiently gave me detailed demonstration no matter what how busy you were. My friends were all full of jealousy when I told them how much help you offered me.

The time has always passed faster than my awareness. This four-year PhD journey rushed to its end like a ray of light. I still remember in our first meeting Professor Cleall said 'I wish we would still like each other four years later'. I can now confirm that my answer is 'Yes, I still like you both'.

I also would like to give my greatest thanks to Dr Riccardo Maddalena for providing me with the MIP equipment which is of greatest importance in my research. The time I spent with you in the DURALAB was not just a critical development in my research skills but also a precious memory when I collaborated with a sincere friend. I also enjoyed working with you during field trips. Your kindness and sense of humour always made all the hard work less tedious and more fun. As we are both members of the LGBTQ+ community, you set me a good example of how to earn respect from others. Being kind, supportive and respectful, as you taught me, are always the unveiled secret for us to be treated the same way.

To Mrs Amanda Kitching, I am full of gratitude to all the help you gave me with my experiments. You were always kind, patient, reliable and helpful whenever I came to you for training, borrowing tools or dealing with device issues. I truly feel lucky and delighted to work

with you. I am even more grateful to the encouragement and comfort you gave me every time we had a chat. We talked about our holidays, the places we had been to, the films we like and the food we recommend. You broadened my eyesight and brought a lot of fun to my life. Especially after I started writing-up and job seeking, it was such a relief to talk with you about the all the difficulties I met. Your warm concern and encouraging words saved me from depression and frustration, helping me rebuild up my confidence to carry on. You are not just a technician or colleague to me but a faithful friend whom I can always rely on.

To my partner Qi Chen, I feel so lucky to have you for the last 6 years. You keep me accompany through many important moments and periods of my life. I cannot imagine how dull and lonely my life would be without you. Especially for this PhD journey, your unceasing support, and selfless care and intense love for me help me get through all the difficult time without suffering too much. I love you and we will always be a family whatever happens in the future.

I also would like to give my great thanks to all the other researchers, colleagues and friends I meet during my PhD journey for the help you gave me in research and all the beautiful memories we shared.

Table of Contents

List of Figures

List of Tables

List of Abbreviations and Symbols

CT	Computed Tomography
CSL	Critical state line
DPT	Differential pressure transducer
GCM	Glasgow Coupled Model
GDS	Global Digital Systems
HAEPD	High-air-entry porous disc
LC	Loading-collapse
LVDT	Linear variable differential transformer
MIP	Mercury Intrusion Porosimetry
NCL	Normal consolidation line
NMR	Nuclear Magnetic Resonance
PSD	Pore size distribution
SD	Suction-decrease
SEM	Scanning Electron Microscopy
SI	Suction-increase
SWCC	Soil-water characteristic curve
ξ_{ij}^{*}	Bishop's effective stress tensor
ξ_{ij}	Bishop's stress tensor
$\overline{p}$	Net mean stress
p	Total mean stress
χ	Bishop's effective stress coefficient
u_{w}	Water pressure
u_{a}	Air pressure
δ_{ij}	Kronecker delta
S_{r}	Degree of Saturation
$S_{\mathrm{r}}^{\mathrm{m}}$	Residual degree of saturation
s	Suction
s^{*}	Modified suction
n	Porosity
e	Void ratio
e_{in}	Intruded void ratio
v	Specific volume
$d\varepsilon_{ij}$	Strain increment tensor
$d\xi_{ij}^{*}$	Effective stress increment tensor
F_{LC}	LC yield surface
F_{SI}	SI yield surace
F_{SD}	SD yield surface
q	Deviatoric stress
M	Slope of critical state line
p^{*}	First Invariant of Bishop's Stress Tensor
p_{0}^{*}	Pre-consolidation Pressure
p'	Effective mean stress

s_{I}^{*}	Modified suction that locates F_{SI}
s_{D}^{*}	Modified suction that locates F_{SD}
k_1	Parameter that defines the coupled movement of SD/SI yield surfaces when yielding on LC yield surface
k_2	Parameter that defines the coupled movement of LC yield surfaces when yielding on SD/SI yield surfaces
S_{e}	Effective Degree of Saturation
$d\lambda_l^j$	Plastic multiplier with j related to the plastic mechanism which is active (e.g. When yield on LC yield surface is activated j is LC and for yield on SI or SD j is LC is β) and l is associated with plastic changes of effective degrees of saturation (when l is β) or volumetric strains (when l is LC).
$d\varepsilon_{\mathrm{v}}^{\mathrm{p}}$	Increment of Plastic Volumetric Strain
$dS_{\mathrm{e}}^{\mathrm{p}}$	Increment of Plastic Effective Degree of Saturation
$\mathbf{D}_{\mathrm{e}}^{*}$	Generalized elastic matrix
$\mathbf{D}_{\mathbf{ep}}^{*}$	Elasto-plastic Matrix
$d\tilde{\boldsymbol{\varepsilon}}$	Elasto-plastic Increment Strain
K	Elastic bulk modulus
λ	Slope of Normal Consolidation Line
κ	Slope of Rebound Curve
λ_{s}	Slope of the Main Curve when the SWCC is simplified and represented by three straight lines
κ_{s}	Slope of the Scanning Curve when the SWCC is simplified and represented by three straight lines
μ	Poisson's ratio
G_{s}	Specific gravity
V	Total pore volume
V_{s}	Total solid volume
D or d	Pore diameter
$f(D)$	Differential PSD function
a_1	Fitting parameter for log-normal distribution
a_2	Fitting parameter for log-normal distribution
μ_1	Fitting parameter for log-normal distribution
μ_2	Fitting parameter for log-normal distribution
σ_1	Fitting parameter for log-normal distribution
σ_2	Fitting parameter for log-normal distribution
K_1^i	Fitting parameter for evolution of a_1 and a_2 (i=1 or 2)
K_2^i	Fitting parameter for evolution of μ_1 and μ_2 (i=1 or 2)
K_3^i	Fitting parameter for evolution of σ_1 and σ_2 (i=1 or 2)
δw	Incremental work input
V_{t}	Total volume
V_{w}	Water volume
V_{a}	Air volume
δV_{w1}	Water volume change generated by the change of pore volume

δV_{w2}	Water volume change induced by the change of suction
e_{w1}	Water ratio at constant suction
R	Pore radius
γ	Surface tension of liquid (water or mercury)
θ	Contact angle between liquid (water or mercury) and pore wall
P_r	Intruding pressure for MIP
c'	Effective cohesion
ϕ'	Effective friction angle
ϕ^b	Angle of friction related to suction
ξ'	Effective stress
τ_f	Shear strength
t	Time
$M(t)$	Magnetization at time t
M_0	Initial magnetization
T_2	Transverse relaxation time
θ_s	Volumetric water content
w	Gravimetric water content
ρ_w	Water density
ρ_s	Soil particle density
ρ_d	Dry density
θ_r	Residual water content;
θ_{sat}	Saturated water content
R^2	Coefficient of determination
$\Re$	Universal gas constant
υ_w	Specific volume of water
ω_υ	Molecular mass of water vapor
p^c	Reference stress for which $v = N(s)$
κ_{vp}	Parameter regarding elastic compressibility due to net mean stress
κ_{vs}	Parameter regarding elastic compressibility due to suction
λ_{vp}	Parameter regarding compressibility due to net mean stress
λ_{vs}	Parameter regarding compressibility due to suction
H(s)	Suction-dependent function for considering the effects of suction on volume change when suction is combined with net mean stress
s_{sa}	Saturation suction
$\dot{\sigma}^M$	Macromechanical effective stress
$\dot{\sigma}^m$	Micromechanical effective stress
$\bar{\sigma}^M$	Macromechanical net mean stress
$\bar{\sigma}^m$	Micromechanical net mean stress
s^M	Macromechanical suction
s^m	Micromechanical suction
χ^M	Macromechanical Bishop's effective stress coefficient
χ^m	Micromechanical Bishop's effective stress coefficient

f_s, f_d and f_u	Three scalar factors
κ_{m}	Dependency of microstructural swelling/shrinkage on the microstructural effective stress
m_c	Model parameter controlling the impact of r_{em} on f_{m} for intermediate values of r_{em}
$\xi_3 - u_{\mathrm{a}}$	Net mean confining stress

ABSTRACT

Microstructure plays a foundational role in the hydro-mechanical behaviour of soils, including volume change, strength, water retention ability and permeability. It is important to study the interaction between microstructure and the hydro-mechanical behaviour of soils, which can provide a better understanding of the behaviour of soil from the perspective of microstructure.

This study presents both experimental and modelling work on microstructural-hydro-mechanical coupled behaviour of fine-grained soils. For the experimental investigation, pore size distribution (PSD) is adopted as the indicator of microstructure, the coupled behaviour is thus the interaction between evolution of PSD and mechanical loading or volume change. Compacted samples of a soil (low-plastic silt) were tested under various loading conditions, including compaction, saturation, consolidation, saturated isotropic loading and saturated and unsaturated shearing. Further, the PSDs of the samples under specific loading conditions were determined by Mercury Intrusion Porosimetry (MIP) tests. The soil-water characteristic curves were also obtained by chilled-mirror dew point tests to study the water retention behaviour of the soil.

For the modelling investigation, a constitutive model based on the evolution of microstructure is established building on the approach of an existing mechanistic model. In this model, the evolution of microstructure is represented via changes in the pore size distribution (PSD) and assumed to be related solely to the change of void ratio induced by loading and unloading. A PSD-dependent Bishop's effective stress coefficient χ, which represents the coupled impact of PSD evolution on hydro-mechanical behaviour of soils, was used to calculate the effective stress. The model can reproduce and predict the hydro-mechanical behaviour and evolution of microstructure and their interaction within a unified framework. It also has a potential in studying soil-water characteristic curve and multi-field-coupling of soils. Model response and sensitivity analysis are reported based on idealized parameters to give a primary evaluation on the performance of the model and feasibility of using PSDs from MIP. Model validation was conducted by comparing the modelling results and the experimental results of the low-plastic soil.

According to both experimental and modelling results, it can be concluded that the compression of volume mostly evolves from the decrease of the volume of larger pores while small pores are less affected but sensitive to change in degree of saturation. The interaction between PSDs and hydro-mechanical behaviour can be satisfactorily reproduced and predicted by the PSD-dependent model. This demonstrates the potential of considering the effects of microstructure when studying the hydro-mechanical behaviour of other soils and applying the microstructural-hydro-mechanical coupled behaviour in engineering applications.

CHAPTER 1

Introduction

1.1 Background and motivations

The hydro-mechanical behaviour of unsaturated soils describes how soils interact with water and mechanical forces. It is a long-term research topic (Fredlund and Morgenstern 1977; Fredlund et al. 1978; Alonso et al. 1990; Davies and Newson 1992; Wheeler et al. 2003; Sheng et al. 2004; Gens et al. 2006; Alonso et al. 2013; Lloret-Cabot et al. 2013; Cai et al. 2018; Rahardjo et al. 2018; Wu et al. 2022) with unsaturated soils behaviour, such as strength and volumetric change, of particular importance in many engineering applications such as the bearing capacity of a foundation (Sabetamal et al. 2022), ground surface displacement due to tunnel excavation (Zhou et al. 2015), rainfall-induced landslide (Collins and Znidarcic 2004; Godt et al. 2013; Sorbino and Nicotera 2013), soil barrier (Delage 2007; Tsiampousi et al. 2024), landfill (Rajesh and Viswanadham 2011) and contaminant transport (Hensley and Savvidou 1993). Besides, the hydro-mechanical behaviour of soils is also sensitive to climate change which is an inevitable topic in many engineering applications. Increased rainfall intensity can lead to rapid infiltration in soils which can reduce the matric suction and strength of soils (Collins and Znidarcic 2004; Cai et al. 2020a). Due to the increasing temperature, thawing of permafrost can occur which results in the instability of slopes and foundations (Gruber and Haeberli 2007; Niu et al. 2016). Therefore, a better understanding of the hydro-mechanical behaviour of soils is helpful for preventing potential hazards in construction and increasing efficiency in contaminant treatment which is also critical for achieving NetZero goals.

Many research studies have demonstrated that the microstructure, which can be defined as the arrangement of soil particles and pores (Marshall et al. 1996), can be a significant factor in the behaviour of soils (Tsuji et al. 1975; Belnap and Gardner 1993; Hu et al. 2001; Alekseeva 2007; Alonso et al. 2010; Al-Mukhtar et al. 2012; Wang and Bai 2012). Moreover, strains induced by loading can also lead to the evolution of the microstructure, including changes in pore sizes, pore shapes and pore size distribution. It has been established that the evolution of microstructure significantly influence the hydro-mechanical behaviour of soils and the storage and transmission of liquid, microorganism, chemical substance or other pollutant stored in pores (Yong 2003; Zhang 2005; Izdebska-Mucha and Trzciński 2008; Izdebska-Mucha et al. 2011; Woignier et al. 2011). There exists a strong interrelationship between the hydro-mechanical behaviour of soils and their microstructure and these interactions require investigation and to be represented adequately within theoretical and numerical models.

The impact of microstructure has received considerable attention from many researchers both in terms of experimentally observed behaviour and modelling approaches. Wang and Bai addressed the connection between pore diameter and compressibility of loess noting that compressibility is positively correlated to the proportion of pores larger than 20 micrometres (Wang and Bai 2012). Wang et al. studied the impact of microstructure on shear behaviour of natural loess (Wang et al. 2021). They found a correlation between the homogenous deformation, with the increase of confining stresses, and the microstructural evolution of pore shapes changing from angular to rounded. It was also found that the evolution of the macro void ratio can account for the observed dilatancy of unsaturated recompacted and intact loess (Ng et al. 2019). To numerically consider the effect of microstructure, Sanchez et al. (Sánchez et al. 2001; Sánchez et al. 2005) selected different constitutive formulations for the macrostructural level and the microstructural level. An interaction formulation was proposed to connect these two levels and establish a microstructurally dependent model. This model was validated against experimental data from tests conducted by Lloret et al on heavily compacted bentonite (Lloret et al. 2003). However, this model was mainly built for unsaturated expansive soils and its applicability in other kinds of soils remained questioned. Besides, separating soil microstructure into macrolevel and microlevel requires separate parameters for each leavel which might cause trouble in parameter calibration and make the model too complex. Wu et al. adopted the effective degree of saturation as microstructural index and established a hydro-mechanical coupled model that considers the microstructure (Wu et al. 2022). The use of effective degree of saturation ignores the effect of water stored in micropores which contributes little to the effective stress (Alonso et al. 2010).

Due to the complexity of soil microstructure (Chen and Banin 1975; Garakani et al. 2015; Alazaiza et al. 2017) (irregular pore and particle shapes, randomly distributed pores and particles, various contacts among particles), it is difficult to consider the comprehensive features of microstructure, attention thus should be focused on the most critical features that can both represent the evolution of microstructure but also have the closest connection with the hydro-mechanical behaviour. Pore size distribution (PSD) is a good option to fulfil the requirements above. PSD presents the relationship between pore sizes and their corresponding volumes. From PSDs, it is easy to know the pore volume difference between two PSDs with a specific pore size range. This difference reflects the evolution of microstructure and is highly related to the volume change or other hydro-mechanical behaviour of soils (Li and Zhang 2009; Vaunat and Casini 2017).

The relationship between pore size distribution and the hydro-mechanical behaviour have been investigated for decades. Based on the observation of water flowing though both saturated and unsaturated sand, Marshall (Marshall 1958) split pore size distribution into several equal fractions and proposed an empirical equation of calculating permeability which is related to the mean pore radius in each equal fractions of pore space. Juang and Holtz (Juang and Holtz 1986) also proposed an empirical equation of permeability based on the integration of pore size density function. It is also found from PSDs that inter-aggregate pores (macropores) are more affected by loading while intra-aggregate pores are less sensitive (Romero et al. 1999; Li and

Zhang 2009). Aside from loading, saturation is another important factor that influences the shape of PSD (Koliji et al. 2010; Oualmakran et al. 2016; Wang et al. 2020; Ying et al. 2023) that the increase of saturation will turn the bimodality to unimodality. All these findings above experimentally reveal the tight but one-directional connections between PSD and soils' behaviour. However, the evolution of PSDs during a triaxial test, which is important for studying the interaction between PSD and soil behaviour, is still lack of investigation. For example, if PSDs at different axial strains (0%, 5%, 10% and 20%) during a specific shearing path can be obtained, not only the evolution of PSDs during shearing can be studied, but also how PSD evolution will affect the hydro-mechanical behaviour can be analysed (Vaunat and Casini 2017). In terms of modelling, currently there are few models that has built the interaction between PSD and hydro-mechanical behaviour. a PSD-dependent Bishop's effective stress coefficient χ, proposed by Vaunat and Casini (2017) described the relationship between PSD and hydro-mechancial behaviour. The PSD-dependent χ was established based on work input theory which gives χ both a thermodynamic basis and a physical meaning. However, while the common Bishop's effective stress coefficient χ is usually assumed to be related to the degree of saturation in constitutive modelling (Wheeler et al. 2003; Nuth and Laloui 2008; Lloret-Cabot et al. 2013; Musso et al. 2020; Zhang and Lu 2020; Wu et al. 2022), the PSD-dependent χ has only been applied in constitutive models in a limited way (Vaunat and Casini 2017; Niu et al. 2021) without considering the triaxial conditions.

The overall aim of this study is to investigate the interaction between soil microstructure and hydro-mechanical behaviour of both saturated and unsaturated soils. This study especially focuses on the pore size distribution evolution during saturated and unsaturated triaxial shearing and its impact on stress-strain, shear strength and water retention behaviour, to provide a better understanding of the engineering-related soil behaviour from the perspective of microstructure. This study for the first time provides the experimental evidence of the interaction between microstructure and hydro-mechanical behaviour of Dundee silt during saturated and unsaturated shearing, and applied the PSD-dependent χ in constitutive modelling to predict the stress-strain behaviour, water retention behaviour and microstructure evolution within one unified framework.

1.2 Study objectives

The main objectives of this study are:

(1) To experimentally study the stress-strain behaviour, water retention behaviour and shear strength of saturated and unsaturated soil under various loading conditions.

(2) To experimentally study the evolution of pore size distribution under various loading paths and its interaction with the hydro-mechanical behaviour.

(3) To study the connection between the soil microstructure and the hydro-mechanical behaviour from the perspective of constitutive modelling and to develop a microstructurally based hydro-mechanical coupled model.

(4) To evaluate the performance of the proposed model based on idealized conditions, through sensitivity analysis, and to study the validity of the proposed model against the observed experimental behaviour.

1.3 Scope and limitations of the study

This study focused on the interaction between the soil microstructure and the hydro-mechanical behaviour of soils from the respect of both the experiments and modelling. The experiments only attach importance to the evolution of pore size distribution, stress-strain behaviour during shearing and water retention behaviour and so does the modelling. Detailed description of soil microstructure (such as morphologic features) and thermal or chemical effects on soil behaviour are beyond the scope of this research.

Furthermore, since the pore size distribution obtained by MIP is not fully representative of the soil microstructure, that puts a limit on the study of the connection between the soil microstructure and the hydro-mechanical behaviour.

1.4 Thesis overview

A brief description of each chapter is presented below.

CHAPTER 1 gives an introduction of the background and motivations, study objectives, scope and limitations of this research with the thesis overview presented at last.

CHAPTER 2 presents the literature review concerning the soil microstructure and the hydro-mechanical behaviour of unsaturated soils. This chapter first give a general information about the definition and classification of soil microstructure and the experimental methods for identifying the microstructure. The pore size distribution is also reviewed in terms of its evolution due to the hydro-mechanical behaviour and its application in soil-water characteristic curves and Bishop's effective stress coefficient. Both experimental and modelling investigations on the hydro-mechanical behaviour are also presented in this chapter.

CHAPTER 3 first describes the properties of the soil used in this study. Subsequently, four experimental methods for obtaining the microstructural-hydro-mechanical behaviour of soils are elaborated in terms of the sample preparation, testing principles, devices used, testing program and expected outcomes. The modelling methods including theoretical relationship and numerical computation are also presented in this chapter.

CHAPTER 4 presents the experimental results of the microstructural-hydro-mechanical coupled behaviour of a natural soil from saturated and unsaturated tests, MIP tests, Chilled-mirror dew-point tests. For saturated and unsaturated tests, soil samples were sheared under various suctions and confining stresses to different axial strains. Those samples were then taken to MIP tests to study the pore size distribution evolution under various conditions and the relationship between the evolution and the hydro-mechanical behaviour. Chilled-mirror dew-point tests were carried out to obtain the soil-water characteristic curves of this natural soil under different dry densities.

CHAPTER 5 presents the indirect consideration of microstructure in constitutive modelling of soils' hydro-mechanical behaviour. The main objective of this chapter is to evaluate the behaviour of a constitutive model with indirect consideration of soil microstructure (indirect microstructure model) and identify its deficiency.

CHAPTER 6 presents the direct method of considering microstructure in constitutive modelling of soils' hydro-mechanical behaviour. The main objective of this chapter is to establish a microstructural-hydro-mechanical coupled model with direct consideration of soil microstructure (direct microstructure model).

CHAPTER 7 primarily evaluates the proposed direct microstructure model's performance based on both published and idealized parameters. The sensitivity analysis is also presented in order to investigate the feasibility of using PSDs obtained by Mercury Intrusion Porosimetry (MIP) in this model, considering that the PSDs obtained by MIP and the fitted PSDs cannot be fully representative of the microstructure.

CHAPTER 8 presents the validation and application of the proposed model. The model was validated by comparing the simulated microstructural-hydro-mechanical coupled behaviour to the experimental results of Dundee silt presented in Chapter 4. The model was also applied to predict the evolution of SWCC with different dry densities.

CHAPTER 9 presents the overall conclusions of the study and possible future work.

CHAPTER 2

Literature review

2.1 Introduction

This research focuses on the interaction between the soil microstructure and the hydro-mechanical behaviour of unsaturated soils in terms of both constitutive modelling and experiments. Therefore, some related topics concerning the microstructure and the hydro-mechanical behaviour from perspectives of modelling and experiments are reviewed in this chapter. The definition and classification of soil microstructure is firstly given, followed by the experimental methods for identifying soil microstructure. The pore size distribution, which is a typical part of soil microstructure is reviewed in the next section in terms of its evolution and application. Subsequently, the experimental investigation on soils' hydro-mechanical behaviour is presented, focusing on the triaxial tests and soil-water characteristic curves. The constitutive models for hydro-mechanical behaviour are reviewed in the last section.

2.2 Definition and classification of soil microstructure

Soil microstructure plays an important role in the hydro-mechanical behaviour of soils. Details of soil microstructure are presented in the following sections.

2.2.1 Definition of soil microstructure

Soil microstructure is defined as the arrangement and morphological features of soil particles and pores (Marshall et al. 1996; Al-Mukhtar et al. 2012; Tang et al. 2020), including pore shapes, particle shapes, pore size and pore size distribution. Soil microstructure is not only a reflection of soils' hydro-mechanical history, formation and environment conditions, but also can have significant impact on soils' hydro-mechanical properties, such as compressibility (Low et al. 2008; Jia et al. 2020), water retention behaviour (Simms and Yanful 2002; Zou 2018) and shear strength (Zhao et al. 2013).

2.2.2 Classification of soil microstructure

Soil microstructure can be classified by pore size distribution (more details are presented in Section 2.4). According to the geometric shapes and the dominant pore sizes, the pore size distribution can be classified as a unimodal PSD, a bimodal PSD or a trimodal PSD. Correspondingly, the microstructure can be classified as single porosity, double porosity and triple porosity. Unimodal PSD is a distribution where most pore sizes fall into a specific range (with only one dominant pore size) and only one peak can be seen in the graph of pore size density distribution (see Figure 2.1, Log Diff. Intrusion is dV/dlog$D$). Bimodal PSD has two

significant peaks (see Figure 2.2, pore size density is dV/(dD·V)). One is related to the macropores (the peak that occurs at a larger pore size) and the other is related to the micropores (the peak at the smaller pore size). Trimodal PSD has three dominant pore sizes for micropores, mesopores and macropores respectively (see Figure 2.3). The type of pore size distribution depends on many factors like soil types, stress levels and saturation conditions. Soils with large pores like sandy soils have a more uniform microstructure and tend to have a unimodal PSD. The PSDs for compacted fine soils like clay usually show clear bimodality or trimodality. However, with increased stress or degree of saturation, the evolution of bimodal or trimodal PSDs will gradually approach unimodality (Li and Zhang 2009; Ma et al. 2020)).

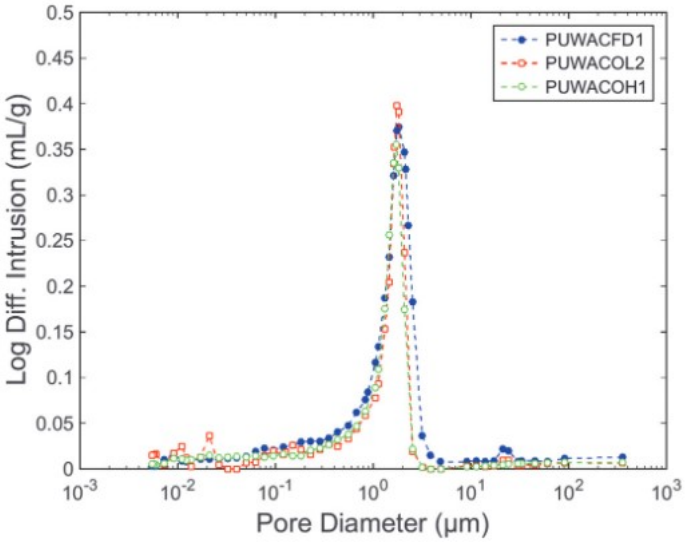

Figure 2.1 Unimodal pore size distributions for a compacted silty soil and evolution (Oualmakran et al. 2016)

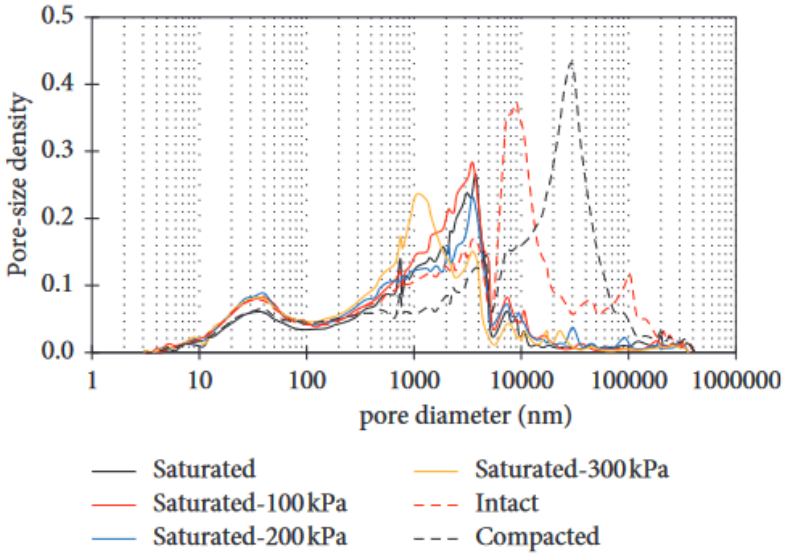

Figure 2.2 Bimodal pore size distributions for saturated loess from China and evolution (Li et al. 2021)

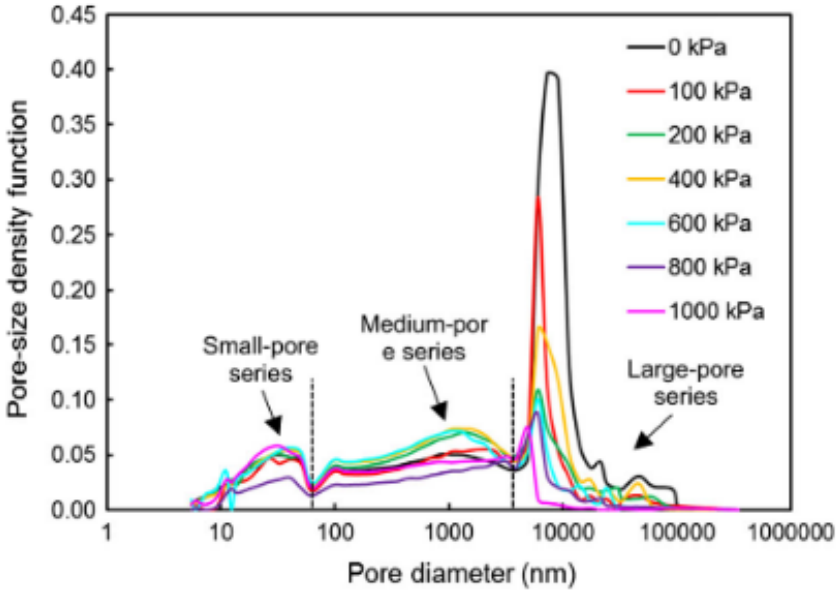

Figure 2.3 Trimodal pore size distributions for saturated loess and evolution (Wang et al. 2020)

It is clear that pore size distribution can denote the arrangement of soil pores in a quantitative way. Since changes in soil pores are the main source for deformation and the most important storage region for the liquid phase, pore size distribution can be used to consider many aspects of soil behaviour such as volume change, water retention and permeability.

2.3 Experimental identification of soil microstructure

Several widely used experimental methods for identifying soil microstructure are presented in this section.

2.3.1 Mercury Intrusion Porosimetry (MIP)

Mercury intrusion porosimetry (MIP) is the most extensively used method for obtaining pore size distribution (more details are presented in Section 2.4). During a MIP test, mercury is forced to intrude into open soil pores when pressure is exerted. Progressively smaller pores can be intruded into with the increasing pressure. The relationship between the intruding pressure and the pore size is typically assumed to be represented by Washburn's equation (Washburn 1921):

$$p_r = \frac{2\gamma \cos\theta}{r} \tag{2-1}$$

where γ is the surface tension of any liquid (equivalent to 0.484 N/m at 25℃ for mercury, 0.072 N/m for water.), θ is the contact angle between the liquid and the pore wall (140° for mercury and 0° for water), and R is the pore radius. It should be noted that adoption of this approach is limited by the assumption of a cylindrical pore shape. By monitoring pressure and the total volume of mercury intruding into open pores, the smallest open pores filled with mercury are determined at a specific pressure and the total volume of open pores equal or larger in size than the smallest pores are taken to be equivalent to the volume of mercury (Tanaka et al. 2003; Simms and Yanful 2004a; Romero and Simms 2008). Based on the pore size and total volume obtained from MIP, the cumulative pore size distribution and differential pore size distribution can be plotted. The measuring range of MIP varies with facilities but the generally MIP can measure pore sizes ranging from 2 nanometres to several hundred micrometres (Juang and Holtz 1986; Burton et al. 2014; Oualmakran et al. 2016; NIU et al. 2020; Gramegna 2022). Therefore, the result obtained from MIP can represent a wide range of pore sizes but in some cases not the entire pore size distribution within a soils microstructure is captured due pore sizes smaller than 2 nanometres or large pores being ignored. This deficiency can limit the application of MIP to fine soils which have a large proportion of small and disconnected pores and sandy soils with large pores.

2.3.2 Scanning Electron Microscope (SEM)

A Scanning Electron Microscope (SEM) is a kind of electron microscope that can provide high-resolution images of a sample surface (Chen and Banin 1975; Ringrose-Voase 1991; Rabot et al. 2018). This device emits a beam of high-energy electrons to scan the sample surface and captures the signals when elections interact with the atoms in the sample. These signals are then converted into an electronic signal to create an image displayed on a monitor. An example SEM device is presented in Figure 2.4. There are several advantages of SEM. First, it can reach high resolutions to 1 nanometre (Joy and Pawley 1992), allowing detailed visualization of microstructure. Second, it is able to provide a three-dimensional image of microstructure due to its large depth of field. An example image is presented in Figure 2.5. However, even though SEM can provide accurate and vivid images of microstructure, it is difficult to quantify microstructure (such as obtaining the pore size distribution) with the images provided by a conventional SEM.

Figure 2.4 Illustration of a SEM device

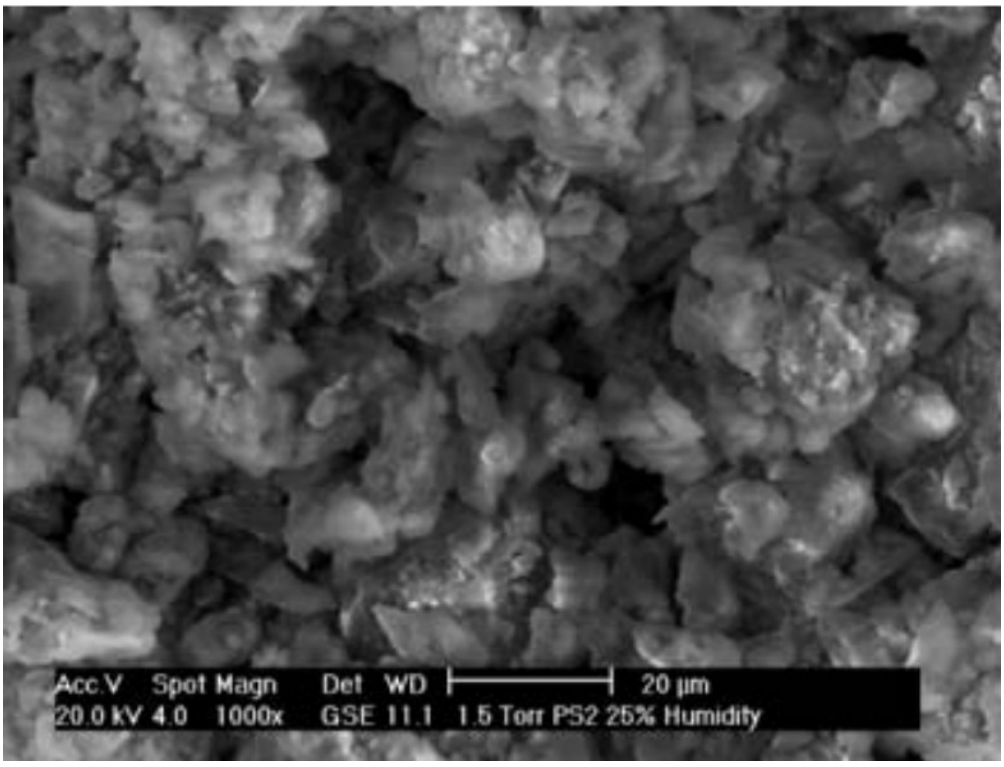

Figure 2.5 An example image of the soil microstructure obtained by SEM (Koliji et al. 2010)

2.3.3 Computed Tomography (CT)

Computed Tomography (CT) is a non-destructive imaging technique. It usually emits X-rays to penetrate the soil sample and then capture the X-rays which pass through the sample before reconstructing a three-dimensional image of microstructure from a series X-ray projections taken from different angles (Sleutel et al. 2008; Taina et al. 2008). Unlike other methods that might alter soil microstructure when sampling, X-ray CT can directly scan the original sample without disturbing the microstructure, which allows for repeated measurements. Besides, X-ray CT is also able to provide three-dimensional images like SEM (see Figure 2.6). The resolution of CT can vary from micrometres to millimetres (Oda et al. 2004; Taina et al. 2008; Schlüter et al. 2020), depending on the equipment and size of the sample. Therefore, X-ray CT can be less better than SEM in terms of resolutions.

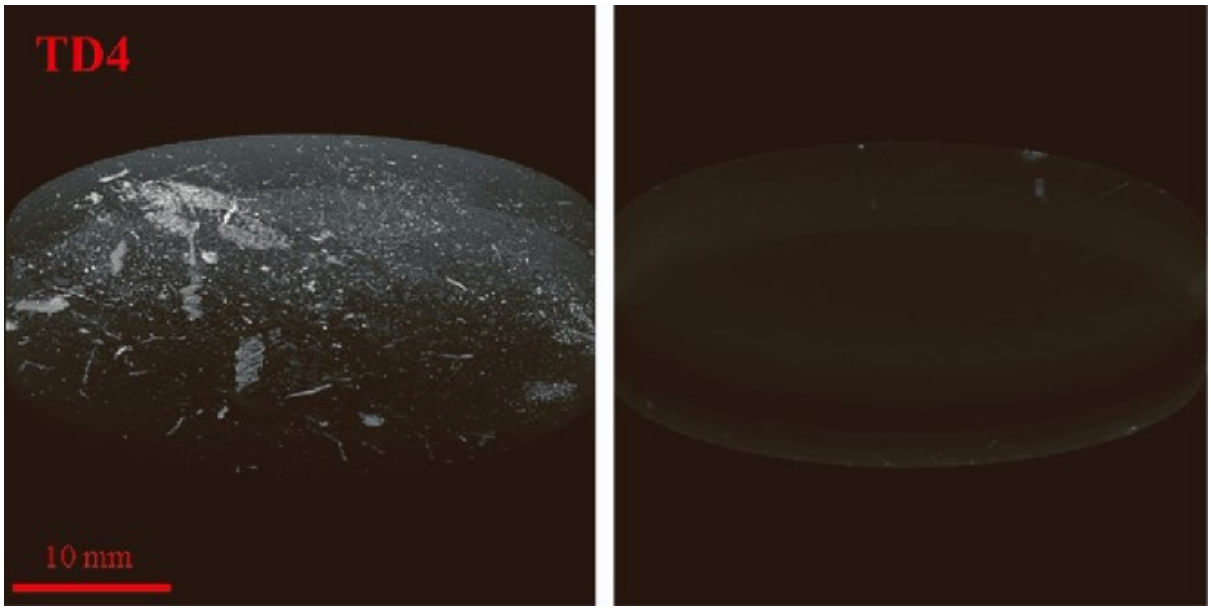

Figure 2.6 An example image of the soil microstructure obtained by X-ray CT (Wang et al. 2023)

2.3.4 Nuclear Magnetic Resonance (NMR)

Nuclear Magnetic Resonance (NMR) (Li et al. 2015; Ma et al. 2020; Kan et al. 2021) is another non-destructive analytical technique used for monitoring soil microstructure but in an indirect way. This technique actually determines the amount and spatial distribution of water within soil pores by monitoring the relaxation times of water molecules after they are excited by a radiofrequency pulse in a magnetic field (see Figure 2.7). The relaxation process can be described by (Tian et al. 2018):

$$M(t) = M_0 \exp(\frac{-t}{T_2}) \tag{2-2}$$

where t is time, $M(t)$ is the magnetization at time t, M_0 is initial magnetization, and T_2 is the transverse relaxation time which describes how quickly the magnetization of a sample decays in the plane perpendicular to the applied magnetic field. Different types of water (bound or free water) will have different relaxation times and that gives the information about moisture content. Because the relaxation time is also affected by the size of the pores where the water resides, it is also possible to estimate the pore size (assumed to be cylindrical or spherical) and its distribution with this technique indirectly from the water-related information. For example, if the relaxation time is shorter than 1 ms, this means the water is stored in small pores. A higher relaxation time will indicate a larger pore size. With this relationship, the pore size can be predicted from Figure 2.7.

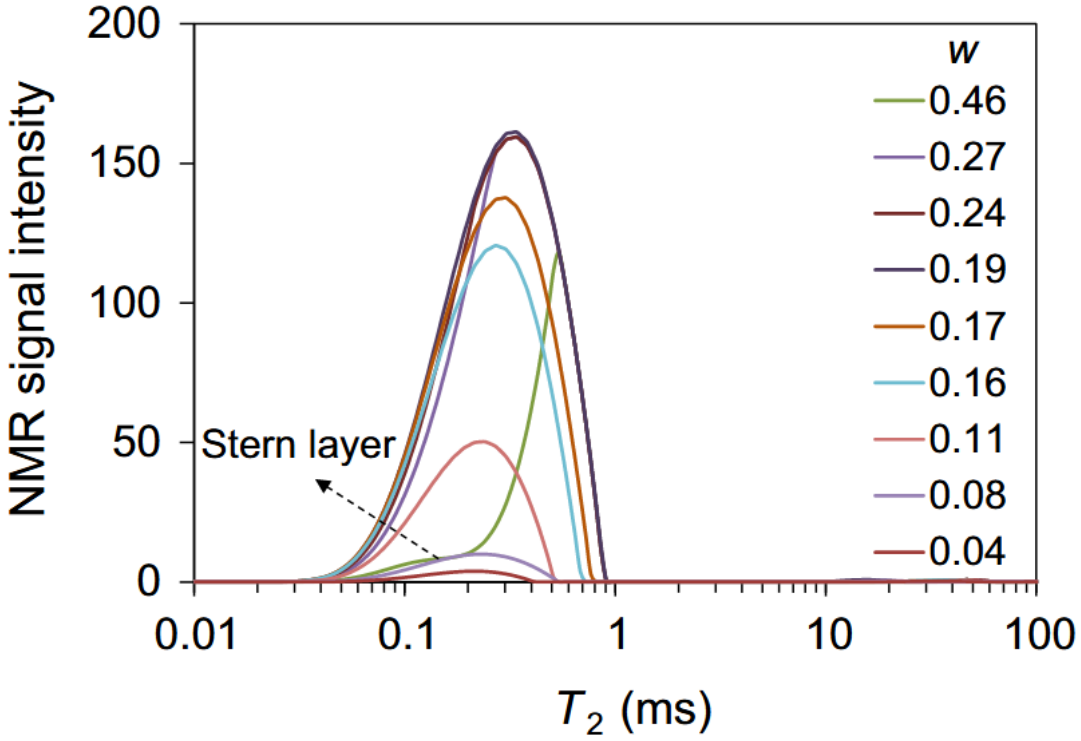

Figure 2.7 An example of NMR results (Ma et al. 2020)

2.4 Pore size distribution, its evolution and application

Pore size distribution represents the numerical range of pore sizes and their volumetric proportions in a representative volume of soils (Nimmo 2013). Pore size distribution can be grouped into cumulative pore size distribution and differential pore size distribution (pore size density distribution). Cumulative pore size distribution can provide the total volume of pores within a specific pore size range. For example (see Figure 2.8), at point P, the X-axis value (pore radius) is 0.1 μm and the Y-axis value (cumulative pore volume) is 0.345 cm^3/g, which means the total volume of pores whose sizes are larger than 0.1μm is 0.345 cm^3 in a unit weight of soil. Differential pore size distribution is the derivative of the cumulative pore size

distribution. Differential pore size distribution represents the volumetric density of the pores at specific sizes, as shown in Figure 2.9. Assuming the cumulative pore size distribution is described by a function $F(r)$, then the equations for the differential pore size distribution $f(r)$ are commonly defined as (Sridharan et al. 1971; Tanaka et al. 2003; Thom et al. 2007; Burton et al. 2014; Guo-Quan et al. 2022):

$$f(r)=\frac{\mathrm{d}F(r)}{\mathrm{d}r},\quad \frac{\mathrm{d}F(r)}{V_s\mathrm{d}r},\quad \frac{\mathrm{d}F(r)}{V\mathrm{d}r}\quad \text{or}\quad \frac{\mathrm{d}F(r)}{\mathrm{dlog}(r)} \tag{2-3}$$

where r is the pore radius, V_s is the volume of the solid phase and V is the total volume of soils. According to the equations above, the area below differential pore size distribution is equivalent to the total volume of pores if the PSD defined as $\frac{\mathrm{d}F(r)}{\mathrm{d}r}$ (or void ratio if PSD is defined as $\frac{\mathrm{d}F(r)}{V_s\mathrm{d}r}$).

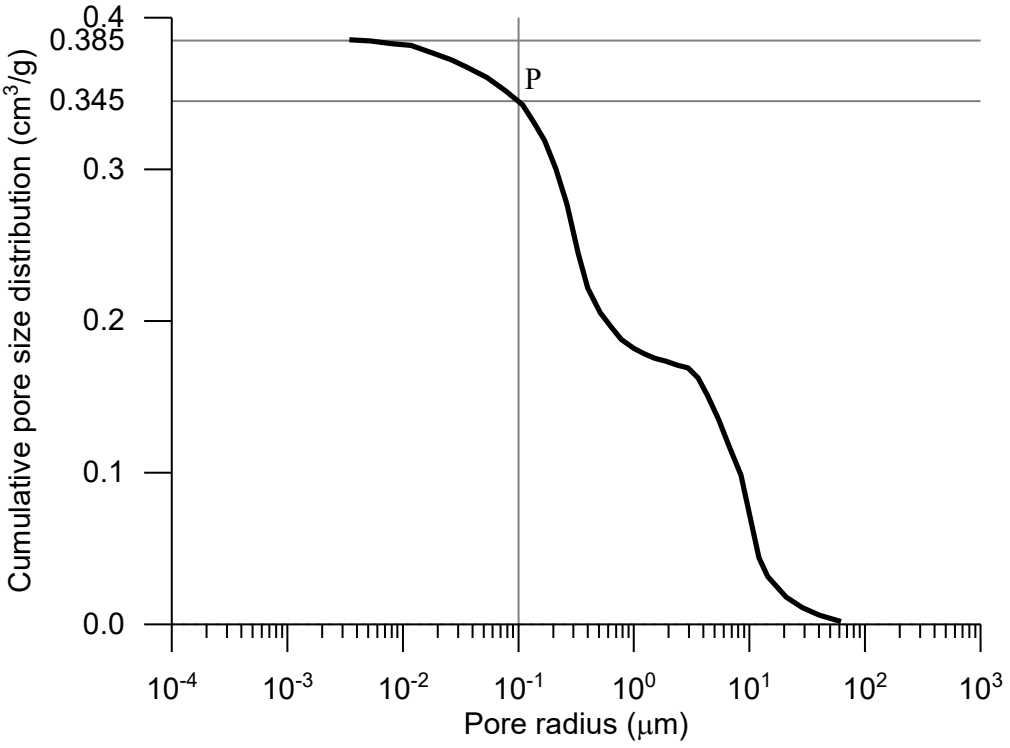

Figure 2.8 An example for the cumulative pore size distribution (Li and Zhang 2009)

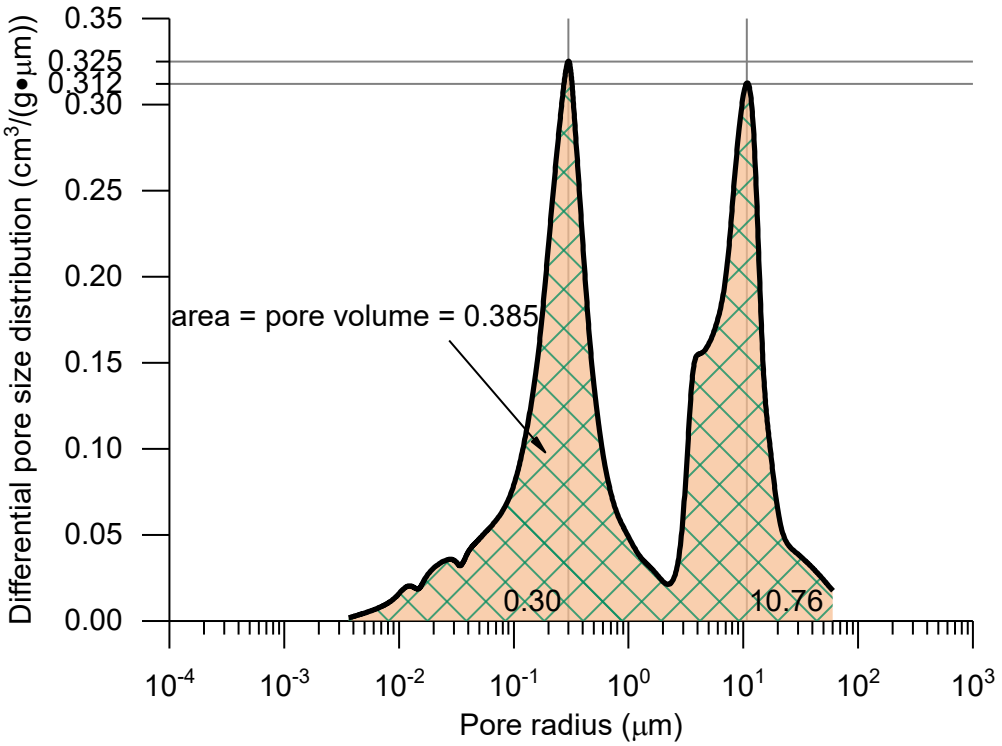

Figure 2.9 An example for the differential pore size distribution (after Li and Zhang) (Li and Zhang 2009)

2.4.1 Evolution of pore size distribution

The evolution of pore size distribution can be seen when soil samples undergo external loading or suction change. Details of pore size distribution evolution are presented below.

2.4.1.1 Evolution due to external loading

External loading, such as compaction, isotropic loading and shearing, usually have a more significant impact on larger pores while affects little on very small pores (Li and Zhang 2009; Wang et al. 2019; Jia et al. 2020; Li et al. 2021). For example, when a soil sample is compacted to various void ratios, more larger pores will be eliminated with the decrease of void ratios, leading to a significant downward movement of pore size distribution (decrease in total pore volumes) and a movement towards the direction of smaller pores (elimination of larger pores), as shown in Figure 2.10.

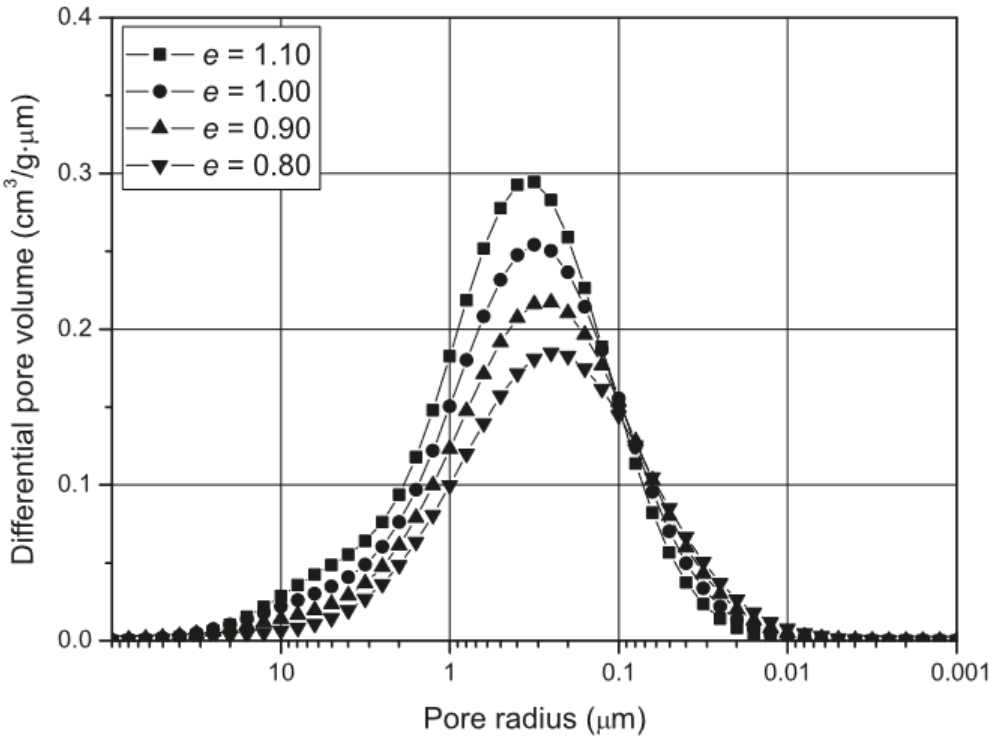

Figure 2.10 Evolution of pore size distribution due to compaction (Li and Zhang 2009)

2.4.1.2 Evolution due to suction change

The evolution of pore size distribution due to suction increase (drying path) is similar to that due to external loading. The volume of macropores decreases as the degree of saturation decreases (Li and Zhang 2009). Besides, for an initially saturated soil sample, its unimodal pore size distribution can evolve into bimodal shape during the drying process (Li and Zhang 2009; Oualmakran et al. 2016; Wang et al. 2020), as shown in Figure 2.11. The evolution of pore size distribution due to suction increase (drying path) is similar to that due to external loading. The volume of macropores decreases as the degree of saturation decreases (Li and Zhang 2009). Besides, for an initially saturated soil sample, its unimodal pore size distribution can evolve into bimodal shape during the drying process (Li and Zhang 2009; Oualmakran et al. 2016; Wang et al. 2020),

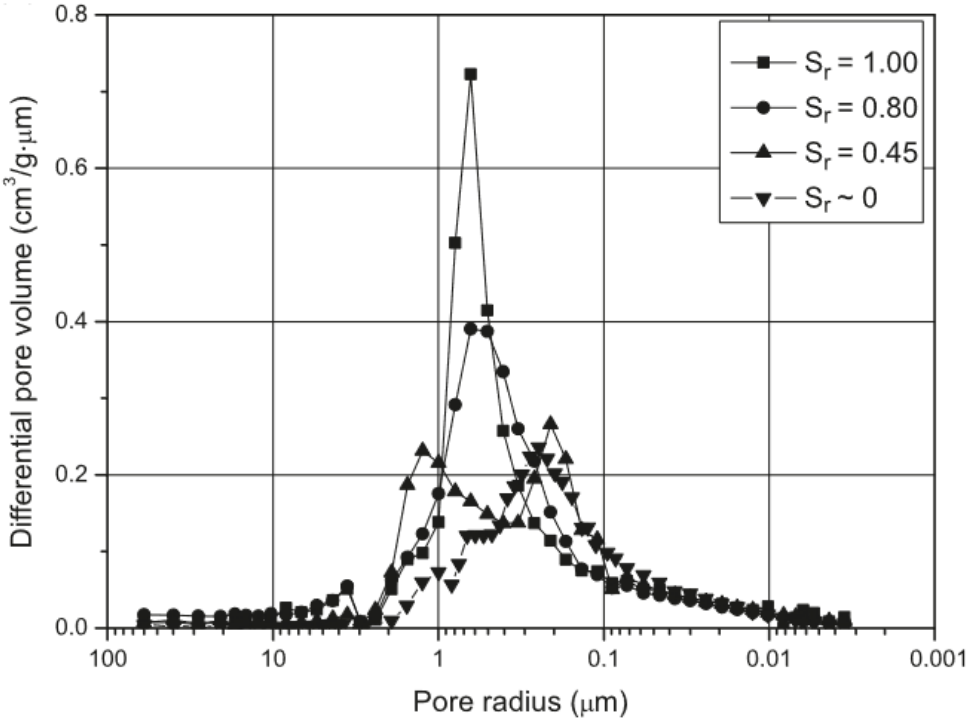

Figure 2.11 The evolution of pore size distribution during a drying path from 100% to 0% degree of saturation (Li and Zhang 2009)

2.4.2 Application of pore size distribution

Pore size distribution contains important information about soil microstructure, namely pore size and pore volume (pore volume density) of each pore size. Since water is maintained within soil pores, it is possible to obtain the water volume from pore size distribution. The application of PSD in soil water characteristic curve and Bishop's effective stress parameter is summarised and analysed here, both of which are related to using PSD to get the water volume.

2.4.2.1 Predicting soil-water characteristics curve (SWCC) from PSD

Soil water characteristic curve (SWCC) is one of the most fundamental properties of soils that denotes soils' behaviour in retaining water (Tripathy et al. 2014b; Tripathy et al. 2014a; Arroyo et al. 2015; Guo-Quan et al. 2022). It is usually defined as the relationship between suction and water content (or degree of saturation). Both water content and degree of saturation are related to the water volume stored in soil pores. If the water volume at a specific suction can be determined, then the corresponding SWCC will be obtained. According to capillary theory and Young-Laplace equation (Finn 1999), there exist a maximum pore size that water can reach at a specific suction and any pores having equivalent or smaller pore sizes can be fully filled with water. Since the largest pore size to hold the water is determined, the water volume stored in pores is equal to the total volume of pores smaller than R which can be

obtained from pore size distribution. For example, if pore size distribution $f(r)$ is defined as the density of cumulative pore volume $F(r)$:

$$f(r)=\frac{\mathrm{d}F(r)}{\mathrm{d}r} \tag{2-4}$$

Then the water volume V_{w} can be calculated as (Zhang and Chen 2005):

$$V_{\mathrm{w}}(s)=\int_0^R f(r)\cdot\mathrm{d}r=\int_0^{\frac{2\gamma\cos\theta}{s}} f(r)\cdot\mathrm{d}r \tag{2-5}$$

Correspondingly, the volumetric water content θ_s, gravimetric water content w and degree of saturation S_{r} can be calculated as below:

$$\theta_s(s)=\frac{V_{\mathrm{w}}(s)}{V}=\frac{\int_0^R f(r)\cdot\mathrm{d}r}{V}=\frac{\int_0^{\frac{2\gamma\cos\theta}{s}} f(r)\cdot\mathrm{d}r}{V} \tag{2-6}$$

$$w(s)=\frac{\rho_{\mathrm{w}}V_{\mathrm{w}}(s)}{\rho_{\mathrm{s}}V_{\mathrm{s}}}=\frac{\int_0^R f(r)\cdot\mathrm{d}r}{G_{\mathrm{s}}V_{\mathrm{s}}}=\frac{\int_0^{\frac{2\gamma\cos\theta}{s}} f(r)\cdot\mathrm{d}r}{G_{\mathrm{s}}V_{\mathrm{s}}} \tag{2-7}$$

$$S_{\mathrm{r}}(s)=\frac{V_{\mathrm{w}}(s)}{V_{\mathrm{v}}}\times 100\%=\frac{\int_0^R f(r)\cdot\mathrm{d}r}{V_{\mathrm{v}}}=\frac{\int_0^{\frac{2\gamma\cos\theta}{s}} f(r)\cdot\mathrm{d}r}{V_{\mathrm{v}}} \tag{2-8}$$

where V is the total volume of soil, V_{s} is the volume of soil particles, V_{v} is the volume of pores, ρ_{w} is the water density, ρ_{s} is the soil particle density and G_{s} is the specific gravity. The soil water characteristic curve can be described from the equations above when the pore size distribution $f(r)$ is determined. This is the basic principle of obtaining SWCC from pore size distribution (Simms and Yanful 2002; Zhang and Chen 2005; Della Vecchia et al. 2015; Yan et al. 2021; Guo-Quan et al. 2022). It should be noted that this strategy is based on simplification and assumptions. Soil pores are assumed to be spherical using this strategy to obtain SWCC from PSD. The assumption that all pores smaller than R are fully filled with water is also possible to be unrepresentative when air becomes trapped in small and occluded pores. Furthermore, since the SWCC is obtained based on a fixed pore size distribution $f(r)$, any change in soil microstructure or pore size distribution during wetting or drying is ignored in such approaches.

Due to the scattered data obtained from MIP, a fitting function for pore size distribution is required to obtain a continuous soil water characteristic curve. One way to select the fitting function is to acquire it from empirical SWCC equations or models. As indicated in equations above, the PSD can also be described as a function of the derivative of SWCC (Zhang and Chen 2005):

$$f(r)=\frac{\mathrm{d}\theta_s(r)V}{\mathrm{d}r}=V\cdot\frac{\mathrm{d}\theta_s(s)}{\mathrm{d}s}\cdot\frac{\mathrm{d}s}{\mathrm{d}r} \tag{2-9}$$

Once the equations or models for SWCC are determined, the corresponding PSD can be obtained. There are many commonly used SWCC equations or models and some of them are summarized in Table 2.1.

Table 2.1 SWCC equations or models

Names	Reference	Equations	Descriptions
Fredlund & Xing	(Fredlund and Xing 1994)	$\theta_s(s)=\theta_r+(\theta_{sat}-\theta_r)\left[1+(\alpha\cdot s)^n\right]^{-m}$ (2-10)	θ_r is the residual water content; θ_{sat} is the saturated water content; α, m, n are empirical parameters.
Van Genuchten	(Van Genuchten 1980)	$\theta_s(s)=\theta_r+(\theta_{sat}-\theta_r)\left[1+(\alpha\cdot s^n)^m\right]^{-(1/m)}$ (2-11)	
Gardner	(Gardner 1958)	$\theta_s(s)=\theta_r+(\theta_{sat}-\theta_r)\left[1+(\alpha\cdot s)^n\right]^{m}$ (2-12)	
Brooks & Corey	(Brooks and Corey 1964)	$\theta_s(s)=\theta_r+(\theta_{sat}-\theta_r)\cdot\exp\left[-(\alpha\cdot s)^{-n}\right]$ (2-13)	

For different types of pore size distribution (single porosity, double porosity and triple porosity), each porosity is assumed to be related to a specific single SWCC equation and $\theta_s(s)$ should be a collection of one or several single SWCC equations with each one having a weight factor t_i. Assuming the equation for a single SWCC is $\phi_i(s)$, then $\theta_s(s)$ can be expressed as:

$$\theta_s(s)=\sum_{i=1}^{n}t_i\phi_i(s) \tag{2-14}$$

where n represents the number of porosity (single porosity=1, double porosity=2, triple porosity=3).

For soils with double porosity, Ding et al. (2022) gave an equation for $\theta_s(s)$ based on the Fredlund and Xing Model as:

$$\theta_s(s) = t\frac{\theta_{\text{sat}}}{\left\{\ln\left[e+(s/a_1)^{n_1}\right]\right\}^{m_1}} + (1-t)\frac{\theta_{\text{sat}}}{\left\{\ln\left[e+(s/a_2)^{n_2}\right]\right\}^{m_2}} \tag{2-15}$$

where θ_{sat} is the volumetric water content when the soil is saturated; a_1, a_2, m_1, m_2, n_1 and n_2 are fitting parameters; e is the base of the natural logarithm.

Then the fitting function for pore size distribution was defined as:

$$f(r) = \frac{tm_1n_1C^{n_1}\theta_{\text{sat}}}{(ea_1^{n_1}r^{n_1+1}+C^{n_1}r)\left\{\ln\left[e+(C/a_1r)^{n_1}\right]\right\}^{m_1+1}} + \frac{(1-t)m_2n_2C^{n_2}\theta_{\text{sat}}}{(ea_2^{n_2}r^{n_2+1}+C^{n_2}r)\left\{\ln\left[e+(C/a_2r)^{n_2}\right]\right\}^{m_2+1}}$$
$$(C = 2\gamma\cos\theta) \tag{2-16}$$

An alternative way to fit pore size distribution is to use multi log normal distributions. The equation is defined below:

$$f(r) = \sum_{i=1}^{j}\frac{a_i}{\sqrt{2\pi}\sigma_i r}\exp\left(-\frac{(\ln(r)-\mu_i)^2}{2\sigma_i^2}\right) \tag{2-17}$$

where *i* and *j* are related to the type of pore size distribution, unimodal (*j*=1), bimodal (*j*=2) or trimodal (*j*=3) and parameters a_i, μ_i and σ_i are fitting variables for the distributions.

Fitting PSD by using multi log normal distributions is more frequently adopted when the evolution of PSD is considered (Li and Zhang 2009; Yu et al. 2016; Li et al. 2020). This is because log normal distribution is a classic distribution whose mathematical features have been thoroughly studied. Therefore, the movement of PSD during loading can be easily described and predicted through log normal distribution with the change of fitting parameters a_i, μ_i and σ_i. However, due to the complexity and irregularity of PSD obtained from MIP, the experimental PSD may not perfectly fit log normal distribution so that the fitting performance might be poorer than using equations derived from SWCC equations or models. Using the first method may give a better performance in fitting PSD and predicting SWCC, but due to the change of soil microstructure (pore size distribution) during SWCC tests, the fitting equation derived from SWCC may not be representative of a single experimental PSD. Besides, it is less convenient in predicting the movement of pore size distribution because of the much more complex format of fitting equations derived from SWCC.

Several PSDs of different soils are used here to give examples of obtaining SWCC from PSD using the two different PSD-fitting methods (either fitting the PSD based on equations/models presented in Table 2.1 or based on log-normal distributions as described in equation (2-17)). The fitting parameters for each method are presented in Table 2.2 and Table 2.3. It can be seen that the goodness of fit R^2 is generally better using equation (2-16) than equation (2-17).

In these examples, the pore size distribution $f(r)$ is defined as:

$$f(r) = \frac{dV}{d\log_{10}(r)} \tag{2-18}$$

Therefore, the volumetric water content can be expressed as:

$$\theta_s(s) = \frac{V_w(s)}{V} = \frac{\int_0^R f(r)\cdot \mathrm{d}\log_{10} r}{V} = \frac{\int_0^{\frac{2\gamma\cos\theta}{s}} \frac{f(r)}{\ln 10 \cdot r}\cdot \mathrm{d}r}{1/\rho_d} \tag{2-19}$$

where ρ_d is the dry density of soil. Since the pore size distribution is usually defined in a unit weight of soil, the total volume of soil can be calculated by $1/\rho_d$. This method directly calculated the total pore volume fully filled with water and uses it as the water volume to calculate the volumetric water content. This method is labelled as Method A for obtaining SWCC from PSD.

Table 2.2 Fitting parameters based on equation (2-16) (Guo-Quan et al. 2022)

No.	Reference	Parameters							
		a_1	n_1	m_1	a_2	n_2	m_2	t	R^2
1	(Zhao et al. 2013)	2.73	4.48	0.12	217.37	4.65	0.10	0.50	0.91
2	(Zhang and Li 2010)	36.87	2.58	5.64	122.35	4.27	0.45	0.13	0.94
3	(Li and Zhang 2009)	7.54	4.04	0.49	428.76	4.13	1.00	0.46	0.97
4	(Miguel and Bonder 2012)	12.82	3.53	0.33	13688.55	2.82	3.29	0.72	0.96

Table 2.3 Fitting parameters based on equation (2-17)

No.	Void ratio	Specific gravity	Parameters						
			a_1	μ_1	σ_1	a_2	μ_2	σ_2	R^2
1	0.62	2.64	4.71	4.52	1.03	0.06	0.25	1.24	0.74
2	0.47	2.90	0.22	1.80	0.30	0.19	0.08	0.60	0.84
3	1.00	2.64	5.38	3.16	0.80	0.14	-1.02	0.56	0.90
4	1.55	3.06	3.21	2.32	0.59	0.005	-4.15	0.53	0.91

Figure 2.12 presents the experimental PSDs of various soils from MIP tests, the fitting curves (parameters from Table 2.2 and Table 2.3) of each PSD obtained by two different methods (equation (2-16) and (2-17)), and the comparison between predicted SWCCs based on Method A. All SWCCs have a geometric character that is possessed by soils with double porosity. Aside from the two platforms observed at lower suctions (boundary zone, smaller than 1kPa in the graph) and higher suctions (residual zone, over 10000 kPa in the graph), there is another platform in the transition zone that can be witnessed at the suction range from 20 kPa to 200 kPa because the suction has reached the boundary between the two peaks of the pore size distribution where there is less volume of pores to store the water. As indicated by R^2, fitting by using equations derived from SWCC models or equations has a better performance in reproducing the experimental PSDs than using multi log normal distributions even though both methods succeed in reflecting the bimodal property of these PSDs. Since the basic principle of getting SWCC from PSD is the same for both methods but different in fitting methods for PSD, it is comprehensible that difference in predicted SWCCs can be observed. As shown in Figure 2.12(a), the difference in predicted maximum volumetric water content can be around 0.005, which can be attributed to the significant disparity in R^2 (0.91 versus 0.74). For SWCCs in Figure 2.12(d), even though the fitted PSDs both have a high R^2 (0.96 versus 0.91), the difference in SWCCs can still be seen due to the ignorance of pores within 0.1 to 1μm in the fitted PSD based on multi log normal distributions. For all SWCCs in in Figure 2.12, they all tend to be zero at a larger suction which is consistent to the observation in the pore size distribution that the distributional value is at a very low level for smaller pores. However, when approaching zero suction, the volumetric water contents do not come to the values where full saturation heads. For example, for the SWCCs in Figure 2.12(a), the volumetric water content at 100% saturation should be $e/1+e$=0.383 while both SWCCs give much smaller values. This is because, first, the PSD obtained by MIP is not fully representative of the real PSD within soil microstructure due to the limitation that not all pores can be intruded by mercury such as extremely small pores with nanometre radius and much larger pores with over several hundred micrometres radius. Therefore, it is possible that the experimental porosity is smaller than the real porosity, which affects the calculation of volumetric water contents. Second, as indicted by R^2, the fitted PSD, based on which the volumetric water content is defined, is also not 100% representing the experimental PSD and can also lead to the disparity in volumetric water content.

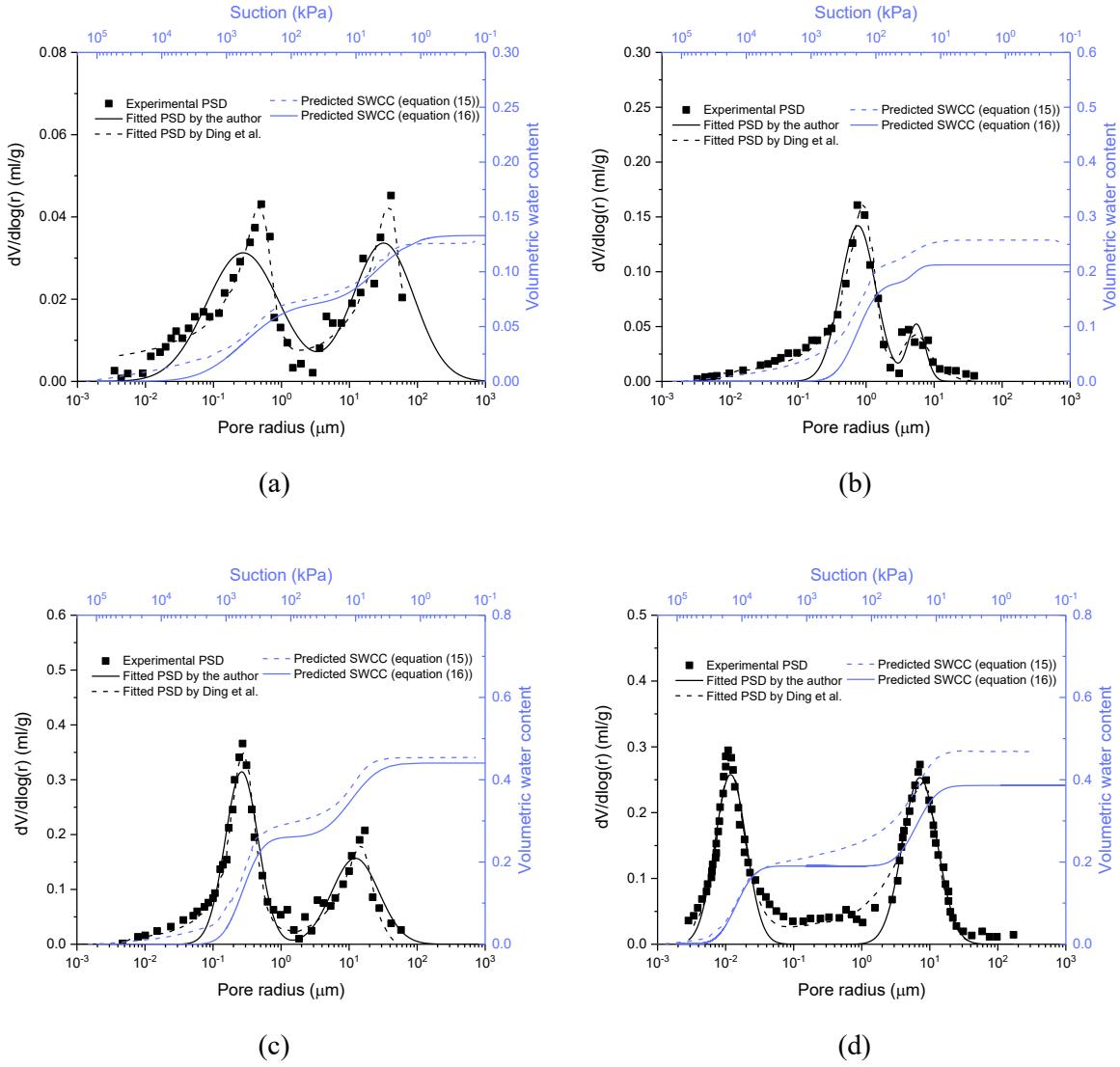

Figure 2.12 Comparison among experimental PSDs, fitted PSDs and predicted SWCCs for various soils: (a)Zhao et al. (Zhao et al. 2013; Guo-Quan et al. 2022); (b) Zhang and Li (Zhang and Li 2010; Guo-Quan et al. 2022); (c) Li and Zhang (Li and Zhang 2009; Guo-Quan et al. 2022);(d) Miguel and Bonder (Miguel and Bonder 2012; Guo-Quan et al. 2022)

In the above examples, the SWCCs predicted by the author are all based on equation (2-17) for fitting PSD and Method A to obtain SWCC. The volumetric water content is calculated within the pore radius range from 0 to $R = 2\gamma \cos\theta / s$, which is related to the pores fully filled with water. Since the fitted pore size distribution obtained from multi log normal distributions tends to reach 0 at smaller pore radius, the volumetric water content will also approach 0 at higher suction. Therefore, this method is more suitable for soils with a low residual degree of saturation. However, due to the limitation of MIP that it cannot fully represent the total pore volume in soils and the difference between fitted PSDs and original PSDs, when R is infinite, the degree of saturation is not necessarily equal to 100%. Another method (Method B) to obtain SWCC is that assuming the degree of saturation is 100% at zero suction and then deduct the pore volume not filled with water (radius from R to infinite) from

the water content in saturation condition (Simms and Yanful 2002). If the void ratio e is known, the volumetric water content at saturation condition can be defined as:

$$\theta_{sat} = \frac{e}{1+e} \tag{2-20}$$

Then the equation for SWCC can be expressed as:

$$\theta_s(s) = \theta_{sat} - \frac{\int_R^{+\infty} f(r) \cdot \mathrm{d}\log_{10} r}{V} = \theta_{sat} - \frac{\int_{\frac{2\gamma\cos\theta}{s}}^{+\infty} \frac{f(r)}{\ln 10 \cdot r} \cdot \mathrm{d}r}{1/\rho_d} \tag{2-21}$$

Both Method A and Method B are commonly used in research (Simms and Yanful 2004b; Li and Vanapalli 2021; Yan et al. 2021). As shown in Figure 2.13, generally, the SWCCs obtained from Method B can give an accurate volumetric water content when it is 100% saturation and a significant residual water content. For example, in Figure 2.13(a), SWCCs obtained by Ding et al. (Guo-Quan et al. 2022) and by method B give a volumetric water content of 0.383 at a low suction. They both show a significant residual water content even at suction as high as 10^5kPa compared with the SWCC obtained by method A. Therefore, the method B is potentially more preferable for soils with a high residual water content. There is still noticeable difference between the SWCCs obtained from Method B and those obtained by Ding et al. (Guo-Quan et al. 2022). This is because they used different fitted curves based on different fitting functions. In Figure 2.13(d), due to the ignorance of experimental pore size distribution at radius range from 0.1 to 1 micrometre when fitted by multi log normal distributions (see Figure 2.12(d)), a significant flat SWCC can be witnessed at the suction range from around 100 to around 6000kPa in the SWCC obtained from Method B.

Both Method A and Method B are commonly used in research (Simms and Yanful 2004b; Li and Vanapalli 2021; Yan et al. 2021). The selection depends on if the residual water content is important. For soils with a low residual water content (such as sand), Method A is more preferable while Method B is a better choice when a significant residual water content (such as clay) is expected. Besides, the logic of Method A is more similar to a wetting path that the water intrudes smaller pores first and then intrude larger pores when the suction decreases. Method B assumes the degree of saturation is 100% at low suction and then the water should be evacuated from larger pores when suction increases, which is similar to a drying path.

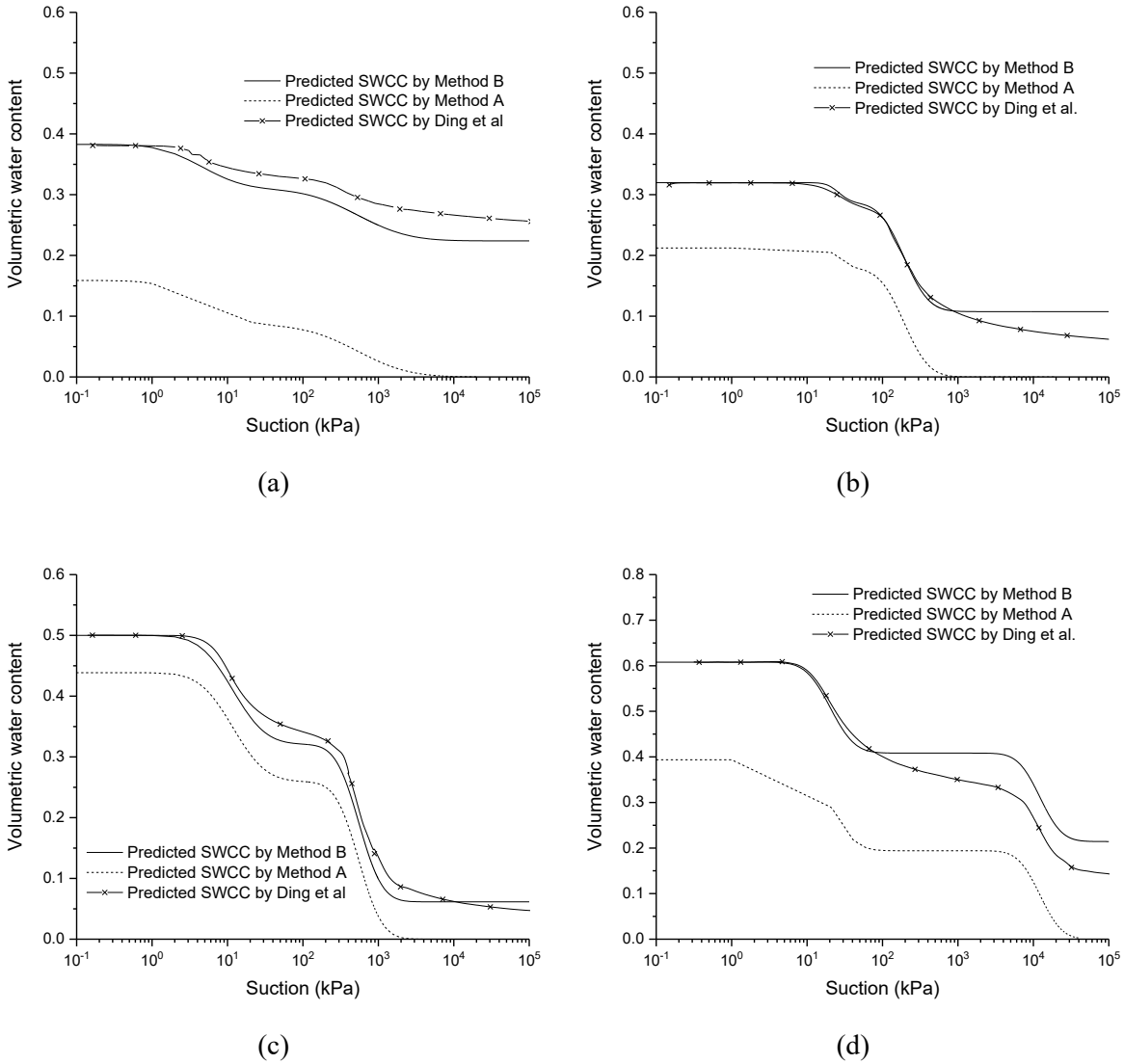

Figure 2.13 Comparison among predicted SWCCs for various soils based on different methods: (a)Zhao et al. (Zhao et al. 2013; Guo-Quan et al. 2022); (b) Zhang and Li (Zhang and Li 2010; Guo-Quan et al. 2022); (c) Li and Zhang (Li and Zhang 2009; Guo-Quan et al. 2022);(d) Miguel and Bonder (Miguel and Bonder 2012; Guo-Quan et al. 2022)

Another example of using both Method A and Method B to predict SWCC is given below based on the experimental PSD of Guilin lateritic clay (see Figure 2.14) (Sun et al. 2016a; You and De-an 2017). The basic properties and fitted parameters for PSD are shown in Table 2.4. As shown in Figure 2.15, the predicted SWCC by Method B has a much better performance when the suction is smaller than 10000 kPa, but significantly overestimates the residual degree of saturation at a higher suction and the degree of saturation maintains a very high value even suction goes to 100000 kPa. In comparison, the SWCC predicted by Method A fails to reach 100% saturation at a low suction, but its performance gets better in higher suction and no undesired residual water content can be seen.

Table 2.4 basic properties (Sun et al. 2016a; You and De-an 2017) and fitted parameters for Guilin lateritic clay

No.	Void ratio	Specific gravity	Parameters						
			a_1	μ_1	σ_1	a_2	μ_2	σ_2	R^2
5	1.0	2.74	6.5	3.558	0.900	0.011	-3.579	0.330	0.94

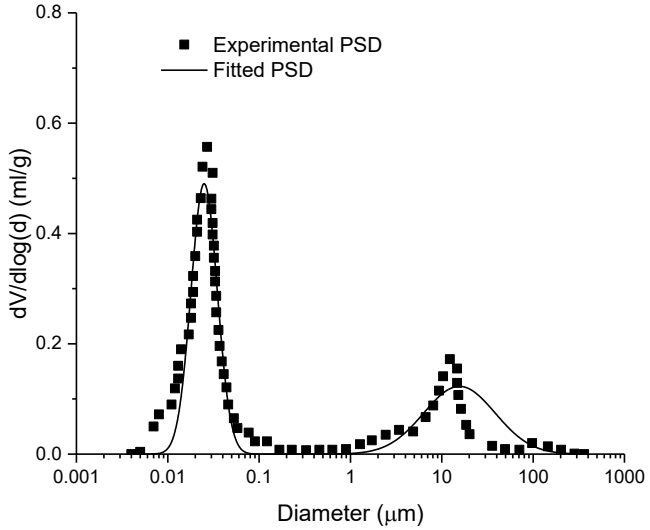

Figure 2.14 PSD for Guilin lateritic clay and fitted PSD

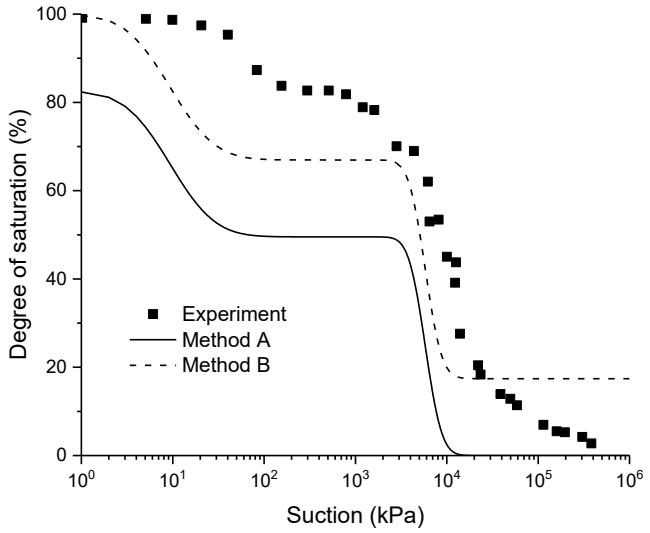

Figure 2.15 Comparison between experimental SWCC(You and De-an 2017) and predicted SWCC

Predicting SWCC from PSD can also be used to study the evolution of SWCC induced by microstructural change when the evolutional properties of PSD are determined. Since pore size distribution is sensitive to void ratio (Casini et al. 2012; Burton et al. 2014; Gao et al. 2020a; Wang et al. 2020; Zhai et al. 2020) , the evolution of SWCC can be determined based

on PSDs at different void ratios. The experimental data of lean clay (Li and Zhang 2009) is adopted here as an example of presenting SWCC evolution induced by void ratio change. The samples were compacted to different void ratios. The fitting parameters proposed by Li and Zhang (Li and Zhang 2009) are presented in Table 2.5. As shown in Figure 2.16, the fitting curves keep the bimodal property of PSDs, so the predicted SWCCs still have a platform in degree of saturation that split the transition zone into two parts. There is slight difference among each other which is related to the difference in their PSDs. If large number of SWCCs at specific void ratios are plotted in a three-dimensional space of suction, degree of saturation and void ratio, they can form a soil water characteristic surface (Tarantino 2009; Tsiampousi et al. 2013; Guoqing et al. 2020). Furthermore, if the relationship between fitting parameters and void ratios are determined, it is not hard to predict the SWCC at a specific void ratio.

Table 2.5 Fitting parameters for lean clay (Li and Zhang 2009) based on equation (2-17)

Void ratio	$f(r)$	Parameters					
		a_1	μ_1	σ_1	a_2	μ_2	σ_2
1.13	$f(r)=\frac{\mathrm{d}F(r)}{\mathrm{d}r}$	0.170	0.91	0.28	0.22	-0.74	0.46
1.05		0.130	0.87	0.28	0.23	-0.66	0.49
1.00		0.120	0.88	0.33	0.24	-0.72	0.46
0.76		0.035	0.84	0.38	0.24	-0.73	0.46

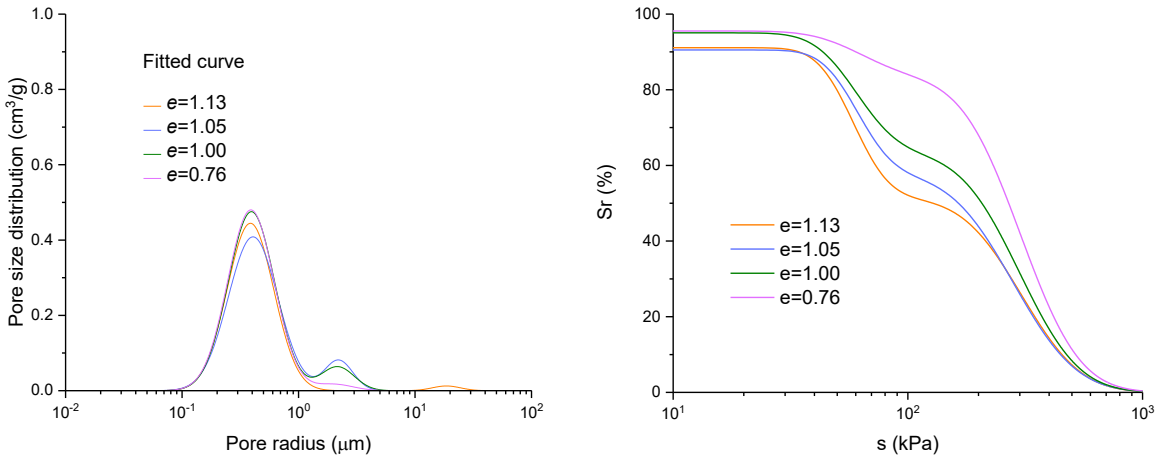

(a) (b)

Figure 2.16 PSDs at various ratios and corresponding SWCCs: (a) PSDs (Li and Zhang 2009); (b) SWCCs

2.4.2.2 Calculating Bishop's effective stress coefficient from PSDs

The effective stress of unsaturated soils ξ^* (Bishop 1959) is usually defined as:

$$\xi^* = \bar{\xi} + \chi \cdot s \tag{2-22}$$

where $\bar{\xi}$ is the net mean stress and χ is the Bishop's effective stress parameter. Vaunat and Casini (Vaunat and Casini 2017) proposed a new method to calculate the χ from pore size distributions. The incremental work input δw during soil deformation can be defined as:

$$\begin{gathered}\delta w = -p\frac{\delta V}{V} + u_{\mathrm{w}}\frac{\delta V_{\mathrm{w}}}{V} + u_{\mathrm{a}}\frac{\delta V_{\mathrm{a}}}{V} \\ (\delta V = \delta V_{\mathrm{V}} + \delta V_s = \delta V_{\mathrm{V}} = \delta V_{\mathrm{w}} + \delta V_{\mathrm{a}})\end{gathered} \tag{2-23}$$

where V is the total volume; V_{V} is the total pore volume; p is the total mean stress; u_{w} is the water pressure; u_{a} is the air pressure; V_{w} is the water volume; V_{a} is the air volume. δ represents the change of volume. The total volume change δV is equal to the total pore volume change δV_V due to the incompressibility of the soil particle. The total pore volume change δV_V is composed of water volume change δV_{w} and air volume change δV_{a}. The water volume change δV_{w} also has two components. Firstly, there is the water volume change induced by pore volume change, which is called δV_{w1} and assumed to be proportional to the δV_{w} with a coefficient χ. And secondly there is the water volume change induced by suction change δV_{w2}. The water volume change δV_{w} then can be expressed as:

$$\delta V_{\mathrm{w}} = \delta V_{\mathrm{w1}} + \delta V_{\mathrm{w2}} = \chi \delta V_V + \delta V_{\mathrm{w2}} \tag{2-24}$$

Take equation (2-24) into equation (2-23), then the work input can be rewritten as:

$$\delta w = -[p - \chi u_{\mathrm{w}} - (1-\chi)u_{\mathrm{a}}]\frac{\delta V}{V} - (u_{\mathrm{a}} - u_{\mathrm{w}})\frac{\delta V_{\mathrm{w2}}}{V} \tag{2-25}$$

The term corresponding to volumetric strain $\frac{\delta V}{V}$ is $[p - \chi u_{\mathrm{w}} - (1-\chi)u_{\mathrm{a}}]$ and has a same form with equation (2-22). Then the Bishop's effective stress parameter can be defined as:

$$\chi = \frac{\delta V_{\mathrm{w1}}}{\delta V_{\mathrm{V}}} = \frac{\delta V_{\mathrm{w1}} / V_{\mathrm{s}}}{\delta V_{\mathrm{V}} / V_{\mathrm{s}}} = \frac{\delta e_{\mathrm{w1}}}{\delta e} \tag{2-26}$$

where δe_{w1} is the water ratio change (ratio of water volume change and solid volume) related to pore volume change and δe is the void ratio change. Since e_{w1} is related to the water volume

stored in pores, it can still be calculated through the way SWCC is obtained and δe_{w1} is actually the difference of e_{w1} for each PSD (see Figure 2.17), when PSDs are defined as $\mathrm{d}F(r)/(V_s \cdot \mathrm{d}r)$ (scaled by void ratio). A similar approach was also proposed by Niu et al. but considered the removal of the water ratio for disconnected water in micropores (Alonso et al. 2010; Niu et al. 2021).

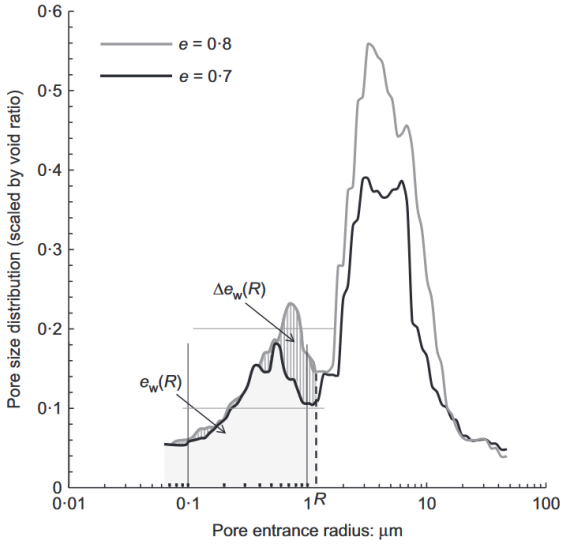

Figure 2.17 Illustration of δe_{w1} (Vaunat and Casini 2017)

Based on the PSDs at void ratio of 1.00 and 0.76 (see Figure 2.16), Figure 2.18 presents the comparison among Bishop's effective stresses χ obtained by various methods, including the χ obtained from fitted PSDs (from Figure 2.16), the χ computed from original PSDs obtained by MIP (Li and Zhang 2009; Vaunat and Casini 2017), the χ assumed to be equal to degree of saturation which is widely used in many constitutive models (Wheeler et al. 2003; Alonso et al. 2010; Lloret-Cabot et al. 2013) and the χ defined as the function of degree of saturation raised to the power of a parameter c (c=5.5 in Figure 2.14) (Alonso et al. 2010; Vaunat and Casini 2017). Both the χ computed from fitted PSDs and original PSDs are identical to the χ calculated by $(S_r)^{5.5}$ despite slight difference in value. All of them increase with increasing degree of saturation but show a great gap compared with the χ equal to degree of saturation and the disparity is only narrowed at higher degree of saturation. Therefore, models using χ equal to degree of saturation will significantly overestimate the effective stress compared with models where χ is calculated from PSDs. It can also be noticed that for χ obtained from PSDs, the χ is not 0 at zero degree of saturation but can only values at a higher degree of saturation. For example, the χ obtained from fitted PSDs does not show any value until the degree of saturation reached 0.62 and any χ on the left side of 0.62 is negative (not shown in the figure) which is not possible in reality because the suction can only make a positive or zero (when suction is at 10^6kPa) contribution to effective stress (Bishop 1959; Li 2003; Mašín 2010; Baille et al. 2014). The physical meaning of the initial degree of saturation that starts to show positive χ is that when a soil has PSDs as shown in Figure 2.16 at void ratios of 1.00 and 0.76, its degree

of saturation must be equal or higher than 62% to have positive contribution of suction, otherwise this contribution is always 0 because χ is 0 when the degree of saturation is below 62%.

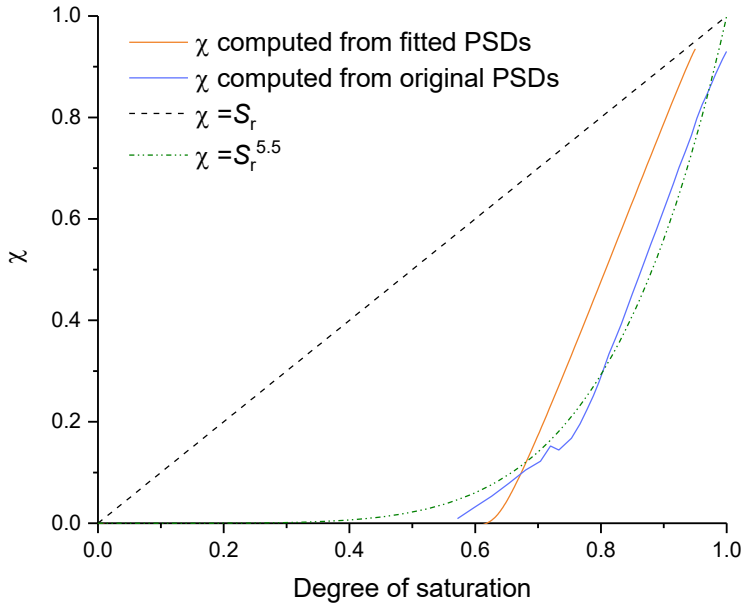

Figure 2.18 Comparison among the χ calculated based on different methods (Li and Zhang 2009; Vaunat and Casini 2017)

2.5 Experimental investigation on soils' hydro-mechanical behaviour

Triaxial tests and SWCC tests are commonly conducted to study the hydro-mechanical behaviour of unsaturated soils. Details of these two tests are presented in the following sections.

2.5.1 Saturated and unsaturated triaxial tests

A triaxial test is a common laboratory method to determine the mechanical behaviour of soils, such as shear strength, cohesion, internal friction angle, critical state and failure (Bishop and Wesley 1975; Rahardjo et al. 2004; Houston et al. 2008; Ng et al. 2012). This test can be conducted in either saturated or unsaturated condition and under various stress conditions to monitor the stress-strain behaviour and change of water content of soils. There are three typical types of triaxial tests including Unconsolidated-Undrained (UU), Consolidated-Undrained (CU) and Consolidated-Drained (CD) tests. During the UU test, the soil sample is sheared without drainage and any previous drainage and consolidation under the applied confining stress. Therefore, the UU test is a quick test for assessing the short-term stability of soils (Chen and Kulhawy 1993; Bol et al. 2019). The CU test allows the sample to consolidate under a predetermined confining stress and then to be sheared without drainage. This test is widely used in embankments, foundations and slopes which are subjected to long-term loading but have a low possibility of significant drainage in the short term (Stróżyk and Tankiewicz 2014;

Casey et al. 2016). The CD test allows the soil sample to consolidate under a confining stress and be sheared under drained conditions. The behaviour of soils during a CD test is similar to that over a long period, which is essential for the study of soil stability and settlement (Fredlund et al. 1978; Rahardjo et al. 2004; Sivakumar et al. 2010). More details about CD tests are presented below.

2.5.1.1 Devices for saturated and unsaturated triaxial tests

A Conventional Saturated GDS device and an Unsaturated GDS device are used to conduct triaxial tests. More details about these two devices are presented in Chapter 3.

2.5.1.2 Saturation and suction equilibrium

Soil samples must be fully saturated or prepared to a predetermined suction in the first stage of CD tests. An effective stress of 10 kPa is placed on soil samples during saturation to prevent the samples from accidental swelling (Rahardjo et al. 2004; Maleki and Bayat 2012). For suction equilibrium, a net mean stress of 20 or 25 kPa is commonly used before unsaturated consolidation and shearing (Ng and Chiu 2001; Sun et al. 2004; Casini 2008; Maleki and Bayat 2012).

2.5.1.3 Shearing

For CD triaxial tests, it is important to predetermine the displacement rate for shearing and the condition when tests should be terminated. Details of both are presented below.

2.5.1.3.1 Displacement rate

The displacement rate, which is the speed of loading platform, must be carefully selected for the CD tests to avoid excess pore water pressure during shearing. If the displacement rate is too high, an undrained condition can occur because the water cannot be discharged from soil pores before the further displacement takes place, which causes the pore water pressure to build up and change of matric suction (Ho and Fredlund 1982; Sun et al. 2016b). Therefore, the accuracy in measurement of undrained behaviour of soils can be disturbed. The displacement rate selected is highly related to the soil types. Sands usually have larger pores and higher permeabilities, so water can be easily drained during shearing, as a result of which a higher displacement rate can be selected while clays with smaller pores and lower permeabilities are quite the contrary. Some displacement rates chosen for various soil types are collected from publications and presented in the table below.

Table 2.6 Displacement rates from publications

References	Soil Types	Displacement rates
(Fredlund and Rahardjo 1993)	Silty Sand	0.006 mm/min
(Shear strength characteristics of Shiraz unsaturated silty clay. 2009)	Silty clay	0.0067 mm/min
(Zhang et al. 2016)	Nanyang expansive soil	0.00192 mm/min
(Rahardjo et al. 2004)	Sandy Clay	0.0009 mm/min
(Ng et al. 2017)	Low plasticity clay	0.0019 mm/min
(Sivakumar et al. 2010)	Kaolin	0.07% /h
(Anantanasakul et al. 2012)	ML	0.018% /min

2.5.1.3.2 Critical state

The critical state describes the state when the axial strain keeps flowing while there is no more change in stress or volume during shearing (Sivakumar 1993; Wheeler and Sivakumar 1995; Estabragh and Javadi 2008). Therefore, CD tests are usually terminated after the critical state has been reached. Different soil types can have very different axial strains at which the critical state is reached. The axial strain at critical state for sands and silts can be between 10% to 30% (Shear strength characteristics of Shiraz unsaturated silty clay. 2009; Zhao and Zhang 2014; Beren et al. 2020), and 5% to 15% for clays (Toll and Ong 2003; Shear strength characteristics of Shiraz unsaturated silty clay. 2009; Stróżyk and Tankiewicz 2014; Scaringi and Di Maio 2016). A common practice is terminating CD tests when the axial strain reaches 20%. Although not all soils will be completely at critical state at this axial strain, the changing rates of the deviatoric stress and volumetric strain are generally small at this axial strain (Liu et al. 2020a).

2.5.1.4 Shear strength

Shear strength is one of the most important hydro-mechanical properties of unsaturated soils. The definition of shearing strength and the effects of net normal stress and suction on shear strength are summarized in the following below.

2.5.1.4.1 Definition of shear strength

Shear strength of soils is defined as the maximum resistance on the failure plane to deformation by shear stress and is usually described by the Mohr-Coulomb (M-C) criterion. For saturated soils, the equation for shear strength is defined as (Lu and Likos 2004):

$$\tau_f = c' + (\zeta - u_w)_f \tan\phi' \tag{2-27}$$

where τ_f is the shear strength, c' is the effective cohesion, $(\zeta - u_w)_f$ is the effective normal stress on the failure plane at failure, and ϕ' is the effective angle of internal friction. For unsaturated soils, since suction is another important factor that will contribute to effective stress, an equation for unsaturated soils was proposed by Bishop (Bishop 1959) as below:

$$\tau_f = c' + (\zeta - u_a)_f \tan\phi' + \chi(u_a - u_w)\tan\phi' \tag{2-28}$$

where $(\zeta - u_a)_f$ is the net normal stress on the failure plane at failure, χ is the Bishop's effective stress coefficient, and $(u_a - u_w)$ is the matric suction. Another equation for unsaturated soils' shear strength proposed by Fredlund et al.(Fredlund et al. 1978) is:

$$\tau_f = c' + (\zeta - u_a)_f \tan\phi' + (u_a - u_w)\tan\phi^{b} \tag{2-29}$$

where ϕ^{b} is the angle of friction related to suction. By comparing equation (2-29) and (2-28), it can be seen that:

$$\tan\phi^{b} = \chi \tan\phi' \tag{2-30}$$

since ϕ' is a constant and χ can vary with suctions within the range from 0 to 1 (Bishop 1959; Wheeler et al. 2003; Alonso et al. 2010), ϕ^{b} is not necessarily a constant but can change with suction and might be smaller than ϕ'.

2.5.1.4.2 Effects of net normal stress on shear strength

Net normal stress is an important factor that will affect the shear strength of soils. A higher net normal stress (radial stress) during shearing will normally result in a higher axial stress at failure and a higher shear strength. This can be described by the Mohr-Coulomb failure envelopes.

2.5.1.4.3 Effects of suction on shear strength

As indicated in equation (2-29), suction can make a positive contribution to the shear strength. However, a higher suction will not always lead to a higher shear strength because ϕ^{b} can decrease with suction as described in equation (2-30). The effects of suction on shear strength depend on types of soils. Soil types can generally be classified into sand, silt and clay. For all types of soils, ϕ^{b} is consistent to ϕ' when the applied suction is smaller than the air entry value (Vanapalli et al. 1996; Lu and Likos 2004; Ng et al. 2017). Within this regime, the

increase of shear strength is linear to the increase of suction. When suction is higher than air entry value, ϕ^b is not identical to ϕ' but starts to decrease. Different types of soils can have different behaviour in this regime (Gao et al. 2020b), as shown in Figure 2.19. For clays (including silty clays), the shear strength still increases with suction with a lower increasing rate compared to that before air entry value. This is because, χ, even though decreases with suction in this regime, it still remains at a relatively high level due to clays' good water retention ability, as a result of which $\chi(u_a - u_w)$ still increases with suction. Therefore, the contribution of suction to shear strength will still increase with the suction. For silts, the shear strength will first increase with suction to a moderate level and then remains almost unchanged with higher suctions (Gao et al. 2020b). For sands, since interparticle pore water menisci dramatically change during desaturation when suction increases, χ will drop significantly and this leads to the decrease of $\chi(u_a - u_w)$ when suction increases. Therefore, the contribution of suction to shear strength actually decreases with suction (Lu and Likos 2004). However, since the minimum value of χ is zero, the general shear strength will never be smaller than that in saturated condition.

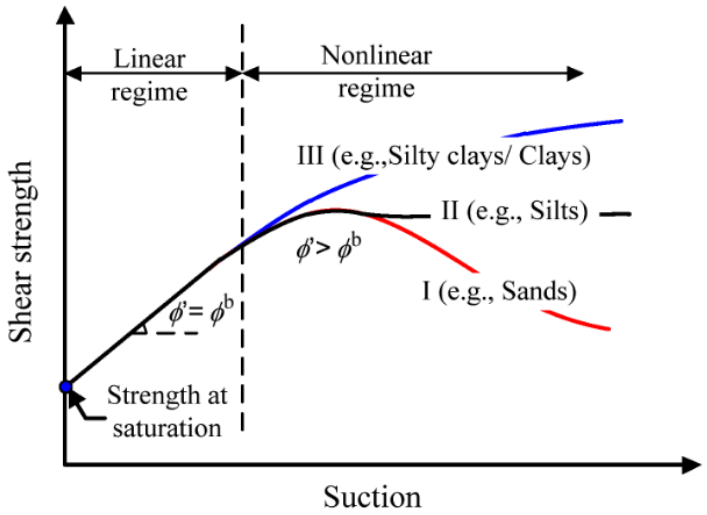

Figure 2.19 Relationship between shear strength and suction for unsaturated soils (Gao et al. 2020b)

2.5.2 Soil-water characteristic curve (SWCC)

The definition of soil-water characteristic curve (SWCC), factors affecting SWCC, experimental and modelling methods for obtaining SWCC are summarised in the following sections.

2.5.2.1 Definition of soil-water characteristic curve

Soil-water characteristic curve (SWCC) is also known as soil-water retention curve (SWRC). It describes the relationship between the water content (or degree of saturation) of soils and the water potential (or suction) of soils. SWCC is one of the most important hydraulic properties of unsaturated soils. It is widely applied in many areas such as studying soil suction (Leong and Rahardjo 1997; Barbour 1998; Miguel and Bonder 2012), effective stress (Wheeler et al. 2003; Lloret-Cabot et al. 2013), shear strength (Vanapalli et al. 1996; Shen et al. 2009; Gao et al. 2020b), settlement (Lloret et al. 2003; Ng et al. 2017) and hydraulic conductivity (Juang and Holtz 1986; Romero et al. 1999; Zhai and Rahardjo 2015).

SWCC usually has a 'S' shape and can be separated into three zones including boundary effect zone, transition zone and residual zone, as shown in Figure 2.20. At low suctions, the SWCC sits within the boundary effect zone where the soil is nearly saturated and most of the soil pores are filled with water. When the suction is beyond the air entry value, the water content (or degree of saturation) starts to decrease sharply with increasing suctions, which means the water is evacuated from larger pores. The corresponding area is called transition zone. When suction reaches a specific value, the curve becomes more flatten again in the residual zone. In this zone, the water is primarily held in small pores, disconnected pores or at menisci and cannot be easily evacuated, which is regarded as residual water content.

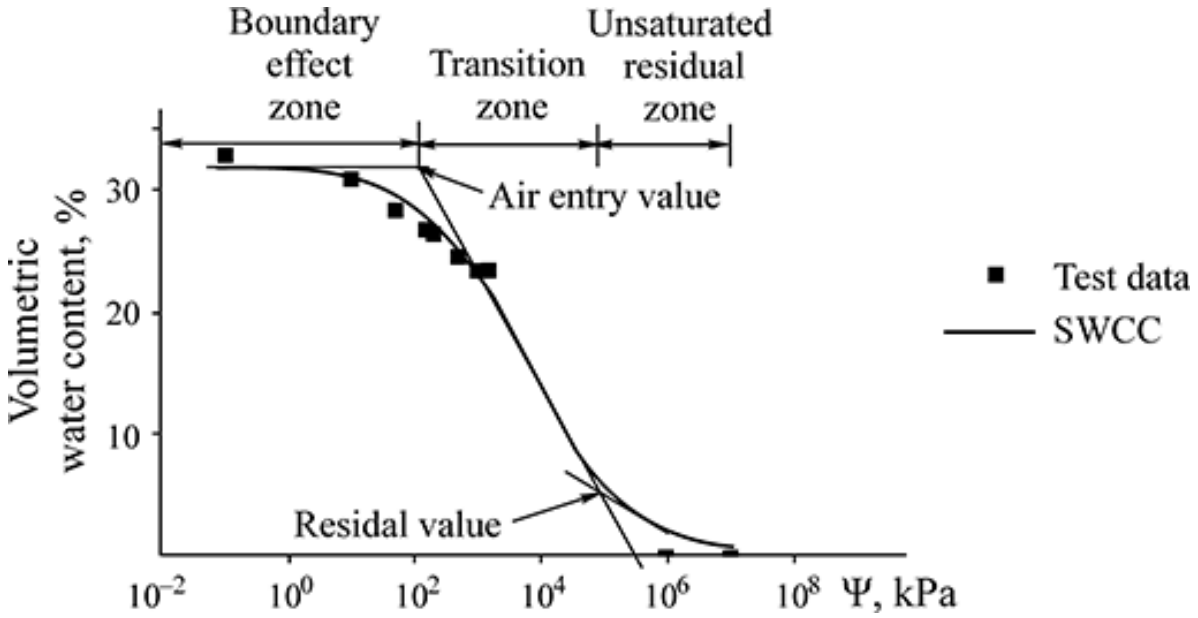

Figure 2.20 Illustration of SWCC (Ma et al. 2021)

2.5.2.2 Factors affecting SWCC

Three factors that influence the shape of SWCC are summarized in this section.

2.5.2.2.1 Soil texture

Soils with different proportions of sand, silt and clay have different SWCCs. Clay usually has the smallest particles and pore sizes, it thus has a much better ability in retaining water. As shown in Figure 2.21, a higher suction is required for clay to reach transition zone and the water content is still the highest compared with sand and silt at high suctions. Besides, clay also has the highest residual water content. Due to the largest particles and pore sizes, sand has the worst performance in retaining water. Therefore, it is obvious that the least suction is required to desaturate sand. The pore size and particle size of silt are between sand and clay, so silt has a medium performance in water retention behaviour. Overall, if a soil sample has a higher proportion of clay, it tends to have a better water retention behaviour while the opposite occurs when more sand is contained.

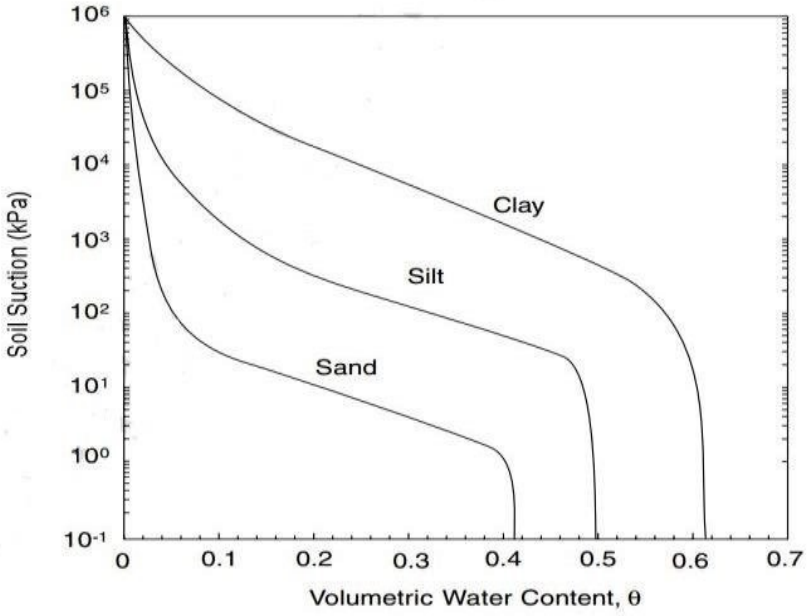

Figure 2.21 Illustration of SWCCs for sand, silt and clay (Likos et al. 2010)

2.5.2.2.2 Soil structure

The shape of SWCC is also highly related to the soil structure, especially the pore size distribution. For soils with single porosity (only one dominant pore size), their SWCCs usually have a unimodal shape that has a single and continuous transition zone as shown in Figure 2.22 (Likos et al. 2010; Wijaya and Leong 2016; You and De-an 2017). Soils with double porosity have two significant dominant pore sizes (Burton et al. 2014; Li et al. 2020; Navarro et al. 2020a). One is related to large pores (macropores) and the other is related to small pores (micropores). The double porosity will split the transition zone into two separate parts with a relatively flat zone in between (see Figure 2.22) (Bagherieh et al. 2009; Russell 2010; Casini et al. 2012). This happens because, for a drying path, water is first evacuated from large pores when suction reaches air entry value and then a significant decrease in water content can be

witnessed which is the first part of the transition zone. With the increase of suction, water will keep being evacuated but the decrease of water content will slow down when water maintained in pores larger than the first dominant pore size (for larger pores) has all been evacuated. This is because after the first dominant pore size, a decrease of pore volume occurs and less water available for evacuation. Since the pore volume will remain at a relatively low level until a rise in pore volume occurs when reaching the second dominant pore size (for small pores), there is a flat platform in SWCC within this suction range before the suction is high enough to evacuate the water in small pores (the second part of transition zone).

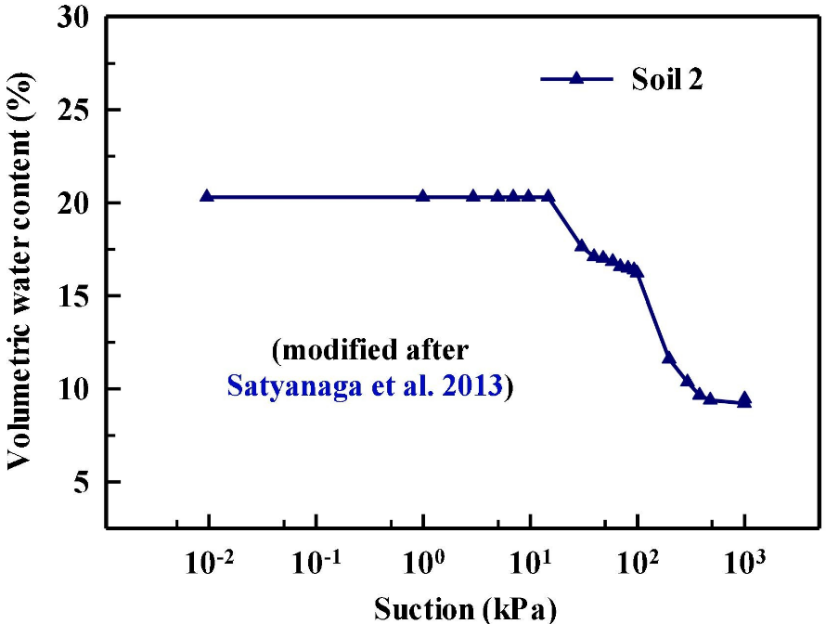

Figure 2.22 Example of SWCC with bimodal PSD (Li and Vanapalli 2021)

2.5.2.2.3 Hysteresis

Hysteresis refers to the phenomenon where the SWCC of a specific soil varies depending on whether the soil is undergoing wetting or drying (Groffman and Tiedje 1988; Wheeler et al. 2003; Pham et al. 2005). Due to hysteresis, there exist two distinct curves: the one for drying is called main drying curve while the other for wetting is main wetting curve. Significant difference can be seen between these two curves as shown in Figure 2.23. The drying curve maintains a much higher water content compared to wetting curve at the same suction. This difference will only be narrowed at very high suctions.

There are many reasons behind hysteresis. The first reason is related to the inhomogeneity of pore size distribution which is also referred as ink bottle effects (Likos and Lu 2004; Chen et al. 2024; Higo and Kido 2024). Since soil pores are randomly distributed in soil structure, it is common to see large pores (macropores) are connected to small pores (micropores). Small pores can serve as narrow throats like a narrow neck in an ink bottle though which a larger reservoir (macropores) is accessed. During drying, water is first evacuated from

the large pores which only requires a small suction. However, due to the existence of narrow throats (small pores) seated among large pores, not all water can be fully removed from large pores because a higher suction is required for water to pass through the narrow throats before being fully released. Therefore, a delay in water content evacuation can be seen in a drying curve.

The variation of contact angles at the solid and liquid interface is another reason for the hysteresis. When contact angles are less than 90°, a smaller contact angle indicates a much hydrophilic solid-liquid interaction while in the opposite, contact angles higher than 90° indicate a nonwetting and hydrophobic interaction (Likos and Lu 2004). For a specific soil, its contact angle during drying can be significantly different from that during wetting. Contact angles during drying can be much lower than the wetting angles (Letey et al. 1962; Likos and Lu 2004; Eral et al. 2013; Eral et al. 2013), which makes soil more hydrophilic and more easier to retain water. Besides, swelling and shrinkage will affect the soil fabric during wetting and drying (Likos and Lu 2004). The soil fabric can have very different responses to drying and wetting (Li and Zhang 2009; Wang et al. 2020; Li et al. 2021), which results in the difference between drying and wetting curves.

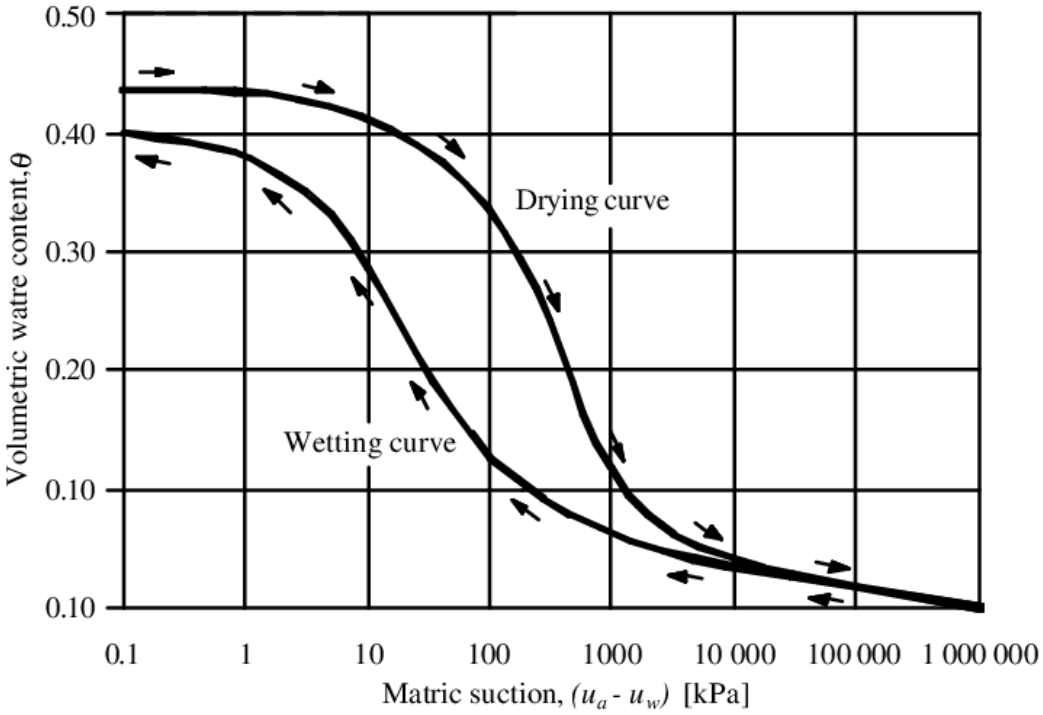

Figure 2.23 Illustration of hysteresis in SWCC (Vanapalli et al. 2002)

2.5.2.3 Experimental methods for obtaining SWCC

Several commonly used experimental methods for obtaining are summarised in this section.

2.5.2.3.1 Tensiometers

A tensiometer (Stannard 1992; Lu and Likos 2004) is a water-filled tube with two ends, as shown in Figure 2.24. One end is a High-Air-Entry (HAE) ceramic tip and the other end is usually a sensor for measuring suction. When the tensiometer is inserted in the soil, water transfers between the tensiometer and soil until equilibrium is reached at which the sensor on the other end detects the suction. The testing range of suction with tensiometers is subjected to the air-entry pressure of the ceramic tip and the cavitation which occurs at high negative pressures. Therefore, early tensiometers are only reliable when suction is smaller than 80 kPa (Lu and Likos 2004). In recent decades, high-capacity tensiometers (Guan and Fredlund 1997; Tarantino and Mongiovì 2001) have been invented and can give a testing range up to 1500 kPa, but in general, tensiometers are meant for low suction detection not for very high suctions.

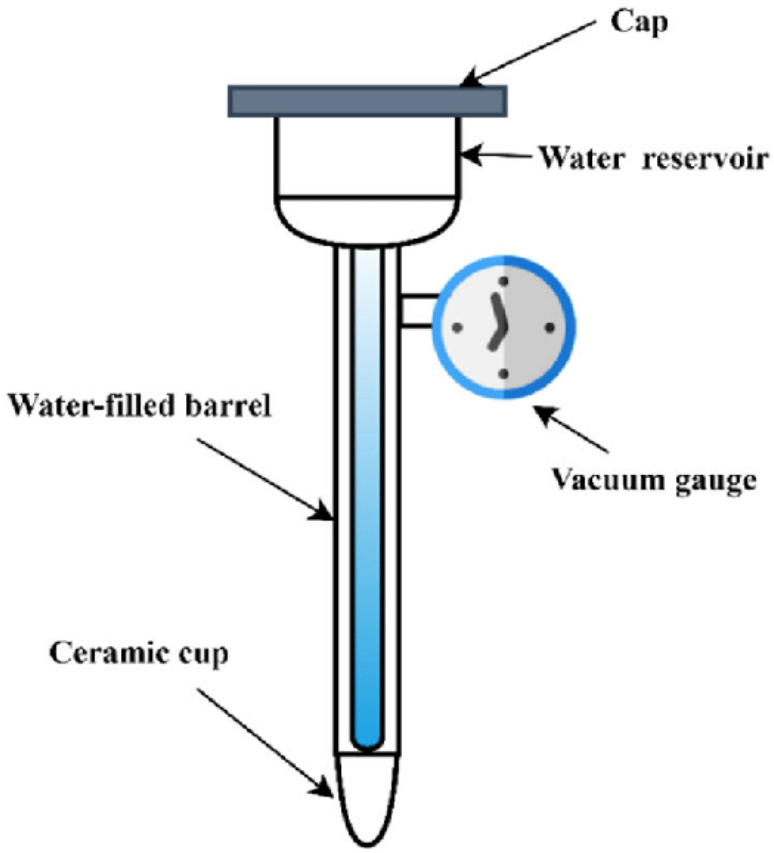

Figure 2.24 Illustration of a tensiometer (Rasheed et al. 2022)

2.5.2.3.2 Axis translation techniques

Axis translation techniques are another commonly used methods for obtaining suctions. By elevating pore air pressure while maintaining pore water pressure with a HAE ceramic, the suction ($u_a - u_w$) can be directly controlled (Lu and Likos 2004). Since the pore water pressure does not have to be negative, these techniques also avoid the possibility of cavitation. During

testing, a soil sample is placed on the upper surface of a saturated HAE ceramic and exposed to air pressure while the bottom surface of the HAE is directly connected to water pressure, which allows the transmission of sample water content with external water. When increasing the air pressure, the water content in the sample will be drained and pass through the HAE ceramic pores until equilibrium at which both the suction and the water content can be determined. To guarantee the smooth water drainage, the air pressure cannot be higher than the air entry value of the ceramic, which puts a limit on the testing range (usually up to 1500 kPa).

2.5.2.3.3 Electrical and thermal conductivity sensors

The electrical and thermal conductivities can be measured to predict the water content considering they are direct functions of water content. From the estimated water content, the matric suction can be obtained by correlation with a predetermined calibration curve (Lu and Likos 2004). The testing range of this method is from 0 to several hundred kPa. Therefore, it is basically for low suction monitoring.

2.5.2.3.4 Chilled-mirror hydrometers

Chilled-mirror hydrometers are one of the humidity measurement techniques. An example of a hydrometer is shown in Figure 2.25. The principle of using this device is to obtain pore water potential (suction) based on its relationship with partial vapor pressure or relative humidity (Gee et al. 1992) , which is defined by Kelvin's equation:

$$s = -\frac{\Re T}{\upsilon_w \omega_\upsilon} \ln(\mathrm{RH}) \tag{2-31}$$

where s is the soil suction, $\Re$ is the universal gas constant (8.314 J/mol·K), T is absolute temperature, υ_w is the specific volume of water, ω_υ is the molecular mass of water vapor and RH is the relative humidity. For chilled-mirror hydrometers, the dew point, which is the temperature at which air becomes saturated with moisture and water vapor condenses into liquid, is accurately measured, based on which the humidity of the air and suction can be determined. Chilled-mirror hydrometers usually have a very wide testing range up to several hundred MPa (Lu and Likos 2004; Tripathy et al. 2014a).

Figure 2.25 Illustration of a chilled-mirror hygrometer

2.5.2.3.5 Filter paper techniques

Filter paper techniques are reliable and relatively simple methods for indirect measurement of the soil suction (including 'noncontact' method and 'contact method' as shown in Figure 2.26). The filter paper can exchange water content with that in soils. By measuring the amount of water transferred from the soil sample to an initially dry filter, the suction can be estimated through a predetermined calibration curve for the particular type of filter paper used (Likos and Lu 2002; Lu and Likos 2004; Bulut et al. 2012). The testing range of this technique is from 1000 to 500,000 kPa, which means it is more reliable for higher suctions (Lu and Likos 2004).

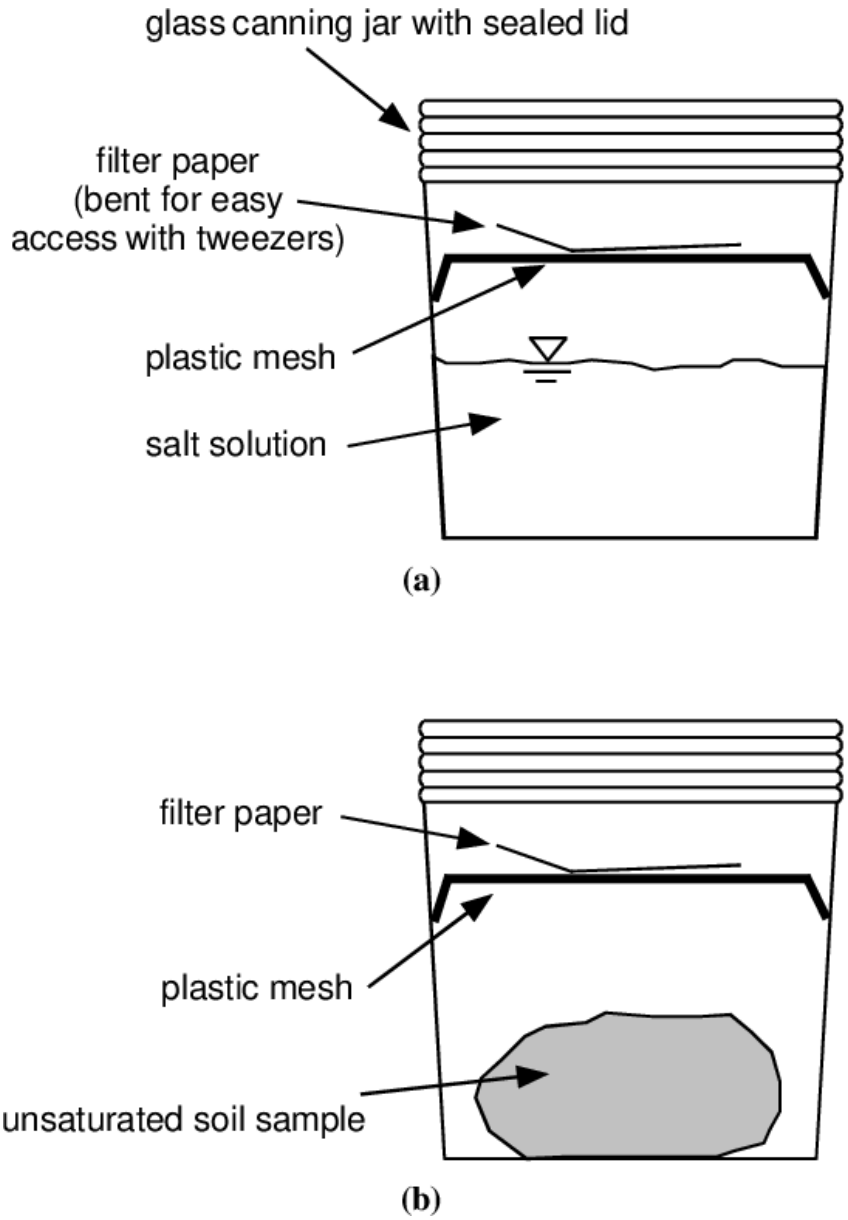

Figure 2.26 Illustration of filter paper techniques (Lu and Likos 2004)

2.5.2.4 Modelling methods for obtaining SWCC

Modelling methods for obtaining SWCC include empirical methods based on fitting and theoretical methods established according to the soil microstructure and the three-phase relationship of soils. Details about these two methods are presented in the following sections.

2.5.2.4.1 Empirical models

Empirical models are mostly proposed by researchers based on observations from a great mass of experimental data. Those empirical models normally use mathematic functions with several fitting parameters which have no physical meanings to describe the relationship

between suction and water content (or degree of saturation). Some typical models have already been presented in Table 2.1.

2.5.2.4.2 Theoretical models

Different from empirical models, theoretical models consider the physical connection between suction and water content. A common practice is to use the soil microstructure (pore size distribution) to derive SWCCs (Fredlund and Xing 1994; Simms and Yanful 2004b; Luo et al. 2024). Details of these models have been summarized in Section 2.4.2.1.

2.6 Constitutive models for hydro-mechanical behaviour

Constitutive modelling of hydro-mechanical behaviour has been a popular topic for decades and due to the tight connection between soil microstructure and hydro-mechanical behaviour, the effects of microstructure in constitutive modelling have also been explored by many researchers. In this section, those existing models have been classified as non-microstructure considered models and microstructure-considered models. Three typical and well-acknowledged models, including Barcelona Basic Model (BBM), Glasgow Coupled Model (GCM) and SFG Model, are illustrated in Section 2.6.1. Although no microstructure is considered in those models, they build up solid and efficient ways to reproduce or predict the hydro-mechanical behaviour of soils and can usually serve as the basic framework when the microstructure is considered. For microstructure considered models, they are grouped based on whether indirect or direct methods are used in modelling. Detailed of these methods are presented in Section 2.6.2.

2.6.1 Non-microstructure considered models

Details of three non-microstructure considered models are presented in the following sections.

2.6.1.1 Barcelona Basic Model (BBM)

Barcelona Basic Model (BBM), first proposed by Alonso et al.(Alonso et al. 1990), is a well-acknowledged and widely used elasto-plastic model for unsaturated soils. The BBM adopts two independent stress state variables including net mean stress ($\overline{p} = p - u_a$) and suction ($s = u_a - u_w$) where p is the total mean stress, u_a is the pore air pressure and u_w is the pore water pressure. One of the most important contributions of the BBM is that it provides an LC yield curve as a boundary between the elastic zone and the elasto-plastic zone, with which the hydro-mechanical behaviour of unsaturated soils can be well explained such as the elasto-plastic volume change. As shown in Figure 2.27(a), there exist two normal consolidation lines. One is related to the saturated state (s=0) and the other is related to an unsaturated state. The unsaturated normal consolidation line is defined as:

$$v = 1 + e = N(s) - \lambda(s) \ln \frac{p}{p^c} \tag{2-32}$$

where v is the specific volume, e is the void ratio, p^c is a reference stress for which $v = N(s)$ and $\lambda(s)$ is the slope of the unsaturated normal consolidation line. Both $N(s)$ and $\lambda(s)$ are variables depending on the suction. Similarly, the saturated normal consolidation line is defined when s=0. In isotropic loading, Alonso et al. (Alonso et al. 1990) believed that a specific unsaturated state on an unsaturated normal consolidation line (Point 1 in Figure 2.27(a)), is on the same yield curve with a specific saturated state (Point 3) when the mean stress is first reduced (the volume change for reloading is $dv = -\kappa \frac{dp}{p}$ where κ is the elastic stiffness parameter) to Point 2 and then saturated to Point 3. The volume change relationship can be found below:

$$v_1 + \triangle v_p + \triangle v_s = v_3 \tag{2-33}$$

where v_1 and v_3 are specific volumes at Point 1 and Point 3 respectively, $\triangle v_p$ is the specific volume change due to mean stress reduction, and $\triangle v_s$ is the specific volume change due to saturation. Taking Equation (2-32) into (2-33), the equation for LC yield surface can be derived (see Figure 2.27(b)):

$$\left(\frac{p_0}{p^c}\right) = \left(\frac{p_0^*}{p^c}\right)^{[\lambda(0)-\kappa]/[\lambda(s)-\kappa]} \tag{2-34}$$

With this LC yield curve, both the elastic and elasto-plastic behaviour can be explained based on the specific zone the stress path is within. In three-dimensional space, the yield surfaces are present in Figure 2.28. However, as pointed out by Wheeler et al. (Wheeler et al. 2002), the BBM can have difficulty of correctly matching the locations of the normal compression lines for different values of suction and the possibility of non-convexity of the yield curve.

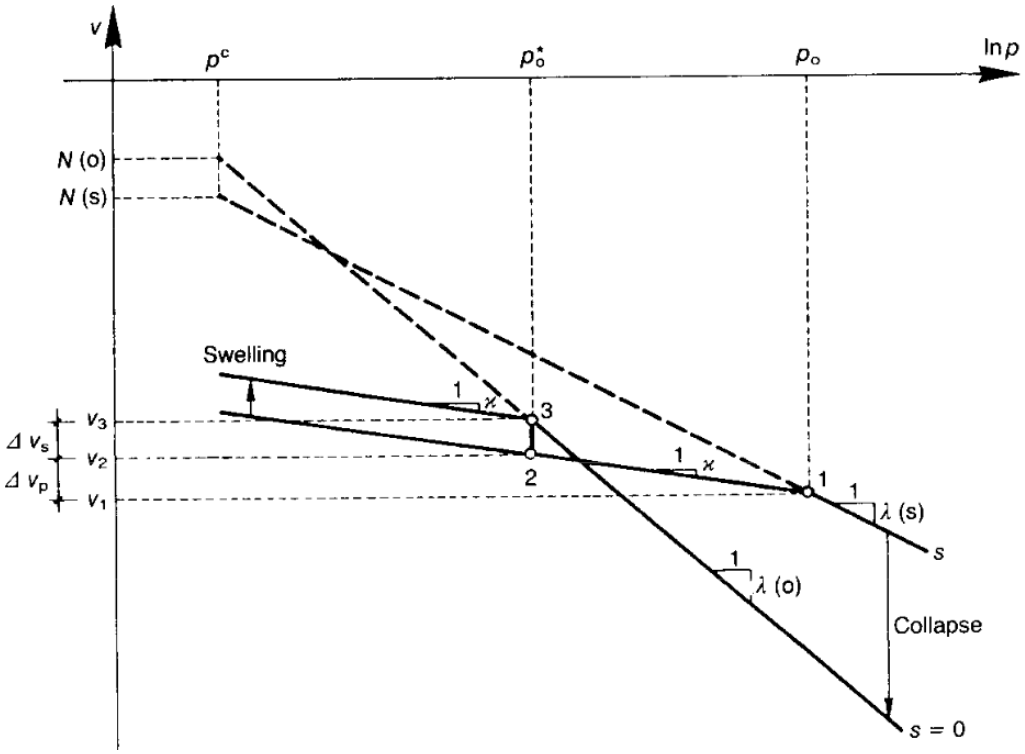

(a) compression curves for saturated and unsaturated soil

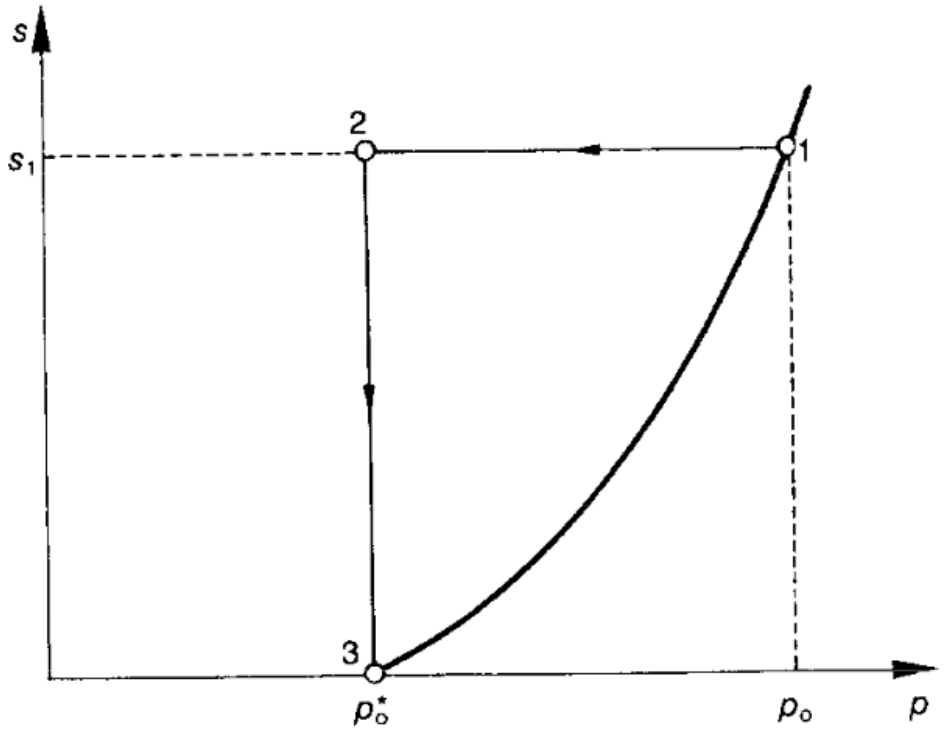

(b) stress path and yield curve in total mean stress-suction plane

Figure 2.27 Illustrations of the derivation of LC yield curve (Alonso et al. 1990)

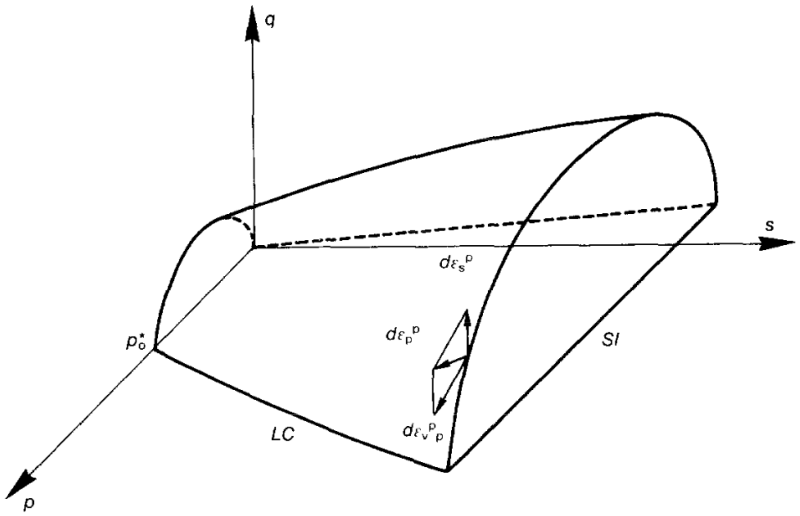

Figure 2.28 Yield surfaces of BBM in three-dimensional space (Alonso et al. 1990)

2.6.1.2 Glasgow Coupled Model (GCM)

The Glasgow Coupled Model (GCM) is a well-established model designed to address the coupled hydro-mechanical behaviour of unsaturated soils (Wheeler et al. 2003). Unlike the BBM which uses two separate stress variables, net mean stress and suction, to describe the

volume change during an isotropic loading, the GCM adopts the mean Bishop's effective stress p^* and modified suction s^*, which are defined below:

$$p^* = p + S_r(u_a - u_w) \tag{2-35}$$

$$s^* = ns \tag{2-36}$$

where n is the porosity. These variables are much more complex than net mean stress and suction, but it considers the effects of suction on stress-strain behaviour and p^* can return to the mean stress in saturated state even when suction is non-zero.

The GCM also has very different yield curves compared with the BBM. The zone of elastic behaviour and the zone of elasto-plastic behaviour are separated by three straight curves in the $p^* : s^*$ plane (see Figure 2.29), including Loading-collapse (LC) yield curve, Suction-increase (SI) yield curve and Suction-decrease (SD) yield surface. The coupling movement of these three yield curves is also considered in the GCM. The yield surfaces in three-dimensional space is presented in Figure 2.30. More details about the GCM will be presented in Chapter 6.

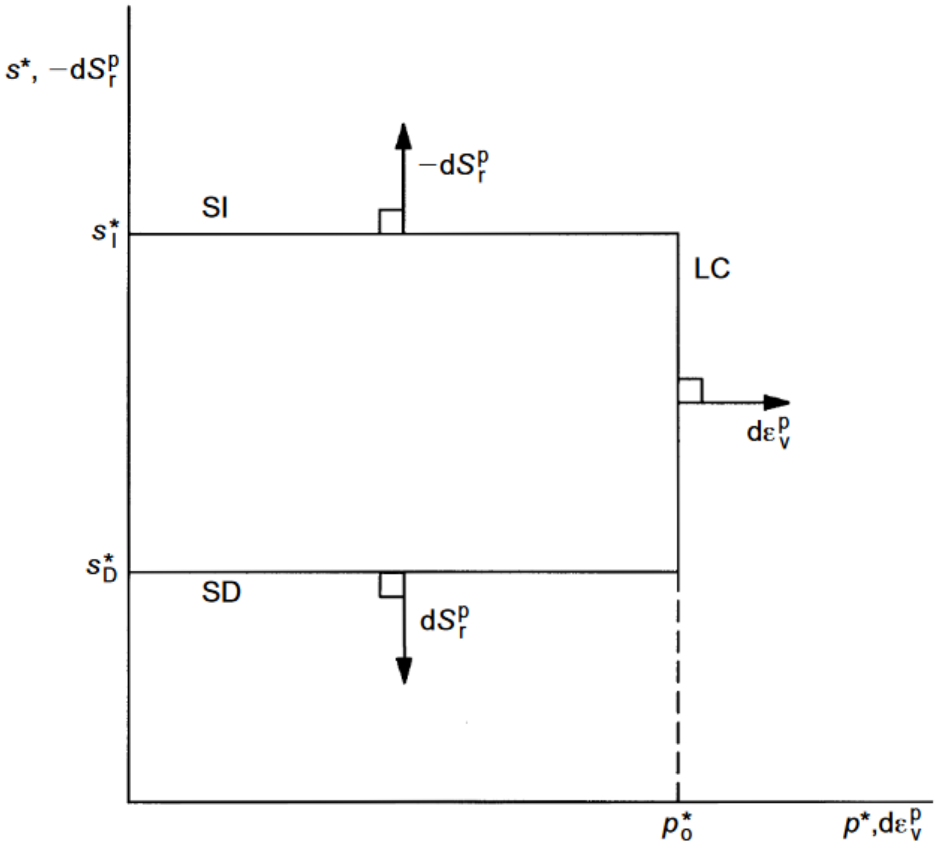

Figure 2.29 LC, SI and SD yield curves for isotropic stress states (Wheeler et al. 2003)

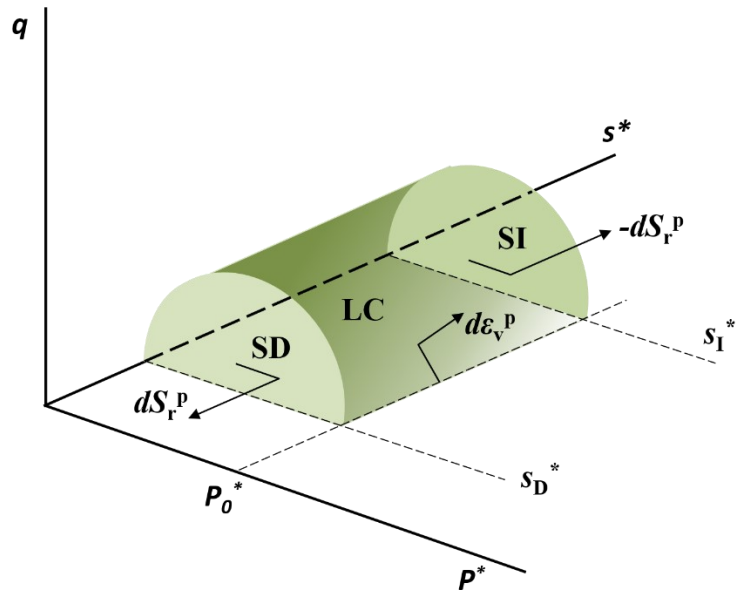

Figure 2.30 Yield surfaces of GCM in three-dimensional space (Lloret-Cabot et al. 2013)

2.6.1.3 SFG Model

Similar to the BBM, the SFG model also adopts two independent stress variables (net mean stress and suction). When it comes to the total volume change, the SFG model neither chooses the approach where the volume change due to stress change is separated from that due to suction change nor the effective stress approach where the net mean stress and suction are combined into effective stress to affect the volume change (Sheng 2011). The SFG model adopts a middle ground approach between the previously mentioned approaches in which the increment of total volumetric strain $d\varepsilon_v$ is defined as (Sheng et al. 2008):

$$d\varepsilon_v = \lambda_{\mathrm{vp}} \frac{d\bar{p}}{\bar{p} + \mathrm{H}(s)} + \lambda_{\mathrm{vs}} \frac{ds}{\bar{p} + \mathrm{H}(s)} \tag{2-37}$$

where λ_{vp} and λ_{vs} are parameters concerning compressibility due to net mean stress and suction, respectively; $\mathrm{H}(s)$ is a suction-dependent function for considering the effects of suction on volume change when suction is combined with net mean stress. A primary function $\mathrm{H}(s) = s$ is provided by Sheng et al. (Sheng et al. 2008). Similar to Equation (2-37), the increment of elastic volumetric strain $d\varepsilon_v^{\mathrm{e}}$ can be defined:

$$d\varepsilon_v^e = \kappa_{\mathrm{vp}} \frac{d\bar{p}}{\bar{p} + \mathrm{H}(s)} + \kappa_{\mathrm{vs}} \frac{ds}{\bar{p} + \mathrm{H}(s)} \tag{2-38}$$

where κ_{vp} and κ_{vs} are parameters regarding elastic compressibility due to net mean stress and suction ($\kappa_{vs} = \kappa_{vp}$ when suction is smaller than saturation suction s_{sa} and $\kappa_{vs} = \kappa_{vp} \frac{s_{sa}+1}{s+1}$ when suction is equal to or larger than s_{sa}). Assuming the plastic volumetric strain should be zero along the initial yield curve for a soil consolidated to a net mean stress of $\overline{p}_{y0}$, the following equation can be acquired:

$$(\lambda_{vp} - \kappa_{vp}) \frac{d\overline{p}_y}{\overline{p}_y + s} + (\lambda_{vs} - \kappa_{vs}) \frac{ds}{\overline{p}_y + s} = 0 \tag{2-39}$$

By integrating Equation (2-39) along the yield curve from $(\overline{p}_{y0}, 0)$ to $(\overline{p}_y, s)$, the yield curve can be defined as:

$$\overline{p}_y = \begin{cases} \overline{p}_{y0} - s & s < s_{sa} \\ \overline{p}_{y0} - s_{sa} - (s_{sa}+1) \ln \frac{s+1}{s_{sa}+1} & s \geq s_{sa} \end{cases} \tag{2-40}$$

Examples of the yield curve and yield surfaces arepresented in Figure 2.31 and Figure 2.32, respectively.

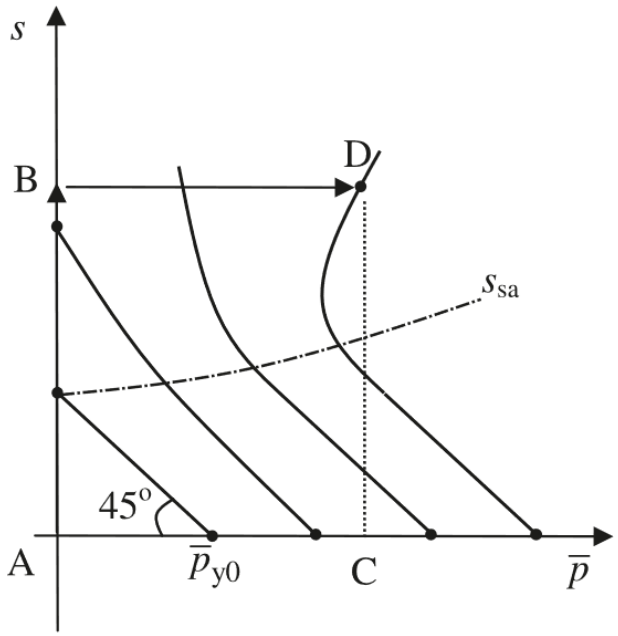

Figure 2.31 Illustration of yield curves for SFG model (Sheng et al. 2008)

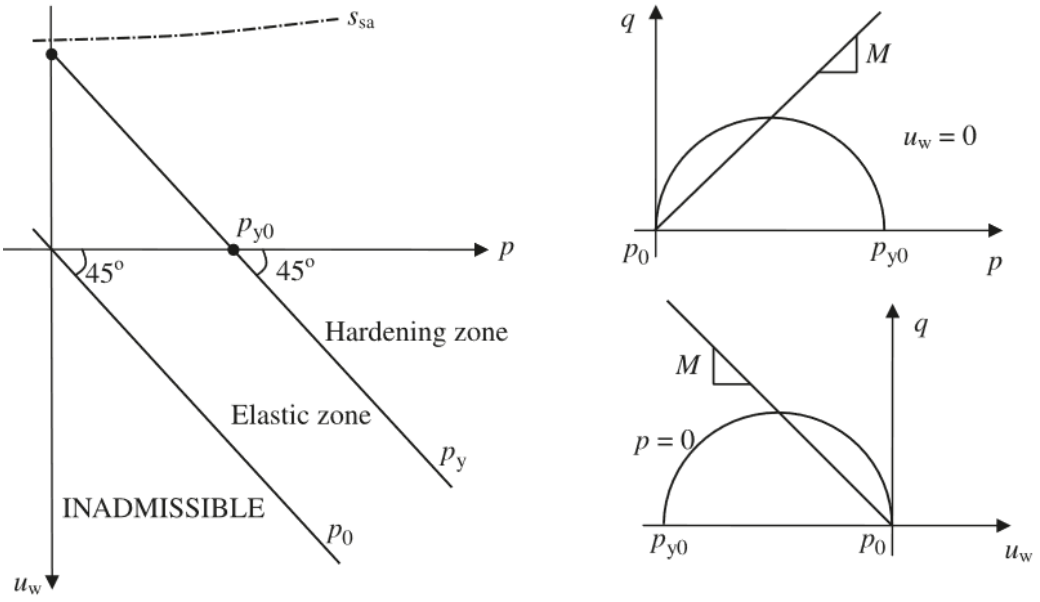

Figure 2.32 Yield surfaces of SFG model in three-dimensional space (Sheng et al. 2008)

2.6.2 Microstructure considered models

Due to the close connection between soil microstructure and hydro-mechanical behaviour, many investigations have been conducted to consider the effects of microstructure in terms of modelling, including indirect consideration and direct consideration of microstructure. Details of these modelling are presented in the following sections.

2.6.2.1 Indirect consideration

Indirect consideration focuses on the effect of microstructure on soil behaviour but ignore the exact microstructural features. One example of indirect consideration is using the effective degree of saturation as the microstructural index. As pointed out by Alonso et al. (Alonso et al. 2010), using the degree of saturation as the Bishop's effective stress coefficient χ can overestimate the shear strength for fine soils. Fine soils can maintain a high value of degree of saturation even under very high suctions, leading to unreasonably high effective stress level when the degree of saturation is used to calculate the effective stress. This is happening because, from the view of microstructure, fine soils usually have a large proportion of micropores within which the water does not contribute to the mechanical behaviour of soils (Alonso et al. 2010). Therefore, the effects of water in micropores should be removed when calculating the effective stress. This assumption and method have been adopted by several researchers (Cai et al. 2018; Li et al. 2019; Wu et al. 2022). Another common method of considering microstructure is using the initial void ratio or initial density, which generally represents the proportion of pore volume in soil microstructure, to model soil-water characteristic curves (Guo-qing et al. 2018; You et al. 2019; Pham and Sutman 2023; Zhai et al. 2023). For example, by incorporating the effects of initial dry density on air entry value into a void ratio-dependent SWCC model, the degree

of saturation can be described as a function of initial dry density or void ratio (Guo-qing et al. 2018). The indirect method requires only one parameter to represent microstructure. However, this method sometimes fails to consider the evolution of microstructure because the residual degree of saturation is assumed to be constant and not impacted by changes to the microstructure.

2.6.2.2 Direct consideration

Direct consideration attaches more importance to the detailed microstructural features such as pore fractal (Russell and Buzzi 2012), pore size and pore size distribution (PSD) (Vaunat and Casini 2017; Niu et al. 2021) or it directly builds up different mechanisms for different microstructural components (Mašín 2013).

For example, the double porosity in microstructure has been acknowledged by many researchers as one of the most typical and common microstructural types which can tightly interact with the hydro-mechanical behaviour of soils (Bagherieh et al. 2009; Casini et al. 2012; Alazaiza et al. 2017; Song et al. 2020). Masin (Mašín 2013) proposed a double porosity-hydromechanical coupling model by adopting separate frameworks for different microstructural levels. This separation first lies in the adoption of macromechanical and micromechanical effective stresses ($\dot{\sigma}^{\mathrm{M}}$ and $\dot{\sigma}^{\mathrm{m}}$), which are defined below:

$$\dot{\sigma}^{\mathrm{M}} = \bar{\sigma}^{\mathrm{M}} - s^{\mathrm{M}}\chi^{\mathrm{M}} \tag{2-41}$$

$$\dot{\sigma}^{\mathrm{m}} = \bar{\sigma}^{\mathrm{m}} - s^{\mathrm{m}}\chi^{\mathrm{m}} \tag{2-42}$$

where the superscripts M and m represent macromechanical and micromechanical respectively. With these separate effective stresses, the stress-strain behaviour of each structure level is defined as:

$$\dot{\sigma}^{\mathrm{M}} = f_s(\Gamma : \dot{\varepsilon}^{\mathrm{M}} + f_d \mathrm{N}\left\|\dot{\varepsilon}^{\mathrm{M}}\right\|) + f_u \mathrm{H} \tag{2-43}$$

$$\dot{\sigma}^{\mathrm{m}} = \frac{p^{\mathrm{m}}}{\kappa_{\mathrm{m}}}\mathrm{tr}\dot{\varepsilon}^{\mathrm{m}} \tag{2-44}$$

where f_s, f_d and f_u are three scalar factors; Γ is the fourth-order constitutive tensor; N and H are two second order constitutive tensors; κ_{m} specifies the dependency of microstructural swelling/shrinkage on the microstructural effective stress. Since the two equations can only represent the strains at each microstructure level, a coupling function f_{m} is needed to combine them to obtain the global strain behaviour, which is defined as:

$$f_{\mathrm{m}} = 1-(r_{em})^{m_c} \tag{2-45}$$

where m_c is a model parameter controlling the impact of r_{em} on f_{m} for intermediate values of r_{em}. Then the global behaviour can be calculated by:

$$\dot{\sigma}^{\mathrm{M}} = f_s(\Gamma : (\dot{\varepsilon} - \kappa_{\mathrm{m}} \frac{\dot{p}^{\mathrm{m}}}{p^{\mathrm{m}}}) + f_d \mathrm{N} \left\| \dot{\varepsilon} - \kappa_{\mathrm{m}} \frac{\dot{p}^{\mathrm{m}}}{p^{\mathrm{m}}} \right\|) + f_u \mathrm{H} \tag{2-46}$$

A similar approach was also adopted by Ghiadistri et al.(Ghiadistri et al. 2018; Ghiadistri et al. 2019) to establish a model that considers the double-structure of expansive clays which is called Imperial College Double-Structure Model (ICDSM). To consider the different contribution of microstructure and macrostructure, a void factor VF was defined as:

$$VF = \frac{e_{\mathrm{m}}}{e} = \frac{e - e_{\mathrm{M}}}{e} \tag{2-47}$$

where e_{m} is the microstructural void ratio and e_{M} is the macrostructural void ratio. Then the total strain ε, total elastic strain ε_{e} and total plastic strain ε_{p} can be defined as:

$$\varepsilon = \varepsilon_{\mathrm{e}} + \varepsilon_{\mathrm{p}} \tag{2-48}$$

$$\varepsilon_{\mathrm{e}} = VF \cdot \varepsilon_{\mathrm{e}}^{\mathrm{m}} + (1-VF) \cdot \varepsilon_{\mathrm{e}}^{\mathrm{M}} \tag{2-49}$$

$$\varepsilon_{\mathrm{p}} = VF \cdot \varepsilon_{\mathrm{p}}^{\mathrm{m}} + (1-VF) \cdot \varepsilon_{\mathrm{p}}^{\mathrm{M}} \tag{2-50}$$

where $\varepsilon_{\mathrm{e}}^{\mathrm{m}}$ and $\varepsilon_{\mathrm{e}}^{\mathrm{M}}$ are microstructural elastic strain and macrostructural elastic strain, respectively; $\varepsilon_{\mathrm{p}}^{\mathrm{m}}$ and $\varepsilon_{\mathrm{p}}^{\mathrm{M}}$ are microstructural plastic strain and macrostructural plastic strain, respectively. The change of $\varepsilon_{\mathrm{e}}^{\mathrm{m}}$ is purely volumetric and defined as:

$$\Delta\varepsilon_{\mathrm{e}}^{\mathrm{m}} = \frac{\Delta p^{\mathrm{m}}}{E^{\mathrm{m}}} \tag{2-51}$$

where Δp^{m} is the change of microstructural effective stress and E^{m} is the elastic bulk modulus. The change of $\varepsilon_{\mathrm{e}}^{\mathrm{M}}$ is influenced by both equivalent stress p_{eq} and equivalent suction s_{eq}:

$$\Delta\varepsilon_{\mathrm{e}}^{\mathrm{M}} = \frac{\Delta p_{\mathrm{eq}} + \Delta s_{\mathrm{eq}}}{E^{\mathrm{M}}} \tag{2-52}$$

where E^{M} is the macrostructural bulk. With equations (2-51) and (2-52), the total elastic strain can be calculated based on equation (2-49).

For the plastic strain, the microstructural plastic strain is assumed to be proportional to the elastic strain with a scalar f_β:

$$\Delta\varepsilon_{\mathrm{p}}^{\mathrm{m}} = f_\beta \cdot \Delta\varepsilon_{\mathrm{e}}^{\mathrm{m}} \tag{2-53}$$

The macrostructural plastic strain follows the hardening law of the critical state framework:

$$\Delta p_0^* = p_0^* \frac{v}{\lambda - \kappa} \Delta\varepsilon_{\mathrm{p}}^{\mathrm{M}} \tag{2-54}$$

where p_0^* is the pre-consolidation Pressure, v is the specific volume, λ is the compressibility coefficient (slope of normal consolidation line) and κ is the elastic compressibility coefficient (slope of rebound curve). The total plastic strain then can be determined by equation (2-50).

Direct methods can have limitations. Direct methods will typically require more parameters to represent microstructure and can make the model much more complex. However, direct methods give the possibility of studying microstructural-hydro-mechanical coupled behaviour within a unified framework and can be applied to predicting the evolution of microstructure and SWCCs.

2.7 Concluding remarks

In this chapter, topics related to the soil microstructure and hydro-mechanical behaviour of unsaturated soils in terms of modelling and experiments are reviewed. Based on the current investigations and publications, the following aspects can be highlighted:

(1) Soil microstructure has a close connection with the hydro-mechanical behaviour of unsaturated soils.

(2) Pore size distribution, a typical part of microstructure, can evolve due to both external loading and suction change. Its evolution can be easily captured by Mercury Intrusion Porosimetry (MIP).

(3) Pore size distribution can be applied to many aspects such as predicting the soil-water characteristic curves and calculating the Bishop's effective stress coefficient.

(4) The hydro-mechanical behaviour of unsaturated soils can be obtained by triaxial tests and soil-water characteristic curve (SWCC) tests. For triaxial tests, the displacement rate for shearing should be carefully selected to prevent the excess pore water pressure which affects the accuracy of a Consolidated-Drained test. The shearing is usually terminated at an axial strain of 20% where the critical state is almost reached.

(5) For SWCC tests, the water retention behaviour of soils can be influenced by many factors such as soil texture, soil structure and hysteresis. There are both empirical and theoretical modelling on SWCC. The former are mostly fitting methods and the latter focused on the physical connection among suction, water content and soil microstructure.

(6) The constitutive modelling of the hydro-mechanical behaviour has been studied with and without the consideration of microstructure. The methods for describing microstructure in constitutive modelling can be classified into indirect methods and direct methods. Indirect consideration focuses on the effect of microstructure on soil behaviour but ignore the exact microstructural features. Direct consideration attaches more importance to the detailed microstructural features such as pore fractal, pore size and pore size distribution (PSD) or it directly builds up different mechanisms for different microstructural components.

According to the literature review, there are two research gaps that remain to be addressed. First, the evolution of pore size distribution during saturated and unsaturated shearing has not been fully studied. Second, the interaction between pore size distribution and hydro-mechanical behaviour of soils has been studied in a limited way and the pore size distribution-dependent Bishop's effective stress coefficient χ (Vaunat and Casini 2017) and the evolution of soil-water characteristic curves has not been considered in a microstructure-related constitutive model.

CHAPTER 3

Materials and methods

3.1 Introduction

The materials used and experimental methods adopted for studying soil microstructure and its effects on hydro-mechanical behaviour are presented in this chapter. This chapter is organized as follows: The materials used for this study are summarized in Section 3.2; the experimental methods for studying the microstructure and its effects on the hydro-mechanical behaviour are presented in Section 3.3; concluding remarks are drawn in Section 3.4.

3.2 Materials

In this study, several kinds of soils, including Dundee silt (for both experiments and modelling), Speswhite kaolin (Sivakumar 1993) and Jossigny silt (Casini 2008) (only for modelling), are selected for investigating the relationship between soil microstructure and hydro-mechanical behaviour. The basic information for Dundee silt is provided in the following sections. Relevant properties of Speswhite kaolin and Jossigny silt are obtained from the literature (Sivakumar 1993; Casini 2008) and are provided in Chapter 5.

3.2.1 Soil used

The soil selected for the experimental study of the relationship between soil microstructure and the hydro-mechanical behaviour, is referred to here as Dundee silt. It is a natural soil from Dundee, UK. It is chosen because it is a naturally existing soil and so its behaviour is of more practical significance compared with laboratory-prepared soils. Also, neither the hydro-mechanical behaviour of Dundee silt or its microstructure have fully studied and so a new contribution can be made to facilitate the understanding of this natural soil. It is noted that some basic properties of Dundee silt have been previously studied by the Geoenvironmental Research Centre of Cardiff University, so more attention can be paid to its microstructural-hydro-mechanical behaviour. For modelling, experimental results of Speswhite kaolin (Sivakumar 1993) and Jossigny silt (Casini 2008) are used to evaluate the performance of the model with indirect consideration of microstructure while those of Dundee silt are used to validate the proposed model with direct consideration of soil microstructure.

3.2.2 Soil properties

Basic properties of Dundee silt are presented in the following sections, including grain size distribution, specific gravity, liquid limit, plastic limit, optimum water content and maximum dry density.

3.2.2.1 Grain size distribution

According to the grain size distribution (see Figure 3.1) provided by the Laboratory of Soil Mechanics at Cardiff University (follow BS 1377-2 1990), the components of Dundee silt include 42.5% sand, 56.3% silt and 1.2% clay. Sand content and silt content take up the largest proportion of Dundee silt while there is very little clay. Therefore, Dundee silt (classified as a low-plastic silt) is expected to behave experimentally between sand and silt.

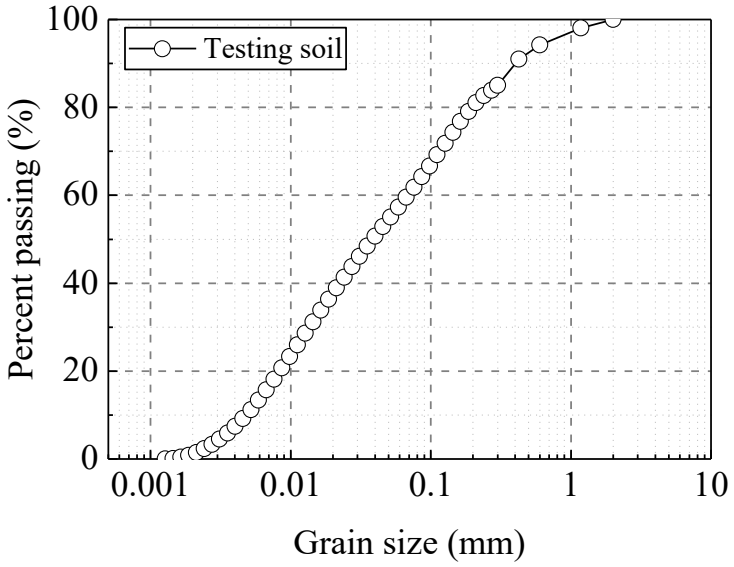

Figure 3.1 Grain size distribution of Dundee silt

3.2.2.2 Specific gravity

According to the Laboratory of Soil Mechanics at Cardiff University, the specific gravity G_s of Dundee silt is 2.61, determined by the pycnometer method (BS 1377-2 1990).

3.2.2.3 Plastic limit, liquid limit

The plastic limit and liquid limit of Dundee silt are 24.8% and 32.4%, respectively. This information is also provided by the Laboratory of Soil Mechanics at Cardiff University, following BS 1377-2 (1990).

3.2.2.4 Optimum water content and maximum dry density

The Laboratory of Soil Mechanics at Cardiff University carried out the standard proctor light compaction tests by following the procedure laid out in BS 1377-4(1990). According to the compaction curve of Dundee silt (see Figure 3.2 and Table 3.1), the maximum dry density of Dundee silt is 1.64 Mg/m^3 with an optimum water content of 17.2%.

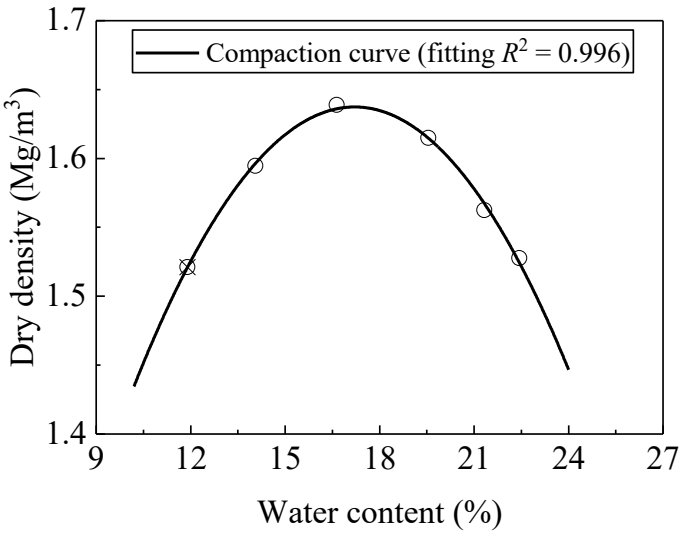

Figure 3.2 Compaction curve of Dundee silt

Table 3.1 Dry densities of Dundee silt at each water content

Sample name	w (%)	ρ_d (Mg/m^3)	S_r (%)
M6	11.2	1.49	38.1
P6	23.2	1.49	79.6
M3	14.2	1.60	58.1
P3	20.2	1.60	80.7

3.3 Experimental methods

To understand the hydro-mechanical behaviour of Dundee silt and its interaction with microstructure, four different kinds of tests have been carried out including saturated and unsaturated triaxial tests, MIP tests and chilled-mirror dew-point tests. Saturated and unsaturated triaxial tests were conducted to study the stress-strain behaviour and water content change of Dundee silt under both saturated and unsaturated conditions. These triaxial samples were then subsampled and tested via Mercury Intrusion Porosimetry (MIP) to obtain pore size distributions (PSDs). By comparing the difference in these PSDs obtained under various loading conditions, the evolution of microstructure during loading can be studied. Chilled-mirror dew-point tests were also conducted with WP4C device to obtain the soil-water characteristic curves (SWCCs) of Dundee silt under various dry densities to study the connection between SWCCs and PSDs. The experimental results from these tests provide data to validate the model proposed in Chapter 5.

3.3.1 Saturated triaxial tests

Saturated triaxial tests were carried out on compacted samples of Dundee silt under consolidated-drained conditions, subject to various constant confining stresses. Details of saturated triaxial tests are provided in the following sections.

3.3.1.1 Sample preparation

The sample preparation for saturated triaxial tests has three major steps, including preparing soil-water mixture, compaction and storage.

(1) soil-water mixture

Dundee silt in its natural condition was oven dried to obtain its initial water content. The initial water content of Dundee silt varies from 12% to 14%. Since the targeted water content was 15% (according to the compaction curve shown in Figure 3.2, the equivalent dry density is 1.62 Mg/m^3 and it is at the dry side of the compaction curve), the soil-water mixture was then prepared by adding predetermined quantities of distilled water to the soil. The distilled water was split evenly and added to the soil in three stages on a glass plate. Each time, the soil was mixed thoroughly with water by using palette knives.

(2) compaction

To reach the targeted dry density of 1.62 Mg/m^3, an equivalent mass of soil-water mixture was transferred into a metal mould of 50mm inner diameter and 110mm height. The mixture was then compacted by a loading frame with a piston on the top of sample to 100mm in height (see Figure 3.3). Several samples were also compacted to a height of 92-94mm with a higher dry density (1.72-1.76 Mg/m^3) to study the effects of initial dry densities on soil behaviour.

After samples were compacted to the targeted height, the same piston was transferred from the top to the bottom of the sample while a thin-wall mental cylinder was placed on the top of the mould (see Figure 3.4). The platform of the loading frame was set to rise again to extrude the sample out of the mould.

Figure 3.3 Sample compaction

Figure 3.4 Sample extrusion

(3) storage

After the samples were extruded, they were weighed again to obtain the final mass of the sample and then stored in a plastic bag sealed by tape and kept in an air-tight bucket with lid for about one week before further tests. This is to ensure the equilibrium and a uniform water content within the sample.

3.3.1.2 Testing device

A conventional automated triaxial Global Digital Systems (GDS) device was used to conduct saturated triaxial tests. As shown in Figure 3.5, this device contains 11 major components, including triaxial cell, pedestal & top-cap, rubber membrane, O-ring & porous discs, cell pressure controller, back pressure controller, load frame, load cell, pore water pressure transducer, axial displacement transducer and data acquisition unit.

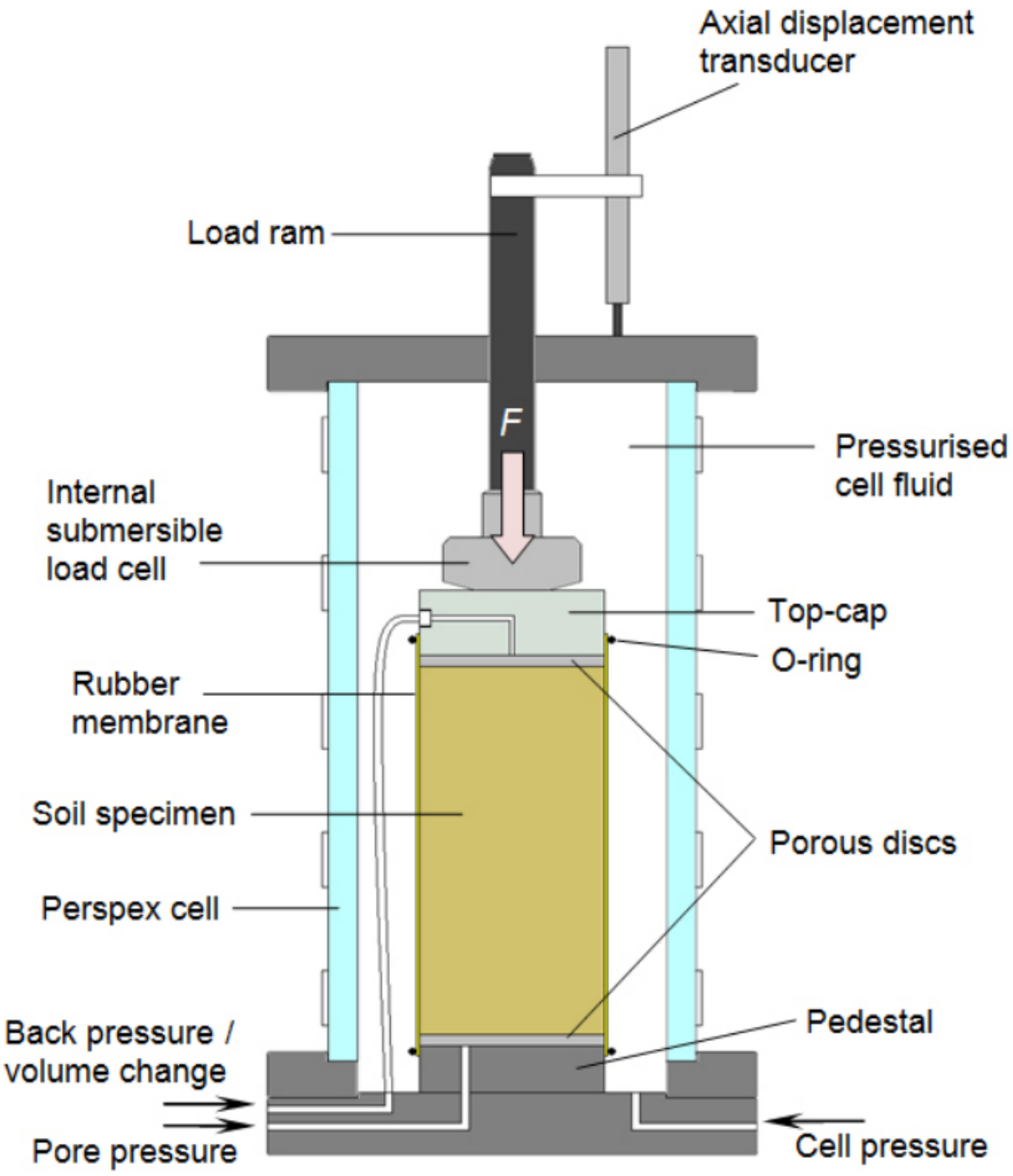

Figure 3.5 General set-up of a soil specimen inside a triaxial cell (Rees 2013)

3.3.1.3 Testing procedure

Following BS 1377-8 (1990), the general testing procedure for using a conventional automated triaxial apparatus is: (1) Deair pressure controllers and the loading frame with deaired water. Saturate the porous stones in a water-filled desiccator on the top of which is connected to the vacuum pump for 10-30 minutes until no air bubbles can be seen; (2) Place the specimen in the cell with saturated porous stone; (3) Stretch a rubber membrane over the specimen and the

bottom of the membrane should be fixed to the pedestal with two O-rings; (4) Place the top-cap in the top of the membrane ,with two more O-rings used to fix the membrane to the top-cap; (5) assemble the triaxial cell and its connection to the data acquisition device; (6) fully fill the triaxial cell with deaired water and adjust the pressure controllers to zero pressure; (7) start the triaxial tests as described by geotechnical test standards (BS 1377-8 1990) including saturation, consolidation and loading. Details of saturation, consolidation and loading are presented in the following sections.

3.3.1.3.1 Back pressure saturation

To ensure the specimen is fully saturated before further actions, an automatic saturation stage is first undertaken. During this stage, a linear increase of the cell and back pressures is placed on the specimen while the effective stress (cell pressure minus back pressure) remains constant (10 kPa) (Rahardjo et al. 2004; Almahbobi 2018) to prevent potential swelling. Skempton's B value (Skempton 1954) is used to check whether the specimen has reached saturation, often termed the B-check. When increasing the cell pressure by 50 kPa, the B is determined based on the following equation:

$$B = \frac{\Delta u_w}{\Delta \xi_3} \tag{3-1}$$

where Δu_w is the change in pore water pressure; $\Delta \xi_3$ is the change in cell pressure. In this study, a B value of 0.95 is adopted as the indication of full saturation as suggest by the manufacturer of the apparatus (Rees 2013), BS 1377-8 (1990) and other researchers (Kokusho 2000; Uchaipichat and Khalili 2009; Leong and Cheng 2016).

3.3.1.3.2 Consolidation

A consolidation state is required to bring the specimen to targeted effective stress before shearing or isotropic loading. During the consolidation stage, the back pressure remains at the same value as at the end of saturation, while the cell pressure is increased immediately to a value in-line with the targeted effective stress. Deformation can be witnessed during this stage which will be terminated when there is no significant change of total volume and at least 95% excess pore pressure has dissipated. For specimens of Dundee silt, preliminary testing indicates that 8 hours of consolidation are sufficient.

3.3.1.3.3 Shearing and isotropic loading

Both Consolidated Drained (CD) shearing and isotropic loading were conducted on specimens of Dundee silt. For the CD tests, all specimens were sheared under a constant confining stress (constant cell and back pressure) at constant displacement rates of 0.0035, 0.007 and 0.014 mm/min (strain-controlled method) to study the effects of displacement rates on behaviour and to find a suitable displacement rate for further shearing tests. The shearing

stage was terminated when the predetermined axial strain was reached. The isotropic loading/unloading was conducted in a stepwise manner. In each step, the cell pressure was set to a specific value while keeping the back pressure unchanged to reach a targeted effective stress (stress-controlled method). Each step lasted two hours (according to preliminary tests, 95% volume change occurs within the first 1 to 1.5 hours of isotropic consolidation), with the cell pressure gradually increasing to the targeted value during that time. This ensures that the specimen can have sufficient time to deform during isotropic loading/unloading.

3.3.1.4 Testing program

The testing program for saturated triaxial tests is summarized in this section. The initial conditions of specimens are presented in Table 3.2. There are five series of tests included in the program. Series 1 consists of CD tests on saturated specimens at three constant confining stresses of 100, 200 and 400 kPa. The displacement rate was 0.0035 mm/min and the shearing was terminated at the axial strain of 20% for all specimens. The information collected and determined from Series 1 includes: (1) elapsed time versus total volume change (void ratio) during consolidation stage; (2) axial strain (ε_a) /effective mean stress (p^*) versus deviator stress (q)/volumetric strain (ε_v)/void ratio (e) during shearing; (3) Mohr circles and effective shear strength parameters (c' and ϕ'); (4) critical state line (CSL); (4) the gradient of CSL (M).

Series 2 consists of CD tests on saturated specimens at a constant confining stress of 100kPa, but the displacement rates vary at 0.0035, 0.007 and 0.014 mm/min for each specimen. The shearing was terminated at an axial strain of 20% for all specimens. The information collected from Serials 2 includes: (1) axial strain (ε_a) versus deviator stress (q); (2) elapsed time versus back pressure/pore water pressure.

Series 3 consists of isotropic compression tests on saturated specimens. The effective stress changed stepwise from 50, 25, 50, 100, 200, 400 to 800 kPa. Each step last two hours for the effective stress to increase/decrease to the targeted value. The information collected and determined from Serials 3 includes: (1) effective mean stress (p^*) versus specific volume (v); (2) normal consolidation line (NCL) and its gradient λ; (3) rebound curve and its gradient κ.

Series 4 consists of CD tests on saturated specimens at three constant confining stresses of 100, 200 and 400 kPa at a displacement rate of 0.007 mm/min. For each confining stress, several specimens were sheared under the same condition, but the shearing was terminated at different axial strains of 20%, 10% and 5%. The information collected from Series 4 includes: (1) elapsed time versus total volume change (void ratio) during consolidation stage; (2) axial strain (ε_a) /effective mean stress (p^*) versus deviator stress (q)/volumetric strain (ε_v)/void ratio (e) during shearing;

Three specimens were prepared for Series 5. M9 only underwent saturation stage and M10 underwent both saturation and consolidation stage (to 200 kPa effective stress). M11 was

the original compacted sample without saturation and consolidation. These three specimens were not used for studying the stress-strain behaviour but only used for Mercury Intrusion Porosimetry. A summary of saturated testing program is presented in Table 3.3.

Table 3.2 Initial conditions of specimens used for saturated triaxial test

Series	Specimen No.	Diameter (mm)	Height (mm)	Dry density (g/cm^3)	Initial void ratio	Initial water content (%)
1	A	50	92	1.76	0.481	15
	B		92	1.76	0.481	
	C		92	1.76	0.481	
2	D		92	1.76	0.481	
	E		94	1.72	0.514	
	F		94	1.72	0.514	
	G		101	1.60	0.610	
3	H		92	1.76	0.481	
4	M2		100	1.62	0.608	
	M3				0.609	
	M5				0.611	
	M6				0.610	
	M13				0.609	
	M14				0.609	
	M15				0.610	
	M18		102	1.59	0.642	
	M19		102		0.641	
5	M9		100	1.62	0.609	
	M10				0.610	
	M11				0.608	

Table 3.3 Summary of testing program for saturated triaxial tests

Series	Specimen No.	Confining stress (kPa) during shearing	Displacement rate (mm/min)	Targeted axial strain (%)
1	A	100	0.0035	20
	B	200	0.0035	
	C	400	0.0035	
2	D	100	0.0035	
	E	100	0.007	
	F	100	0.014	
	G	100	0.0035	
3	H	Isotropic compression Stress path: 50-25-50-100-200-400-800 kPa		
4	M2	200	0.007	20
	M3			10
	M5			5
	M6	400		20
	M13			10
	M14			5
	M15	100	0.007	20
	M18			10
	M19			5
5	M9	Saturation		
	M10	Saturation and consolidation (under effective stress of 200kPa)		
	M11	Compaction		

3.3.2 Unsaturated triaxial tests

Suction-controlled unsaturated triaxial CD tests were carried out on compacted samples of Dundee silt under various loading conditions to study the hydro-mechanical behaviour. The specimens used for unsaturated triaxial tests were also subsampled after testing and subjected to MIP tests. Details of unsaturated triaxial tests are provided in the following sections.

3.3.2.1 Sample preparation

Specimens used for unsaturated triaxial tests were all prepared in the same way the specimens were prepared for saturated triaxial tests. Details can be found in section 3.3.1.1.

3.3.2.2 Testing device

The GDS Triaxial Automated System (GDSTAS) is a load frame-based and suction-controlled triaxial testing system for conducting unsaturated triaxial tests (see Figure 3.6). This system contains seven important components, including a load frame, an outer cell, an inner cell, two pressure controller, six transducers, a digital transducer interface and a computer.

A triaxial load frame designed for conducting constant strain rate tests was employed to apply axial loads to the triaxial cell piston. The load cell is affixed to a loading ram within the triaxial cell to gauge the axial force exerted on each specimen during shearing. The outer triaxial cell is a Bishop & Wesley stress-path cell (Bishop and Wesley 1975). Enclosed within the triaxial cell is a secondary cell wall where the specimen is positioned. This setup facilitates the measurement of cell volume change solely within the inner chamber, thus minimizing errors stemming from temperature and pressure fluctuations. Two GDS pressure controllers are utilized: one is an automatic pneumatic regulator with dual channels for managing cell pressure in both the inner and outer cell cavities, as well as regulating pore air pressure in the soil specimen, while the other is a digital hydraulic pressure/volume controller. The pressure/volume controller employs microprocessor-controlled hydraulic actuators capable of regulating back-water pressure and measuring water volume changes in the soil specimen. These two GDS controllers can be operated independently. The six transducers include a load cell for measuring axial force, a linear variable differential transformer (LVDT) for monitoring axial displacement, a wet–wet differential pressure transducer (DPT) (a component of the total volume change measurement system), and three additional pressure transducers for monitoring cell pressure, pore air pressure, and pore water pressure. The primary unsaturated testing module utilized in this study is the 4-dimensional stress path (GDS Instruments Ltd, 2014), which allows for simultaneous control of pore air, pore water, radial stress, and axial stress controllers.

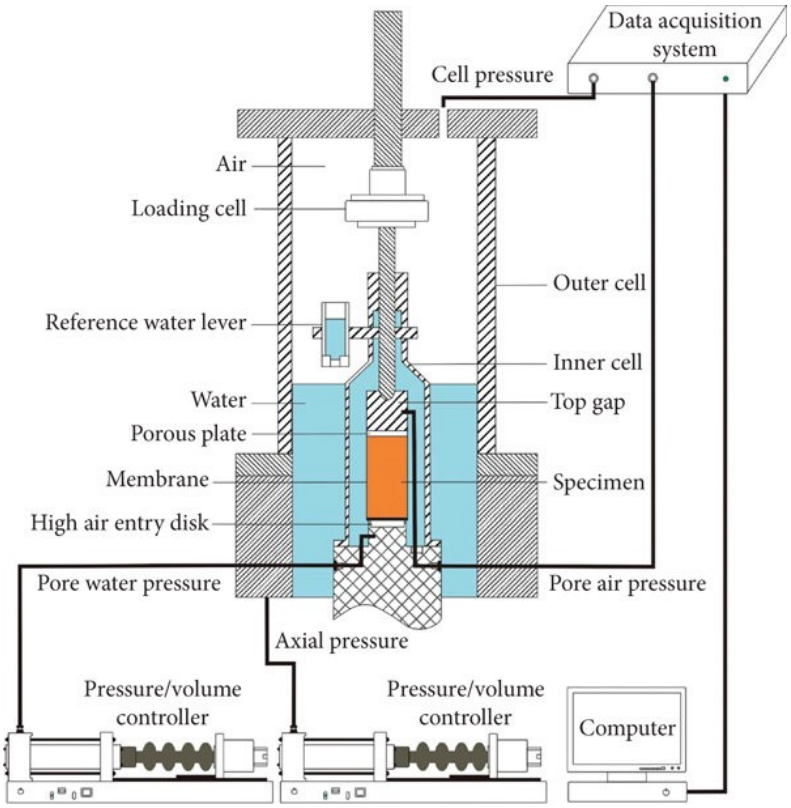

Figure 3.6 A schematic of the GDS Triaxial Automated System (GDSTAS) (Zhang et al. 2020)

3.3.2.3 Testing procedure

Unsaturated triaxial tests require the saturation of a high-air-entry porous disc (HAEPD) and a check for the water permeability of the disc before further tests. In this study, the saturation of HAEPD followed the procedure proposed by Fredlund and Rahardjo (1993). A positive water pressure of 30 kPa was applied to the bottom surface of the disc until the top surface of the disc was pooled with water. The cell was then filled with de-aired water and a high air pressure of 500 kPa was applied to evacuate the air in the disk with the flowing water. This pressure was maintained for one hour before applying 30 kPa of water pressure to remove air bubbles and dissolved air in the water. The water permeability of the disc was checked by constant head method in order to spot potential cracking of the disk which can result in a sudden increase in permeability. The result of permeability check is presented in Table 3.4. The average saturated water permeability of the disk was 1.90×10^{-10} m/sec. After the permeability check was completed, further stages including suction equilibrium, consolidation and shearing were conducted.

Table 3.4 Permeability check under different hydraulic heads

Hydraulic head (m)	Permeability (m/s)
50	2.10×10^{-10}
50	2.10×10^{-10}
50	2.08×10^{-10}
39.5	2.55×10^{-10}
39.5	1.51×10^{-10}
39.23	1.68×10^{-10}
39.23	1.34×10^{-10}
50	1.81×10^{-10}
50	1.41×10^{-10}
50	1.39×10^{-10}
50	1.18×10^{-10}
50	1.11×10^{-10}
50	5.02×10^{-10}
40	1.27×10^{-10}

3.3.2.3.1 Suction equilibrium

The axis-translation technique was adopted to control the matric suction (Hilf 1956). In this technique, it is important to separate the air pressure and the pore water pressure to maintain the matric suction which is the differential pressure of air pressure and pore water pressure. A high-air-entry porous disc (HAEPD) was used to achieve this separation. The air entry value of this HAEPD is 500 kPa. After saturating the HAEPD, it is able to maintain an air pressure on one side while a lower water pressure is maintained on the other side. As long as the differential of air pressure and water pressure does not exceed 500 kPa, air will not enter the HAEPD and desaturate it. Therefore, the maximum matric suction can be applied is 500kPa.

In this study, two different matric suctions, 25 kPa and 100 kPa were selected for constant suction CD tests on Dundee silt. The water pressure was set to 0 kPa while the air pressures were set to 25 and 100 kPa respectively. The confining stress during suction equilibrium was 25 kPa. The axial stress was 5 kPa higher than the confining stress to ensure the proper operation of tests, as suggested by the manufacturer, and it was assumed not to significantly affect volume change. The time period to reach the targeted stress condition was set to 5 min. During suction equilibrium, the total volume change/axial strain/specimen water volume versus the elapsed time were monitored. Suction equilibrium was assumed to be reached when the changes of total volume and specimen water volume were both smaller than 100 mm^3/day (Sivakumar 1993; Estabragh and Javadi 2008; Ng et al. 2012; Zhang et al. 2016; Almahbobi 2018). For Dundee silt, it can take ~15 days to finish this stage (detailed results are shown in Chapter 4).

3.3.2.3.2 Consolidation

The consolidation was carried out to reach the targeted confining stress of 200 kPa (constant suction of 100 kPa) for all specimens tested for unsaturated CD tests. The axial stress was 5 kPa higher than the confining stress. The time period to reach the targeted stress condition was also set to 5 min. Attention was paid to total volume change and pore water pressure during consolidation. Consolidation was completed when there is no more significant total volume change and at least 95% pore water pressure has dissipated (Rees 2013). This stage can also take ~15 days to complete (detailed results are shown in Chapter 4).

3.3.2.3.3 Shearing

While stress control was employed for the suction equilibrium stage and consolidation stage, strain control was used for shearing. The suction and the net confining stress were maintained at 100 kPa and 200 kPa respectively during shearing. The displacement rate was set to 0.007 mm/min for unsaturated CD tests. Tests were terminated when the targeted axial strain reached.

3.3.2.4 Testing program

The constant suction unsaturated CD tests contain two series. For Series 6 three specimens (M4, M7 and M12) were prepared to the same initial conditions but were sheared to different axial strains (see Table 3.5). The suction remained 100 kPa during each stage (see Table 3.6). For Series 7, two specimens (M20 and M21) were also prepared to the same initial conditions but were sheared to different axial strains. The suction remained 25 kPa during each stage, as shown in Table 3.7.

Table 3.5 Initial conditions and targeted axial stains for specimens used for unsaturated CD tests

No.	Wet mass (g)	Diameter (mm)	Height (mm)	Dry density (g/cm^3)	Initial void ratio	Degree of saturation (%)	Targeted axial strain during shearing stage (%)
M4	366.26	50	100	1.62	0.609	64.28	20%
M7	366.20	50	100	1.62	0.609	64.28	10%
M12	366.30	50	100	1.62	0.609	64.29	5%
M20	365.54	50	100	1.62	0.612	63.94	10%
M21	365.14	50	100	1.62	0.614	63.76	15%

Table 3.6 Loading conditions for Serials 6

Stage	σ_1 (kPa)	σ_3 (kPa)	u_a (kPa)	u_w (kPa)	σ_1-u_a (kPa)	σ_3-u_a (kPa)	σ_1-σ_3 (kPa)	$u_a - u_w$ (kPa)
Suction equilibrium	130	125	100	0	30	25	5	100
Consolidation	305	300	100	0	205	200	5	100
Shearing	/	300	100	0	/	200	/	100

Table 3.7 Loading conditions for Serials 7

Stage	σ_1 (kPa)	σ_3 (kPa)	u_a (kPa)	u_w (kPa)	σ_1-u_a (kPa)	σ_3-u_a (kPa)	σ_1-σ_3 (kPa)	$u_a - u_w$ (kPa)
Suction equilibrium	55	50	25	0	30	25	5	25
Consolidation	230	225	25	0	205	200	5	25
Shearing	/	225	25	0	/	200	/	25

3.3.3 Mercury intrusion porosimetry (MIP) tests

Mercury intrusion porosimetry (MIP) is the most extensively used method for obtaining pore size distribution (PSD). During a MIP test, mercury is forced to intrude into open soil pores under progressively increasing pressure. Increasingly smaller pores are intruded with increasing pressure. The relationship between the intruding pressure P_r and the pore size is typically assumed to be represented by Washburn's equation (Washburn 1921):

$$P_r = \frac{2\gamma \cos\theta}{R} = \frac{4\gamma \cos\theta}{D} \tag{3-2}$$

where γ is the surface tension of any liquid (equivalent to 0.484 N/m at 25℃ for mercury, 0.072N/m for water.), θ is the contact angle between the liquid and the pore wall (140° for

mercury and 0° for water), R is the pore radius and D is the pore diameter. It should be noted that adoption of this approach is limited by the assumption of a cylindrical pore shape. By monitoring pressure and the total volume of mercury intruding into open pores, the smallest open pores filled with mercury are determined at a specific pressure and the total volume of open pores equal or larger in size than the smallest pores are taken to be equivalent to the volume of mercury (Tanaka et al. 2003; Simms and Yanful 2004a; Romero and Simms 2008). Based on the pore size and total volume obtained from MIP, the cumulative pore size distribution and differential pore size distribution can be determined. The measuring range of MIP varies with facilities but the generally MIP can measure pore sizes ranging from 2 nanometres to several hundred micrometres (Juang and Holtz 1986; Burton et al. 2014; Oualmakran et al. 2016; NIU et al. 2020; Gramegna 2022). Therefore, the result obtained from MIP can represent a wide range of pore sizes but in some cases not the entire pore size distribution within a soils microstructure is captured due pore sizes smaller than 2 nanometres or large pores being ignored. This deficiency can limit the application of MIP to fine soils which have a large proportion of small and disconnected pores and also for sandy soils with large pores.

3.3.3.1 Sample preparation

After completion of the unsaturated and saturated triaxial tests, the tested samples were also used for MIP tests. Sample preparation for MIP tests requires two major steps, drying and resizing. First, samples must be dried before getting tested. There are two common methods for drying samples, namely freeze-drying and oven-drying. Due to the volumetric restriction of MIP cell, large samples must be cut to fit in the cell. Details of sample preparation are presented in the following sections.

3.3.3.1.1 Freeze-drying

Freezing drying is a common and well-accepted method to dry soil samples used in microscopy and mercury intrusion tests (Ahmed et al. 1974; Delage et al. 1996; Penumadu and Dean 2000; Liu et al. 2016; Oualmakran et al. 2016). There are two steps to conduct freeze-drying of samples.

Step 1: submerging soil samples (stored in a 50 ml falcon tube sealed with top cap) in liquid nitrogen (boiling temperature -196 centigrade). This allows rapid freezing of soil moisture to pass into amorphous ice. To prevent recrystallization which may cause volume increase of water, the time when samples are kept in liquid nitrogen should not be longer than 5 min (Delage et al. 1996; Galle 2001). In this step, the rapid freezing has the largest possibility of keeping the microstructure undisturbed and preventing samples from deformation (Oualmakran et al. 2016).

Step 2: carrying out the sublimation of ice in freeze-dryer (such as Christ ALPHA 1-2 (Liu et al. 2016) and Alpha I/5 Martin Christ type (Galle 2001)) at a temperature of -20 centigrade or lower and subjected to a vacuum pressure of 0.01 mmHg (equivalent to 1.333 Pa)

(Delage et al. 1996; Penumadu and Dean 2000). This is to reduce the shrinkage during drying caused by the formation of air-water menisci (Delage et al. 1996). The sublimation is recommended to last between 24 and 36 h (Delage et al. 2006).

3.3.3.1.2 Oven-drying

Oven drying can be classified into high temperature oven drying and low temperature oven drying. Sample are usually dried at 105℃ for 24 hours under high temperature oven drying. For low temperature drying, the oven can be set to 40℃ and samples should be weighed occasionally until no mass change is detected. This procedure can take over 72 hours to complete (Oualmakran et al. 2016). It has been widely confirmed that the higher temperature can lead to more significant compression of soil microstructure (Lawrence et al. 1979; Delage et al. 1996).

3.3.3.1.3 Cutting Samples

Due to the large size of triaxial samples (over 150cm^3) and small volume of a MIP standard cell (3-5mL), samples must be cut into a proper size to fit in the MIP cell. In this study, the samples were cut into two different sizes. One is a large size with the longest length of ~10mm (the largest size that can fit in the cell easily) as shown in Figure 3.7(a) and the other is a small size with the longest length of ~4mm as shown in Figure 3.6(b). This is to study how the size of the sample will affect the result of MIP. A smaller size has a larger specific surface area where large open voids can be generated during cutting, which might lead to an unexpected increase in void ratio and affect the PSD.

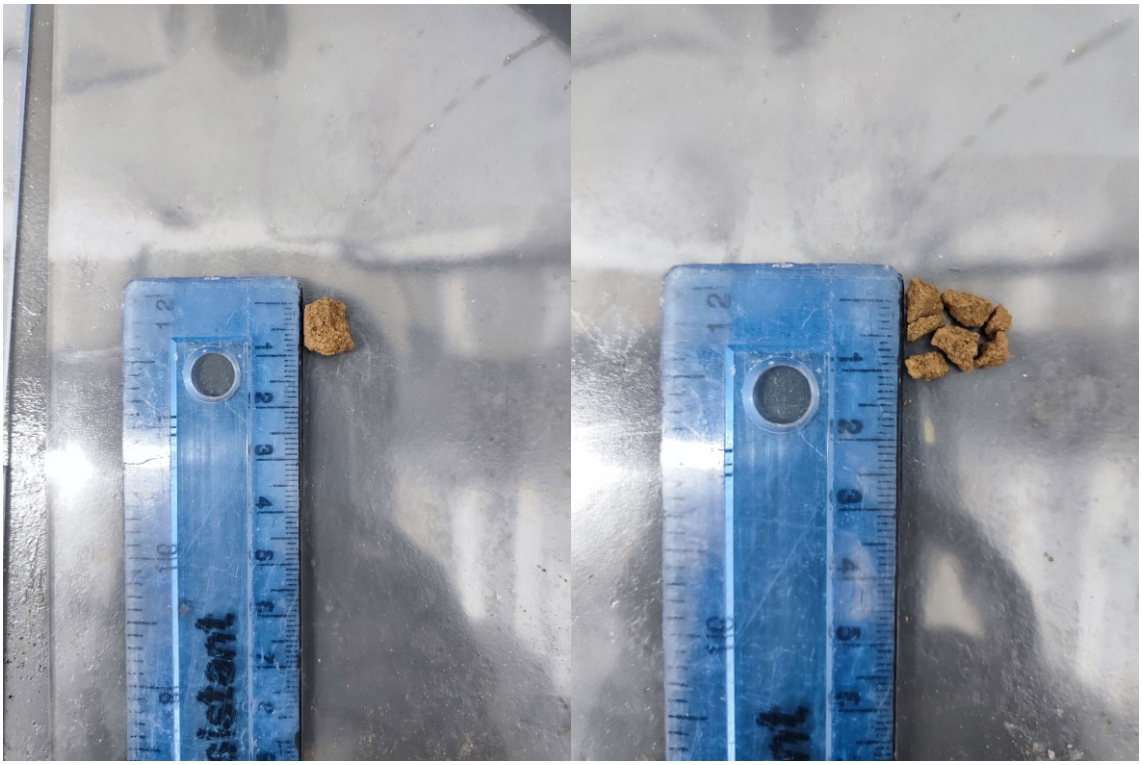

(a) Large size (b) Small size

Figure 3.7 Sizes of samples for MIP tests

3.3.3.2 Testing device

A Quantachrome PoreMaster 60 was used for MIP tests, as shown in Figure 3.8. This device facilitates mercury intrusion into pores of a soil sample to obtain the pore size and pore volume. It has two stations, a low-pressure station (LP station) and a high-pressure station (HP station). The pressure range in the low-pressure station is from 1.379 to 344.738 kPa (~0.2 to 50 psia), the equivalent pore diameter based on equation (3-2) is from ~1000μm to ~4μm. For the high-pressure station, the range is from 137.895 kPa to 413685.440 kPa (20 psia to 60000 psia) and the equivalent pore diameter is from ~10000 nm to 3.6 nm. Therefore, the overall testing range in diameter is from 3.6 nm to 1000000 nm. The accessories needed for MIP tests are presented in Figure 3.9.

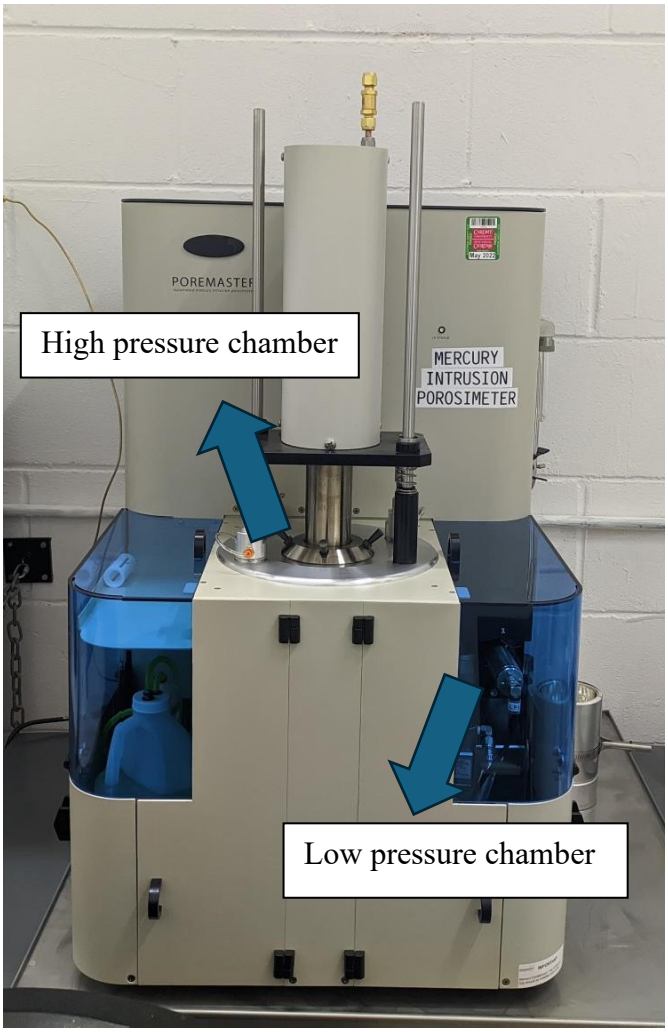

Figure 3.8 Quantachrome PoreMaster 60 device

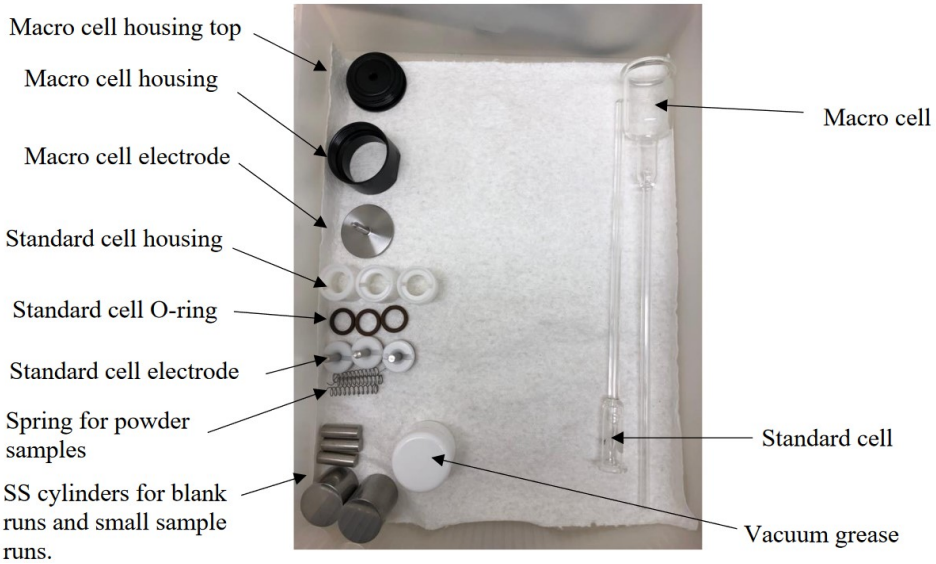

Figure 3.9 Accessories for MIP

3.3.3.3 Testing procedure

The general procedure of MIP tests includes three stages such as cell assembly, low pressure analysis and high pressure analysis. The details of each step are elaborated in the following sections.

3.3.3.3.1 Cell assembly

Samples were sealed in the standard cell with O-ring, upper cell housing and electrode as shown in Figure 3.10. Silicon grease was used between the upper surface of etched circle and electrode to guarantee the sealing performance. It is better to fill the cell with as much soil as possible to reduce the mercury needed for cell filling, as shown in Figure 3.11.

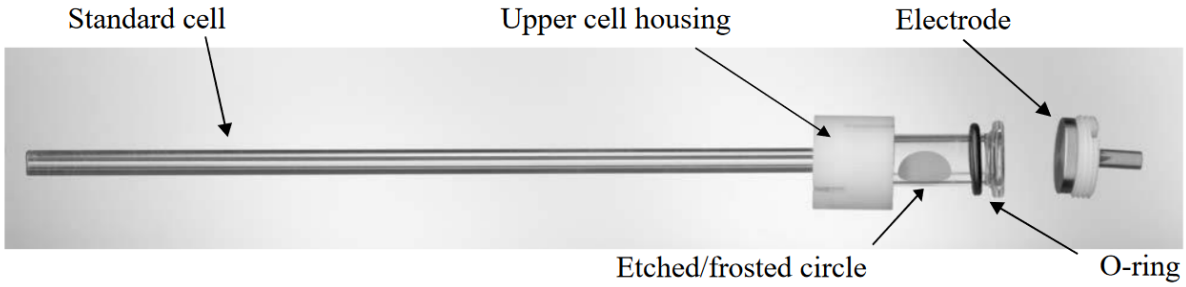

Figure 3.10 Illustration of cell assembly

Figure 3.11 Example of cell filling with a Dundee silt sample

3.3.3.3.2 Low pressure analysis

Samples were first taken to low-pressure station to do the low pressure analysis. After sliding the cell into the station and locking it (see Figure 3.12), the analysis can be run. The

surface tension of mercury was selected as 480.00 erg/cm^2 (0.480 N/m) and the contact angle between mercury and pore wall was defined as 140.00 degrees. The 'Low pressure and Refill' mode was chosen for the best merge results when the high pressure analysis is needed as recommend by the manufacturer. During low pressure analysis, the pressure started from the minimum pressure 1.379 kPa (~0.2 psia) to 344.738 kPa (50 psia). The completion of low pressure analysis included both of the intrusion and extrusion of mercury (not full extrusion, remaining mercury stayed in the cell and would be used in the following high pressure analysis).

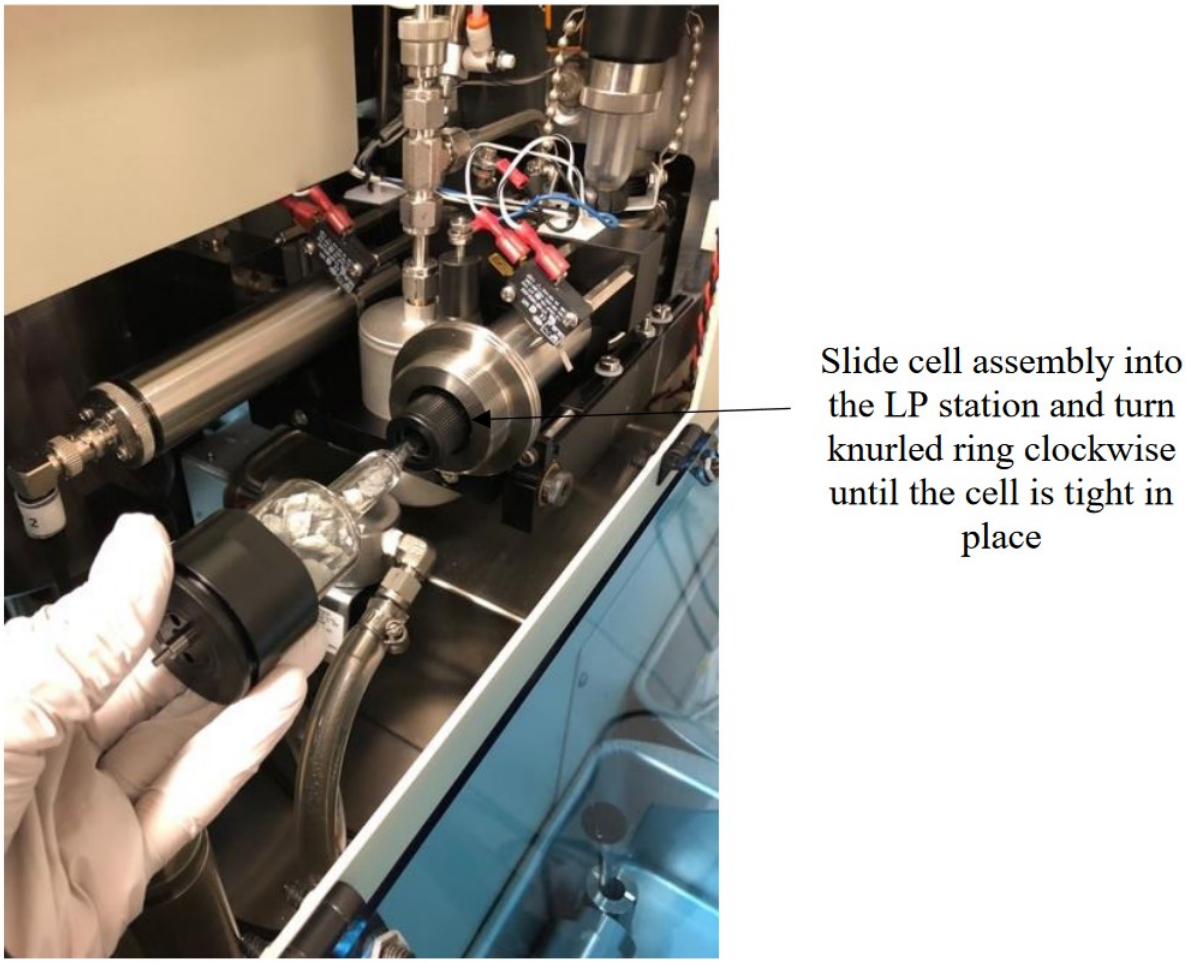

Figure 3.12 Sliding cell assembly into LP station

3.3.3.3.3 High pressure analysis

After the low pressure analysis was completed, hydraulic oil is added to fill the cell stem above the mercury. Then the cell assembly is assembled with an extra metal housing and weight (see Figure 3.13). The cell is then transferred to the bottle with hydraulic oil and the filled stem again until no air bubbles appear. The HP station is then sealed before running the analysis.

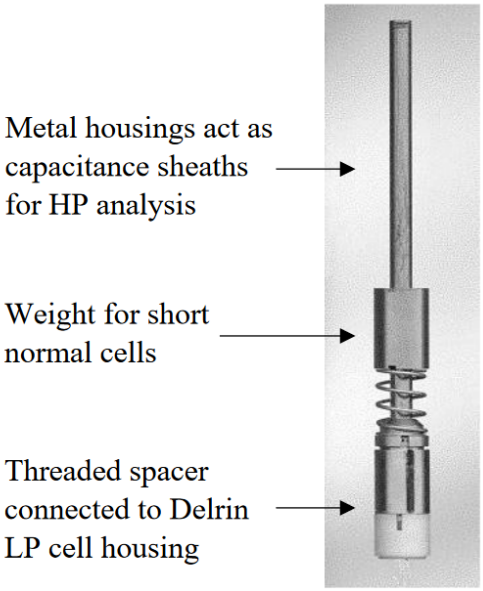

Figure 3.13 Standard cells with metal housing for high pressure station

3.3.3.4 Testing program

The purpose of MIP tests is to obtain the PSDs of the soil under various conditions and to study their evolution in relation to the macroscopic hydro-mechanical behaviour. Therefore, specimens used for both saturated and unsaturated triaxial tests were considered for MIP in this study. The conditions of these specimens before MIP have been summarized in Table 3.8.

Saturated specimens M2, M3 and M5 were sheared to different axial strains (20%,10% and 5%) but under the same confining stress of 200kPa. Saturated specimens M6, M13 and M14 were sheared to different axial strains (20%,10% and 5%) but under the same confining stress of 400kPa. Saturated Specimens A, B and C were sheared under various confining stresses (100, 200 and 400kPa) to the same axial strain (20%). PSDs of these specimens were used to study the evolutional behaviour of PSDs of Dundee silt and their relationship with the behaviour of saturated specimens. PSDs of specimens M9, M10 and M11 were used to study the evolution of PSD during the primary stages of triaxial tests including compaction, saturation and consolidation. Unsaturated specimens M7 and M12 were sheared under constant suction of 100kPa and net confining stress of 200kPa but to different axial strains (10% and 5%) to investigate the microstructural-hydro-mechanical behaviour of unsaturated Dundee silt.

To fully study how heterogeneity, drying methods and sample size fits in MIP cell affect the obtained PSDs, the specimens were relabelled based on the way they were prepared. Specimens A, B and C were all oven-dried and prepared as a small size (indicated in section 3.3.3.1.3). For each specimen, the samples were obtained from both the edge (labelled by ‘E’) and the centre (labelled by ‘C’), and then they were taken to MIP separately to consider the effect of heterogeneity. Specimens M2, M3, M5, M6 and M7 were from the centre of each specimen and were all freeze-dried. They were also prepared as a small size except M7 which

had a large size. To consider the effects of drying methods and sample size, the specimen M11 were prepared under three conditions. M11-FR-L was from the centre, freeze-dried and had a large size. M11-OV-L was from the centre, oven-dried and had a large size. M11-OV-L was from the centre, oven-dried and had a small size. By comparing the PSDs of M11-FR-L and M11-OV-L, the impact of drying methods on PSD can be discovered while the comparison between M11-OV-L and M11-OV-S can present the impact of sample size. The testing program has been summarized in Table 3.9. A similar program was also designed for M9 and M10. Since M11, M9 and M10 are related to the procedure before shearing (compaction, saturation and consolidation) respectively. The PSDs of these three specimens can represent the evolution of microstructure after compaction, after saturation and after consolidation.

Table 3.8 Conditions of specimens before MIP

Specimen No.	Net confining stress (kPa)	Axial strain (%)	Void ratio obtained from GDS
M2	200	20	0.476
M3		10	0.533
M5		5	0.524
M6	400	20	0.436
M13		10	0.476
M14		5	0.492
M9	/	Tested after saturation	0.610
M10		Tested after saturation and consolidation (under 200 kPa effective stress)	0.574
M11		Tested after compaction	0.609
A	100	20%	0.505
B	200	20%	0.458
C	400	20%	0.415
M7	200	10%	0.477
M12	200	5%	0.511
M15	100	20%	0.548
M18	100	10%	0.561
M19	100	5%	0.578
M20	200	10%	0.478
M21	200	15%	0.490

Table 3.9 Testing program for MIP

MIP No.	Specimen No.	Positions inside of samples	Oven-dried/Freeze-dried	Specimen sizes inside of MIP cell
11E	A	Edge	Oven-dried	Small
21C	A	Centre	Oven-dried	Small
55E	B	Edge	Oven-dried	Small
65C	B	Centre	Oven-dried	Small
36E	C	Edge	Oven-dried	Small
46C	C	Centre	Oven-dried	Small
M2	M2	Centre	Freeze-dried	Small
M3	M3	Centre	Freeze-dried	Small
M5	M5	Centre	Freeze-dried	Small
M6	M6	Centre	Freeze-dried	Small
M7	M7	Centre	Freeze-dried	Large
M11-FR-L	M11	Centre	Freeze-dried	Large
M11-OV-L	M11	Centre	Oven-dried	Large
M11-OV-S	M11	Centre	Oven-dried	Small
M9-OV-L	M9	Centre	Oven-dried	Large
M9-OV-S	M9	Centre	Oven-dried	Small
M9-FR-L	M9	Centre	Freeze-dried	Large
M10-FR-L	M10	Centre	Freeze-dried	Large
M10-OV-L	M10	Centre	Oven-dried	Large
M10-OV-S	M10	Centre	Oven-dried	Small
M12	M12	Centre	Freeze-dried	Large
M13	M13	Centre	Freeze-dried	Large
M14	M14	Centre	Freeze-dried	Large
M15	M15	Centre	Freeze-dried	Large
M18	M18	Centre	Freeze-dried	Large
M19	M19	Centre	Freeze-dried	Large
M20	M20	Centre	Freeze-dried	Large
M21	M21	Centre	Freeze-dried	Large

3.3.4 Chilled-mirror dew-point hygrometer tests

Chilled-mirror dew-point hygrometer tests were carried out on compacted samples of Dundee silt under predetermined dry densities (1.62 and 1.54 Mg/m^3) by means of WP4C device from METER Group. The purpose of these tests is to obtain soil-water characteristic curves (SWCCs) of Dundee silt at various dry densities and compare them with the SWCCs obtained by the PSDs at the same dry densities. Details of these tests are provided below.

3.3.4.1 Sample preparation

To obtain the SWCCs of soils by means of WP4C, soil-water mixtures were prepared at several water contents. Compacted specimens are prepared directly in the sample cup of the device. The diameter and height of the sample mould are 36.92 mm and 9.14 mm, respectively. Each specimen was manually compacted by a piston to half height of the cup to reach the targeted dry density and then was sealed by a top cap.

3.3.4.2 Testing device

The WP4C was used to establish SWCCs of the soil. This device is mainly composed of a display screen and a sample chamber as shown in Figure 3.14. The sample chamber has five main components, including a thermoelectric cooler (for controlling the mirror temperature), a photoelectric cell (for detecting the exact point when condensation first appears on the mirror), a photodetector (for sensing the change in reflectance when condensation occurs on the mirror), a thermocouple (for temperature recording) and an internal fan (for circulating the air to reduce the time to equilibrium) (see Figure 3.15). The basic principle of obtaining suction by this device is detecting the water potential of air, which, at equilibrium, is the same with the water potential of the sample. The testing range of this device is from 0 to -300 MPa. The accuracy is ±0.05 MPa from 0 to -5 MPa while it is 1% from -5 to -300 MPa.

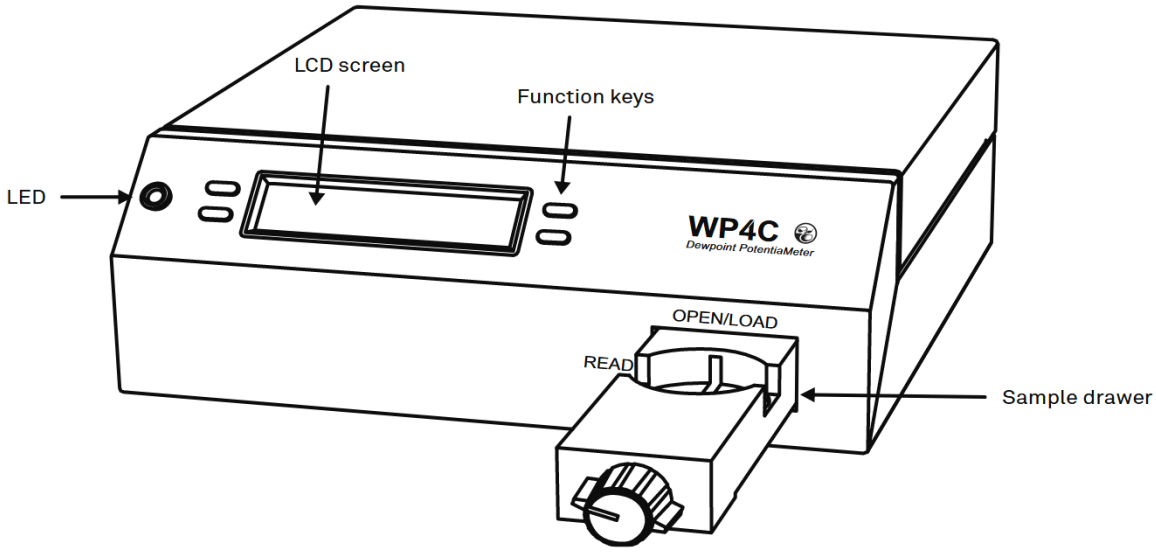

Figure 3.14 Illustrative graph of WP4C (WP4C Manual. 2019)

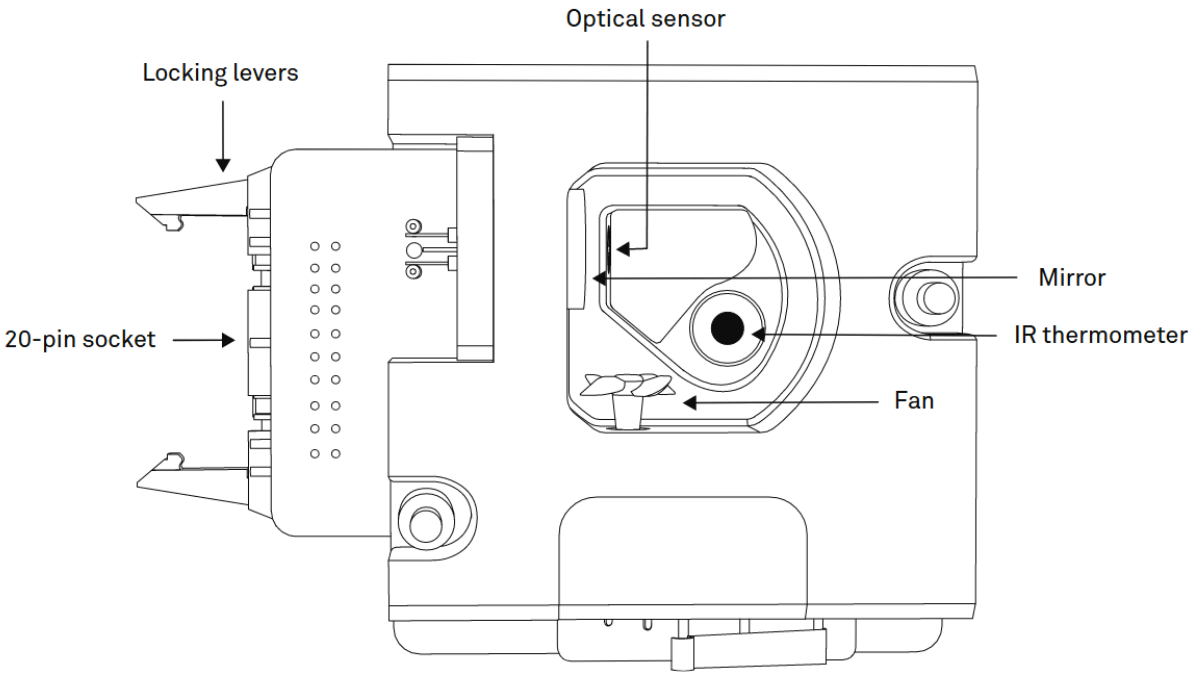

Figure 3.15 Illustrative graph of WP4C sample chamber (WP4C Manual. 2019)

3.3.4.3 Testing procedure

The basic testing procedure of using WP4C includes three steps, warmup, calibration and measurement.

The device should be turned on at least 30 minutes ahead of starting any test to ensure the optimal testing temperature is established. After the warmup is finished, the second step is calibration, for which 0.5 mol/kg potassium chloride (KCL) solution is recommended. In this step, it is necessary to ensure the sample temperature is below sample block temperature before entering the calibration mode. The KCL solution is then poured into a sample cup and placed in the sample drawer. Extra caution is taken when sliding the drawer to avoid spilling and contamination to the chamber. After the reading is completed, the water potential of the standard solution should be within ± 0.05 MPa of the correct value of the KCL standard at that temperature (see Table 3.10). If the reading is not within the range, the chamber might be contaminated and needs to be cleaned before repeating the previous process. After repeating the process, if the reading is still outside of that range, a manual calibration should be done by pressing the button to move the value up or down to the standard value in Table 3.10.

After the device calibration is completed, the measurement of samples can be conducted. In this study, the WP4C sample block temperature was preset to 25 ℃ while the sample cups with top caps were placed in a temperature-controlled plate at 24 ℃ for at least 10 minutes to make sure the sample temperature is lower than the chamber temperature. The top cap is removed and the sample cup placed in the drawer before a reading is taken when the sample

temperature reaches 25 ℃. The absolute value of the water potential is the matric suction of the sample.

Table 3.10 Standard water potential of 0.5 mol/kg KCL solution (WP4C Manual. 2019)

Temperature (℃)	Standard water potential of 0.5 mol/kg KCL
15	-2.14
20	-2.18
25	-2.22
30	-2.26

3.3.4.4 Testing program

In this study, SWCCs at two dry densities (1.62 and 1.54 Mg/m^3) have been obtained. The testing program is presented in Table 3.11.

Table 3.11 Testing program with WP4C

Dry density (Mg/m^3)	Sample cup No.	Water content (%)
1.54	S1	13.9
	S2	14.4
	S3	17.3
	S4	17.5
	S5	19.3
	S6	19.5
	S7	21.3
	S8	21.5
	S9	25.9
	S10	26.8
1.62	W1	18.3
	W2	20.2
	W3	21.3
	W4	23.0

3.4 Concluding remarks

This chapter describes the material used and the methodology for studying the microstructural-hydro-mechanical coupled behaviour of soils. Dundee silt, a natural soil, was selected as the soil for testing. The experimental methodology includes saturated triaxial tests, unsaturated triaxial tests, MIP tests and chilled-mirror dew point tests. Saturated and unsaturated triaxial tests were conducted for studying the hydro-mechanical behaviour of soils. Triaxial tests were then taken to MIP tests to investigate the pore size distributions under each

loading condition and their evolution with external loading. Chilled-mirror dew point tests were carried out to study the water retention behaviour of soils and its relationship with microstructure.

CHAPTER 4

Microstructural-hydro-mechanical coupled behaviour of a natural soil

4.1 Introduction

The hydro-mechanical behaviour of soils (Musso et al. 2013; Navarro et al. 2020b; Wang et al. 2023; Wu et al. 2024), such as stress-strain behaviour, shear strength, volume change and water content change during loading/unloading, plays an important role in engineering application including studies of landslide (Tsaparas et al. 2002; Troncone 2005; Sorbino and Nicotera 2013), foundation (Terzaghi 1925; Barden et al. 1969; Baker and Frydman 2009) and soil barrier to waste (Lee and Tank 1985; Delage 2007; Sellin and Leupin 2013). Abundant evidence (Delage et al. 2006; Cuisinier et al. 2011; Al-Mukhtar et al. 2012; Vaunat and Casini 2017; Cai et al. 2020b; Wu et al. 2024) has revealed that the soil microstructure has a tight connection with the hydro-mechanical behaviour of soils. Therefore, it is essential to experimentally study the coupling between the soil microstructure and the hydro-mechanical behaviour.

The hydro-mechanical behaviour of soils can be obtained by triaxial tests and chilled-mirror dew-point hygrometer tests. A triaxial test is a common laboratory method to determine the mechanical behaviour of soils, such as shear strength, cohesion, internal friction angle, critical state and failure (Bishop and Wesley 1975; Rahardjo et al. 2004; Houston et al. 2008; Ng et al. 2012). This test can be conducted in either saturated or unsaturated condition and under various stress conditions to monitor the stress-strain behaviour and change of water content of soils. There are three typical types of triaxial tests including Unconsolidated-Undrained (UU), Consolidated-Undrained (CU) and Consolidated-Drained (CD) tests. During the UU test, the soil sample is sheared without drainage and any previous drainage and consolidation under the applied confining stress. Therefore, the UU test is a quick test for assessing the short-term stability of soils (Chen and Kulhawy 1993; Bol et al. 2019). The CU test allows the sample to consolidate under a predetermined confining stress and then to be sheared without drainage. This test is widely used in embankments, foundations and slopes which are subjected to long-term loading but have a low possibility of significant drainage in the short term (Stróżyk and Tankiewicz 2014; Casey et al. 2016). The CD test allows the soil sample to consolidate under a confining stress and be sheared under drained conditions. The behaviour of soils during a CD test is similar to that over a long period, which is essential for the study of soil stability and settlement (Fredlund et al. 1978; Rahardjo et al. 2004; Sivakumar et al. 2010).

The chilled-mirror dew-point hygrometer tests can be conducted through chilled-mirror hydrometers to obtain soil-water characteristic curve (SWCC) of soils which describes the

relationship between the water content (or degree of saturation) of soils and the water potential (or suction) of soils. The principle of using this device is to obtain pore water potential (suction) based on its relationship with partial vapor pressure or relative humidity (Gee et al. 1992). Many researchers have adopted this technique or other methods to obtain SWCCs of various kinds of soils which is one of the most important aspects of hydro-mechanical behaviour (Malaya and Sreedeep 2012; Tripathy et al. 2014a; Tripathy et al. 2014b; Rahardjo et al. 2019, p.; Cai et al. 2020b). All these tests mentioned above for obtaining the hydro-mechanical behaviour of soils does not consider the effects of microstructure on the hydro-mechanical behaviour and how microstructure evolves under external loading or suction change.

Pore size distribution, which can be obtained by mercury intrusion porosimetry (MIP) tests (Nagpal et al. 1972; Tanaka et al. 2003), represents the numerical range of pore sizes and their volumetric proportions in a representative volume of soils (Nimmo 2013). Therefore, pore size distribution can be regarded as an indicator of soil microstructure. The evolution of pore size distribution (soil microstructure) can be seen when soil samples undergo external loading or suction change. External loading, such as compaction, isotropic loading and shearing, usually have a more significant impact on larger pores while affects little on very small pores (Li and Zhang 2009; Wang et al. 2019; Jia et al. 2020; Li et al. 2021). For example, when a soil sample is compacted to various void ratios, more larger pores will be eliminated with the decrease of void ratios, leading to a significant downward movement of pore size distribution (decrease in total pore volumes) and a movement towards the direction of smaller pores (elimination of larger pores). The evolution of pore size distribution due to suction increase (drying path) is similar to that due to external loading. The volume of macropores decreases as the degree of saturation decreases (Li and Zhang 2009). Besides, for an initially saturated soil sample, its unimodal pore size distribution can evolve into bimodal shape during the drying process (Li and Zhang 2009; Oualmakran et al. 2016; Wang et al. 2020). The evolution of pore size distribution due to suction increase (drying path) is similar to that due to external loading. The volume of macropores decreases as the degree of saturation decreases (Li and Zhang 2009). Besides, for an initially saturated soil sample, its unimodal pore size distribution can evolve into bimodal shape during the drying process (Li and Zhang 2009; Oualmakran et al. 2016; Wang et al. 2020). All these tests merely focus on the evolution of pore size distribution under external loading or suction change but fail to monitor the hydro-mechanical behaviour of soils, they thus cannot consider the interaction between soil microstructure and the hydro-mechanical behaviour such as detecting the evolution of pore size distribution, volume change and water content change in a continuous shearing path.

In this chapter, the evolution of pore size distribution and the hydro-mechanical behaviour of Dundee silt was both monitored in each test. The objectives of this chapter include: (1) study the microstructural-hydro-mechanical coupled behaviour of Dundee silt; (2) study the effects of displacement rate on the hydro-mechanical behaviour of Dundee silt; (3) study the factors that affect the pore size distribution and its evolution including initial dry density, confining stress, suction, heterogeneity, drying methods and sample sizes; (5) determine the some basic properties of hydro-mechanical behaviour such as the slopes of normal

consolidation line and rebound curve, friction angle, cohesion and the slope of critical state; (6) study the difference in the hydro-mechanical behaviour between saturated and unsaturated soils sheared at the same net confining stress.

This chapter is organized as follows. The experimental program (Section 3.3) is recalled in Section 4.2 where saturated and unsaturated CD tests are presented in Section 4.2.1, MIP tests are in Section 4.2.2 and chilled-mirror dew-point tests are in Section 4.2.3. Under results and discussion (Section 4.3), the water content and volumetric strain change during suction equilibrium and consolidation is presented in Section 4.3.1, the effects of displacement rate on hydro-mechanical behaviour is studies in Section 4.3.2, the microstructural-hydro-mechanical coupled behaviour is presented in Section 4.3.3, the effects of initial dry density, confining stress and suction are studied in Section 4.3.4, the effects of heterogeneity, drying methods and sample sizes are studied in Section 4.3.5, the normal consolidation line, friction angle, cohesion and critical state are presented in Section 4.3.6 and the comparisons among saturated and unsaturated shearing under the same net confining stress are studied in Section 4.3.7. The concluding remarks are presented in Section 4.4.

4.2 Experimental program

In order to study the microstructural-hydro-mechanical coupled behaviour of Dundee silt, a serial of tests have been conducted including saturated triaxial CD tests, unsaturated CD tests, mercury intrusion porosimetry (MIP) tests and chilled-mirror dew-point hygrometer tests. The experimental program (see Section 3.3) is recalled below.

4.2.1 Saturated and unsaturated CD triaxial tests

Saturated and unsaturated CD tests were carried out to provide the hydro-mechanical behaviour of Dundee silt including stress-strain behaviour, shear strength, void ratio change and water content change. Saturated tests include five series of tests. Series 1 consists of CD tests on saturated specimens A, B and C (initial dry density of ~1.76 Mg/m^3) at three constant confining stresses of 100, 200 and 400 kPa. The displacement rate was 0.0035 mm/min and the shearing was terminated at the axial strain of 20% for all specimens. Series 2 consists of CD tests on saturated specimens D, E, F and G (initial dry densities of ~1.62 Mg/m^3 and ~1.76 Mg/m^3) at a constant confining stress of 100kPa, but the displacement rates vary at 0.0035, 0.007 and 0.014 mm/min for each specimen. The shearing was terminated at an axial strain of 20% for all specimens. Series 3 consists of isotropic compression tests on the saturated specimen H (initial dry density of ~1.76 Mg/m^3). The effective stress changed stepwise from 50, 25, 50, 100, 200, 400 to 800 kPa. Each step last two hours for the effective stress to increase/decrease to the targeted value. Series 4 consists of CD tests on saturated specimens (initial dry density of ~1.62 Mg/m^3) at three constant confining stresses of 100 (M15, M18 and M19), 200 (M2, M3 and M5) and 400 kPa (M6, M13 and M14) at a displacement rate of 0.007 mm/min. For each confining stress, several specimens were sheared under the same condition, but the shearing was terminated at different axial strains of 20%, 10% and 5%. Three specimens

(initial dry density of ~1.62 Mg/m^3) were prepared for Series 5. M9 only underwent saturation stage and M10 underwent both saturation and consolidation stage (to 200 kPa effective stress). M11 was the original compacted sample without saturation and consolidation. These three specimens were not used for studying the stress-strain behaviour but only used for MIP tests.

The constant suction unsaturated CD tests contain two series. For Series 6 three specimens (M4, M7 and M12) were prepared to the same initial conditions but were sheared to different axial strains (20%, 10% and 5%). The suction remained 100 kPa during the tests. For Series 7, two specimens (M20 and M21) were also prepared to the same initial conditions but were sheared to different axial strains (20%, 10% and 5%). The suction remained 25 kPa during the tests.

Aside from obtaining the hydro-mechanical behaviour of Dundee silt, these series of tests can also help with the study on the effects of initial dry density on soil behaviour (Series 1 and Series 4), the effects of displacement rates on soil behaviour (Serial 2), normal consolidation line (Series 3), shear strength and Mohr circles (Series 1 and Series 4), and critical state (Series 1 and Series 4).

4.2.2 MIP tests

After triaxial tests were completed, those specimens above were double sealed with plastic bags again and well stored in a sealed plastic bucket for further MIP tests. The purpose of MIP tests is to obtain the PSDs of the soil under various conditions and to study their evolution in relation to the macroscopic hydro-mechanical behaviour.

Saturated specimens M2, M3 and M5 were sheared to different axial strains (20%,10% and 5%) but under the same confining stress of 200kPa. Saturated specimens M6, M13 and M14 were sheared to different axial strains (20%,10% and 5%) but under the same confining stress of 400kPa. Saturated Specimens A, B and C were sheared under various confining stresses (100, 200 and 400kPa) to the same axial strain (20%). PSDs of these specimens were used to study the evolutional behaviour of PSDs of Dundee silt and their relationship with the behaviour of saturated specimens. PSDs of specimens M9, M10 and M11 were used to study the evolution of PSD during the primary stages of triaxial tests including compaction, saturation and consolidation. Unsaturated specimens M7 and M12 were sheared under constant suction of 100kPa and net confining stress of 200kPa but to different axial strains (10% and 5%) to investigate the microstructural-hydro-mechanical behaviour of unsaturated Dundee silt.

To fully study how heterogeneity, drying methods and sample size fits in MIP cell affect the obtained PSDs, the specimens were relabelled based on the way they were prepared. Specimens A, B and C were all oven-dried and prepared as a small size (indicated in section 3.3.3.1.3). For each specimen, the samples were obtained from both the edge (labelled by ‘E’) and the centre (labelled by ‘C’), and then they were taken to MIP separately to consider the effect of heterogeneity. Specimens M2, M3, M5, M6 and M7 were from the centre of each

specimen and were all freeze-dried. They were also prepared as a small size except M7 which had a large size. To consider the effects of drying methods and sample size, the specimen M11 were prepared under three conditions. M11-FR-L was from the centre, freeze-dried and had a large size. M11-OV-L was from the centre, oven-dried and had a large size. M11-OV-L was from the centre, oven-dried and had a small size. By comparing the PSDs of M11-FR-L and M11-OV-L, the impact of drying methods on PSD can be discovered while the comparison between M11-OV-L and M11-OV-S can present the impact of sample size. A similar program was also designed for M9 and M10. Since M11, M9 and M10 are related to the procedure before shearing (compaction, saturation and consolidation) respectively. The PSDs of these three specimens can represent the evolution of microstructure after compaction, after saturation and after consolidation.

4.2.3 Chilled-mirror dew-point hygrometer tests

Chilled-mirror dew-point hygrometer tests were carried out on compacted samples of Dundee silt under predetermined dry densities (1.62 and 1.54 Mg/m^3) by means of WP4C device from METER Group. The purpose of these tests is to obtain soil-water characteristic curves (SWCCs) of Dundee silt at various dry densities and compare them with the SWCCs obtained by the PSDs at the same dry densities. For the dry density of 1.54 Mg/m^3, the specimens were prepared to the following water contents when obtaining the suctions: 13.9, 14.4, 17.3, 17.5, 19.3, 19.5, 21.3, 25.9, 26.8%. For the dry density of 1.62 Mg/m^3, the water contents were 18.3%, 20.2%, 21.3% and 23.0%.

4.3 Results and discussion

The test results are presented and discussed in the section below.

4.3.1 Axial strain, water volumetric strain and volumetric strain change during suction equilibrium and consolidation

Before specimens were sheared, they were saturated or subjected to specific suctions and then were consolidated to predetermined stresses. The behaviour of these specimens during these stages can affect the behaviour during shearing. Therefore, the axial strain, water volumetric strain and volumetric strain change during these stages are presented below.

4.3.1.1 Suction equilibrium

Figure 4.1 presents the change of volumetric strain, axial strain and water volumetric strain (the ratio of water volume change over initial water volume) during suction equilibrium stage. For Specimen M4, M7 and M12, there were subjected to a suction of 100 kPa and a net mean stress of 25 kPa. It can take up to 18 days to reach the equilibrium. During this stage, these three specimens all generally show shrinkage despite slight fluctuation in strains as shown in Figure 4.1(a) and Figure 4.1(b). The ultimate volumetric strain varies from 2.5% to 3.5%

and the ultimate axial strain varies from 1.5% to 4%. This difference might be attributed to the difference in initial dry densities. As shown in Figure 4.1(c), Specimen M4 and M12 both slightly drain the water during the early stage of suction equilibrium but start to absorb water at the late stage. Specimen M7 always absorbs water during this stage. The different behaviour in water absorption indicates the difference in initial water contents of these three samples. A similar behaviour of Specimen M20 and M21 can also be witnessed when they were subjected to a suction of 25 kPa and a net mean stress of 25 kPa. However, it should be noted that while Specimen M20 and M21 had similar volumetric strain change and water volumetric strain change, Specimen M20 had a much higher axial strain during suction equilibrium (see Figure 4.1(b)).

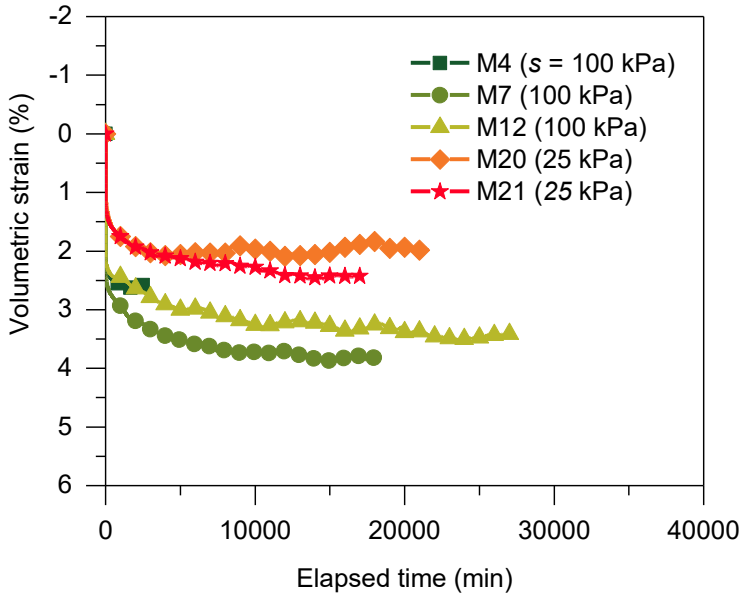

(a) Elapsed time – Volumetric strain

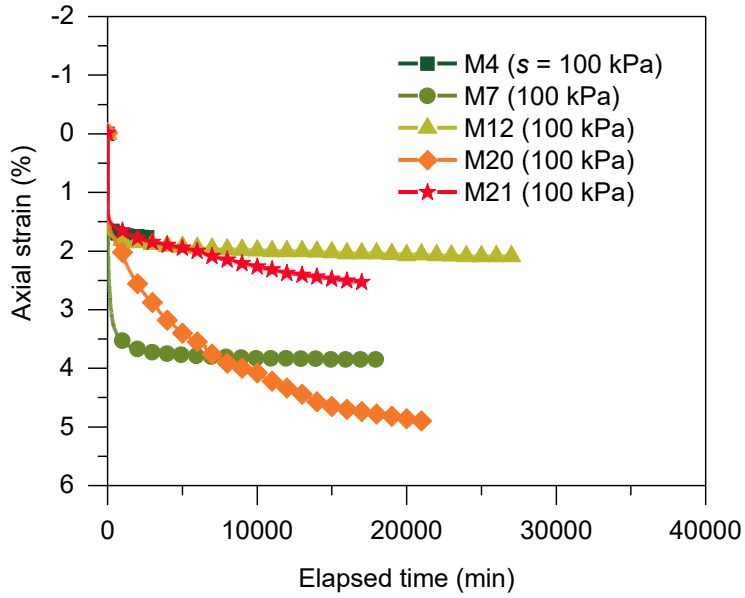

(b) Elapsed time – Axial strain

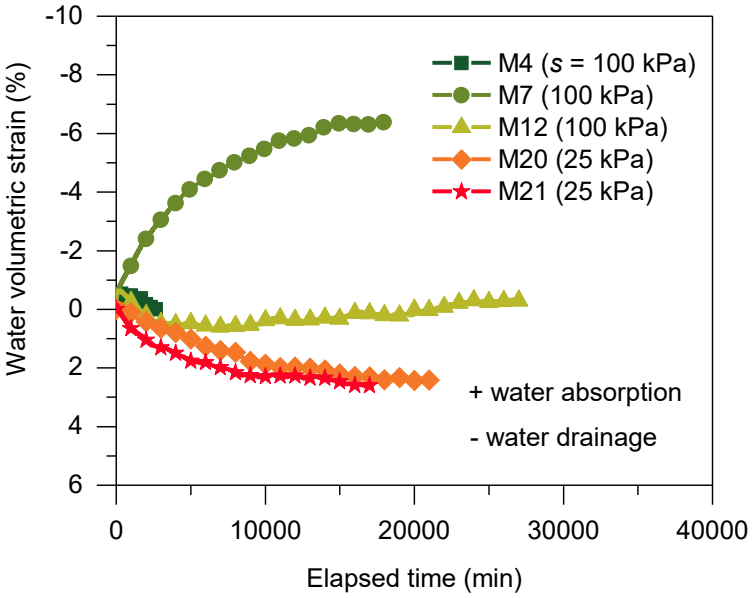

(c) Elapsed time – Water volumetric strain

Figure 4.1 Changes of volumetric stain, axial strain and water volumetric strain during suction equilibrium

4.3.1.2 Consolidation

Specimens (saturated, initial dry density of ~1.76 Mg/m^3) were consolidated under different effective stresses before shearing. Specimen A were consolidated under 100 kPa while Specimen B and C were consolidated under 200 and 400 kPa, respectively. As shown in Figure

4.2, it took 7 to 8 hours for each specimen to reach 100% consolidation (positive volumetric strain means compression). A higher volumetric strain was witnessed under a higher effective stress.

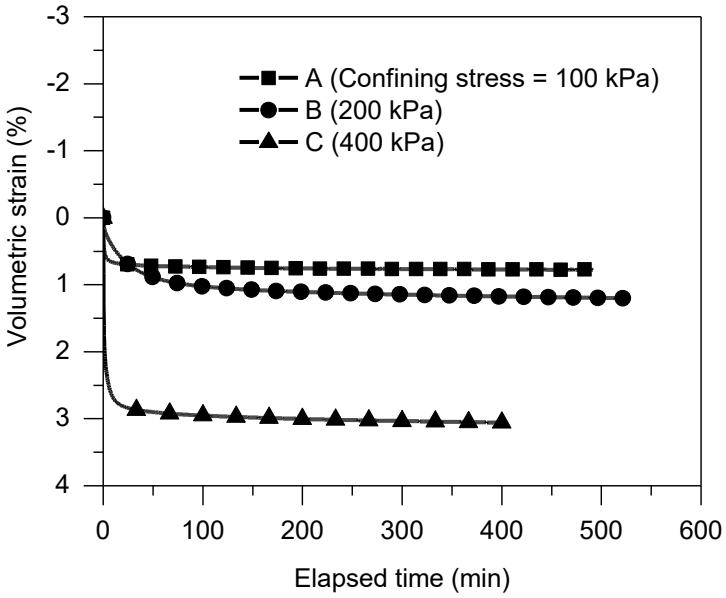

Figure 4.2 Volumetric strain versus elapsed time during saturated consolidation stage for specimens with initial dry density of ~1.76 Mg/m^3

Specimens (saturated, initial dry density of ~1.62 Mg/m^3) were consolidated under different effective stresses before shearing. Specimen M15, M18 and M19 were consolidated under an effective stress of 100 kPa. Specimen M2, M3 and M5 were consolidated under an effective stress of 200 kPa while Specimen M6, M13 and M14 were consolidated under 400 kPa, respectively. As shown in Figure 4.3, all specimens were subjected to an 8-hour consolidation. For specimens consolidated under the same effective stress, the volumetric strains of each specimen are similar to each other. Besides, a higher volumetric strain was witnessed under a higher effective stress as if the volumetric strains of M6, M13 and M14 are compared with that of M2, M3, M4, M15, M18 and M19.

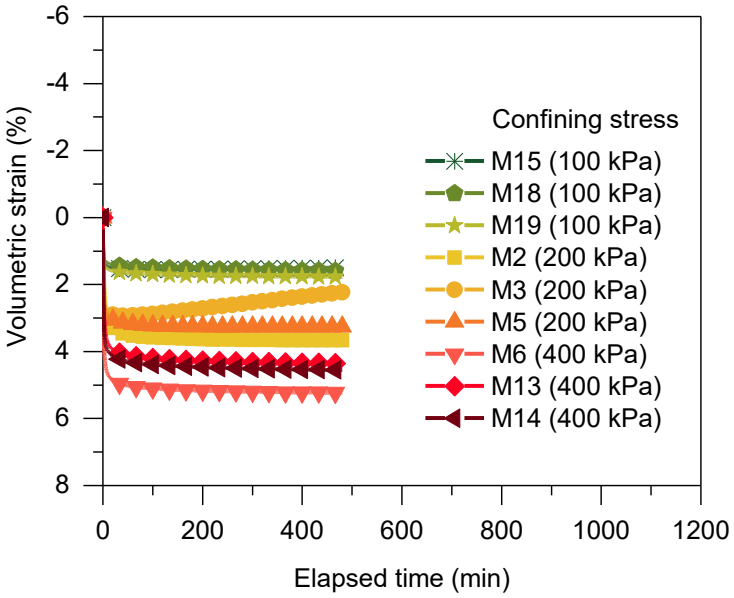

Figure 4.3 Volumetric strain versus elapsed time during saturated consolidation stage for specimens with initial dry density of ~1.62 Mg/m^3

Figure 4.4 presents strain behaviour during the consolidation stage for unsaturated specimens with initial dry density of ~1.62 Mg/m^3. Specimen M4, M7 and M12 were all consolidated under a net mean stress of 200 kPa while the suction was maintained 100 kPa. It takes about 15 days for each sample to reach 100% consolidation. Despite small difference in strain behaviour among these specimens, the maximum volumetric strain can reach ~ 2.5% while the maximum axial strain can reach ~0.5% during consolidation (see Figure 4.4(a) and (b)). Both Specimen M4 and M7 drain water during consolidation but to different strains (~-3% for Specimen M7 and ~-1% for Specimen M4), as shown in Figure 4.4(c). Specimen M12 kept absorbing water during consolidation to 3%. This difference in strain behaviour can lead to the difference in initial void ratios and degrees of saturation before shearing. Specimen M20 and M21 were all consolidated under a net mean stress of 200 kPa while the suction was maintained 25 kPa. A similar behaviour of Specimen M20 and M21 can also be found during this stage (see Figure 4.4).

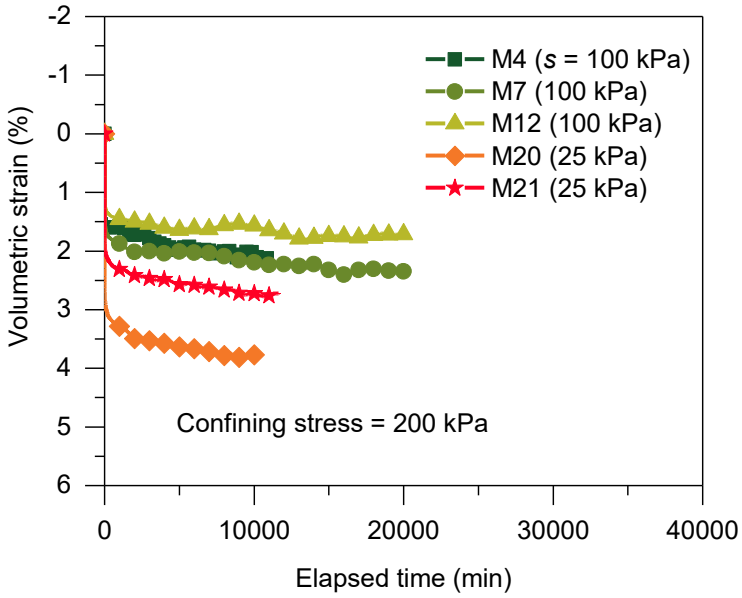

(a) Elapsed time – Volumetric strain

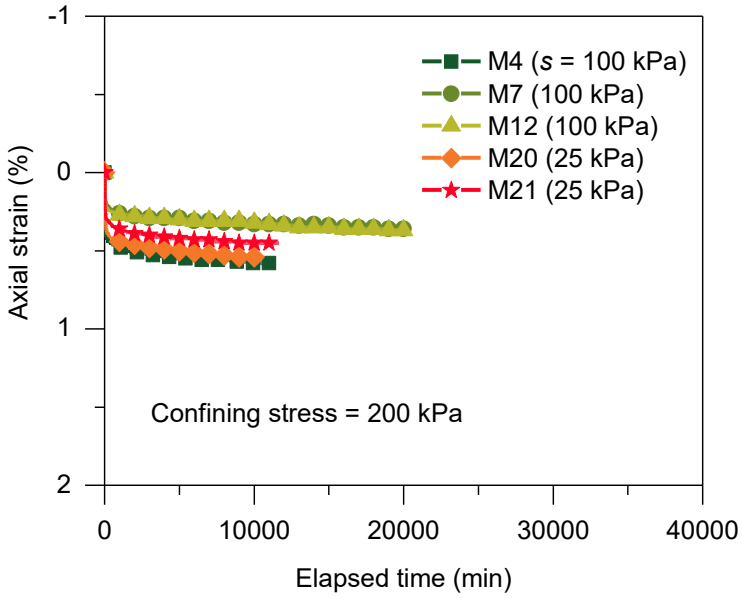

(b) Elapsed time – Axial strain

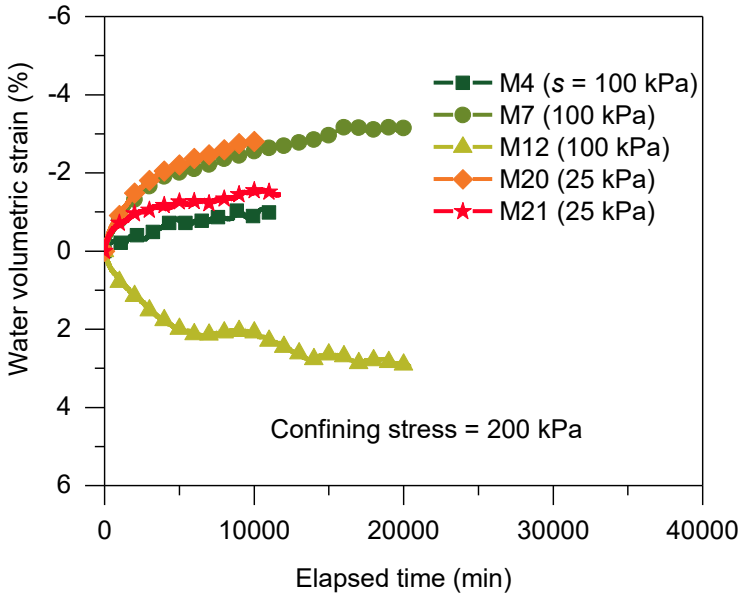

(c) Elapsed time – Water volumetric strain

Figure 4.4 Changes of volumetric strain, axial strain and water volumetric strain during unsaturated consolidation

4.3.2 Effects of displacement rate on hydro-mechanical behaviour

A high displacement rate during shearing will induce excess pore water pressure that will affect the behaviour of soils. Therefore, it is important to find a slow enough displacement rate to prevent excess pore water pressure (Ho and Fredlund 1982; Sun et al. 2016b; Almahbobi 2018). Three displacement rates were selected (0.0035, 0.007, 0.014 mm/min) for shearing specimens of different initial heights (dry densities), and the back pressure and pore water pressure were monitored during shearing. In the conventional GDS device, the pore water pressure transducer is directly connected to the back pressure, so the pore water pressure should be equal to the back pressure in value. If there is excess pore water pressure, the pore water pressure will be higher than the back pressure. As shown in Figure 4.5, the back pressure was invariably higher than the pore water pressure regardless of the displacement rates, which means all displacement rates selected are slow enough for shearing without generating excess pore water pressure. The reason why the pore water pressure was not equal to the back pressure may be attributed to the B-value of 0.95. Unconnected water still existed in pores and may delay the synchronous changes of pore water pressure with the back pressure.

Even though all displacement rates selected did not induce excess pore water pressure during shearing, they still had an impact on the stress-strain behaviour of Dundee silt. A higher displacement rate can lead to a lower shear strength and a larger axial strain is required to reach the peak deviatoric stress (see Figure 4.6).

The initial density is another factor that affects the stress-strain behaviour of Dundee silt. While specimens with an initial dry density of ~1.76 Mg/m^3 showed significant strain-softening, the decrease of deviatoric stress with increasing axial strains was almost negligible for the specimen with an initial dry density of ~1.62 Mg/m^3 (see Figure 4.6). Besides, the specimen with a lower dry density had a much smaller peak deviatoric stress than that of the specimens of a higher dry density. However, the specimen with a lower dry density tends to have a similar deviatoric stress as the specimen with a higher dry density when approaching critical state.

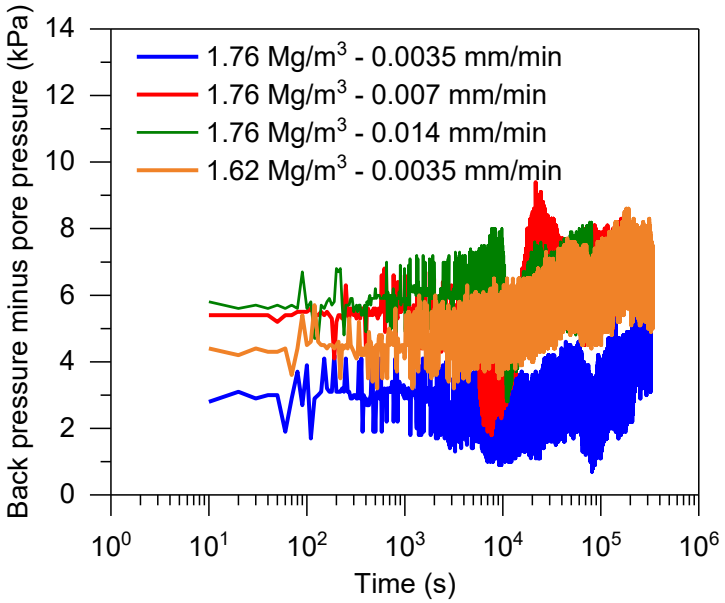

Figure 4.5 The difference between back pressure and pore water pressure versus time during shearing under different displacement rates

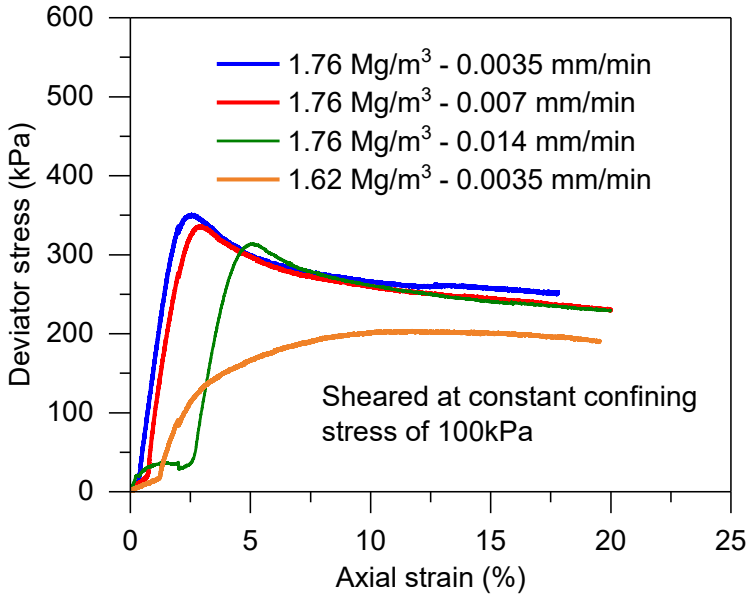

Figure 4.6 Deviatoric stress versus axial strain for specimens of different initial dry densities and displacement rates

4.3.3 Microstructural-hydro-mechanical coupled behaviour of Dundee silt

After soil specimens were prepared and consolidated to the targeted suction and net mean stress, these specimens were sheared under predetermined conditions with the stress-strain behaviour, volumetric change, void ratio change and water content change monitored. After the triaxial tests were completed, these specimens were dried and taken to MIP tests to obtain their PSDs to study the coupling between soil microstructure and the hydro-mechanical behaviour. Results of these tests are presented in the sections below.

4.3.3.1 Evolution of microstructure in a sequence of compaction, saturation and consolidation

A loading path of compaction, saturation and consolidation was represented by three freeze-dried samples. One sample was directly taken to MIP after the compaction was finished. Another sample was compacted and saturated before MIP. The other sample underwent the whole procedure of compaction, saturation and consolidation. The effective stress for isotropic consolidation was 200 kPa. Evolution of microstructure under this loading path can be easily studied from the MIP tests of these three samples, as shown in Figure 4.7. The initial sample prepared after compaction had an initial water content (15%), which was at the dry side of the compaction curve. The differential PSD of this sample has significant bimodality with one peak occurring at the pore diameter of ~ 20 μm and the other peak at the pore diameter of ~ 0.5 μm. After saturation, the swelling of sample can be witnessed as indicated by the increase of volume intruded (see Figure 4.7(a)). However, the swelling not necessarily increase the volume of all pores. As shown in Figure 4.7(b), saturation leads to a compression of relatively larger pores

and an expansion of relatively smaller pores, which makes the PSD evolve from bimodal shape to unimodal shape. After consolidation, the volume intruded is significantly reduced (see Figure 4.7(a)) which is due to the compression of larger pores while there is little change of very small pores (diameter smaller than 1 μm).

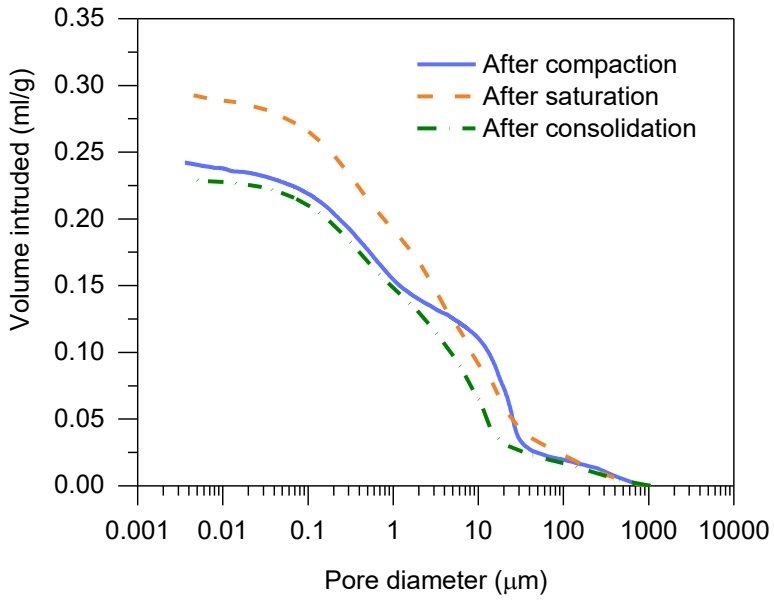

(a) Cumulative PSDs

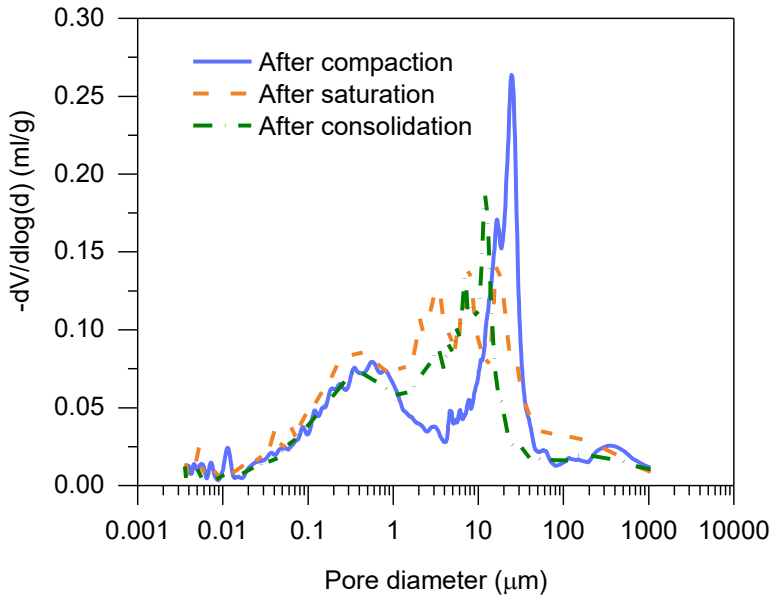

(b) Differential PSDs

Figure 4.7 Evolution of PSDs for Specimen M9, M10 and M11 in a sequence of compaction, saturation and consolidation

4.3.3.2 Evolution of microstructure in saturated triaxial tests

Specimen A, B and C were sheared under a constant confining stress of 100, 200 and 400 kPa, respectively to 20% axial strain. As shown in Figure 4.8(a), the maximum deviatoric stress increases with the increase of confining stress. Therefore, a higher confining stress will lead to a higher shear strength. For Specimen A, a significant strain-softening (Read and Hegemier 1984; Chu et al. 1992; Wood and Belkheir 1994) can be witnessed. After the maximum deviatoric stress was reached, the deviatoric stress decreased while the axial strain kept flowing. However, the strain-softening became less significant under a higher confining stress, especially for Specimen C which were sheared under a confining stress of 400 kPa. This is consistent to the findings reported by other researchers that the increase of confining stress will reduce the possibility of strain-softening (Troncone 2005; Wanatowski et al. 2008). Correspondingly, Specimen A and B also showed a great dilatancy (Matsuoka 1974; Stone and Wood 1992; Ng et al. 2019) during shearing after reaching the maximum deviatoric stress (see Figure 4.8(b)). Especially for Specimen A, the volumetric strain was increasing to a maximum positive strain which represented the shrinkage in volume during the early stage of shearing. After the maximum deviatoric stress was reached, the volumetric strain started to derease and became negative (volumetric expansion) eventually. This phenomenon was also reduced under a higher confining stress.

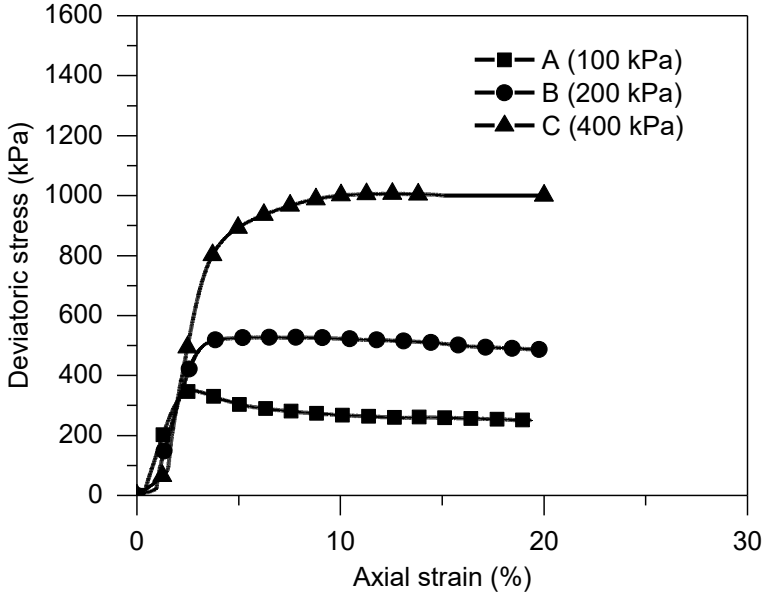

(a) Axial strain – Deviatoric stress

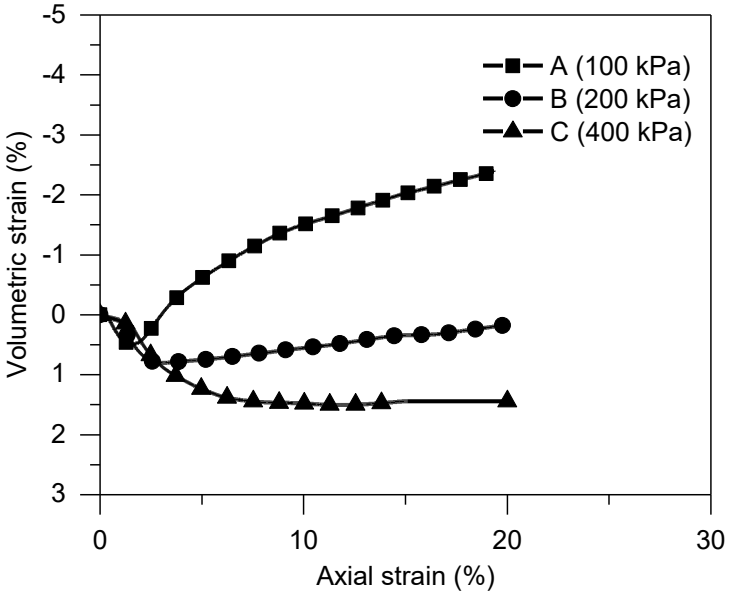

(b) Axial strain – Volumetric strain

Figure 4.8 Stress-strain behaviour of Specimen A, B and C under various confining stresses

Triaxial specimens sheared under various conditions and to different axial strains were further used for MIP tests. Saturated Specimen A, B and C at dry density of 1.76 Mg/m^3 were sheared under various confining stresses of 100 kPa, 200 kPa and 400 kPa to 20% axial strain. Specimen A, B and C were all oven dried at temperature of 105℃ for 24 hours before MIP tests. As shown in Figure 4.9(a), the volume intruded for each sample decreases with the increase of confining stresses during shearing which means the sample is more compressed under a higher confining stress. The compression of pore volume mostly comes from the compression of larger pores within the diameter range from 2 to 30 μm while pores whose diameters are smaller than 1 μm remain almost unchanged (see Figure 4.9(b)).

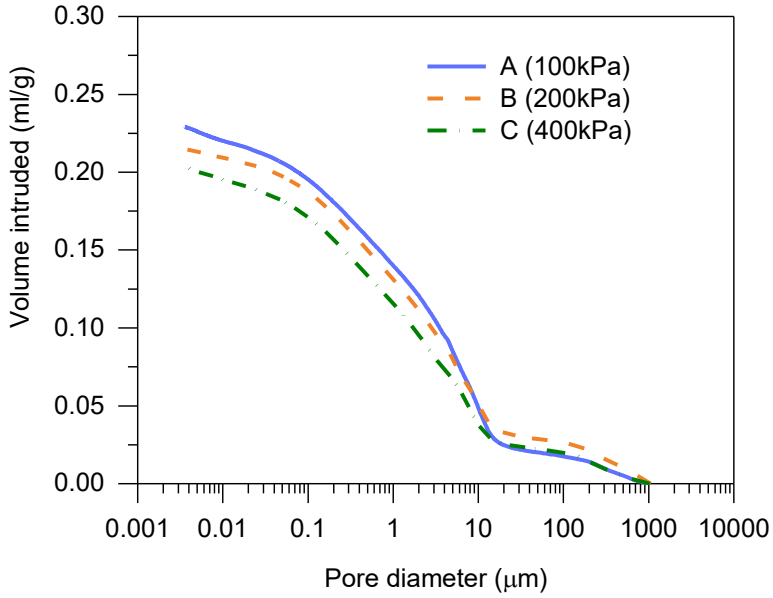

(a) Evolution of cumulative PSDs

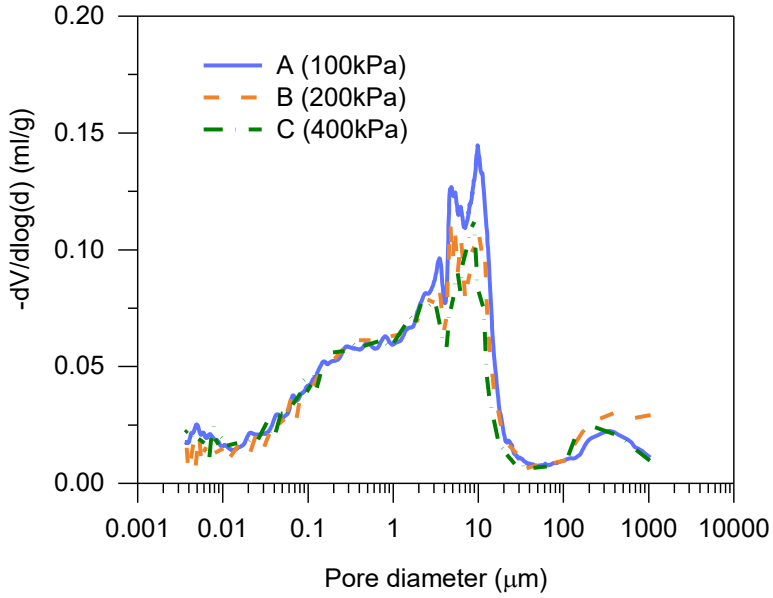

(b) Evolution of differential PSDs

Figure 4.9 Evolution of PSDs of Specimen A, B and C with increasing confining stresses during saturated shearing

Specimen M15, M18 and M19 (initial dry density of ~1.62 Mg/m^3) were all sheared under a constant confining stress of 100 kPa and to 20%, 10% and 5% axial strains respectively. The displacement rate was 0.007 mm/min. Specimen M15 shows significant strain softening (see Figure 4.10(a)) and a little dilatancy (see Figure 4.10(b))). The peak deviatoric stress is ~ 250 kPa and occurs at ~10% axial strain. As shown in Figure 4.10(b)), the maximum volumetric strain for M15 is ~2.5% while that for M18 and M19 is ~4%. This can be attributed to the initial

dry densities of M18 and M19. Because they have an initial height of 102 mm, their initial dry densities are ~1.59 Mg/m^3 slightly smaller than 1.62 Mg/m^3. However, when it comes to void ratio, the difference among these three specimens is almost negligible (see Figure 4.10(c)). Generally, despite the small difference in stress-strain behaviour, the changing tendency of deviatoric stress, volumetric strain and void ratio for each specimen is consistent to each other. Therefore, these specimens are still representative of the behaviour during saturated shearing under 100 kPa confining stress.

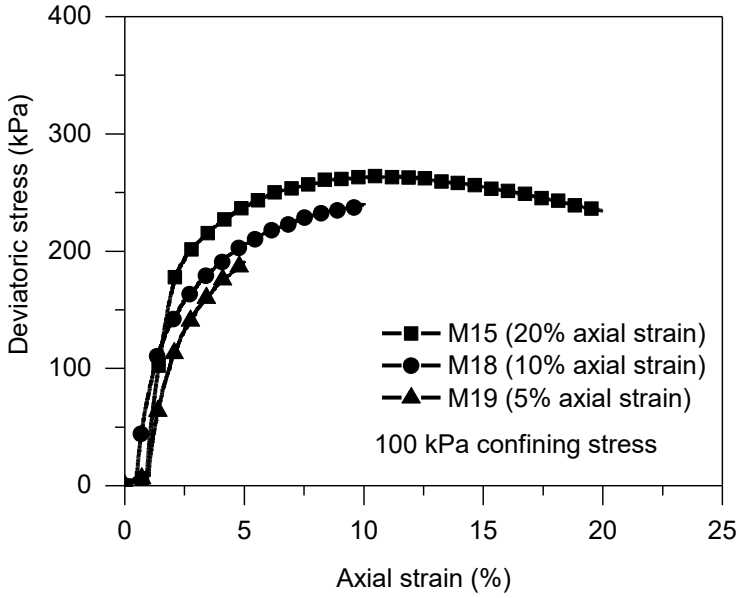

(a) Axial strain – Deviatoric stress

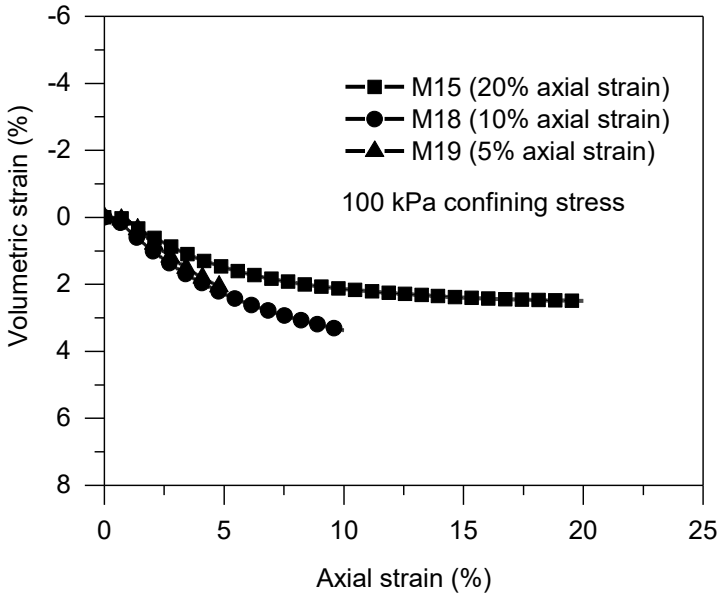

(b) Axial strain – Volumetric strain

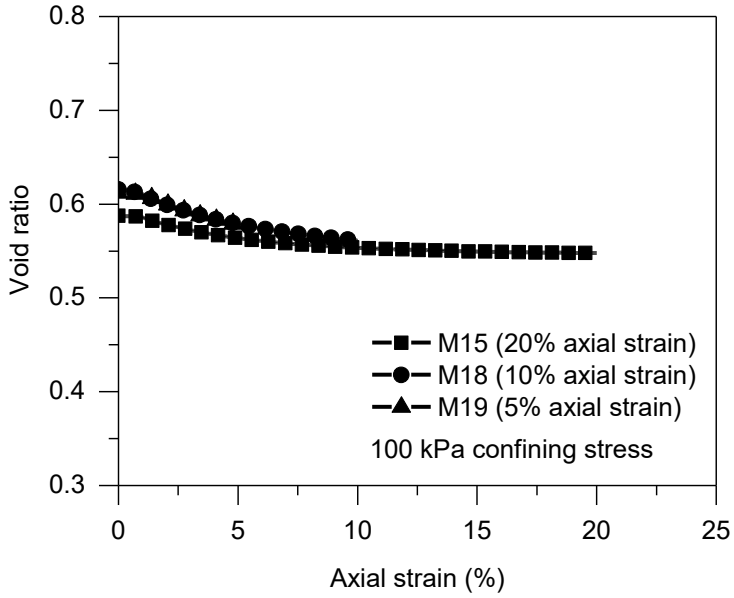

(c) Axial strain – Void ratio

Figure 4.10 Stress-strain behaviour of Specimen M15, M18 and M19 sheared under the same confining stress of 100 kPa to different axial strains

Saturated specimens M15, M18 and M19 with an initial dry density of 1.62 Mg/m^3 were sheared under confining stress of 200 kPa but to 20%, 10% and 5% axial strains, respectively. All specimens were freeze dried before MIP tests. As expected, Specimen M19 has the largest intruded volume because it was sheared to 5% axial strain and less pores were compressed compared to Specimen M15 and M16 which were sheared to higher axial strains (see Figure 4.11). It can also be seen from Figure 4.11(b) that with the increase of axial strain, more larger pores will be eliminated, which is indicated by a significant left movement of PSDs.

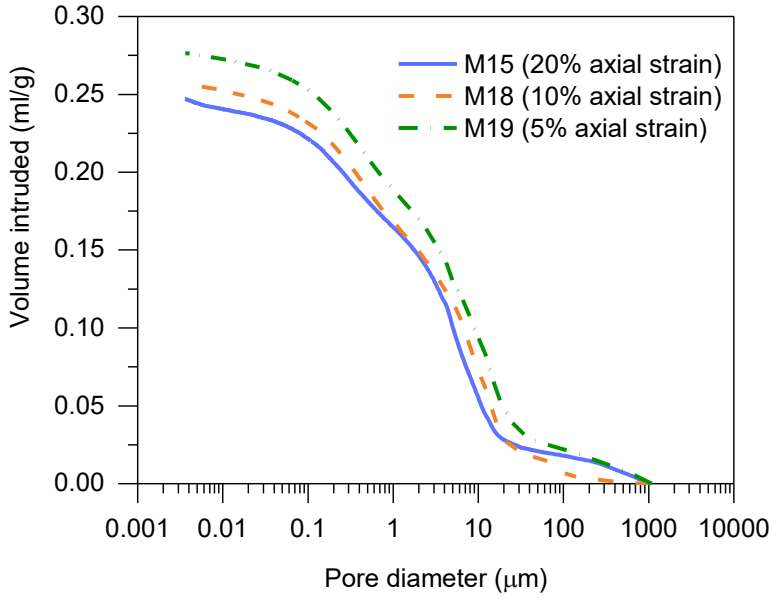

(a) Evolution of cumulative PSDs

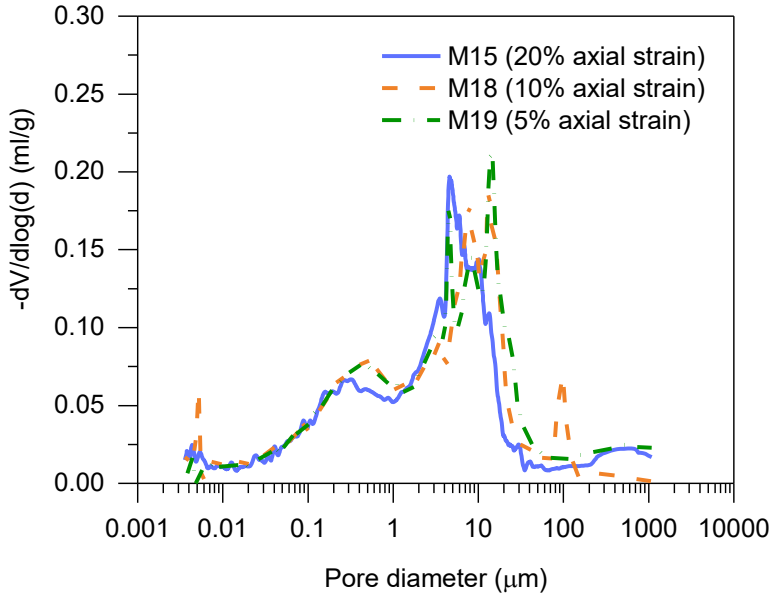

(b) Evolution of differential PSDs

Figure 4.11 Evolution of PSDs of Specimen M15, M18 and M19 with increasing axial strains during saturated shearing (100 kPa confining stress)

Specimen M2, M3 and M5 (initial dry density of ~1.62 Mg/m^3) were all sheared under a constant confining stress of 200 kPa and to 20%, 10% and 5% axial strains respectively. The displacement rate was 0.007 mm/min. As shown in Figure 4.12, due to a lower initial dry density of these samples, no strain softening and dilatancy can be witnessed during shearing. At 20% axial strain, the maximum deviatoric stress is ~ 600 kPa (see Figure 4.12(a)) and the maximum volumetric strain is ~ 5% (see Figure 4.12(b)). It should be noted that the void ratio

of M3 at 10% axial strain is higher than that at 5% (see Figure 4.12(c)). This is because M3 had a higher initial void ratio before shearing. Specimen M2, M3 and M5 were prepared with the same initial water content and dry density, thus there is little difference in the stress-strain behaviour among these sample considering they were also sheared under the same condition. This is beneficial to the further MIP tests on these specimens because if there is significant disparity among these samples, the pore size distribution obtained for each axial strain will be less representative.

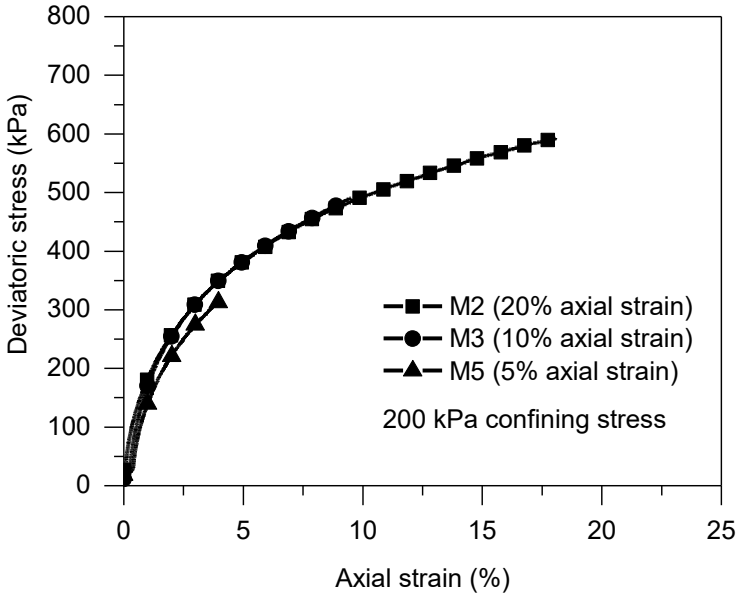

(a) Axial strain – Deviatoric stress

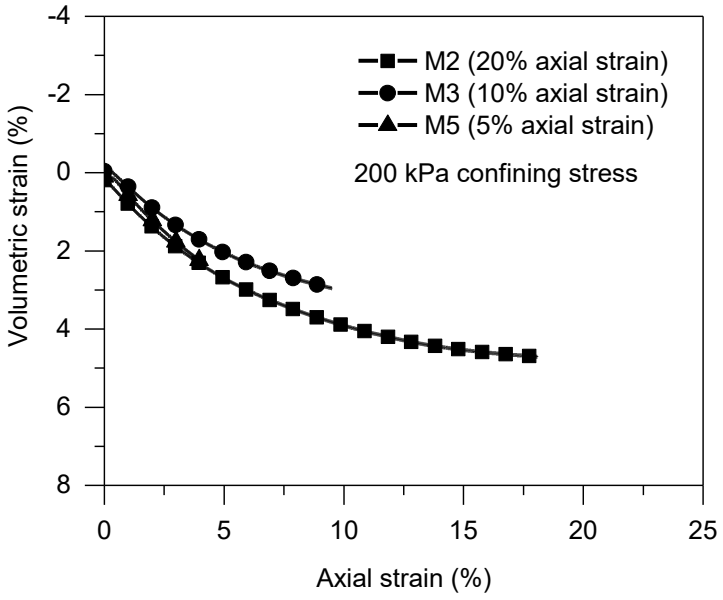

(b) Axial strain – Volumetric strain

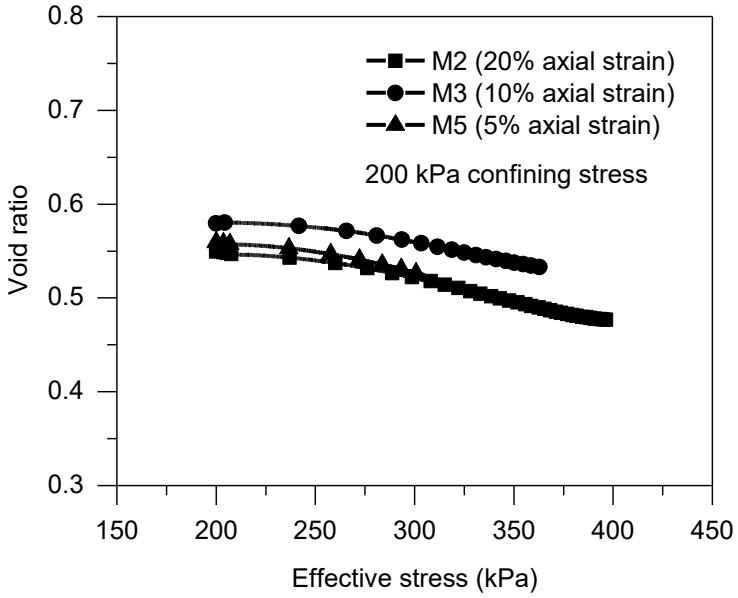

(c) Axial strain – Void ratio

Figure 4.12 Stress-strain behaviour of Sample M2, M3 and M5 sheared under the same confining stress of 200 kPa to different axial strains

Saturated specimens M2, M3 and M5 with an initial dry density of 1.62 Mg/m^3 were sheared under confining stress of 200 kPa but to 20%, 10% and 5% axial strains, respectively. Specimen M2, M3 and M5 were freeze dried before MIP tests. Figure 4.13 presents the evolution of pore size distribution in the path that samples were sheared under the same confining stress of 200 kPa but to different axial strains of 20%, 10% and 5%. According to the previous results, it is expected that the pore volume will decrease when the axial strain increases from 5% to 20% and the compression will mostly derive from the decrease of larger pores. However, as shown in Figure 4.13(a), at 10% axial strain there exists the largest volume intruded. This is because the Specimen M3 has the largest void ratio at the start of shearing. Despite that, the evolution of pore size distribution adheres to the expectation that larger pores are mainly compressed during shearing (see Figure 4.13(b)).

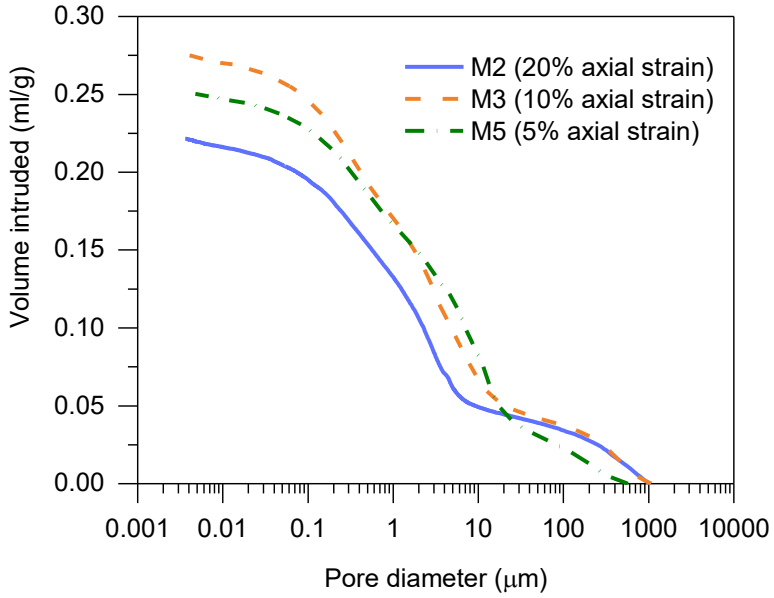

(a) Cumulative PSDs

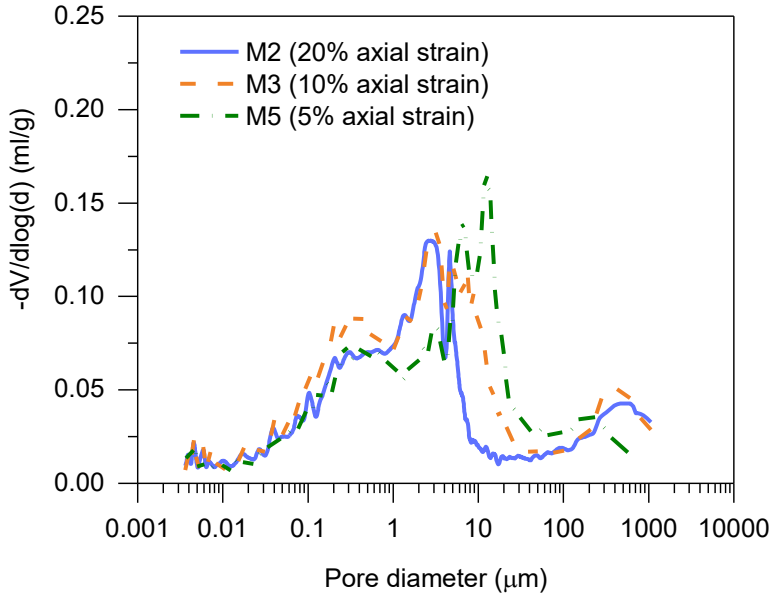

(b) Differential PSDs

Figure 4.13 Evolution of PSDs of Specimen M2, M3 and M5 with increasing axial strains during saturated shearing (200 kPa confining stress)

Under a constant confining stress of 400 kPa, Specimen M6, M13 and M14 (initial dry density of ~1.62 Mg/m^3) were sheared to 20%, 10% and 5% axial strains respectively. The displacement rate was also 0.007 mm/min. It can be seen from Figure 4.14 that the maximum deviatoric stress is ~1000 kPa while the maximum volumetric strain goes to ~6%. Despite small difference, the results of each specimen are still consistent to each other. Therefore, the results of each specimen are all representative of the shearing behaviour.

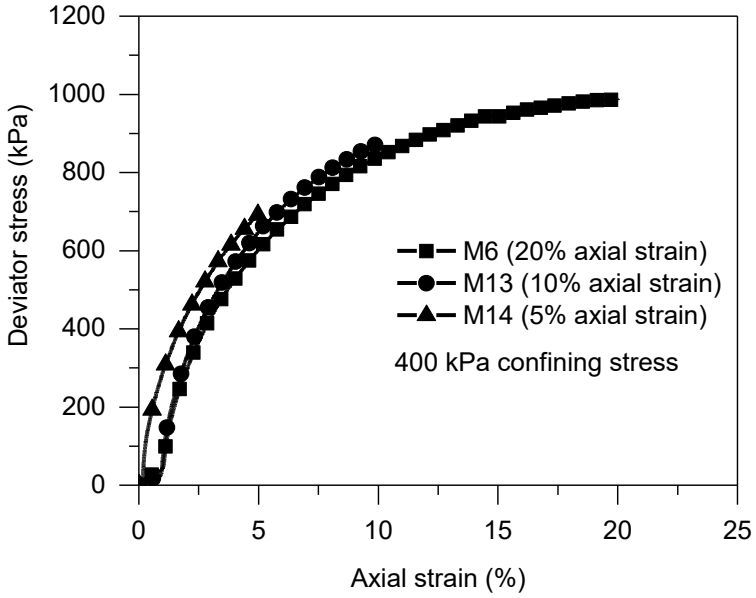

(a) Axial strain – Deviatoric stress

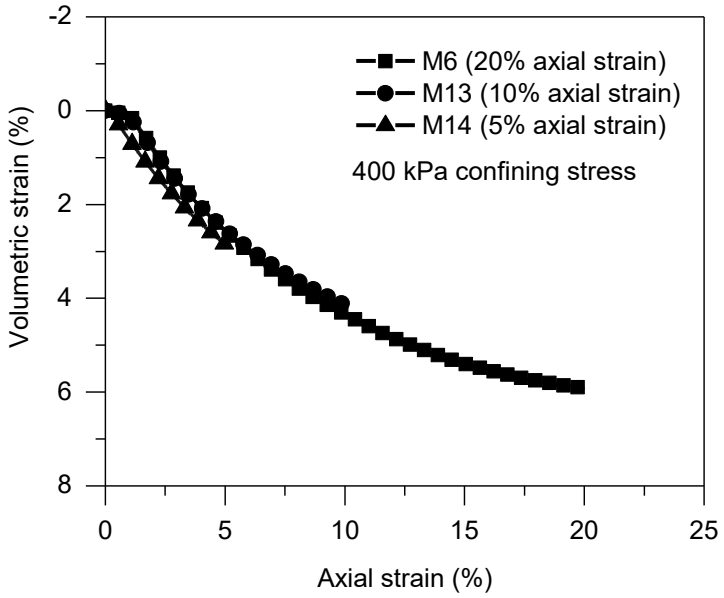

(b) Axial strain – Volumetric strain

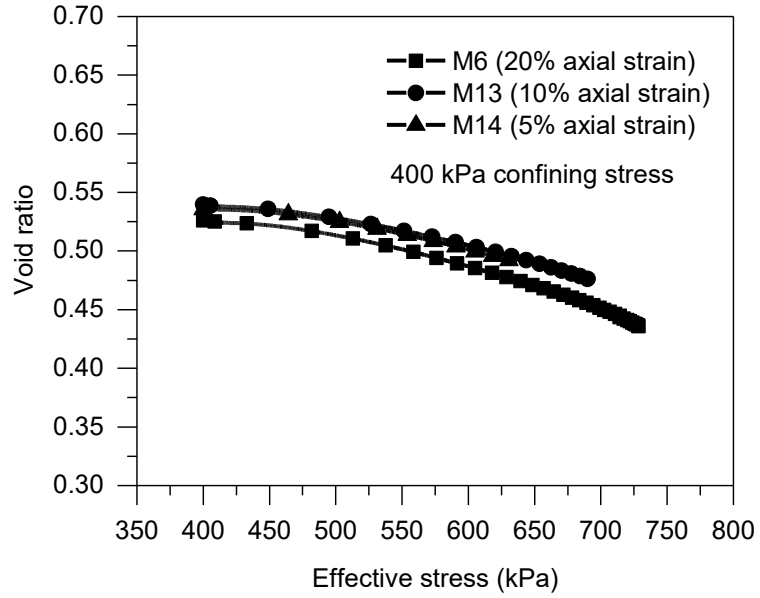

(c) Axial strain – Void ratio

Figure 4.14 Stress-strain behaviour of Sample M6, M13 and M14 sheared under the same confining stress of 400 kPa to different axial strains

Saturated sample M6, M13 and M14 at dry density of 1.62 g/cm^3 was sheared under confining stress of 400kPa to 20%, 10% and 5% axial strain. M6, M13 and M14 were freeze dried before MIP tests. As shown in Figure 4.15, A similar conclusion can also be drawn that the total intruded volume decreases with the increasing axial strain and the compression of specimens mostly come from the downward and leftward movement of large pores.

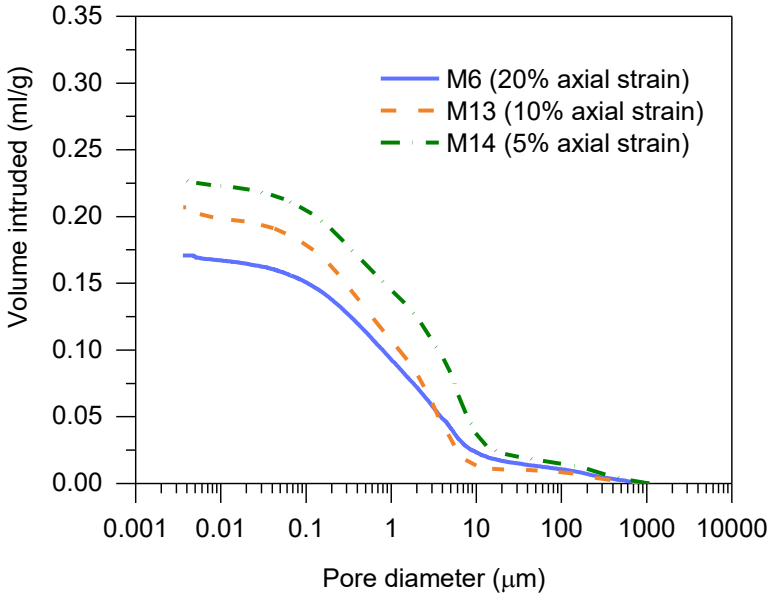

(a) Cumulative PSDs

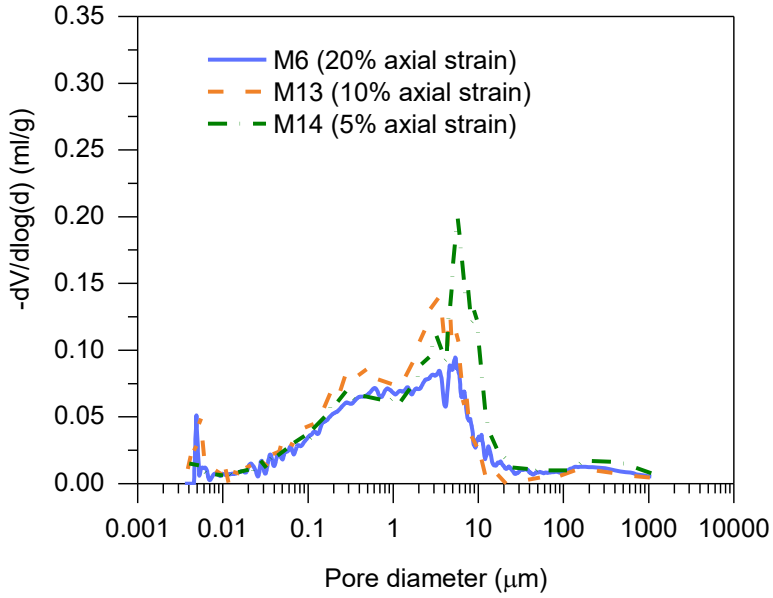

(b) Differential PSDs

Figure 4.15 Evolution of PSDs of Specimen M6, M13 and M14 with increasing axial strains during saturated shearing (400 kPa confining stress)

4.3.3.3 Evolution of microstructure in unsaturated triaxial tests

Figure 4.16 presents the change of deviatoric stress, volumetric strain, void ratio and degree of saturation with axial strain during unsaturated shearing under a constant suction of 25 kPa. As shown in Figure 4.16(a), (b) and (c), there is no significant strain softening and dilatancy when Specimen M21 was sheared to 15% axial strain. The degree of saturation increased from ~75% to ~80% during shearing (see Figure 4.16(d)). The behaviour of Specimen M20 is very similar to that of M21 when it was sheared to 10% axial strain. This indicates that both specimens are representative of the hydro-mechanical behaviour under 25 kPa suction and the specimens can be used for MIP to represent the microstructure at each axial strain.

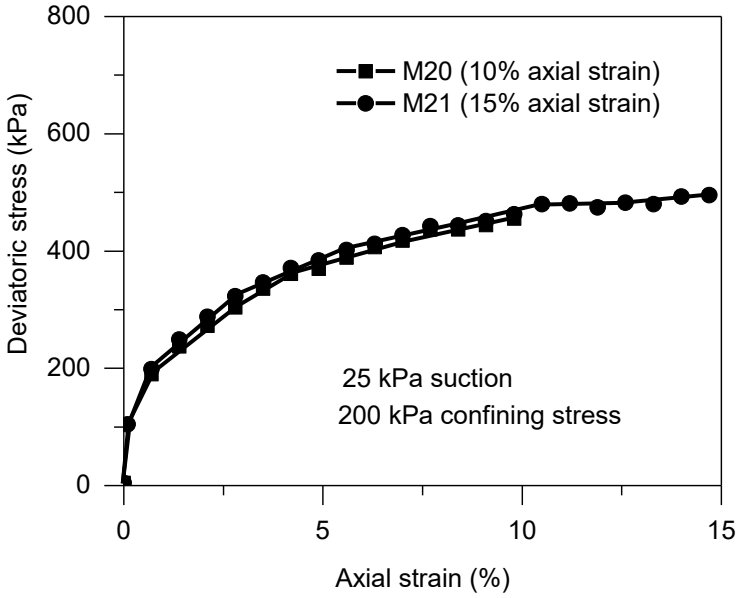

(a) Axial strain – Deviatoric stress

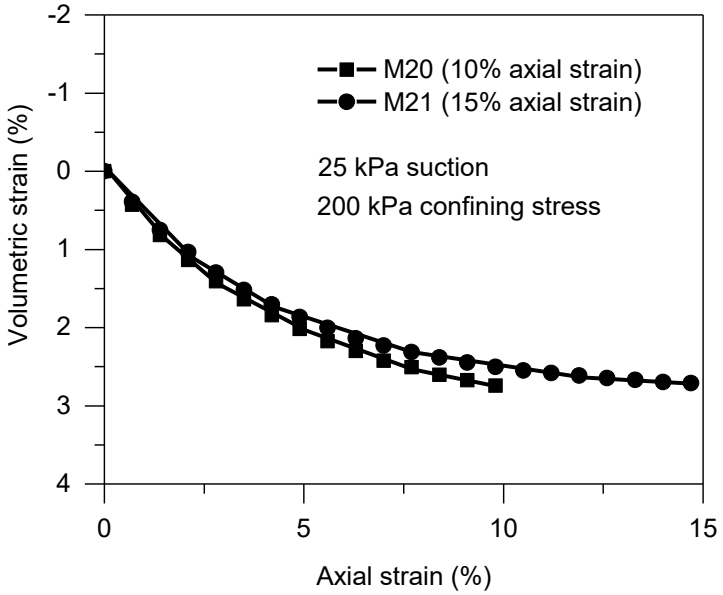

(b) Axial strain – Volumetric strain

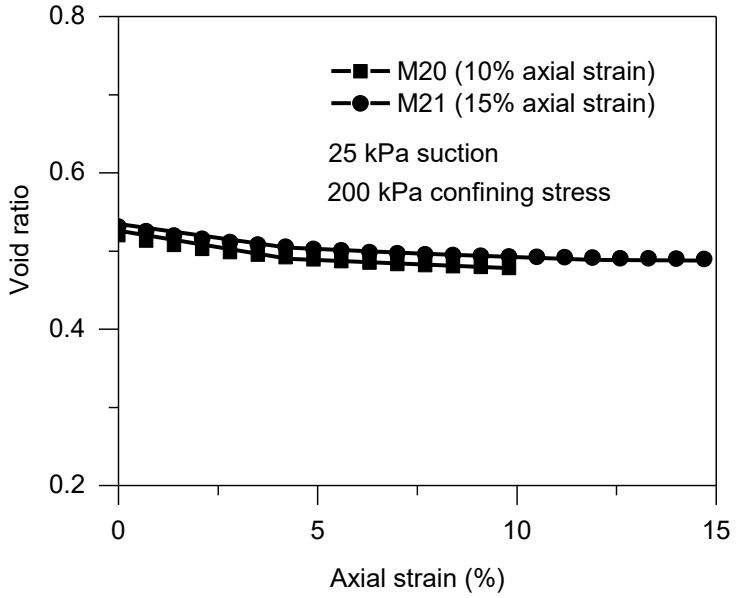

(c) Axial strain – Void ratio

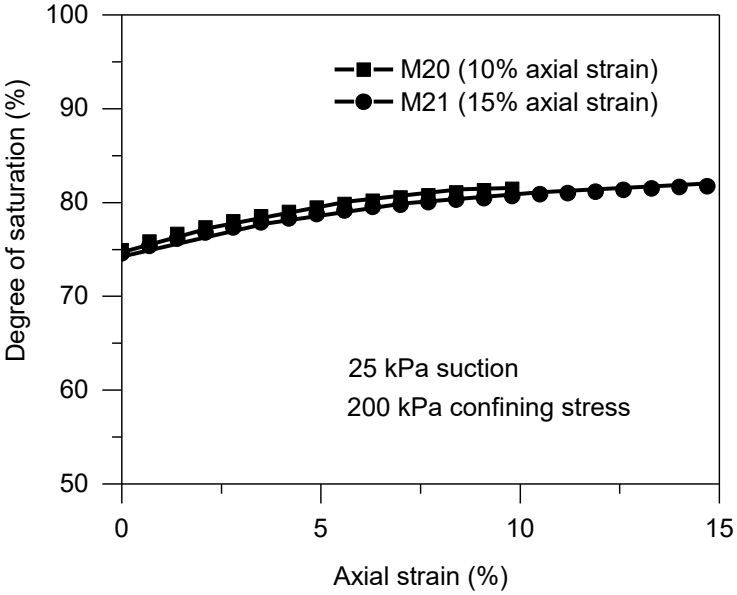

(d) Axial strain – Degree of saturation

Figure 4.16 Hydro-mechanical behaviour of Specimen M20 and M21 sheared under the same net confining stress of 200 kPa and constant suction of 25 kPa

Figure 4.17 presents the evolution of PSDs during shearing under a constant confining stress of 200 kPa and a constant suction of 25 kPa. Specimen M20 was sheared to 10% axial strain while Specimen M21 was sheared to 15% axial strain. Due to the factors stated in Section 4.3.5, even though M20 has a lower void ratio than M21 at the termination of shearing, M20 still has a higher total intruded volume than M21, as shown in Figure 4.17(a). However, it still

can be seen that with the increase of axial strain, more larger pores will be compressed. Therefore, a significant left movement of inter-aggregate PSD (for macropores) can be found in Figure 4.17(b) while there is a slight downward movement of intra-aggregate PSD (for micropores).

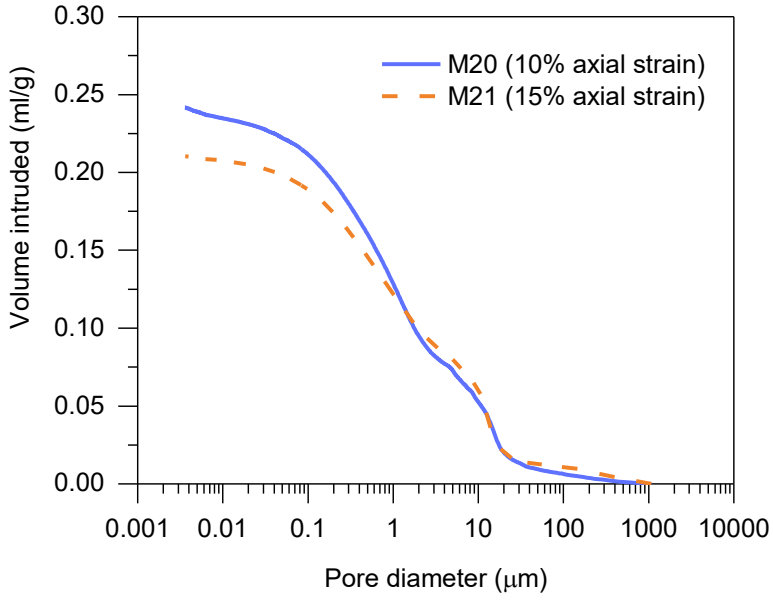

(a) Cumulative PSDs

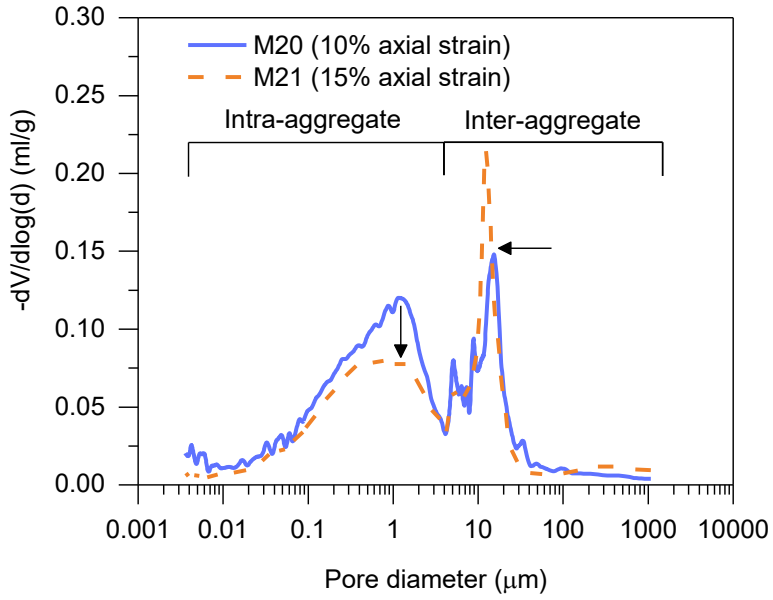

(b) Differential PSDs

Figure 4.17 Evolution of PSDs of Specimen M20 and M21 during unsaturated shearing under under the same net confining stress of 200 kPa and constant suction of 25 kPa

Figure 4.18 presents the change of deviatoric stress, volumetric strain, void ratio and degree of saturation with axial strain during unsaturated shearing under a constant suction of 100 kPa. Specimen M4 sheared to 18% axial strain shows a little strain softening (see Figure 4.18(a)) and dilatancy (see Figure 4.18(b)) when approaching 18% axial strain. The maximum deviatoric stress during shearing is ~ 550 kPa. The results of Specimen M7 (10% axial strain) and M12 (5% axial strain) have small difference in value with that of Specimen M4 but generally they are identical to each other in changing tendency. Therefore, the results of each specimen are regarded representative of the behaviour at each axial strain.

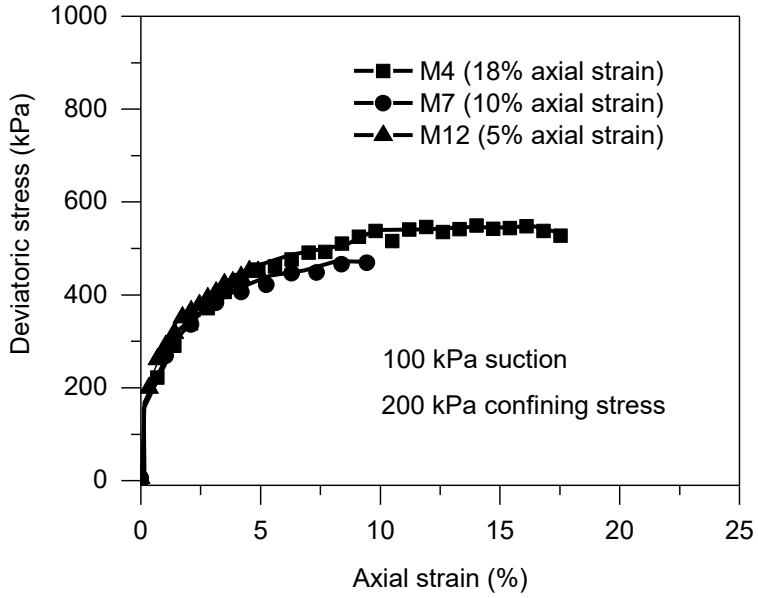

(a) Axial strain – Deviatoric stress

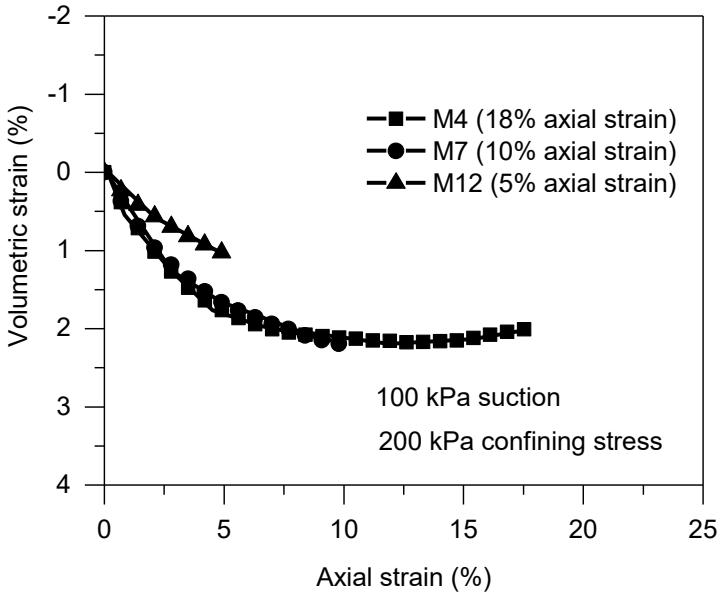

(b) Axial strain – Volumetric strain

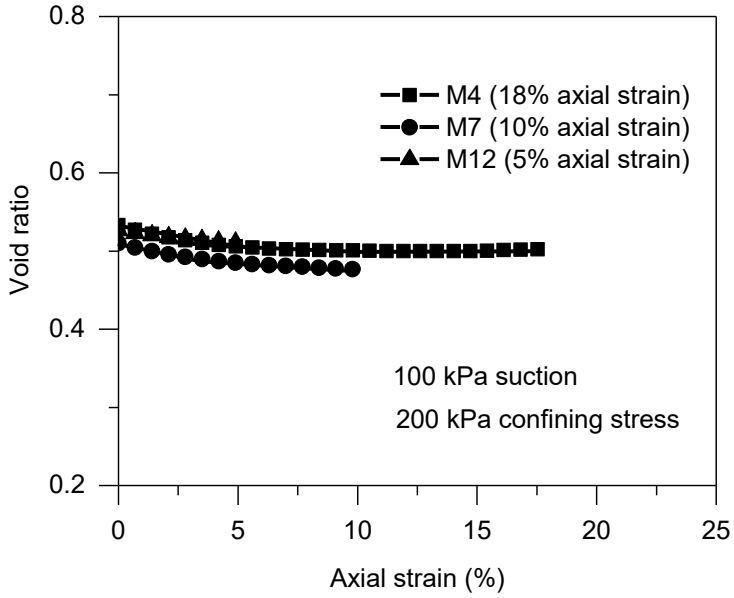

(c) Axial strain – Void ratio

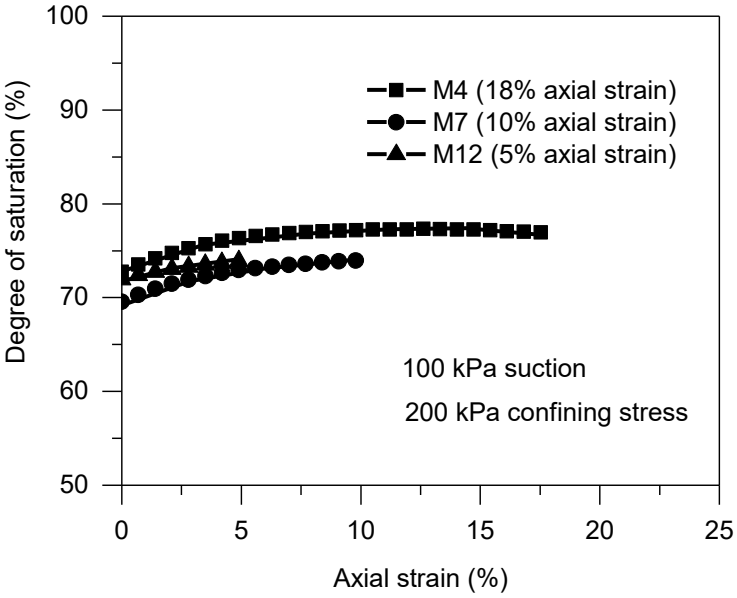

(d) Axial strain – Degree of saturation

Figure 4.18 Hydro-mechanical behaviour of Specimen M4, M7 and M12 sheared under the same net confining stress of 200 kPa and constant suction of 100 kPa

Figure 4.19 presents the evolution of pore size distribution during unsaturated shearing under a suction of 100 kPa and a net confining stress of 200 kPa. Since the PSDs of unsaturated specimens are bimodal, the evolution of PSDs includes the change of intra-aggregate PSDs (for micropores) and the change of inter-aggregate PSDs (for macropores). Similar to saturated specimens, it can be noticed that the inter-aggregate PSDs show a downward movement which indicates the compression of macropores when the sample was sheared from 5% to 10%.

However, for intra-aggregate PSDs, a slight increase of micropores can be witnessed during shearing.

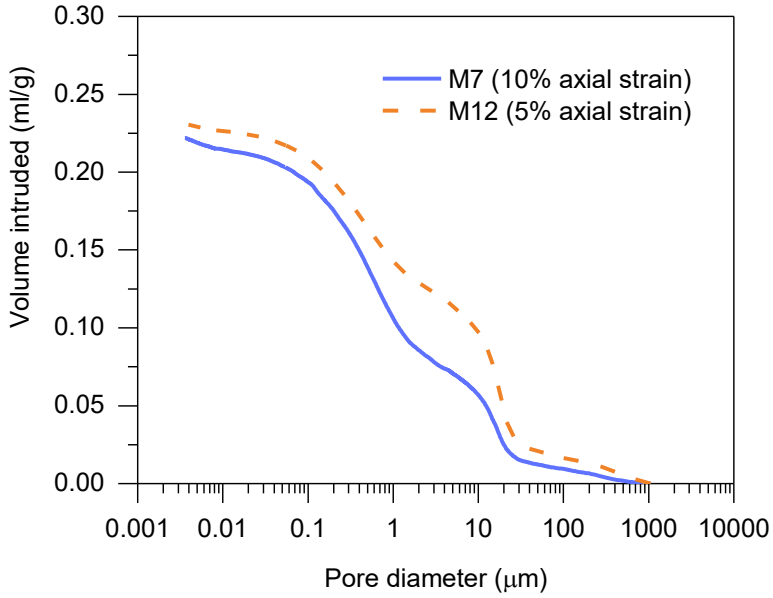

(a) Cumulative PSDs

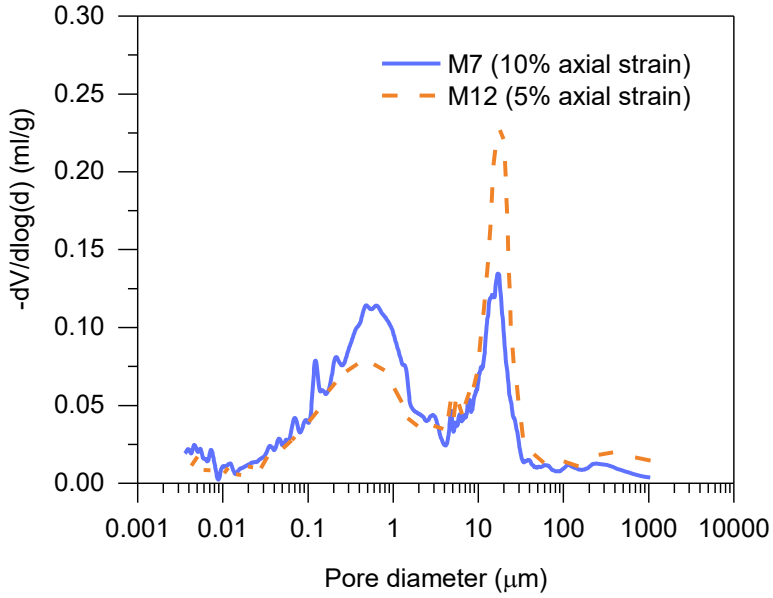

(b) Differential PSDs

Figure 4.19 Evolution of PSDs of Specimen M7 and M12 during unsaturated shearing under the same net confining stress of 200 kPa and constant suction of 100 kPa

4.3.3.4 Soil-water characteristic curves of Dundee silt at different dry densities

Soil-water characteristic curves (SWCCs) of Dundee silt were obtained through various methods including WP4C and Unsaturated GDS. SWCCs obtained by WP4C were prepared at two constant dry densities (1.62 and 1.54 Mg/m^3). With Unsaturated GDS, the SWCC was obtained from the water volume information at the termination of suction equilibrium stage. Two different suctions (25 and 100 kPa) were conducted on specimens under a constant net radical stress of 25 kPa. SWCCs for Dundee silt are presented in Figure 4.20. It can be seen that SWCCs obtained by various methods are different to each other. This can be attributed to the difference in dry densities and microstructure.

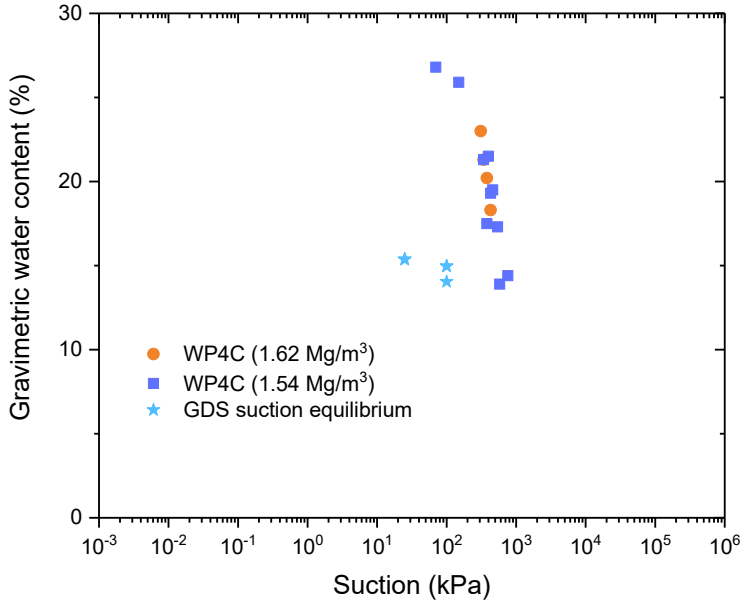

(a) Suction – gravimetric water content

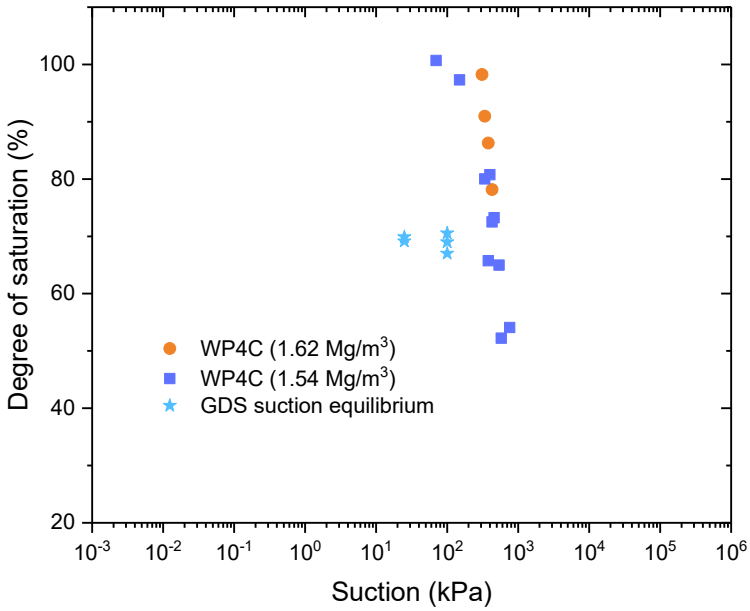

(b) Suction – degree of saturation

Figure 4.20 Soil-water characteristic curves of Dundee silt

4.3.4 Effects of initial dry density, confining stress and suction on soil microstructure

The effects of initial dry density, confining stress and suction on soil microstructure are presented in the following sections.

4.3.4.1 Initial dry density

The effects of initial dry density on PSD evolution were studied based on two dry densities of 1.62 and 1.76 Mg/m^3. Samples of different initial dry densities were sheared under the same conditions before their pore size distributions were obtained by MIP tests. As shown in Figure 4.21(a), saturated samples 21C and M15 were both sheared under a constant confining stress of 100 kPa to 20% axial strain, it is obvious that Sample M15, which has a lower initial dry density and higher porosity, has much more pores within the diameter range from ~3 µm to ~10 µm than Sample 21C while the pore size distributions of these samples are almost identical outside of the previous diameter range. However, with the increase of the confining stress, the difference in pore size distribution within the previous diameter range is reduced as can be seen in Figure 4.21(b) and (c). It can also be noticed that samples 65C and 46C which have a higher initial dry density and lower porosity have more larger pores (> 10 µm) than their counterparts with a lower initial dry density. This phenomenon can be attributed to some factors which are discussed in Section 4.3.5.

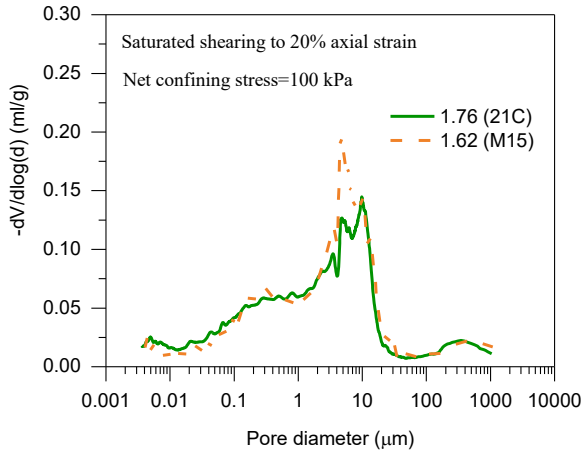

(a) Sample 21C and M15

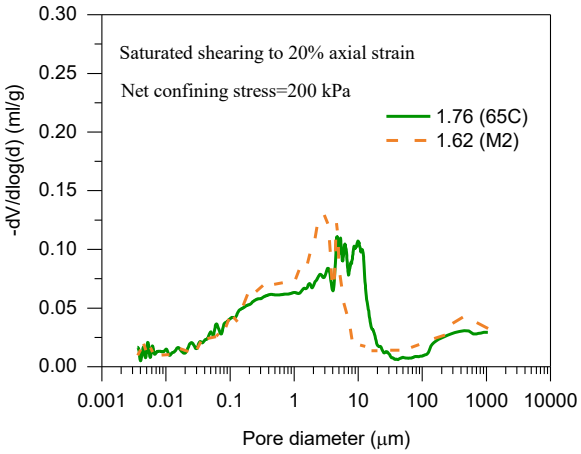

(b) Sample 65C and M2

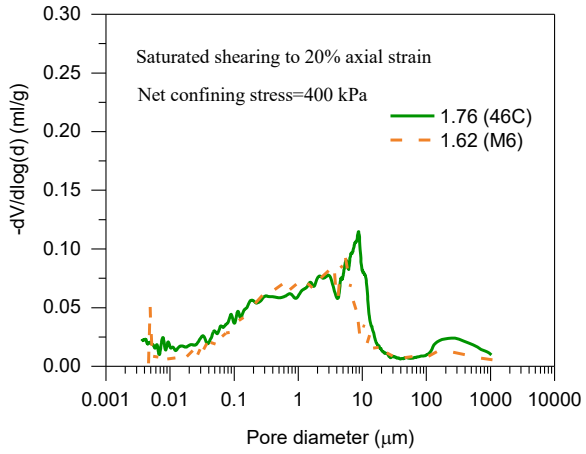

(c) Sample 46C and M6

Figure 4.21 Effects of initial dry density on PSD evolution

4.3.4.2 Confining stress

The effects of confining stress on PSD evolution are similar to that of initial dry density. With the increase of the confining stress (100, 200 and 400 kPa), a significant downward and leftward movement can be witnessed for samples sheared to 20% axial strain, which indicates a reduction in relatively large pores (see Figure 4.22). This is because a sample usually has a much lower porosity when sheared under a higher confining stress. However, very large pores and very small pores are not significantly reduced with increasing confining stresses. As shown in Figure 4.22(a), this is little change in pores smaller than ~ 3 μm and pores larger than ~20 μm.

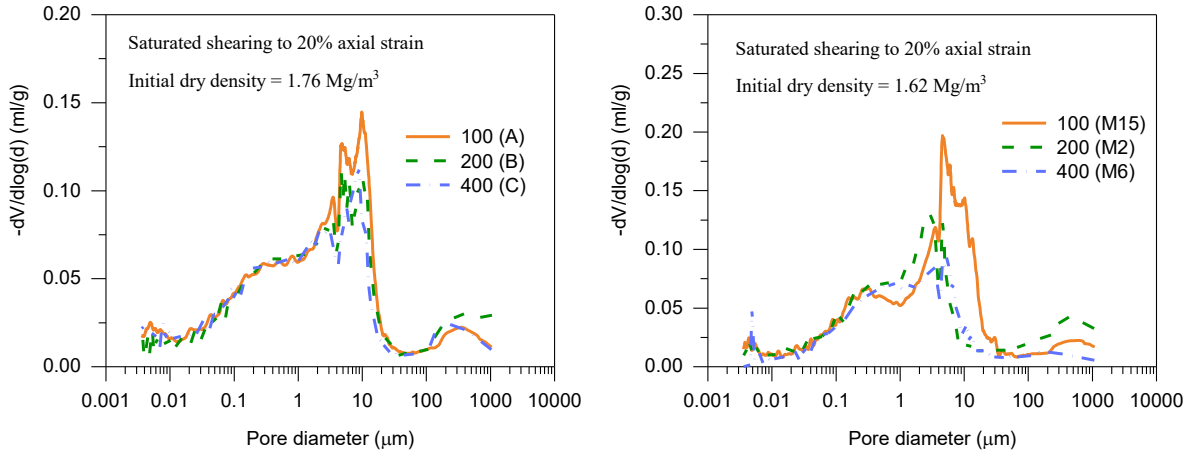

(a) Sample A, B and C (b) Sample M15, M2 and M6

Figure 4.22 Effects of confining stress on PSD evolution

4.3.4.3 Suction

Suction is another important factor that affects the PSD evolution, especially in terms of PSD shapes. Sample M3, M7 and M20 all had an initial dry density of 1.62 Mg/m^3 and were sheared under a net confining stress of 200 kPa to 10% axial strain but at different suctions. As shown in Figure 4.23, the PSD of the saturated sample M3 (suction is 0 kPa) is almost unimodal (if its PSD is ignored in the range over 100 μm and the reason is discussed in section 4.3.5). With the increase of suction, the PSD shows significant bimodality within the pore range from ~0.3 μm to 30 μm while the other parts of the PSD are still similar to that of the saturated sample.

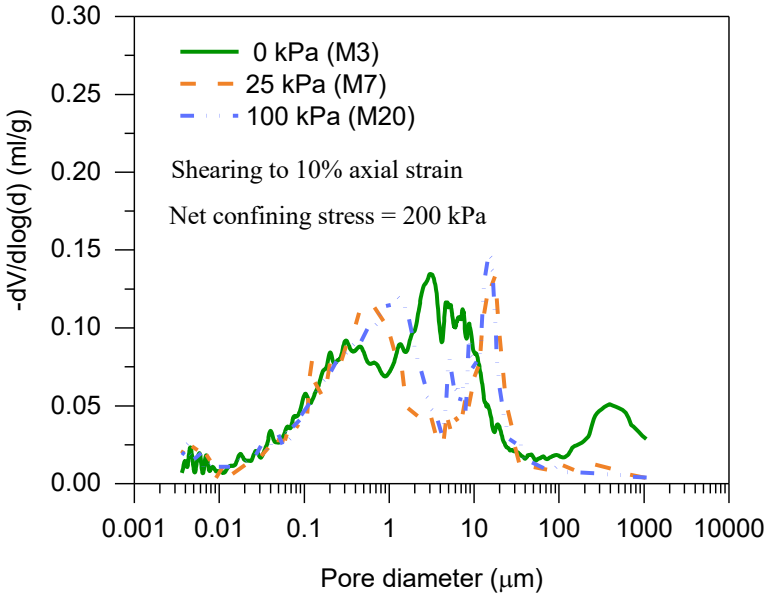

Figure 4.23 Effects of suction on PSD evolution

4.3.5 Effects of heterogeneity, drying methods and sample size on soil microstructure

The effects of heterogeneity, drying methods and sample size on soil microstructure are presented in the following sections. However, due to the limited numbers of parallelled samples, the statistical variability cannot be further provided.

4.3.5.1 Heterogeneity

Since the specimens prepared for triaxial tests were much larger than the required size of the sample that can fit in the cell for MIP tests, it is inevitable to extract a much smaller sample from the original triaxial specimen. Therefore, the heterogeneity in triaxial specimens must be considered to study how it will affect the pore size distribution which is critical in studying the microstructural-hydro-mechanical coupled behaviour. In this study, the triaxial specimens were divided into three layers. The top and bottom layers were named as edger layers and the middle layers were named as centre layers, as shown in Figure 4.24. Smaller samples from these layers were taken to MIP tests to study the difference in PSD for different parts of the specimen.

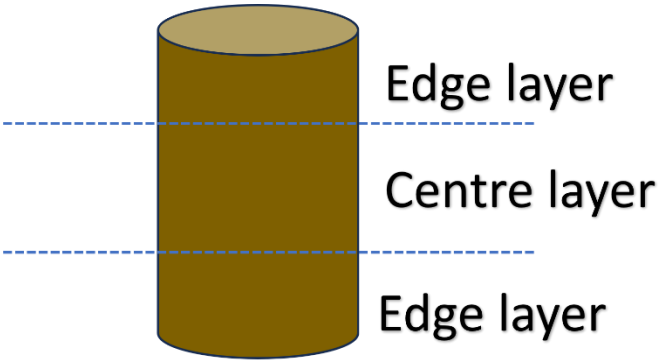

Figure 4.24 Schematic diagram of layers in a triaxial specimen

4.3.5.1.1 In different layers

For Specimen A, lumps from both the edge and the centre were collected separately to different containers. One container was labelled as 11E (E stands for edge layer) and the other one was labelled as 21C (C stands for centre layer). The MIP results of both containers are shown in Figure 4.25. The similar procedure was also conducted for both Specimen B (labelled as 55E and 65C) and Specimen C (labelled as 36E and 46C), results of which are presented in Figure 4.26 and Figure 4.27. From the MIP results of all samples, it can be witnessed that the PSD varies with the position where it is obtained. For Specimen A, the PSD of the centre has a much higher intruded volume than that of the edge (see Figure 4.25(a)). The intruded void ratio of the centre is 0.598 and that of the edge is much smaller of 0.409. In comparison, the void ratio obtained from triaxial test results is 0.505. This is because the edge was contacting or closer to the loading piston and might be more affected by the loading, which makes it denser and less porous than the centre which is more distant to the loading piston. Since the void ratio obtained by GDS only represents the average void ratio in a triaxial sample, when the void ratio from the centres is larger than the average one, it is reasonable to find the void ratio from the edge is less in value. However, for Specimen B and C, void ratios from the edge are slightly larger than the void ratios from GDS (see Figure 4.26 and Figure 4.27). Therefore, the influences of other factors should be considered.

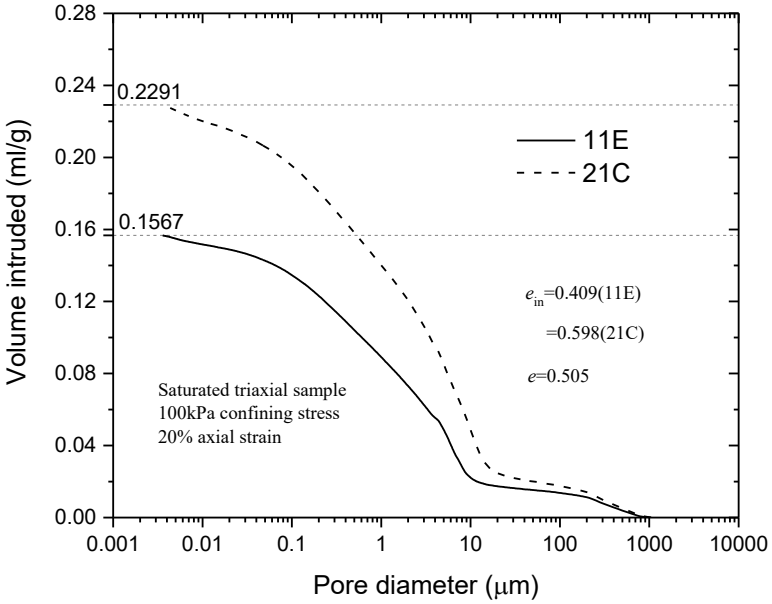

(a) Cumulative PSDs

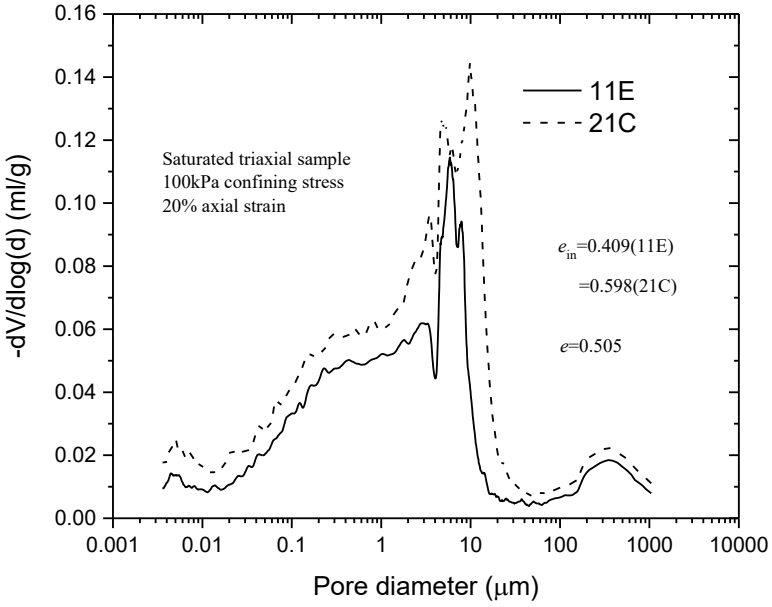

(b) Differential PSDs

Figure 4.25 PSDs for Specimen A (11E and 21C)

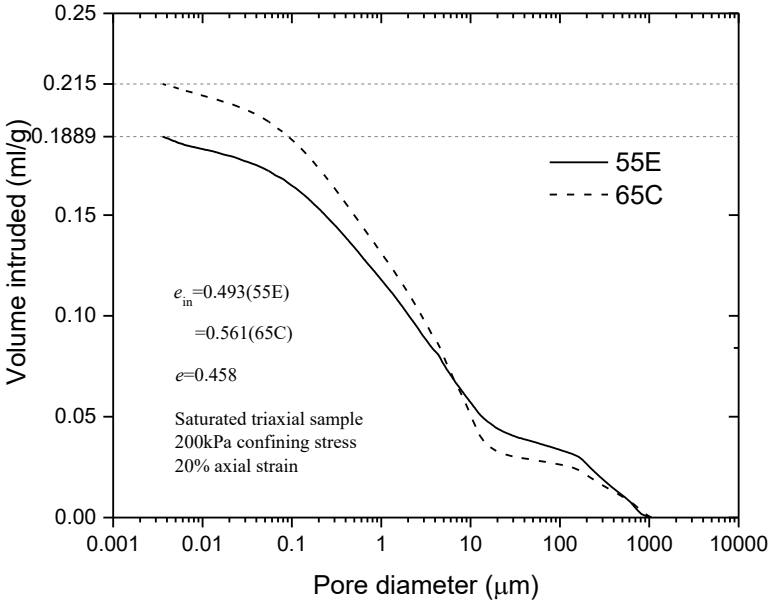

(a) Cumulative PSDs

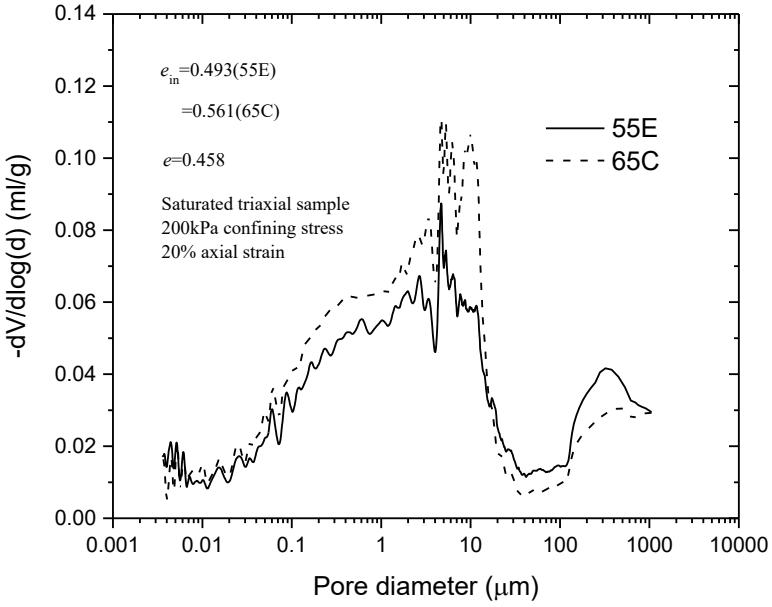

(b) Differential PSDs

Figure 4.26 PSDs for Specimen B (55E and 65C)

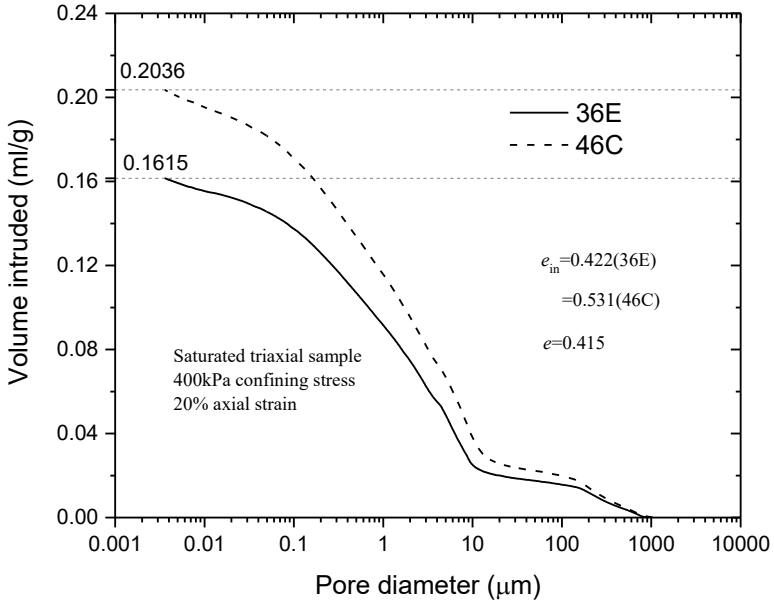

(a) Cumulative PSDs

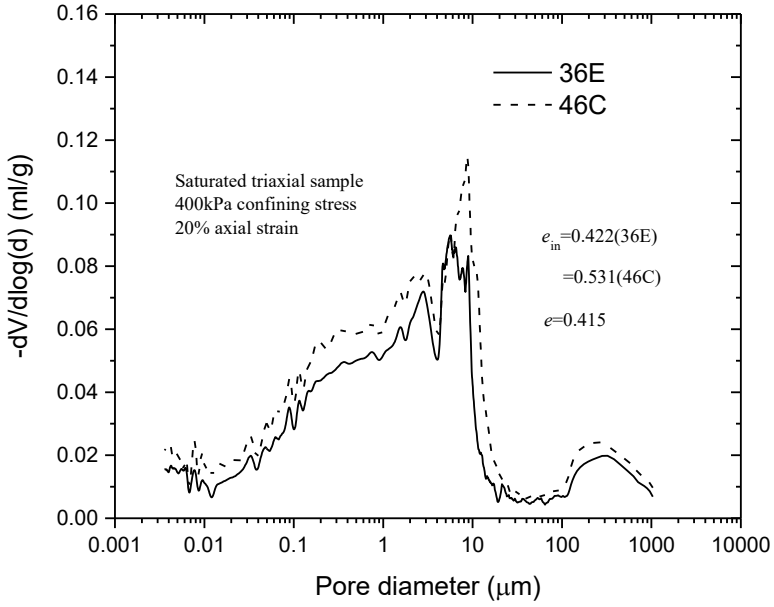

(b) Differential PSDs

Figure 4.27 PSDs for Specimen C (36E and 46C)

4.3.5.1.2 In same layers

To study the heterogeneity within the same layer, three lumps from the same centre layer of a specific sample were taken to MIP separately. Figure 4.28 presents the PSD results of three lumps of Specimen M6 (M6-a, M6-b and M6-c) which was sheared under a saturated condition to 20% axial strain. Even though these lumps come from the same layer, the difference in total

intruded volumes can still be witnessed. As shown in Figure 4.28(a), the largest intruded void ratio from M6-a can be 30% higher than that from M6-c. From the comparison among differential PSDs (see Figure 4.28(b)), the PSD of M6-c has much fewer pores within the pore diameter range from 0.1 μm to 3 μm. However, despite the difference in intruded volumes and intruded void ratios, the shapes of these three PSDs are quite similar to each other and the dominant pore sizes where the peak values lie are almost identical to each other. Therefore, all three PSDs are all valid to some extent due to the good reliability of PSD shapes and positions. Especially in modelling, PSDs used are all scaled by void ratio and the disparity can be significantly narrowed (see Figure 4.28(c)) which will not severely affect the modelling result. Therefore, either of these three PSDs can be used to represent the PSD at 20% axial strain and the ultimate selection depends on which can provide a more reasonable and expected result when the PSDs at 10% and 5% are considered. In this case, we expect a minimum intruded void ratio at 20% axial strain, a medium intruded void ratio at 10% axial strain and the maximum intruded void ratio at 5% axial strain. Therefore, the PSD of M6-c was selected in modelling. A similar finding can also be obtained from Specimen M12 which was sheared under an unsaturated condition to 5% axial strain. As shown in Figure 4.29, all three PSDs from the same layer have similar shapes and peak positions but are only different in values at specific pore diameters. The difference is still small when PSDs are scaled by void ratio (see Figure 4.29(c)). In this case, M12-c was adopted in modelling to guarantee a larger intruded void ratio at 5% axial strain than that at 5% axial strain.

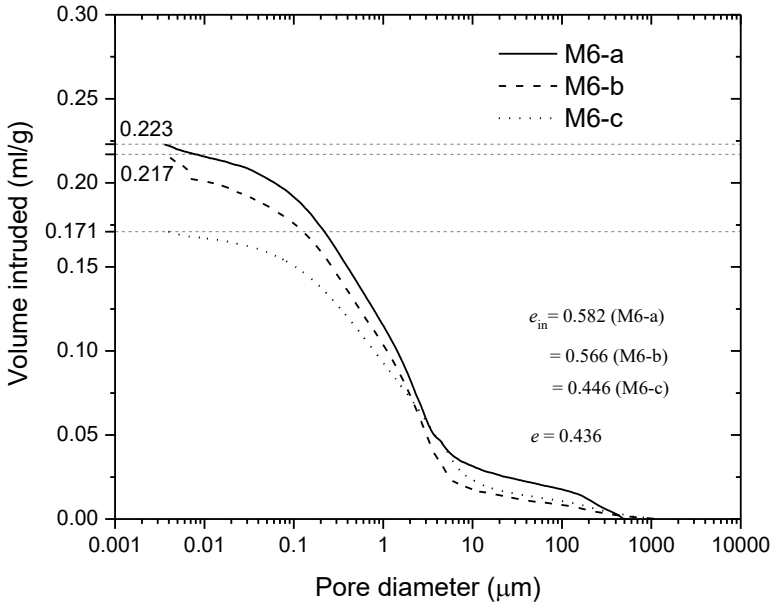

(a) Cumulative PSDs

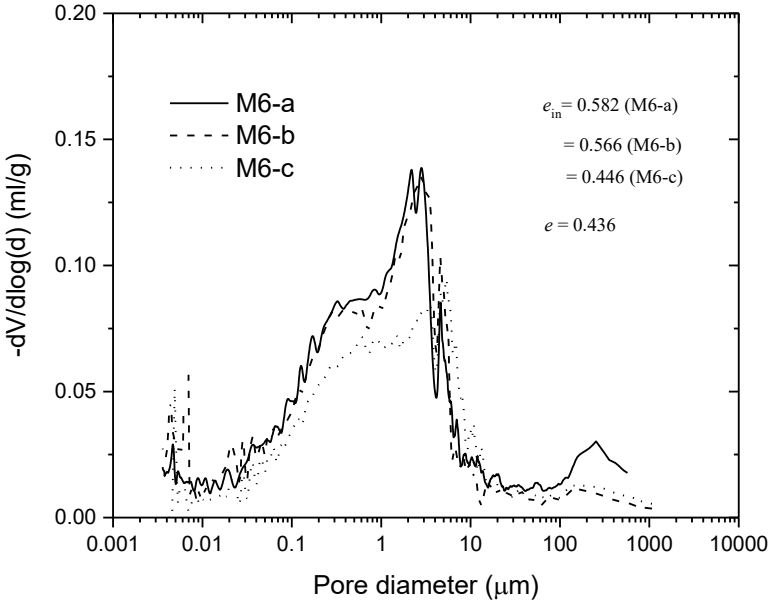

(b) Differential PSDs

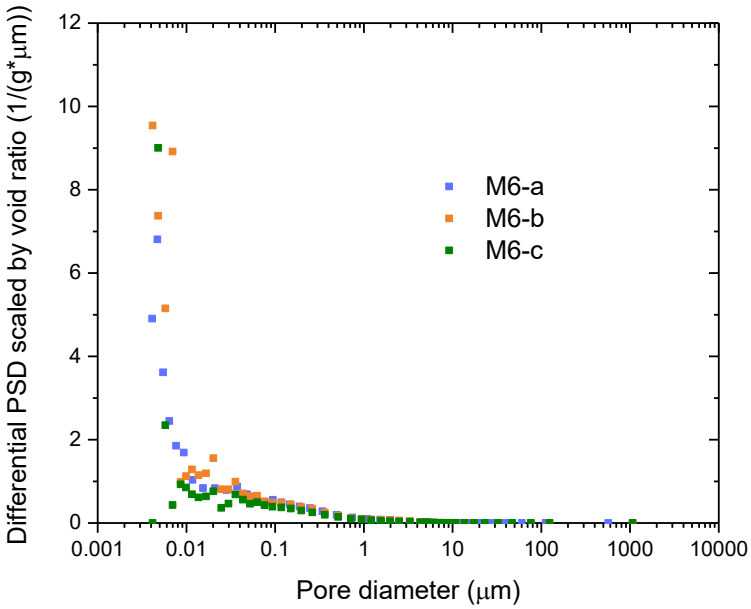

(c) Differential PSDs scaled by void ratio

Figure 4.28 PSDs for Specimen M6

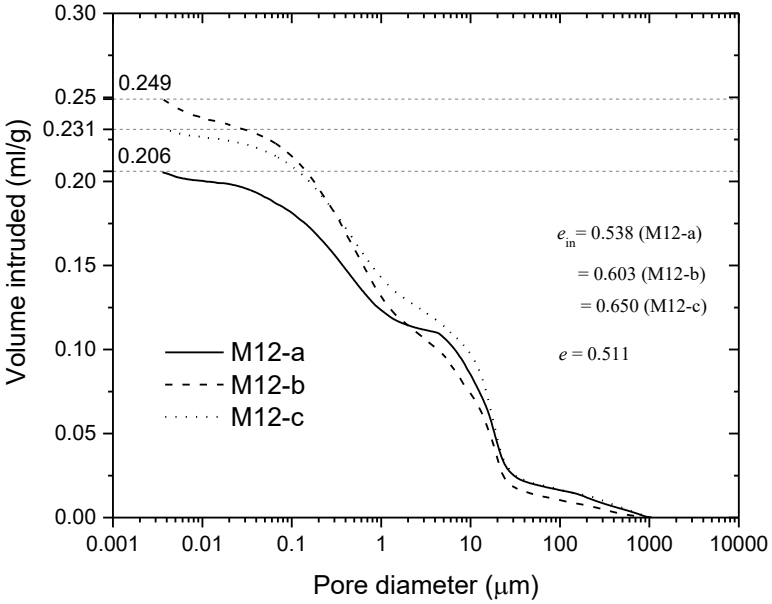

(a) Cumulative PSDs

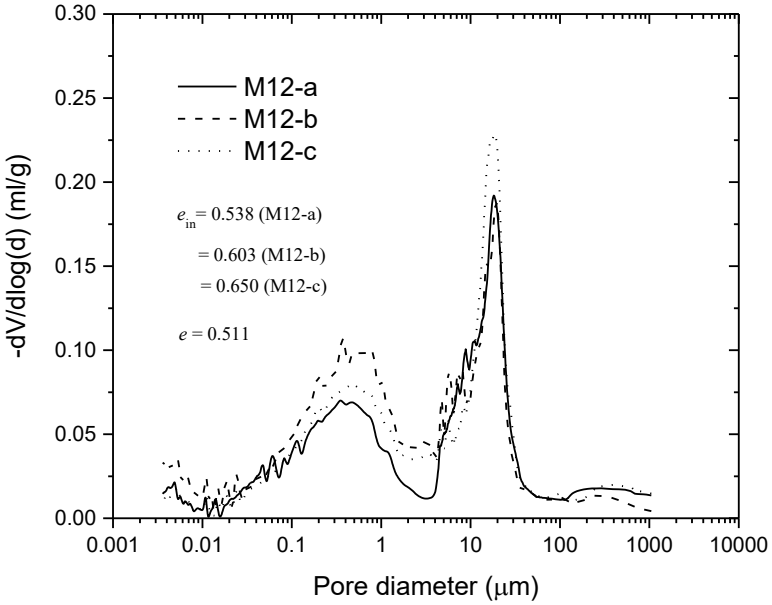

(b) Differential PSDs

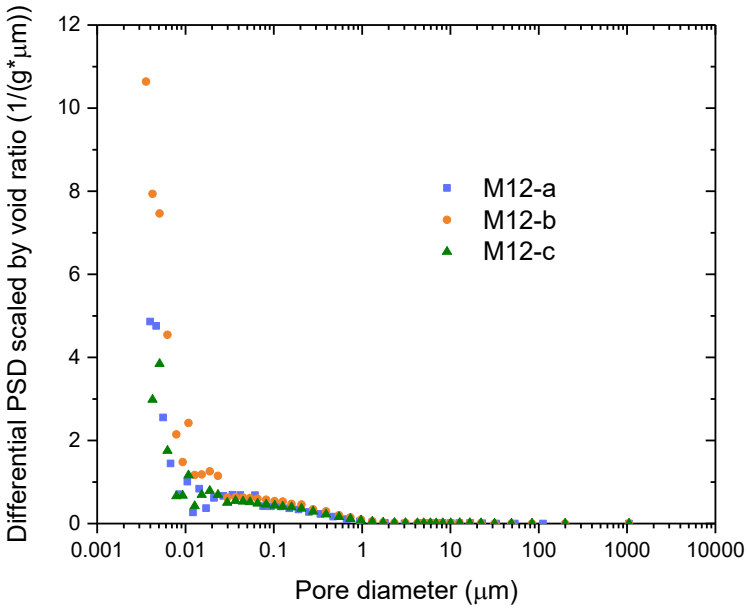

(c) Differential PSDs scaled by void ratio

Figure 4.29 PSDs for Specimen M12

4.3.5.2 Drying methods and sample size

Drying methods and sample sizes are another two important factors that will affect the pore size distribution obtained by MIP. Drying methods include oven drying and freeze drying. In this study, oven dried samples were dried at 105 ℃ for 24 hours. It has been widely confirmed that the higher temperature can lead to more significant compression of soil microstructure (Lawrence et al. 1979; Delage et al. 1996). Freezing drying is another common and well-accepted method to dry soil samples used in microscopy and mercury intrusion tests (Ahmed et al. 1974; Delage et al. 1996; Penumadu and Dean 2000; Liu et al. 2016; Oualmakran et al. 2016). There are two steps to conduct freeze-drying of samples including rapid freezing of soil moisture to pass into amorphous ice in liquid nitrogen (boiling temperature -196 centigrade) and sublimation of ice at a temperature of -20 centigrade or lower and subjected to a vacuum pressure (Delage et al. 1996; Penumadu and Dean 2000) for 24 and 36 h (Delage et al. 2006). To prevent recrystallization which may cause volume increase of water, the time when samples are kept in liquid nitrogen should not be longer than 5min (Delage et al. 1996; Galle 2001). In this step, the rapid freezing has the largest possibility of keeping the microstructure undisturbed and preventing samples from deformation (Oualmakran et al. 2016). Due to the limited size of the penetrometer used for containing samples during MIP, triaxial samples must be cut into smaller sizes to fit in the penetrometer. Since open voids might occur on the surface of the cutting edge and the pore size of these voids can be very large, the size of the cut samples will also play an important role in the pore size distribution and the total volume intruded. For example, Figure 4.30 presents the differential PSDs of several saturated specimens. It is expected that saturated soils should have a unimodal shape with only one

significant peak. However, these saturated specimens all have another peaks within 100 μm to 1000 μm which may be related to the open voids generated after cutting.

To study the impact of drying methods and sample sizes, the centre layers of Specimen M9, M10 and M11 were separated into three parts and taken to MIP (15% initial water content and 1.62 Mg/m^3 initial dry density). One part was freeze-dried and cut into relatively large lumps (about 10mm in longest length) to fill the penetrometer for MIP. The second part was oven-dried and was also prepared as similarly large lumps. The other part was also oven-dried but was prepared as a small lump with the longest length of about 4mm. When both prepared as large lumps, the freeze-drying method has a better performance in maintaining the original microstructure, especially small pores, while a significant compression in pore volume can be seen with oven-drying (see Figure 4.31 and Figure 4.32). For the comparison of oven-dried samples between large lumps and small lumps, even though the intruded void ratio of small lumps is not always larger than that of large lumps (considering the induced void ratio can be affected by other factors), it is still obvious that the PSD of small lumps usually has a much more significant increase in larger pores over 80μm in diameter, as shown in Figure 4.31(b), Figure 4.32(b) and Figure 4.33(b). This is the evidence to the assumption that cutting can generate large and open voids on the surface of specimens. For small lumps, due to their larger specific surface area, a higher proportion of large voids will be generated and monitored by MIP. This conclusion also supports the reason why the intruded void ratio is larger than the void ratio obtained by GDS, because cutting sample is inevitable in MIP and large pores generated during sample preparation cannot be avoided.

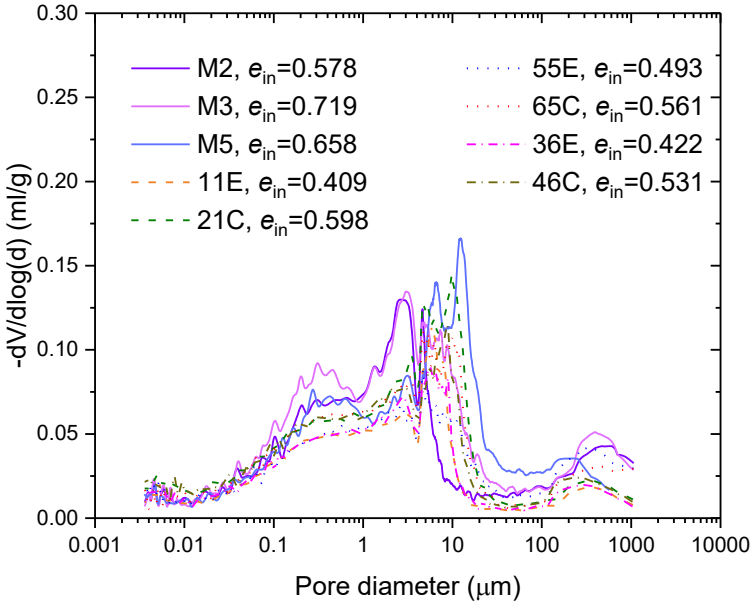

Figure 4.30 Differential PSDs of several saturated specimens

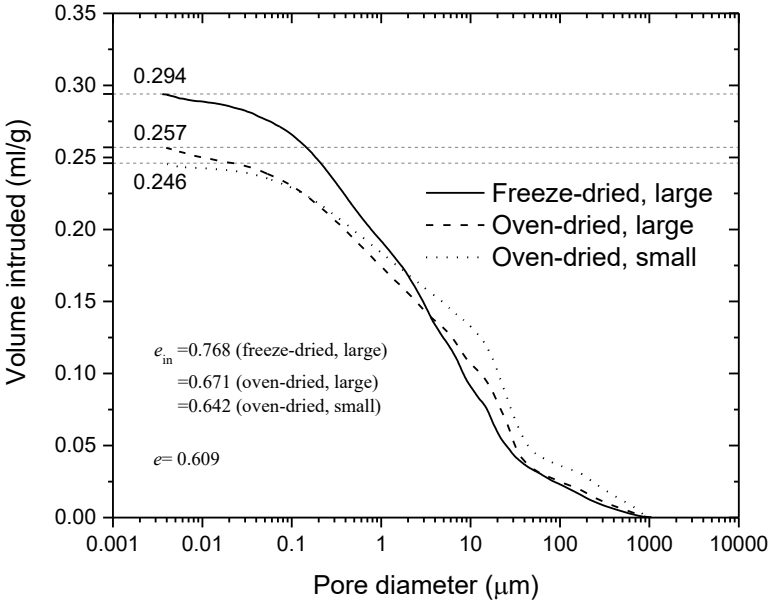

(a) Cumulative PSDs

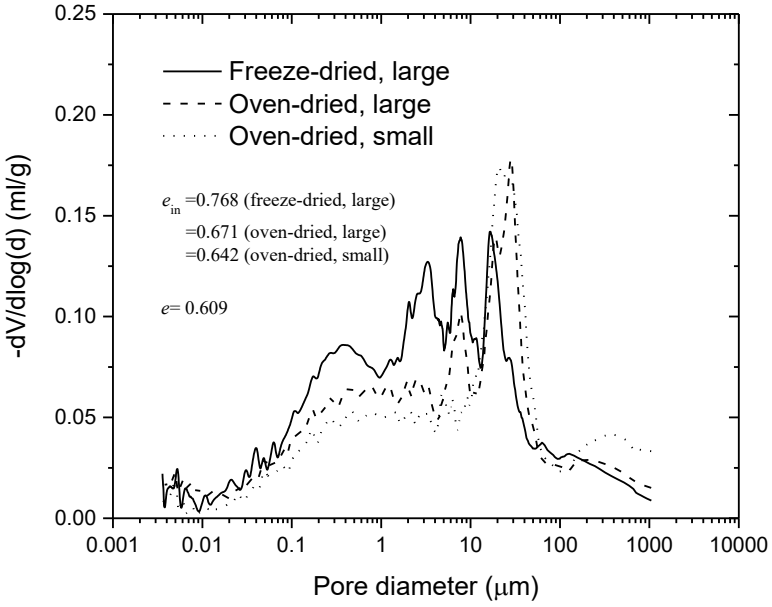

(b) Differential PSDs

Figure 4.31 PSDs for Specimen M9 prepared with different drying methods and sample sizes

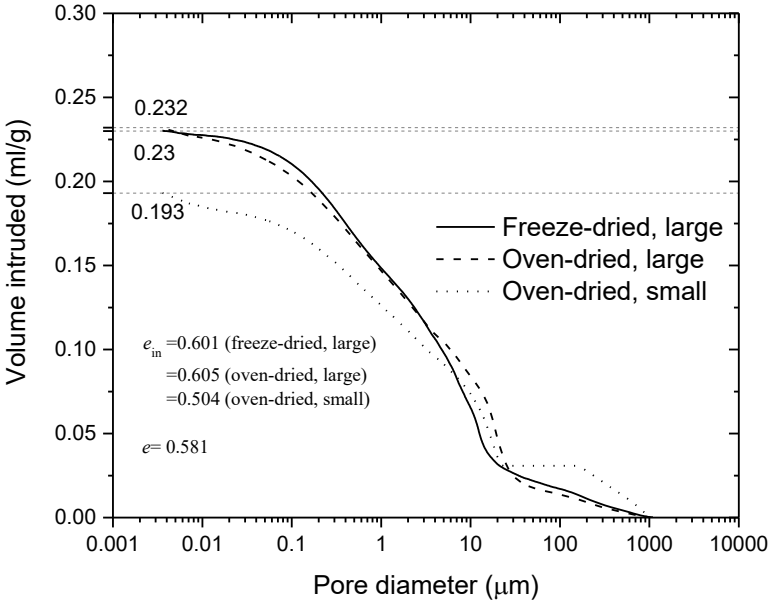

(a) Cumulative PSDs

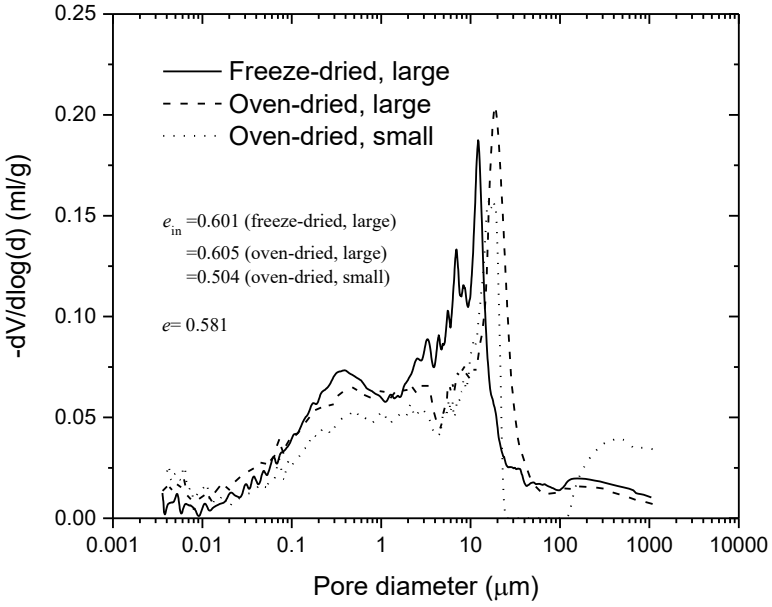

(b) Differential PSDs

Figure 4.32 PSDs for Specimen M10 prepared with different drying methods and sample sizes

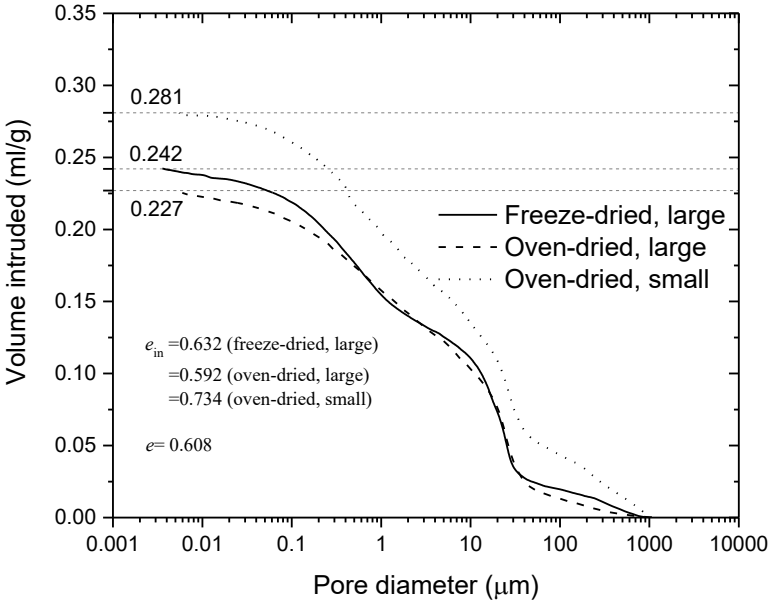

(a) Cumulative PSDs

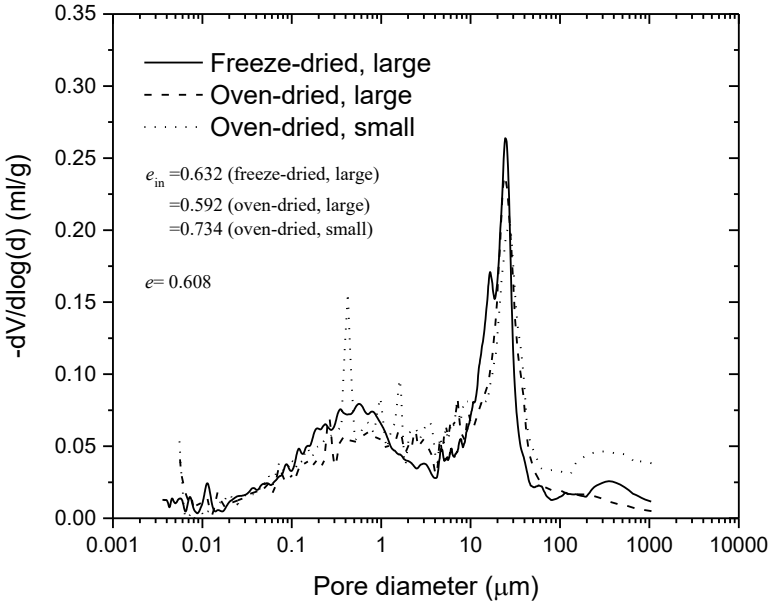

(b) Differential PSDs

Figure 4.33 PSDs for Specimen M11 prepared with different drying methods and sample sizes

4.3.6 Normal consolidation line, friction angle, cohesion and critical state

Some basic hydro-mechanical properties of Dundee silt are presented below.

4.3.6.1 Slopes of normal consolidation line and rebound curve

After compaction, Specimen H was saturated and subjected to consolidated under effective stress of 50kPa. The specimen was then taken to isotropic compression. The specimen first underwent a unloading path from 50kPa to 25kPa and then was stepwise compressed to 50, 100, 200, 400 and 800kPa. From isotropic compression test, the preconsolidation stress for the initial compacted sample (75kPa), normal consolidation line and rebound curve can be obtained as shown in Figure 4.34. The gradient of NCL λ is 0.016 and the gradient of rebound curve κ is 0.006. These two parameters will be adopted for constitutive modelling.

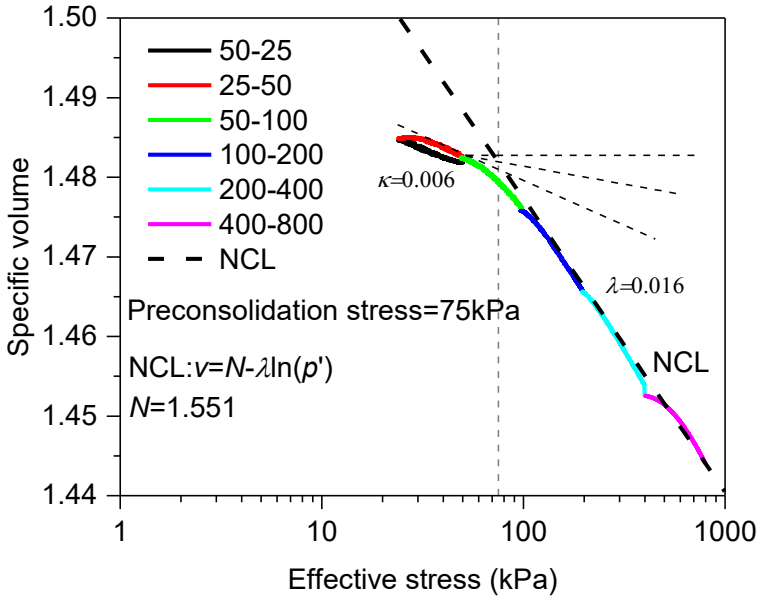

Figure 4.34 Effective stress versus specific volume during isotropic loading

4.3.6.2 Friction angle and cohesion

The shear strength τ_f of saturated soils is defined as (Terzaghi 1936):

$$\tau_f = c' + \xi' \tan \phi' \tag{4-1}$$

where c' is the effective cohesion, ξ' is the effective stress and ϕ' is the effective friction angle. To obtain c' and ϕ', Mohr circles should be drawn based on the confining stress and the peak deviatoric stress. c' and ϕ' are the parameters of a common tangent of Mohr circles. As shown in Figure 4.35, the effective cohesion c' is 30.5 kPa and the effective friction angle ϕ' is 32.6° for Dundee silt with a dry density of 1.76 Mg/m^3.

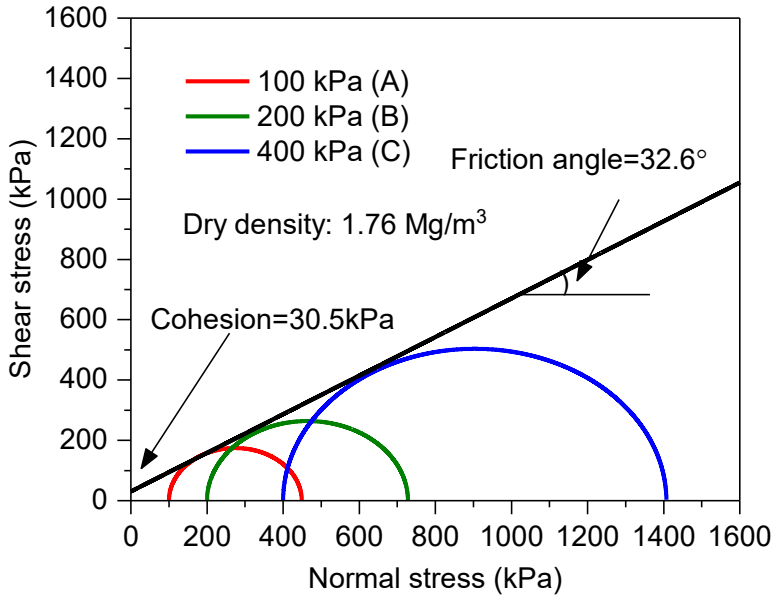

Figure 4.35 Mohr-Coulomb failure envelope for Specimen A, B and C

As presented in Figure 4.36, since Specimen M2, M6 and M15 have a lower initial dry density of 1.62 Mg/m^3, the cohesion and friction angle were reduced to 16.5 kPa and 32.2° compared with the results of specimens with a higher initial dry density of 1.76 Mg/m^3. This is consistent with the findings from other research (Abu-Farsakh et al. 2007; Andersen and Schjetne 2013; Liu et al. 2020b) .

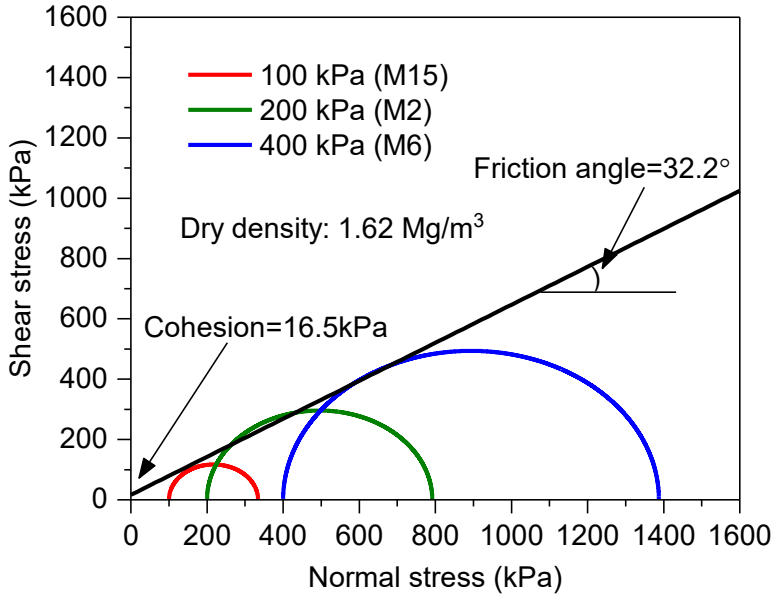

Figure 4.36 Mohr-Coulomb failure envelope for Specimen M15, M2 and M6

4.3.6.3 Slope of critical state line

Critical state defines the condition that the soil is continuously distorted or sheared under constant stress, but the total volume remains constant. Therefore, CD tests are usually terminated after the critical state has been reached. Different soil types can have very different axial strains at which the critical state is reached. The axial strain at critical state for sands and silts can be between 10% to 30% (Shear strength characteristics of Shiraz unsaturated silty clay. 2009; Zhao and Zhang 2014; Beren et al. 2020), and 5% to 15% for clays (Toll and Ong 2003; Shear strength characteristics of Shiraz unsaturated silty clay. 2009; Stróżyk and Tankiewicz 2014; Scaringi and Di Maio 2016). A common practice is terminating CD tests when the axial strain reaches 20%. Although not all soils will be completely at critical state at this axial strain, the changing rates of the deviatoric stress and volumetric strain are generally small at this axial strain (Liu et al. 2020a).

In critical state, there exists a specific critical state line which is expressed as a linear relationship between effective mean stress and deviatoric stress:

$$q = Mp' \tag{4-2}$$

where q is deviatoric stress, p' is effective mean stress and M is a constant. Figure 4.37 and Figure 4.38 present the stress paths of Dundee silt during shearing. For each specimen and stress path, the increment of deviatoric stress was always three times of that of net mean stress which is equal to effective mean stress for saturated soils. For Specimen A and B, since these two specimens show great strain-softening during shearing, after reaching peak values, both deviatoric stress and net mean stress reduced when the axial strain was approaching 20%. A straight line can be drawn to cover the end point of each path which is assumed as the critical state. This line is regarded as the critical state line for Dundee silt and M is 1.38. A similar result can also be seen for Specimen M2, M6 and M15.

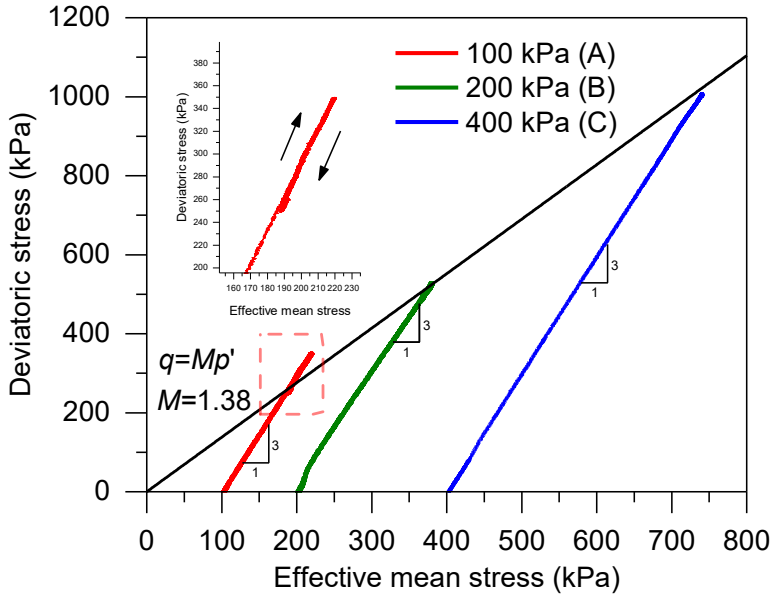

Figure 4.37 Effective mean stress versus deviatoric stress during shearing for Specimen A, B and C

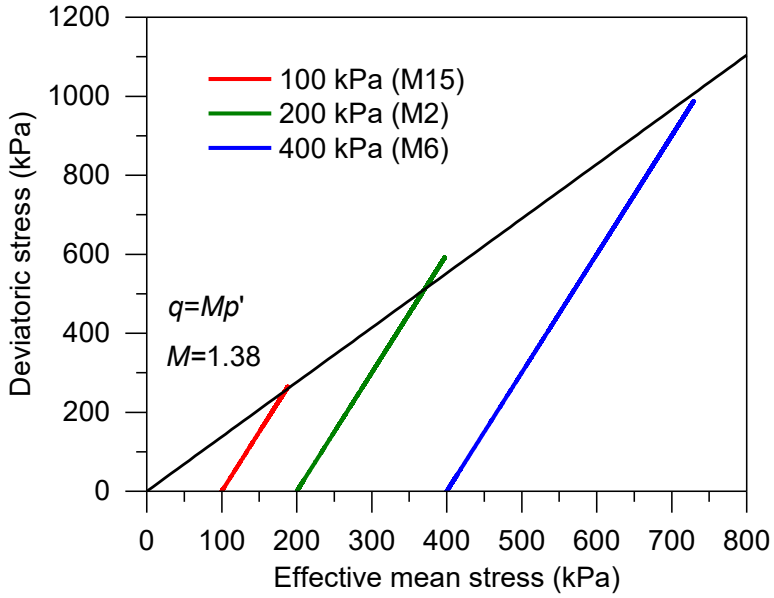

Figure 4.38 Effective mean stress versus deviatoric stress during shearing for M15, M2 and M6

4.3.7 Comparisons among saturated and unsaturated shearing under the same net confining stress

Figure 4.39 presents the comparison among saturated and unsaturated shearing under the same net confining stress of 200 kPa. Regardless of the difference in specimens (such as initial

densities and initial water content), these three specimens M2, M4 and M21 have a very similar behaviour during shearing and end up with almost the same deviatoric stress, even though there were sheared under different suctions. This is because Dundee silt has a large proportion of sand of which the shear strength will not necessarily increase with suction. For sandy soils, when the applied suction is higher than the air entry value, the shear strength can decrease due to the significant decrease of effective stress (Ng et al. 2017; Gao et al. 2020b).

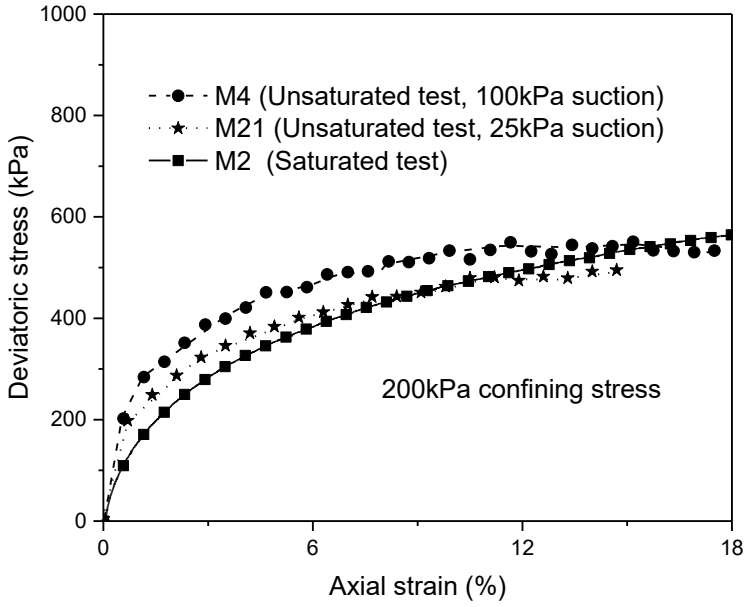

Figure 4.39 Comparisons in deviatoric stress among saturated and unsaturated tests

4.4 Concluding remarks

The microstructural-hydro-mechanical coupled behaviour of Dundee silt is studied in this chapter though experiments on compacted samples. The experiments include saturated triaxial tests, unsaturated tests, mercury intrusion porosimetry (MIP) tests and soil-water characteristics curve (SWCC) tests. For saturated triaxial tests, specimens were compacted to two different dry densities at an initial water content of 15% and then saturated and consolidated to targeted effective stresses before being shearing under various confining stresses. For unsaturated triaxial tests, all specimens were prepared to the same dry density and same initial water content of 15%. All specimens underwent a suction equilibrium stage under 25 kPa net radical stress and targeted suctions. They were then taken to consolidation stage with controlled-suctions and net mean stresses before shearing. After triaxial tests, these specimens were then either oven-dried or freeze-dried before conducting MIP tests to capture the pore size distribution and its evolution during mechanical loading. Aside from directly obtaining water content-suction relationships from the suction equilibrium stage of unsaturated tests, SWCC tests were also carried out based on devices WP4C. According to the experimental results of these mentioned tests, the following points can be obtained:

(1) Although many specimens were prepared aiming at the same water content and initial dry density, difference in their behaviour during suction equilibrium and consolidation can still be witnessed. This can be attributed to their difference in actual initial water content and initial dry density. This difference can also bring about their different behaviour in shearing and the evolution of microstructure.

(2) For Dundee silt, three different displacement rates (0.0035, 0.007 and 0.014 mm/min) all did not lead to the excessive water pressure during shearing, which means they are all suitable displacement rates for shearing. However, it should be noted that a higher displacement rate can lead to a lower shear strength and a larger axial strain is required to reach the peak deviatoric stress.

(3) A synchronous evolution of soil microstructure (pore size distribution) along with the changes of axial strain, confining stress, suction, void ratio and water content can be witnessed during different loading paths, which presents the interaction between the soil microstructure and the hydro-mechanical behaviour. The evolution of PSD follows a clear and regular principle that the decrease of volume or void ratio mostly comes from the compression of larger pores while very small pores are less affected by the external loading. This provides the potential for the microstructural-hydro-mechanical coupled behaviour to be simulated by constitutive modelling given the tight connection between the void ratio change and the evolution of pore size distribution.

(4) A higher initial dry density and confining stress lead to the left movement of pore size distribution due to the compression of larger pores while the decrease of suction can turn the bimodal PSD to unimodal PSD.

(5) It is obvious that the heterogeneity exists in triaxial specimens. Samples extracted from the layers or different layers of the same specimen can have different PSDs. However, this difference does not significantly affect the overall shape of the pore size distribution and will not affect the further modelling because the difference can be narrowed when the pore size distribution is scaled by void ratio.

(6) The freeze-drying method has a better performance in maintaining the original microstructure, especially small pores, while a significant compression in pore volume can be seen with oven-drying. A smaller sample size in MIP tests can bring about unreasonable increase in very large pores.

(7) Some basic hydro-mechanical properties of Dundee silt had been determined from the triaxial tests. The slopes of normal consolidation line and rebound curve are 0.016 and 0.006, respectively. The friction angle and cohesion both increased with initial dry density from 32.2° and 18.5 kPa to 32.6° and 30.5 kPa. This is consistent with the findings from other

research (Abu-Farsakh et al. 2007; Andersen and Schjetne 2013; Liu et al. 2020b) . The slope of the critical state line was not affected by the initial dry density.

(8) Three specimens M2, M4 and M21 have a very similar behaviour during shearing and end up with almost the same deviatoric stress, even though there were sheared under different suctions. This is because Dundee silt has a large proportion of sand of which the shear strength will not necessarily increase with suction. For sandy soils, when the applied suction is higher than the air entry value, the shear strength can decrease due to the significant decrease of effective stress (Ng et al. 2017; Gao et al. 2020b).

CHAPTER 5

Indirect consideration of microstructure in constitutive modelling

5.1 Introduction

As indicated in Chapter 4, there is strong interaction between the soil microstructure (represented by pore size distribution) and the hydro-mechanical behaviour of soils. Therefore, it is important to consider the soil microstructure in constitutive modelling.

A review of the literature (Mašín et al. 2005; Li et al. 2013; Mašín 2013; Cai et al. 2018; Li et al. 2019) suggests that there are two ways to consider the effects of soil microstructure on the hydraulic and mechanical behaviour of unsaturated soils. The first way (indirect consideration) is adopting a specific microstructural index to represent the main features of soil microstructure. Indirect methods only consider the impact of microstructure on soil behaviour. For example, the effective degree of saturation can be adopted as this index considers the different impacts of water within macropores and micropores, which provides an indirect way to take features of double porosity into consideration. Adopting this approach, Cai et al. (2018) established a hydro-mechanical coupled constitutive model based on the Glasgow Coupled Model that was validated against isotropic compression tests of double-porosity soils. Li et al. (2019) also used the effective degree of saturation to establish a model for unsaturated soils with double porosity. Their model used average effective stress, deviator stress and modified suction as the main stress variables. However, the model established by Cai et al (2018) is limited to isotropic loading and so cannot consider shear response. Also whilst the model established by Li et al. (2019) can consider shear response it adopts average effective stress as one of the main stress variables and so cannot consider how the three principal stresses will change respectively in a triaxial space, such as during shear at a constant net mean stress. A second way (direct consideration) is to focus on geometric and structural features of microstructure such as pore size distribution (PSD) or to establish mutually independent models for the loading behaviour of macropores and micropores. For example, Mašin (2013) used different constitutive models for the behaviour of macropores and micropores and satisfactorily reproduced macro-mechanical properties by establishing a corresponding coupling relationship. However, this model has a complex form and requires determination of numerous material parameters, which limits its practical application.

This chapter considers an indirect method of considering microstructure in constitutive modelling of soils' hydro-mechanical behaviour originally presented in Wu (2020). This method has not previously been compared with the original Glasgow Coupled Model which does not consider the effects of microstructure. Therefore, the advantage of considering microstructure in modelling remains unclear. The main objective of this chapter is to evaluate

the behaviour of a constitutive model with indirect consideration of soil microstructure and compare it with a non-microstructure considered model to study the importance of considering microstructure and provide further insight on building a model with direct consideration of microstructure.

The indirect microstructure model is presented in Section 5.2. In the model, the effective degree of saturation is adopted as a microstructural index because it is defined to neglect the residual degree of saturation stored in intra-aggregate pores (micropores) (Alonso et al. 2010; Wu et al. 2022; Wu et al. 2023). The model is validated and compared with the Glasgow Coupled Model (GCM) based on the experimental results of Jossigny silt and low-plastic clay. The concluding remarks are presented in Section 5.3.

The work of this chapter has been published by Wu et al. (2022) and Wu et al. (2023).

5.2 Indirect microstructure model

In this section, an indirect method of considering microstructure in modelling is presented and follows the approach presented by Wu et al. (2022). Validation of this model and its comparison with GCM and experimental results of Jossigny silt and low-plastic clay are also demonstrated.

5.2.1 Formulation of a model with indirect consideration of microstructure

The indirect microstructure model adopts the effective degree of saturation S_e as the microstructural index because it neglects the residual degree of saturation S_r^m stored in intra-aggregate pores (micropores) (Alonso et al. 2010; Wu et al. 2022; Wu et al. 2023), as defined below:

$$S_e = (S_r - S_r^m)/(1 - S_r^m) \tag{5-1}$$

where S_r is the degree of saturation. This microstructural index only considers the effect of microstructure on degree of saturation without describing the geometric properties of microstructure. Therefore, it is regarded as an indirect representation of microstructure.

Based on the framework of Glasgow Coupled Model (a more detailed presentation of the model is given in Chapter 6 (Section 6.2.3)), the model forms with the use of an effective degree of saturation-dependent effective stress where the Bishop's effective stress coefficient χ is represented by S_e instead of S_r. The effective stress tensor σ_{ij}^* is defined below (Alonso et al. 2010; Wu et al. 2022; Wu et al. 2023):

$$\xi_{ij}^* = \xi_{ij} - (\chi u_w + (1-\chi)u_a)\delta_{ij} \quad (\chi = S_e) \tag{5-2}$$

where ξ_{ij} is the stress tensor, δ_{ij} is the Kronecker delta, u_{w} is the water pressure, u_{a} is the air pressure.

With the incorporation of the effective degree of saturation-dependent effective stress, a one-directional effect of microstructure on effective stress is considered in the model. It should also be noted that the residual degree of saturation $S_{\mathrm{r}}^{\mathrm{m}}$ is assumed to be constant during loading. The effect of microstructure is thus considered unchanged without microstructural evolution.

5.2.2 Model performance

In the following sections, the indirect microstructure model's performance is evaluated based on the experimental results of two kinds of soils, including Jossigny silt and low-plastic clay. The comparison between the model and GCM which is noted as a non-microstructural model is also presented.

5.2.2.1 Jossigny silt

Jossigny silt is a non-expansive soil (Cui and Delage 1996). Various isotropic compression and shear tests were conducted by Cui and Delage on unsaturated samples of the soil. The samples were prepared under the initial states shown in Table 5.1. The model parameters (see Table 5.2) were obtained based on the experimental results. The microscopic degree of saturation was derived based on the method suggested by Alonso (Alonso et al. 2010). The soil samples first underwent a drying process to the targeted suctions. Further, the samples were compressed to predetermined net mean stresses and sheared until failure.

Table 5.1 Initial states for the Jossigny silt samples

Initial states	Value
$\overline{p}$/kPa	25.00
s/kPa	200.00
e	0.629
S_{r}	76.4%
$S_{\mathrm{r}}^{\mathrm{m}}$	56.0%
p_0^*/kPa	374.60
S_{D}^*/ kPa	77.23
S_{I}^*/ kPa	103.84

Table 5.2 Model parameters for the Jossigny silt samples

Parameters	Value
λ	0.091
κ	0.013
λ_s	0.131
κ_s	0.008
k_1	0.65
k_2	0.66
M	1.23
μ	0.3
G_s	2.78

Figure 5.1 presents the experimental axial strain versus deviator stress results during the shearing process conducted at constant suction of 200kPa and at constant confining stresses of 50kPa, 200kPa and 600kPa. Figure 5.2 presents the change in void ratio with the axial strain in the same tests. The simulation results are also shown in Figure 5.1 and Figure 5.2.

For the soil samples tested, the deviator stress increased and reached a maximum value at an axial strain of greater than 10%. It can be observed that samples sheared at a higher confining stress had a higher peak deviator stress, which is as expected, means that the shear strength increases with an increasing confining stress. Both the micro-related and non-micro-related models performed well in simulating the tendency of deviator stress change during shearing. However, both the models underestimated the deviator stress at all axial strains. This is a common issue that originates from the deficiency of the Modified Cam-Clay Model ((Lloret-Cabot et al. 2013; Wu et al. 2022)) upon which both the models are based.

During the early stage of shearing where the axial strain is smaller than 4%, the results from the micro-related model seem to be more consistent to the experimental results than the results from the non-micro-related model. However, the micro-related model significantly overestimated the axial strains when the stress path approached failure.

In terms of the void ratio, both the models successfully reproduced the trend of decreasing void ratio during shearing (see Figure 5.2). The micro-related model demonstrates

better consistency with the experimental results than the non-micro-related model. The latter tended to yield a higher volume change during shearing. This is because under the same loading condition, the effective stress is much larger in the non-micro-related model due to the fact that the microscopic degree of saturation, which barely contributes to the effective stress, is incorporated into the Bishop's effective stress parameter. When the stress path yields on both the LC and SD yield surfaces and generates large irreversible volumetric strains, the difference in the effective stresses calculated by these two different models will further amplify the disparity in the void ratio change. In Figure 5.2 the starting point of the simulation results are different from the experimental void ratios because both the models use the results of simulated isotropic compression to define the initial state.

Figure 5.3 shows how the deviator stress changes during shearing at the same confining stress but at different suctions of 200 kPa, 400 kPa and 800 kPa. Figure 5.4 presents the change in void ratio in the same tests. Both the models still have a satisfactory performance in simulating the deviator stress change and the void ratio change. When the samples were sheared at suctions of 200 and 400 kPa, both the models overestimated the development of axial strain and the non-micro-related model produced results closer to the experimental results. When modelling shear at a constant suction of 800 kPa, the non-micro-related model significantly overestimated the shear strength while the micro-related model produced a more reasonable output.

The micro-related model performed better than the non-micro-related model in terms of the void ratio (see Figure 5.4). The micro-related model slightly underestimated the void ratio change while the non-micro-related model overestimated the void ratio change at the suction of 400 and 800 kPa. Both the micro-related model and the non-micro-related model overestimated the void ratio change when the suction was 200 kPa, but the micro-related model produced a closer simulation of the experimental results.

Since both the models were found to overestimate the axial strain to reach the critical state in most cases, the 20% axial strain was adopted as a reference strain for the critical state of the modelling results. Table 5.3 shows the results of the simulated degree of saturation values at this specific axial strain and the experimental results at various suctions and confining stresses. It can be noticed that the micro-model was not necessarily better than the non-micro-related model in predicting the degree of saturation. The adoption of the effective degree of saturation is an oversimplified way to consider the microstructure and more investigations are needed to describe the microstructure more effectively.

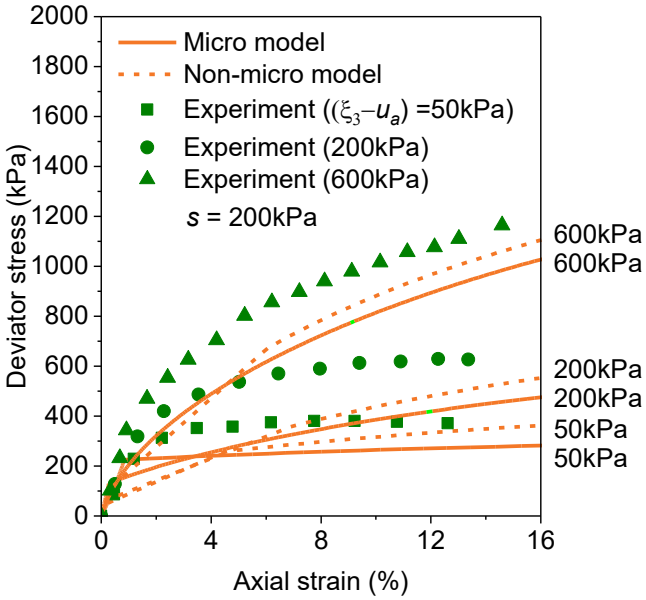

Figure 5.1 Comparison of model and experimental results in terms of deviator stress for Jossigny silt (Cui and Delage 1996) at s = 200 kPa.

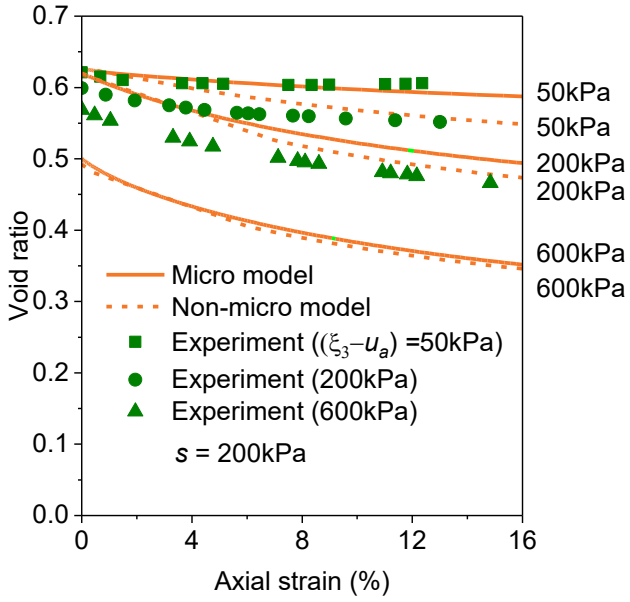

Figure 5.2 Comparison of model and experimental results in terms of void ratio for Josisigny silt (Cui and Delage 1996) at s = 200 kPa.

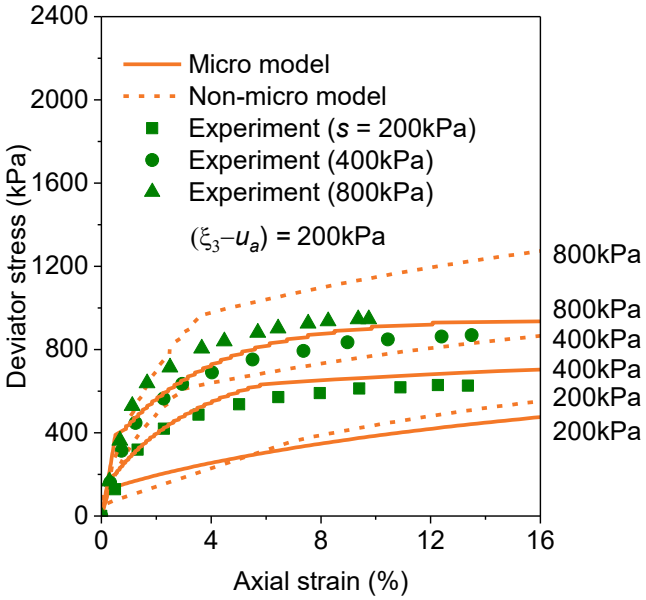

Figure 5.3 Comparison of model and experimental results for Jossigny silt (Cui and Delage 1996) at various suctions and $(\xi_3 - u_a) = 200$ kPa.

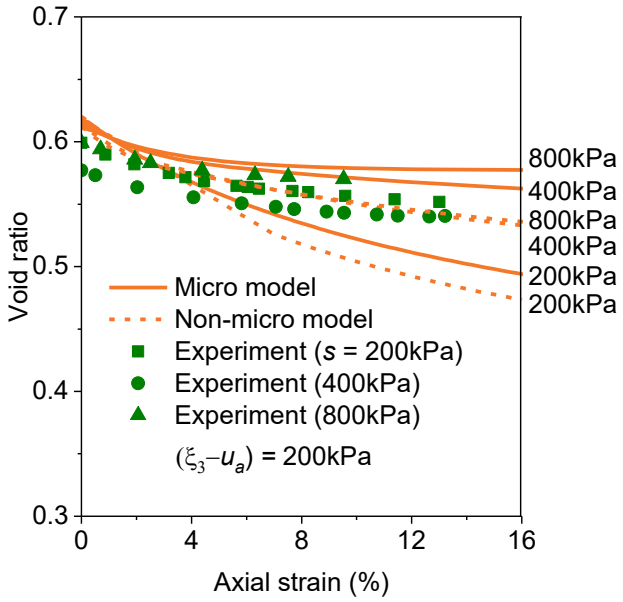

Figure 5.4 Comparison of void ratio between model and experimental results (Cui and Delage 1996) at various suctions and $(\xi_3 - u_a) = 200$ kPa.

Table 5.3 Comparison of experimental and model results in terms of degree of saturation for Jossigny silt at confining stress of 50, 200 and 600 kPa and at constant suctions of 200, 400 and 800 kPa.

s /kPa	σ_3 /kPa	S_r /% (micro)	S_r /% (non-micro)	S_r /% (experiments)
200	600	90.9	100	98.0
200	200	83.3	95.2	79.0
200	50	78.4	86.2	79.0
400	200	75.1	77.6	77.0
800	200	70.0	67.4	70.0

5.2.2.2 Low-plastic clay

A low-plastic clay (Almahbobi 2018) was a mixture of 40% Leighton Buzzard sand, 40% M400 silt and 20% Speswhite kaolin. The compacted soil samples were initially at a suction of 563 kPa and degree of saturation of 36.2%. The samples were wetted to targeted suction of 300 kPa at a constant confining stress of 20 kPa. The samples were then compressed to predetermined confining stresses of 100, 250, 400 kPa before shearing. The initial states and the model parameters of the samples are shown in Table 5.4 and Table 5.5 respectively.

Figure 5.5 presents the experimental axial strain versus deviator stress results during the shearing process conducted at constant suction of 300 kPa and at constant confining stresses of 100 kPa, 250 kPa and 400 kPa. Figure 5.6 presents the change in void ratio with the axial strain in the same tests. The simulation results are also shown in Figure 5.5 and Figure 5.6.

As shown in Figure 5.5, the micro-related model performed better in simulating the increasing deviator stress during shearing while the non-micro-related model slightly overestimated the deviator stress at constant confining stresses of 250 and 400 kPa. This overestimation became more significant at the confining stress of 100 kPa. Correspondingly, while the micro-related model produced results that are closer to the experimental results, the difference between the micro-related model and the non-micro-related model narrowed with the increase of the confining stress (see Figure 5.6).

Table 5.4 Initial states for the low-plastic clay

Initial states	Value
$\overline{p}$/kPa	20.00
s/kPa	563.00
e	0.732
S_{r}	36.2%
$S_{\mathrm{r}}^{\mathrm{m}}$	10.0%
p_0^*/kPa	250.00
S_{D}^*/ kPa	237.94
S_{I}^*/ kPa	/

Table 5.5 Model parameters for the low-plastic clay

Parameters	Value
λ	0.07
κ	0.008
λ_{s}	0.12
κ_{s}	0.02
k_1	0.6
k_2	0.3
M	1.076
μ	0.3
G_{s}	2.65

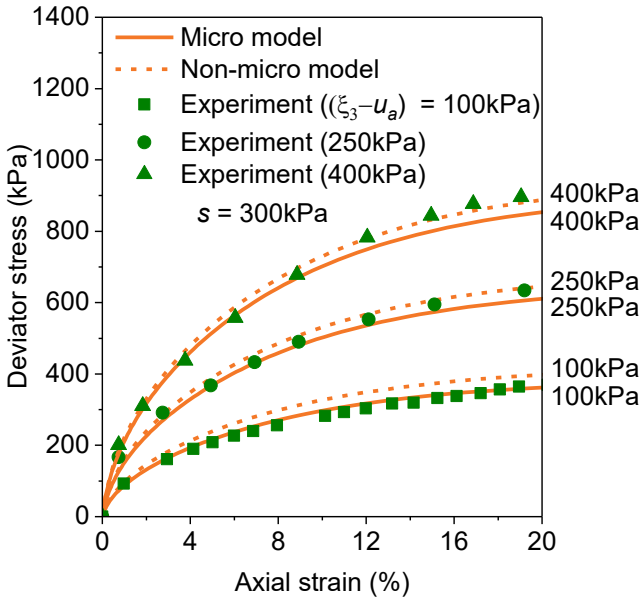

Figure 5.5 Comparison of model and experimental results in terms of deviator stress for the low-plastic clay (Cui and Delage 1996) at s = 300 kPa.

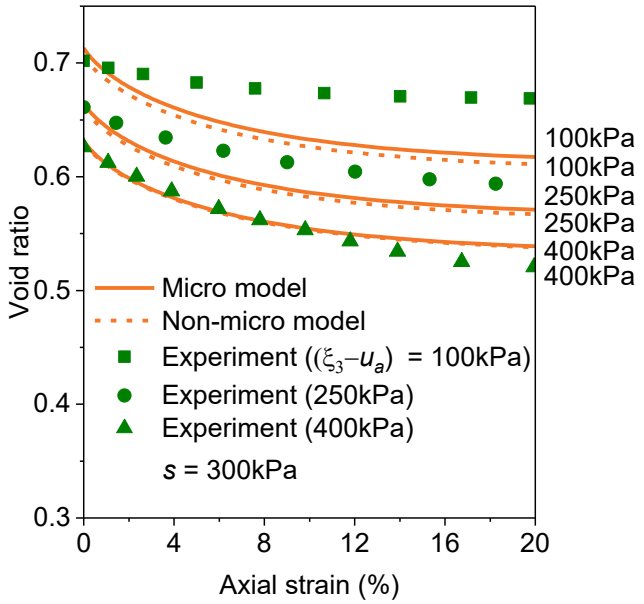

Figure 5.6 Comparison of model and experimental results in terms of void ratio for the low-plastic clay (Cui and Delage 1996) at s = 300 kPa.

5.3 Concluding remarks

This chapter investigates an indirect method of considering microstructure in constitutive modelling of soils' hydro-mechanical behaviour. The indirect microstrcuture model adopts a single parameter, the effective degree of saturation, to represent the effects of microstructure

on effective stress. According to the comparison in simulating the hydro-mechanical behaviour of Jossigny silt and low-plastic clay among the model with indirect method, GCM and the experimental results, it can be concluded that the microstructure-related model tends to produce a slightly better estimation of the void ratio change despite the fact that the difference can be narrowed between these two models at a higher confining stress or suction. When modelling the behaviour of Jossigny silt, both the models overestimated the axial strain to reach failure. The indirect microstructure model performed better in predicting the void change, whereas the GCM overpredicted the volume change during shearing. In terms of modelling the behaviour of a low-plastic clay, the deviator stress at a specific axial strain, the shear strength and the void ratio change were overestimated by the GCM, whereas the results from the microstructure-related model were found to be in good agreement with the experimental results. The differences between the results from the two models became smaller at higher confining stresses.

However, due to the simplification of describing the microstructure through the effective degree of saturation, the indirect microstructure model fails to consider the interaction between microstructure and soil behaviour, and cannot reproduce or predict the evolution of microstructure, which puts a limit on the practicability of this model. Therefore, a direct method of considering microstructure by adopting PSD as the microstructural index should be further studied.

CHAPTER 6

Direct consideration of microstructure in constitutive modelling

6.1 Introduction

As identified in Chapter 5, a model that indirectly considers microstructure fails to fully consider the interaction between microstructure and soil behaviour, and is not able to reproduce or predict the evolution of microstructure, which puts a limit on its practicability. Therefore, to fully represent the interaction between soil microstructure and the hydro-mechanical behaviour, a model with direct consideration of microstructure should be developed.

The hydro-mechanical behaviour of unsaturated soils is a long-term research topic (Fredlund and Morgenstern 1977; Fredlund et al. 1978; Alonso et al. 1990; Davies and Newson 1992; Wheeler et al. 2003; Sheng et al. 2004; Gens et al. 2006; Alonso et al. 2013; Lloret-Cabot et al. 2013; Cai et al. 2018; Rahardjo et al. 2018; Wu et al. 2022) with unsaturated soils behaviour, such as strength and volumetric change, of particular importance in many engineering applications. Many research studies have demonstrated that the microstructure, which can be defined as the arrangement of soil particles and pores (Marshall et al. 1996), can be a significant factor in the behaviour of soils (Tsuji et al. 1975; Belnap and Gardner 1993; Hu et al. 2001; Alekseeva 2007; Alonso et al. 2010; Al-Mukhtar et al. 2012; Wang and Bai 2012). Moreover, strains induced by loading can also lead to the evolution of the microstructure, including changes in pore sizes, pore shapes and pore size distribution. It has been established that the evolution of microstructure significantly influence the hydro-mechanical behaviour of soils and the storage and transmission of liquid, microorganism, chemical substance or other pollutant stored in pores (Yong 2003; Zhang 2005; Izdebska-Mucha and Trzciński 2008; Izdebska-Mucha et al. 2011; Woignier et al. 2011). There exists a strong interrelationship between the hydro-mechanical behaviour of soils and their microstructure and these interactions require investigation and to be represented adequately within theoretical and numerical models.

The impact of microstructure has received considerable attention from many researchers both in terms of experimentally observed behaviour and modelling approaches. Wang and Bai addressed the connection between pore diameter and compressibility of loess noting that compressibility is positively correlated to the proportion of pores larger than 20 micrometres (Wang and Bai 2012). Wang et al. studied the impact of microstructure on shear behaviour of natural loess (Wang et al. 2021). They found a correlation between the homogenous deformation, with the increase of confining stresses, and the microstructural evolution of pore shapes changing from angular to rounded. It was also found that the evolution of the macro

void ratio can account for the observed dilatancy of unsaturated recompacted and intact loess (Ng et al. 2019). To numerically consider the effect of microstructure, Sanchez et al. (Sánchez et al. 2001; Sánchez et al. 2005) selected different constitutive formulations for the macrostructural level and the microstructural level. An interaction formulation was proposed to connect these two levels and establish a microstructurally dependent model. This model was validated against experimental data from tests conducted by Lloret et al on heavily compacted bentonite (Lloret et al. 2003). Wu et al. adopted the effective degree of saturation as microstructural index and established a hydro-mechanical coupled model that considers the microstructure (Wu et al. 2022). The use of effective degree of saturation ignores the effect of water stored in micropores which contributes little to the effective stress (Alonso et al. 2010). Pasha et al. explored the dependency of the water retention curve (WRC) on void ratio and proposed a model for WRC with hysteresis considered (Pasha et al. 2017). Russell and Buzzi adopted a fractal method that considers the microstructure as a successive orders of pores and throats with different sizes when building a soil-water characteristic model (Russell and Buzzi 2012). According to the thermodynamic theory, both Jiang et al. (2017) and Nikooee et al. (2013) proposed microstructure-dependent equations for Bishop's effective stress coefficient.

The evolution of microstructure, often reported in terms of changes in pore size distribution, induced by hydro-mechanical loading has been investigated by a number of researchers (Thom et al. 2007; Li and Zhang 2009; Oualmakran et al. 2016; Vaunat and Casini 2017). The pore size distribution, which can be considered as a microstructural index, is highly sensitive to compaction conditions and the change of the void ratio during a loading process (Vaunat and Casini 2017; Gao et al. 2020a; Li et al. 2021; Niu et al. 2021; Qian et al. 2022). For soils with double porosity the pore size distribution related to micropores is usually unaffected by compaction or void ratio change with most compression occurring within the macropores (Li and Zhang 2009; Yu et al. 2016; Wang et al. 2019; Wang et al. 2020).

Many of the studies discussed above only focus upon modelling the one-directional relationship between the microstructure and the hydro-mechanical behaviour of soils and do not fully consider the mutual interaction between them. For example they do not consider the effects of microstructure on stress-strain behaviour and the impact of external loading and suction on microstructure evolution in one unified framework. Also, these studies cannot be used to predict the evolution of soil-water characteristic curves under loading. The objective of this chapter is to develop a microstructural-hydro-mechanical model with direct consideration of soil microstructure.

Section 6.2 proposes a direct consideration of microstructure in constitutive modelling to eliminate the limitation of the previously presented indirect method. In the model, microstructure is represented by pore size distribution (PSD) in Section 6.2.1, which is mathematically described by log-normal distribution (Section 6.2.2). The macroscopic behaviour of unsaturated soils such as volume change, shear strength and degree of saturation is determined by Glasgow Coupled Model (GCM) (Wheeler et al. 2003; Lloret-Cabot et al. 2013) in Section 6.2.3. The interaction between microstructure and macroscopic behaviour is

also considered in this model (Section 6.2.4). The evolution of PSD (microstructure) is assumed to be solely related to the change of void ratio which can be determined by GCM. A PSD-dependent Bishop's effective stress is introduced in this model to consider the effects of microstructure on macroscopic behaviour. The application of this model in predicting soil-water characteristic curve (SWCC) is also presented (Section 6.2.5). In Section 6.3 concluding remarks are drawn.

The work of this chapter has been published in Wu et al. (2024).

6.2 Direct microstructure model

Indirect microstructure models, such as considered in Chapter 5, have three significant deficiencies. First, they ignores the geometric and structural properties of soil microstructure but only considers its impact on soil behaviour such as degree of saturation. Therefore, an indirect microstructure model fails to give a direct description of microstructure. Second, when using the effective degree of saturation as the microstructural index, the residual degree of saturation stored in intra-aggregate pores is assumed to be constant. This assumption overlooks the change of soil microstructure during loading. Third, a indirect microstructure model only considers the one-directional effect of microstructure on soil behaviour (effective stress) but cannot investigate the mutual interaction between microstructure and soil behaviour. In this section, a direct microstructure model is proposed. With the adoption of pore size distribution (PSD) and a PSD-dependent effective stress, the interaction between microstructure and soil behaviour is considered and the microstructural evolution of soils can also be predicted.

6.2.1 Selected representation of microstructure

Direct consideration of microstructure requires detailed description of microstructural features and properties such as fabric, pore shape, pore size, pore volume and pore size distribution. In the model, pore size distribution (PSD) is adopted to represent microstructure. There are three reasons to choose PSD. First, volume change and degree of saturation change are two of the most valued output in a hydro-mechanical model. These two factors are both highly related to pore sizes and their volumes while the other microstructural properties are less significant. Pore size distribution happens to contain both two factors. Second, due to the irregularity of fabric and pore shape, it is difficult to mathematically describe fabric and pore shape while pore size distribution can be easily fitted by normal distribution or log-normal distribution, because of which PSD can be applied to constitutive modelling. Third, since water is stored in soil pores, based on pore size distribution, the degree of saturation or water content can be easily obtained, which gives the model a higher potential for studying SWCC and permeability.

6.2.2 Mathematic description of microstructure

Microstructure of soils is described by pore size distribution (PSD) in this study. PSD can be classified into cumulative PSD and differential PSD. Cumulative PSD is usually plotted as pore diameter (radius) versus total pore volume of pores larger than this diameter (radius) in a unit of weight. Assuming cumulative PSD can be described by a function $V(r)$, differential PSD is the derivative function of $V(r)$, which can be defined as:

$$f(r) = \frac{-\mathrm{d}V(r)}{\mathrm{d}r} \tag{6-1}$$

$$f(r) = \frac{-\mathrm{d}V(r)}{V_s \mathrm{d}r} \tag{6-2}$$

$$f(r) = \frac{-\mathrm{d}V}{\mathrm{d}\log(\mathrm{r})} \tag{6-3}$$

where r is the pore radius (can be replaced by pore diameter d) and V_s is the total solid volume per unit weight. An example of cumulative and differential PSDs is shown in Figure 6.1. Differential PSD is more frequently studied because the area below it is related to the pore volume and it is straightforward to observe the pore volume within a specific range of pore sizes from differential PSD. According to the geometric features of differential PSD, it can also be grouped into three types including single unimodal PSD, bimodal PSD and trimodal PSD. Unimodal PSD has only one peak and indicates that the microstructure is single porosity. Bimodal PSD usually has two significant peaks. One is related to micropores (intra-aggregate pores) and the other is related to macropores (inter-aggregate pores). Therefore, this microstructure is also called double porosity. Trimodal PSD has three peaks and aside from micropores and macropores, there is another peak related to mesopores. Examples of unimodal, bimodal and trimodal PSDs are shown in Figure 6.2.

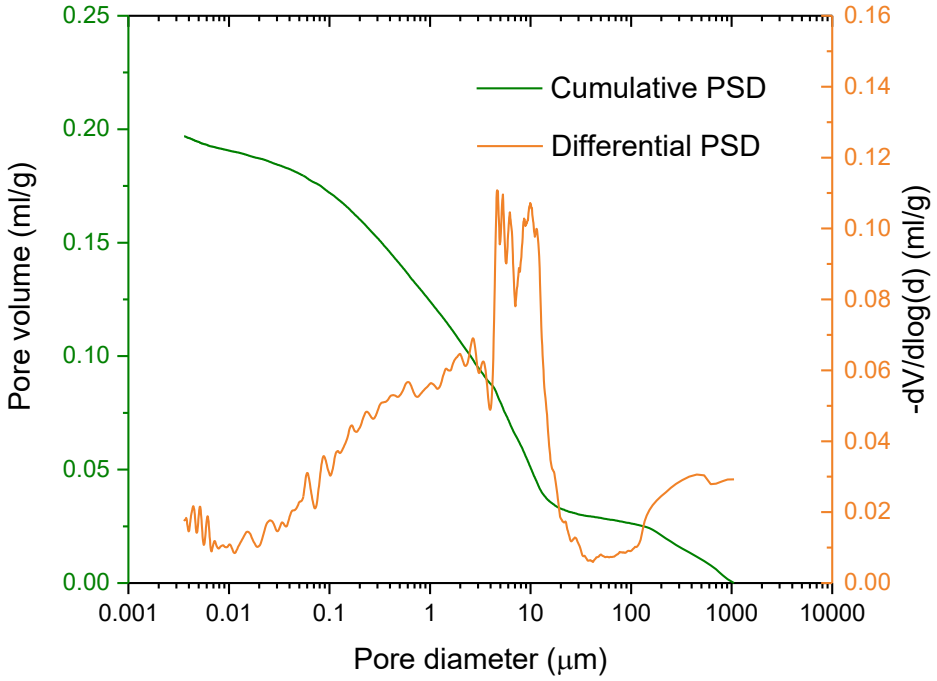

Figure 6.1 Illustration of cumulative and differential PSDs

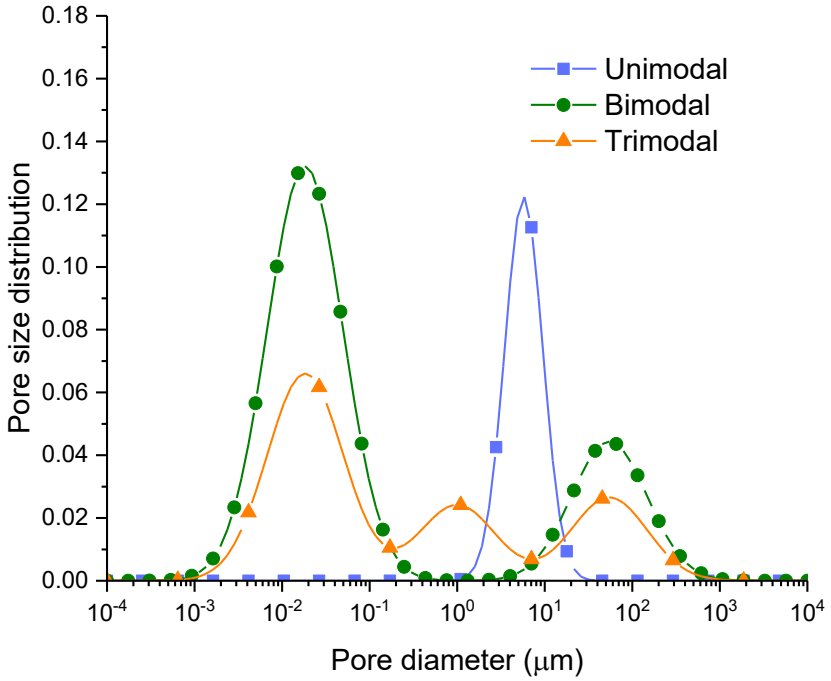

Figure 6.2 Illustration of unimodal, bimodal and trimodal PSDs

To mathematically describe differential pore size distribution, multi log-normal distributions are used in this study, which is defined as:

$$f(r)=\sum_{i=1}^{j}\frac{a_i}{\sqrt{2\pi}\sigma_i r}\exp(-\frac{(\ln(r)-\mu_i)^2}{2\sigma_i^2}) \tag{6-4}$$

where j indicates the type of PSD. If the PSD is unimodal, then j is 1. Correspondingly, j is 2 or 3 if the PSD is bimodal or trimodal, respectively. a_i, σ_i and μ_i are fitting parameters for log-normal distribution.

6.2.3 Basic framework for macroscopic behaviour of unsaturated soils

The hydro-mechanical behaviour is one of the most important macroscopic behaviour of unsaturated soils, including shear strength, volume change and degree of saturation change. Glasgow Coupled Model (GCM), a well-developed and widely acknowledged model, is adopted to reproduce the hydro-mechanical behaviour of unsaturated soils. There are three advantages of using GCM as the basic framework. First, in the plane of effective stress and modified suction, yield curves are simplified to three straight lines such as LC yield curve, SD yield curve and SI yield curve. Each curve takes charge of a specific mechanism. LC yield curve is boundary between elastic volume change and elasto-plastic volume change. SD yield curve and SI yield curve are both boundaries between elastic water change and elasto-plastic water change for suction decrease path and suction increase path, respectively. This makes GCM straightforward to study the mechanism activated during a specific stress path. The second advantage is that the coupling among three yield curves is considered in GCM which makes the model more compatible and consistent to unsaturated soil mechanics. Third, the performance of GCM has been validated by many researchers. Therefore, GCM is an excellent choice for studying the hydro-mechanical behaviour of unsaturated soils. More details about GCM have been given in this section.

6.2.3.1 Stress and strain variables

The expression of the Bishop's effective stress tensor ξ_{ij}^* and the modified suction s^* are defined as:

$$\xi_{ij}^*=\xi_{ij}-(\chi u_{\mathrm{w}}+(1-\chi)u_{\mathrm{a}})\delta_{ij} \qquad (\chi=S_{\mathrm{r}}) \tag{6-5}$$

$$s^*=(u_{\mathrm{a}}-u_{\mathrm{w}})n \tag{6-6}$$

where n is the porosity; δ_{ij} is the Kronecker delta.

Correspondingly, the stress and strain increment vectors have been adopted as follows:

$$\mathbf{d}\xi^*=(d\xi_{xx}^*,d\xi_{yy}^*,d\xi_{zz}^*,d\xi_{xy}^*,d\xi_{yz}^*,d\xi_{xz}^*,ds^*)^T \tag{6-7}$$

$$\mathbf{d}\tilde{\boldsymbol{\varepsilon}} = (d\varepsilon_{xx}, d\varepsilon_{yy}, d\varepsilon_{zz}, d\varepsilon_{xy}, d\varepsilon_{yz}, d\varepsilon_{xz}, -dS_e)^T \tag{6-8}$$

where $d\varepsilon_{ij}$ is the strain increment tensor and $d\xi_{ij}^*$ is the effective stress increment tensor.

6.2.3.2 Yield surfaces and coupling

Three yield surfaces, including the loading-collapse surface (LC), suction increase surface (SI) and suction decrease surface (SD) were adopted based on Lloret-Cabot et al., (2013), as seen in Figure 6.3, in the q: p^*: s^* stress space (where q is the deviatoric stress, p^* is the first invariant of Bishop's stress tensor). The Modified CamClay Model (MCC), with a unique M (assuming that a unique Critical State Line in the q: p^* plane exists), was adopted as the reference model for the saturated condition. Then the algebraic expressions of the three yield surfaces are given as follows:

$$F_{LC} = q^2 - M^2 p^* (p_0^* - p^*) = 0 \tag{6-9}$$

$$F_{SI} = s^* - s_I^* = 0 \tag{6-10}$$

$$F_{SD} = s_D{}^* - s^* = 0 \tag{6-11}$$

where p_0^* is the Bishop's pre-consolidation pressure which defines the position of F_{LC}, s_I^* and s_D^* are the modified suctions that locate F_{SI} and F_{SD}, respectively.

Yielding on either of the three surfaces will lead to the movement of the other two surfaces. The plastic mechanisms and couplings of yield surfaces are defined as follows:

1) yielding on the LC yield surface (F_{SI}) will bring about plastic volumetric strain with no irreversible change of the effective degree of saturation S_e, which in turn triggers upward movements of the SI and SD surfaces. This coupling is established, with a coupling parameter k_2, by:

$$\frac{ds_I^*}{s_I^*} = \frac{ds_D^*}{s_D^*} = k_2 \frac{dp_0^*}{p_0^*} \quad \text{(yield on LC)} \tag{6-12}$$

2) yielding on the SI/SD yield surfaces (F_{SI} / F_{SD}) will lead to a plastic reduction of S_e but no change of plastic volumetric strain, which in turn induces upward/downward movement of the SD/SI surfaces and outward/inward movement of the LC surface. This coupling is established, with a coupling parameter k_1, by:

$$\frac{dp_0^*}{p_0^*} = k_1 \frac{ds_I^*}{s_I^*} = k_1 \frac{ds_D^*}{s_D^*} \quad \text{(yield on SD/SI)} \tag{6-13}$$

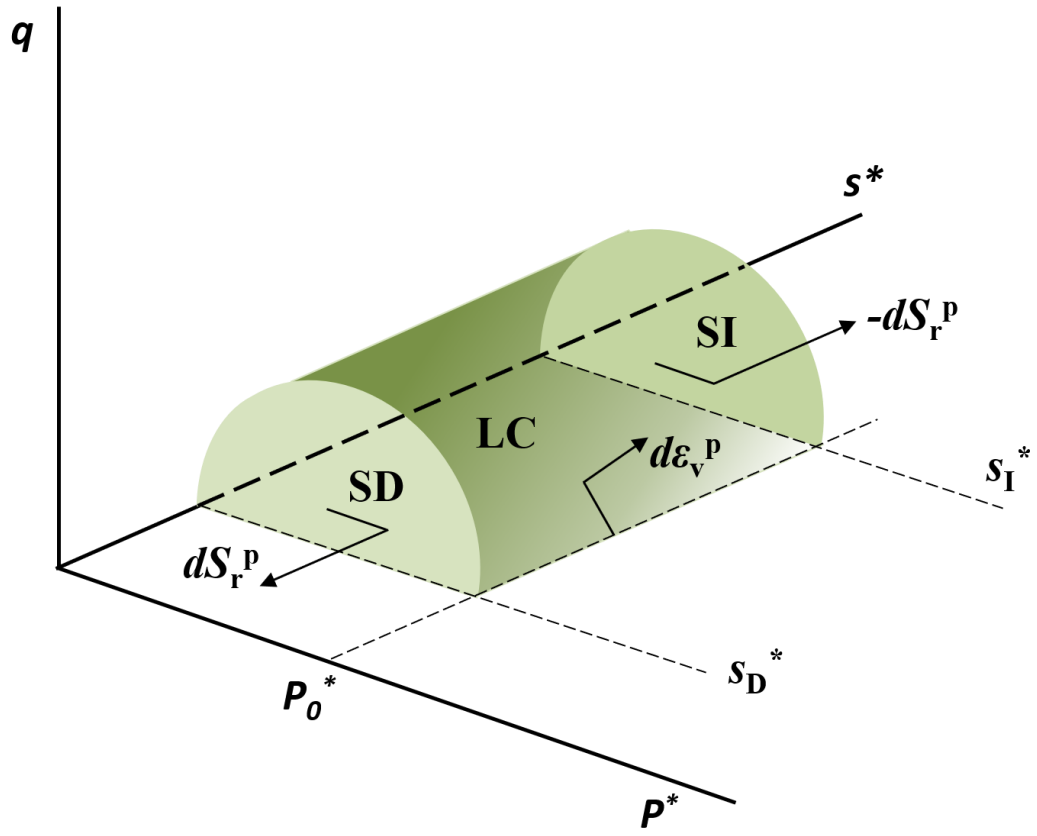

Figure 6.3 Yield surfaces of the 3D generalized model (after Lloret-Cabot et al., 2013)

6.2.3.3 Flow rules

Flow rules define the orientation of the generalized plastic strain increments during yielding. This paper assumes associated flow rules and adopts the generalized expression presented by Lloret Cabot et al. (Lloret-Cabot et al. 2013) :

$$d\tilde{\boldsymbol{\varepsilon}}_j^{\mathrm{p}} = d\lambda_l^j \frac{\partial F_l}{\partial \boldsymbol{\xi}^*} \quad \text{with} \quad \begin{array}{l} l = \mathrm{LC}, \beta; j = \mathrm{LC}, \beta, \mathrm{LC}+\beta; \\ \beta = \mathrm{SI} \quad \text{or} \quad \mathrm{SD} \end{array} \tag{6-14}$$

where $d\lambda_l^j$ is the plastic multiplier with *j* related to the plastic mechanism which is active (e.g. when yield on LC yield surface is activated *j* is LC and for yield on SI or SD *j* is LC is β) and *l* is associated with plastic changes of effective degrees of saturation (when *l* is β) or volumetric strains (when *l* is LC).

6.2.3.4 Hardening laws

The generalized hardening laws determining the relationships between increments of plastic volumetric strain $d\varepsilon_{\mathrm{v}}^{\mathrm{p}}$, increments of the plastic effective degree of saturation $dS_{\mathrm{e}}^{\mathrm{p}}$, and increments of the hardening variables dp_o^*, ds_{I}^*, ds_{D}^* are as follows:

$$dp_o^* = p_0^* \left[\frac{v d\varepsilon_{\mathrm{v}}^{\mathrm{p}}}{\lambda - \kappa} - \frac{k_1 dS_{\mathrm{r}}^{\mathrm{p}}}{\lambda_{\mathrm{s}} - \kappa_{\mathrm{s}}} \right] \tag{6-15}$$

$$ds_{\mathrm{I/D}}^* = s_{\mathrm{I/D}}^* \left[-\frac{dS_{\mathrm{r}}^{\mathrm{p}}}{\lambda_{\mathrm{s}} - \kappa_{\mathrm{s}}} + k_2 \frac{v d\varepsilon_{\mathrm{v}}^{\mathrm{p}}}{\lambda - \kappa} \right] \tag{6-16}$$

where parameters λ_{s} and κ_{s} are the slope of the main curve and the slope of the scanning curve when the SWCC is simplified and represented by three straight lines; λ and κ are the slope of normal consolidation line and the slope of rebound curve under saturated condition respectively

6.2.3.5 Constitutive relationship between stress and strain

(1) Elastic behaviour

When only one elastic mechanism is activated, the generalized stress-strain relationship can be expressed as:

$$d\boldsymbol{\xi}^* = \mathbf{D}_{\mathrm{e}}^* d\tilde{\boldsymbol{\varepsilon}}^{\mathrm{e}} \tag{6-17}$$

where $\mathbf{D}_{\mathrm{e}}^{*}$ is the generalized elastic matrix written in terms of the elastic bulk modulus K, the slope of the scanning curve in the water retention plane κ_{s} and the Poisson's ratio μ; $d\tilde{\boldsymbol{\varepsilon}}^{\mathrm{e}}$ is the elastic increment strain.

(2) Elasto-plastic behaviour

$$d\boldsymbol{\xi}^{*} = \mathbf{D}_{\mathrm{e}}^{*} d\tilde{\boldsymbol{\varepsilon}}^{\mathrm{e}} = \mathbf{D}_{\mathrm{ep}}^{*} d\tilde{\boldsymbol{\varepsilon}} \tag{6-18}$$

where $\mathbf{D}_{\mathrm{ep}}^{*}$ is the generalized elasto-plastic matrix; $d\tilde{\boldsymbol{\varepsilon}}$ is elasto-plastic increment strain. More details about $\mathbf{D}_{\mathrm{ep}}^{*}$ can be found in (Lloret-Cabot et al. 2013; Wu et al. 2022; Wu et al. 2024).

6.2.4 Interaction between microstructure and macroscopic behaviour of unsaturated soils

After the fitting function for PSD and the basic framework for hydro-mechanical behaviour are determined, it is important to build a connection between microstructure and macroscopic behaviour. The interaction between microstructure and macroscopic behaviour is divided into two parts. The first part is the effects of macroscopic behaviour on microstructure. This part is considered to ensure that the evolution of microstructure can be predicted or reproduced during loading. The second part is the effects of microstructure on macroscopic behaviour to establish a model with direct consideration of microstructure.

6.2.4.1 Effects of macroscopic behaviour on microstructure

Macroscopic behaviour of soils such as volume change induced by loading and saturation change induced by suction has a significant effect on microstructure. The evolution of microstructure can be witnessed when there is change of load or suction. When soil with double porosity is compressed during loading, it is common to observe that most compression lies in the volumetric reduction of larger pores through the downward movement of the PSD for larger pores while there is little change for the PSD for smaller pores (see Figure 6.4). Saturation will have an impact on both smaller pores and larger pores. With the increase of saturation, the double porosity of soil will be reduced with the peaks of each pores moving closer to each other, which makes the whole PSD more similar to a unimodal shape (see Figure 6.5). However the evolution of PSD is trigged (loading or saturation), there is obvious and strong connection between the PSD evolution and the change of pore volume or void ratio.

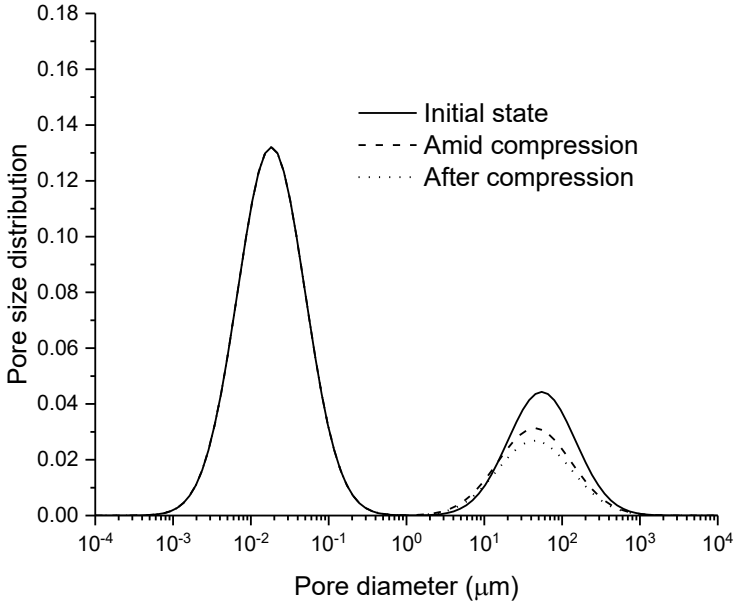

Figure 6.4 Illustration of PSD evolution due to compression

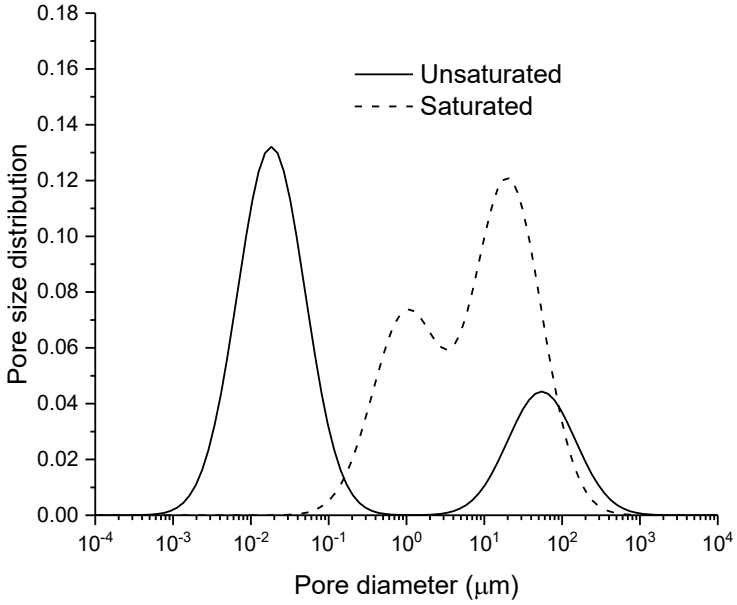

Figure 6.5 Illustration of PSD evolution due to saturation

After obtaining the parameters at different void ratios by fitting experimental data, the evolution of pore size distributions with changing void ratios can also be acquired by a fitting method. Assuming that the change of each parameter is linearly related to the change of void ratio, the variation of parameters can be defined as:

$$\Delta a_i = K_1^i \Delta e \tag{6-19}$$

$$\Delta \mu_i = K_2^i \Delta e \tag{6-20}$$

$$\Delta\sigma_i = K_3^i \Delta e \tag{6-21}$$

where K_1^i, K_2^i and K_3^i are fitting parameters. The relationship between these parameters and the void ratio can also be taken to be nonlinear depending on the geometric features of experimental results in a parameter-void ratio graph (Li and Zhang 2009; Li et al. 2020). Since the change of void ratio can be readily calculated by a traditional constitutive model, it is proposed here to use a constitutive model to reproduce and predict the evolution of pore size distribution.

6.2.4.2 Effects of microstructure on macroscopic behaviour

It has been indicated that the evolution of pore size distribution can be reproduced or predicted by the change of void ratio (Li and Zhang 2009; Li et al. 2020; Gramegna 2022) if a specific constitutive model is selected and the loading path is predetermined. However, this only considers how the loading can induce the evolution of pore size distribution and does not address how the variation of microstructure affects the mechanical behaviour of soils. If the work done by filtration forces is ignored, the impact of changing microstructure can be studied through the incremental work input per unit volume during isotropic loading (Houlsby 1997; Vaunat and Casini 2017):

$$\delta w = -p\frac{\delta V_{\mathrm{t}}}{V_{\mathrm{t}}} + u_{\mathrm{w}}\frac{\delta V_{\mathrm{w}}}{V} + u_{\mathrm{a}}\frac{\delta V_{\mathrm{a}}}{V} \tag{6-22}$$

where V_{t} is the total volume; p is the total mean stress; u_{w} is the water pressure; u_{a} is the air pressure; V_{w} is the water volume; V_{a} is the air volume. δ represents the change of volume. Considering that the solid is incompressible, the change of volume is equal to the change of pore volume δV_{V} and is composed of the changes of both water volume and air volume:

$$\delta V = \delta V_{\mathrm{V}} = \delta V_{\mathrm{w}} + \delta V_{\mathrm{a}} \tag{6-23}$$

The change of water volume can also be separated into two components δV_{w1} and δV_{w2}:

$$\delta V_{\mathrm{w}} = \delta V_{\mathrm{w1}} + \delta V_{\mathrm{w2}} = \chi\delta V_{\mathrm{V}} + \delta V_{\mathrm{w2}} \tag{6-24}$$

δV_{w1} is the water volume change generated by the change of pore volume and it is assumed to be proportional to the total change of pore change through a proportionality coefficient χ. δV_{w2} is the water volume change induced by the change of suction. By substituting equations (6-23) and (6-24) into (6-22), the work input can be expressed as:

$$\delta w = -[p - \chi u_{\mathrm{w}} - (1-\chi)u_{\mathrm{a}}]\frac{\delta V}{V} - (u_{\mathrm{a}} - u_{\mathrm{w}})\frac{\delta V_{\mathrm{w2}}}{V} \tag{6-25}$$

Since $\frac{\delta V}{V}$ is the volumetric strain increment, then equation (6-25) can also be expressed as:

$$\delta w = -[p - \chi u_{\mathrm{w}} - (1-\chi)u_{\mathrm{a}}]\delta\varepsilon_{\mathrm{V}} - (u_{\mathrm{a}} - u_{\mathrm{w}})\frac{\delta V_{\mathrm{w2}}}{V} \tag{6-26}$$

It can be noticed that the term '$[p - \chi u_{\mathrm{w}} - (1-\chi)u_{\mathrm{a}}]$' is consistent with the Bishop's effective stress expression (Bishop 1959). Therefore, the proportionality coefficient χ can also serve as the Bishop's effective stress parameter. The coefficient χ is defined as:

$$\chi = \frac{\delta V_{\mathrm{w1}}}{\delta V_{\mathrm{V}}} = \frac{\delta e_{\mathrm{w1}}}{\delta e} \tag{6-27}$$

where e_{w1} is the water ratio at constant suction and e is the void ratio. To obtain the coefficient χ, the change of void ratio δe can be easily acquired by a constitutive model. The change of water ratio δe_{w1} can be determined via consideration of the pore size distribution (scaled by the void ratio). Figure 6.6 presents two pore size distribution curves at two different void ratios presented by Vaunat and Casini (Vaunat and Casini 2017). Curve 1 is compressed to Curve 2 in a loading path where the void ratio decreases from 0.8 to 0.7. The pore size distributions have been scaled by the void ratio, so the area below each curve is equal to the void ratio. The difference in total area between these two curves is the change of void ratio δe. Since water is stored in pores, if the volume of pores fully filled with water can be determined, the water volume and so the water ratio can be obtained. According to capillary theory and Washburn's equation (Washburn 1921), there exists a largest pore size that the liquid can reach and every pore that has a smaller pore size will be fully filled. The equation for the largest pore size is defined as:

$$R = \frac{2\gamma\cos\theta}{s} \tag{6-28}$$

where R is the pore radius; γ is the surface tension of water; θ is the contact angle between water and pore wall (assumed to be 0) and s is the suction. Once R is determined, the water volume is equivalent to the pore volume of pores smaller than R and so the water ratio is equivalent to the void ratio of pores smaller than R. The area difference within the range that

radius is smaller than R between Curve 1 and Curve 2 is the change of water ratio δe_{w1}. Then the coefficient χ can be calculated from:

$$\delta e_{\mathrm{w1}} = \int_0^R [\mathrm{PSD}_1(r) - \mathrm{PSD}_2(r)]\mathrm{d}r \tag{6-29}$$

$$\chi = \frac{\delta e_{\mathrm{w1}}}{\delta e} = \frac{\int_0^R [\mathrm{PSD}_1(r) - \mathrm{PSD}_2(r)]\mathrm{d}r}{\delta e} \tag{6-30}$$

Since the coefficient χ can be calculated via consideration of pore size distribution evolution and it is also an important stress variable in a constitutive model, a relationship between the variation of pore size distribution (microstructure) and the behaviour of a constitutive model can be established. The evolution of the pore size distribution is assumed to be solely related to the void ratio, which can be calculated by the constitutive model, while the pore size distribution-dependent coefficient χ is adopted in the model to consider the effect of the microstructural evolution on the effective stress and hydro-mechanical behaviour. Adopting the GCM as the basic framework for the hydro-mechanical behaviour and using log-normal distributions to describe the pore size distribution and its evolution, has allowed the establishment of a model that can represent the stress-strain behaviour, the hydraulic behaviour, the evolution of the microstructure and the interaction among them within the same framework.

It should be noted that the equation (6-22) was established based on isotropic loading condition. For triaxial shearing under constant confining stresses, the equation can be rewritten as (Houlsby 1997):

$$\begin{aligned}
\delta w &= -\xi_{ij}\varepsilon_{ij} + u_{\mathrm{w}}\frac{\delta V_{\mathrm{w}}}{V} + u_{\mathrm{a}}\frac{\delta V_{\mathrm{a}}}{V} \\
&= -(\xi_{11}\varepsilon_{11} + \xi_{22}\varepsilon_{22} + \xi_{33}\varepsilon_{33}) + u_{\mathrm{w}}\frac{\delta V_{\mathrm{w}}}{V} + u_{\mathrm{a}}\frac{\delta V_{\mathrm{a}}}{V} \\
&= -\left[(p+\frac{2}{3}q)\varepsilon_{11} + (p-\frac{1}{3}q)\varepsilon_{22} + (p-\frac{1}{3}q)\varepsilon_{33}\right] + u_{\mathrm{w}}\frac{\delta V_{\mathrm{w}}}{V} + u_{\mathrm{a}}\frac{\delta V_{\mathrm{a}}}{V} \\
&= -p\frac{\delta V}{V} - \frac{2}{3}q(\varepsilon_{11} - \varepsilon_{22}) + u_{\mathrm{w}}\frac{\delta V_{\mathrm{w}}}{V} + u_{\mathrm{a}}\frac{\delta V_{\mathrm{a}}}{V}
\end{aligned} \tag{6-31}$$

The only difference between equation (6-31) and equation (6-22) is that equation (6-31) has a part related to the work input induced by the deviatoric stress q. However, this difference does not affect the way equations (6-23) and (6-24) are incorporated into equation (6-31). Therefore, the equation (6-27) is still valid for triaxial shearing under constant confining stresses.

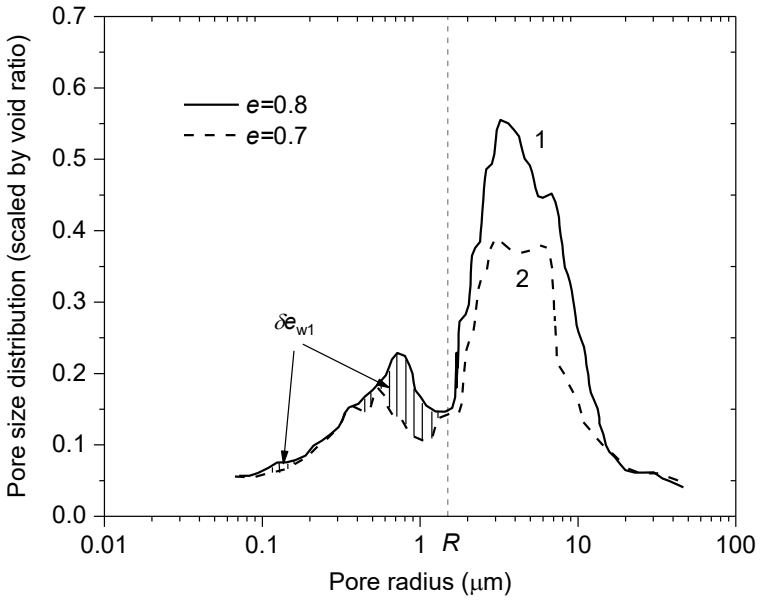

Figure 6.6 Illustrations of calculating χ through pore size (Vaunat and Casini 2017)

The algorithm for the direct microstructure model is presented in the figure below. When simulating the stress-strain behaviour and microstructure evolution for a specific stress path, this stress path can be divided into many incremental steps. For the initial step, the incremental effective stress can be calculated through the predetermined increments of net mean stress/suction, with which the stress-strain behaviour (include the change of void ratio) can be obtained by Glasgow Coupled Model. The evolution of pore size distributions can then be determined based on the change of void ratio and parameters for PSD evolution. A new PSD after the incremental effective stress is thus obtained to calculate a new χ that will be used for the next incremental step. This loop runs until the ultimate stress level is reached.

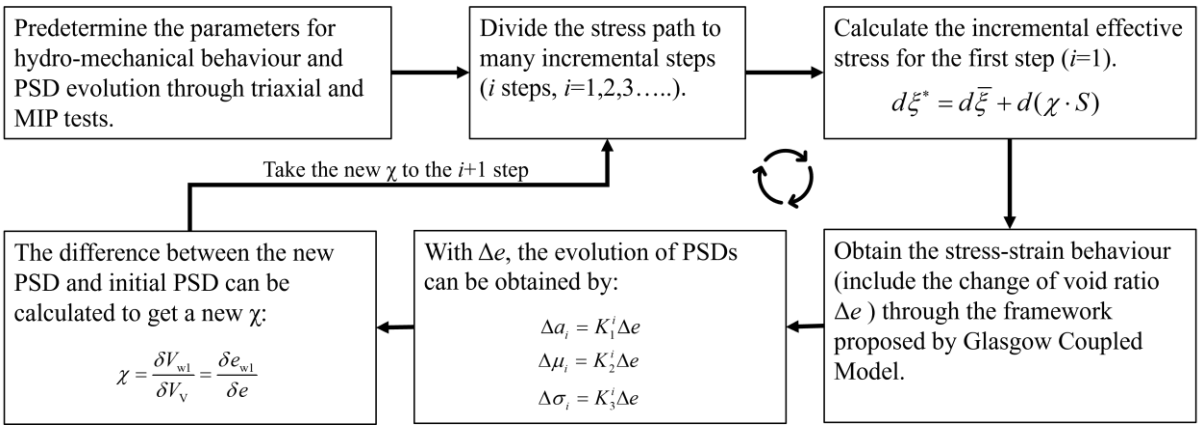

Figure 6.7 Algorithm for the direct microstructure model

6.2.5 Application of the model in SWCC

Soil water characteristic curve (SWCC) is one of the most fundamental properties of soils that denotes soils' behaviour in retaining water (Tripathy et al. 2014b; Tripathy et al. 2014a; Arroyo et al. 2015; Guo-Quan et al. 2022). It is usually defined as the relationship between suction and water content (or degree of saturation). Both water content and degree of saturation are related to the water volume stored in soil pores. If the water volume at a specific suction can be determined, then the corresponding SWCC will be obtained. According to capillary theory and Young-Laplace equation where the mercury surface tension is replaced by the surface tension of water γ based on Young-Laplace equation , there exist a maximum pore size R that water can reach at a specific suction and any pores having equivalent or smaller pore sizes can be fully filled with water:

$$R = \frac{2\gamma \cos\theta}{s} \tag{6-32}$$

Since the largest pore size to hold the water is determined, the water volume stored in pores is equal to the total volume of pores smaller than R which can be obtained from pore size distribution $f(r)$.

$$V_{\mathrm{w}}(s) = V_{\mathrm{s}} \cdot \int_0^R f(r) \cdot \mathrm{d}r = V_{\mathrm{s}} \cdot \int_0^{\frac{2\gamma\cos\theta}{s}} f(r) \cdot \mathrm{d}r \tag{6-33}$$

$$\theta_s(s) = \frac{V_{\mathrm{w}}(s)}{V} = \frac{V_{\mathrm{s}} \cdot \int_0^R f(r) \cdot \mathrm{d}r}{V} = \frac{V_{\mathrm{s}} \cdot \int_0^{\frac{2\gamma\cos\theta}{s}} f(r) \cdot \mathrm{d}r}{V} \tag{6-34}$$

$$S_{\mathrm{r}}(s) = \frac{V_{\mathrm{w}}(s)}{V_{\mathrm{v}}} \times 100\% = \frac{V_{\mathrm{s}} \cdot \int_0^R f(r) \cdot \mathrm{d}r}{V_{\mathrm{v}}} = \frac{\int_0^{\frac{2\gamma\cos\theta}{s}} f(r) \cdot \mathrm{d}r}{e} \tag{6-35}$$

where V is the total volume of soil, V_{s} is the volume of soil particles, V_{v} is the volume of pores, ρ_{w} is the water density, ρ_{s} is the soil particle density and G_{s} is the specific gravity. The soil water characteristic curve can be described from the equations above when the pore size distribution $f(r)$ is determined. This is the basic principle of obtaining SWCC from pore size distribution (Simms and Yanful 2002; Zhang and Chen 2005; Della Vecchia et al. 2015; Yan et al. 2021; Guo-Quan et al. 2022). It should be noted that this strategy is based on simplification and assumptions. Soil pores are assumed to be spherical using this strategy to obtain SWCC from PSD. The assumption that all pores smaller than R are fully filled with water is also possible to be unrepresentative when air becomes trapped in small and occluded pores.

Furthermore, since the SWCC is obtained based on a fixed pore size distribution $f(r)$, any change in soil microstructure or pore size distribution during wetting or drying is ignored in such approaches.

For the equations above, the volumetric water content/degree of saturation is calculated within the pore radius range from 0 to $R = 2\gamma\cos\theta / s$, which is related to the pores fully filled with water. This is Method A. Since the fitted pore size distribution obtained from multi log normal distributions tends to reach 0 at smaller pore radius, the volumetric water content will also approach 0 at higher suction. Therefore, this method is more suitable for soils with a low residual degree of saturation. However, due to the limitation of MIP that it cannot fully represent the total pore volume in soils and the difference between fitted PSDs and original PSDs, when *R* is infinite, the degree of saturation is not necessarily equal to 100%. Another method (Method B) to obtain SWCC is that assuming the degree of saturation is 100% at zero suction and then deduct the pore volume not filled with water (radius from *R* to infinite) from the water content in saturation condition (Simms and Yanful 2002). If the void ratio e is known and $f(r)$ is defined as $dV / d\log(r)$, the volumetric water content $\theta_s(s)$ or degree of saturation $S_{\mathrm{r}}(s)$ can be defined as:

$$\theta_s(s) = \theta_{sat} - \frac{\int_R^{+\infty} f(r)\cdot \mathrm{d}\log_{10} r}{V} = \frac{e}{1+e} - \frac{\int_{\frac{2\gamma\cos\theta}{s}}^{+\infty} \frac{f(r)}{\ln 10 \cdot r}\cdot \mathrm{d}r}{1/\rho_d} \tag{6-36}$$

(θ_{sat} is the volumetric water content at saturation)

$$S_{\mathrm{r}}(s) = \left(1 - \frac{\int_R^{+\infty} f(r)\cdot \mathrm{d}\log_{10} r}{V_{\mathrm{v}}}\right)\times 100\% = \left(1 - \frac{\int_{\frac{2\gamma\cos\theta}{s}}^{+\infty} \frac{f(r)}{\ln 10 \cdot r}\cdot \mathrm{d}r}{V_{\mathrm{v}}}\right)\times 100\% \tag{6-37}$$

An example of using both Method A and Method B to predict SWCC is given below based on the experimental PSD of Guilin lateritic clay (see Figure 6.8) (Sun et al. 2016a; You and De-an 2017). The basic properties and fitted parameters for PSD are shown in Table 6.1. As shown in Figure 6.9, the predicted SWCC by Method B has a much better performance when the suction is smaller than 10000kPa, but significantly overestimates the residual degree of saturation at a higher suction and the degree of saturation maintains a very high value even suction goes to 100000kPa. In comparison, the SWCC predicted by Method A fails to reach 100% saturation at a low suction, but its performance gets better in higher suction and no undesired residual water content can be seen.

Table 6.1 Basic properties (Sun et al. 2016a; You and De-an 2017) and fitted parameters for Guilin lateritic clay

Void ratio	Specific gravity	Parameters						
		a_1	μ_1	σ_1	a_2	μ_2	σ_2	R^2
1.0	2.74	6.5	3.558	0.900	0.011	-3.579	0.330	0.94

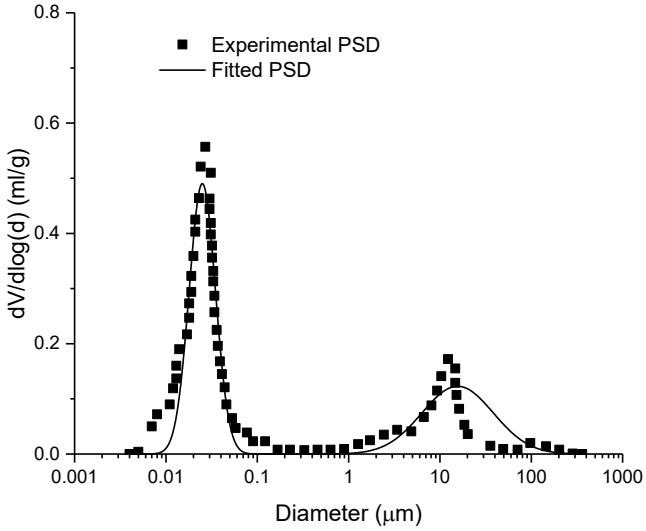

Figure 6.8 PSD for Guilin lateritic clay and fitted PSD

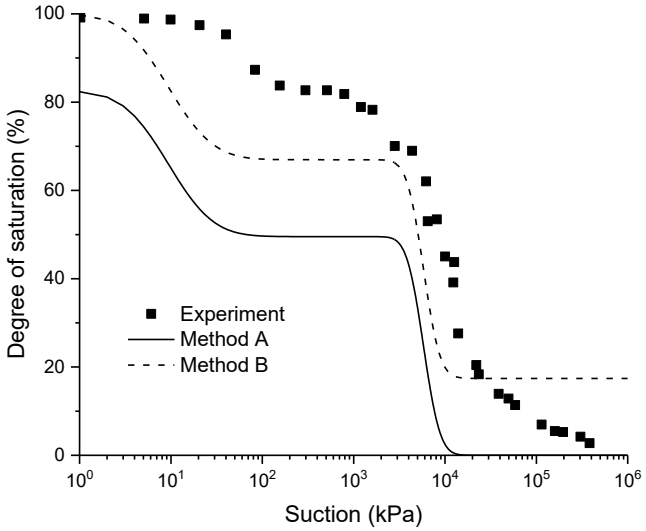

Figure 6.9 Comparison between experimental SWCC (You and De-an 2017) and predicted SWCC

6.3 Concluding remarks

This chapter present the direct method of considering microstructure in constitutive modelling of soils' hydro-mechanical behaviour. In the direct microstructure model, the pore size distribution is used to represent changes in microstructure and is described as a log-normal distribution and its evolution is assumed to be solely related to the change of void ratio which can be obtained by the stress-strain behaviour. The stress-strain behaviour represented following the approach proposed by Glasgow Coupled Model, but with a different effective stress incorporated such that the Bishop's effective stress is based on the evolution of pore size distribution instead of the degree of saturation. Therefore, the mutual interaction between the stress-strain behaviour and the pore size distribution is established in this model. The direct microstructure model is able to represent the hydro-mechanical behaviour and microstructural evolution within the same framework. Besides, based on the relationship between water content and PSD, this model can also be applied to predict the evolution of SWCC during loading.

CHAPTER 7

Model response and sensitivity analysis

7.1 Introduction

In this chapter, an initial evaluation of the proposed direct microstructure model's performance is carried out based on both published and idealized parameters. A sensitivity analysis is also undertaken in order to investigate the feasibility of using PSDs obtained by Mercury Intrusion Porosimetry (MIP) in this model, considering that the PSDs obtained by MIP and the fitted PSDs cannot be fully representative of the microstructure. The objectives of this chapter include: (1) evaluate the performance and feasibility of the proposed model based on experimental results of Speswhite kaolin, to provide guidance for the further validation on the proposed model with other soils; (2) analyse the model's sensitivity to pore size distribution related parameters and study the reliability of using PSDs obtained from MIP tests in the model.

This chapter is organized as follows. The model response based on Speswhite kaolin is summarised in Section 7.2. The sensitivity analysis is presented in Section 7.3. The concluding remarks are presented in Section 7.4.

The work of this chapter has been published by Wu et al. (2024).

7.2 Model response

In this section an initial assessment of model performance is presented via consideration of reported experimental behaviour of a 'standard' clay. In particular, the hydro-mechanical behaviour of Speswhite kaolin is considered during an isotropic loading path experimentally reported by Lloret-Cabot et al. (2013).

7.2.1 Stress path

An isotropic loading path with an increase in net mean stress from 50 kPa to 250 kPa was considered. The suction remained constant at 300 kPa during this loading.

7.2.2 Initial states for modelling

The initial states for modelling were adopted from experimental results reported by Lloret-Cabot (2013), as presented in Table 7.1.

Table 7.1 Initial states for Speswhite kaolin

Initial states	Value
p_{net}/kPa	50
s/kPa	300
e	1.208
S_{r}/%	60.1
p_0^*/kPa	273
S_{D}^*/kPa	164
S_{I}^*/kPa	/

7.2.3 Parameters for modelling

The parameters for modelling are presented in Table 7.2. The parameters related to the hydro-mechanical behaviour of Spewhite kaolin are as reported by Lloret-Cabot et al. (2013). The parameters for the initial pore size distribution are determined based on the experimental soil-water characteristic curve (SWCC) of Speswhite kaolin reported by Tripathy et al. (2014). According to Tripathy et al. (2014b), the SWCC of Speswhite kaolin starts to have a significant change of degree of saturation at a suction of about 400kPa, this can be assumed as being the suction at which the largest pores are being evacuated and so can be used to infer the largest pore size of the PSD. According to the Young-Laplace equation, the equivalent pore radius at this suction is 0.35μm. Since the reported void ratio at this suction is 0.9 and the initial void ratio adopted for modelling is 1.208, it is reasonable to assume that the initial PSD will have macropores larger than 0.35μm, and hence the pore radius at peak density is assumed to be around 0.35μm. Also to ensure consistency, the area below the selected initial pore size distribution is set to be equal to the initial void ratio of 1.208. It is recognised that due to the limitation of MIP, in which mercury fails to fully inundate very large pores and cannot intrude very small pores (leading to a measuring range usually from several nanometres to several hundred micrometres), the pore size distribution obtained from MIP cannot fully represent all pores of soils. Therefore, the intruded void ratio e_{in} can be smaller than the actual void ratio e (Wang et al. 2020) and calibration and modification of the pore size distribution shall be implemented to ensure consistency in modelling.

Due to a lack of experimental evidence (i.e. MIP data) parameters concerning the evolution of pore size distributions were selected by means of the enumeration method to achieve physically meaningful results. All parameters selected are within a reasonable range and result in pore size distributions that have similar geometric shapes and evolutional features as those of reported by others (Thom et al. 2007; Li and Zhang 2009; Burton et al. 2014; Vaunat and Casini 2017). Based on the previously adopted parameters, a sensitivity analysis was then conducted by changing several PSD-related parameters to study the impact of these parameters on the modelled pore size distribution evolution and hydro-mechanical behaviour.

Table 7.2 Parameters for modelling

Hydro-mechanical parameters	Value	Pore size distribution and evolution parameters	Value
λ	0.124	a_1	1.198
κ	0.006	σ_1	0.6
λ_s	0.098	μ_1	-1
κ_s	0.0076	a_2	0.01
k_1	0.662	σ_2	0.5
k_2	0.803	μ_2	-5
M	0.71	K_1^1	1
μ	0.3	K_2^1	0.3
G_s	2.6	K_3^1	-0.12
		K_1^2	0
		K_2^2	0
		K_3^2	0

7.2.4 Modelling results

Figure 7.1 presents the evolution of the PSD during the isotropic loading. All these PSDs have a bimodal shape where both inter-aggregate PSDs (for macropores) and intra-aggregate PSDs (for micropores) can be easily distinguished. The peak density of inter-aggregate PSDs occurs at around 0.35microns while that of intra-aggregate PSDs is at about 0.005 microns. The highest density of inter-aggregate PSDs is about 2.7 and that of intra-aggregate PSDs is about 1.40. During the isotropic loading, peak densities of the inter-aggregate PSDs drop and the dominant pore size moves left, which is related to the compression and volume decrease of macropores. For the intra-aggregate PSDs, since the evolutional parameters were assumed to be zero, these PSDs remain almost constant in shapes and positions during the loading. This style of PSDs evolution reflects the trends observed in reported experimental data. According to the experimental results from various researchers (Sridharan et al. 1971; Tanaka et al. 2003; Thom et al. 2007; Li and Zhang 2009; Burton et al. 2014), volume change mainly derives from the compression of macropores such that a downward movement of the inter-aggregate PSD is often witnessed. Due to the reduction of macropores during compression, the dominant pore size can also decrease, as indicated by the left movement of inter-aggregate PSD.

Figure 7.2 shows the comparison between modelling and experimental results reported by (Sivakumar 1993; Lloret-Cabot et al. 2013). For the modelling result, the χ remains almost constant at the early stage of loading and then starts to increase after yielding on both LC and SD yield surfaces. The evolution of χ is similar to the change of degree of saturation but χ is always smaller than the degree of saturation, which is consistent with the findings reported by Vaunat and Casini (2017a). Yielding on both LC and SD yield surfaces occurs at a net mean stress of approximately 130kPa. At the yielding point, the simulated behaviour is sharper in nature that the experimental results. This can be attributed to the adoption of the classical

elasto-plasticity theory (Lloret-Cabot et al. 2013). Generally, the proposed model succeeds in predicting the development of both void ratio and degree of saturation based on the selected model parameters.

Figure 7.1 and Figure 7.2 highlight the most significant contribution of the proposed direct microstructure model, which is that the microstructurally based model can not only satisfactorily reproduce the hydro-mechanical behaviour based on the idealized parameters but can also represent the evolution of pore size distributions, something which non-microstructure based models are unable to do. Since pore size distribution is one of the most important pieces of information on the particle rearrangement in particulate systems and can be applied to many areas such as volume change, water retention and permeability, the proposed model has significant potential in engineering application.

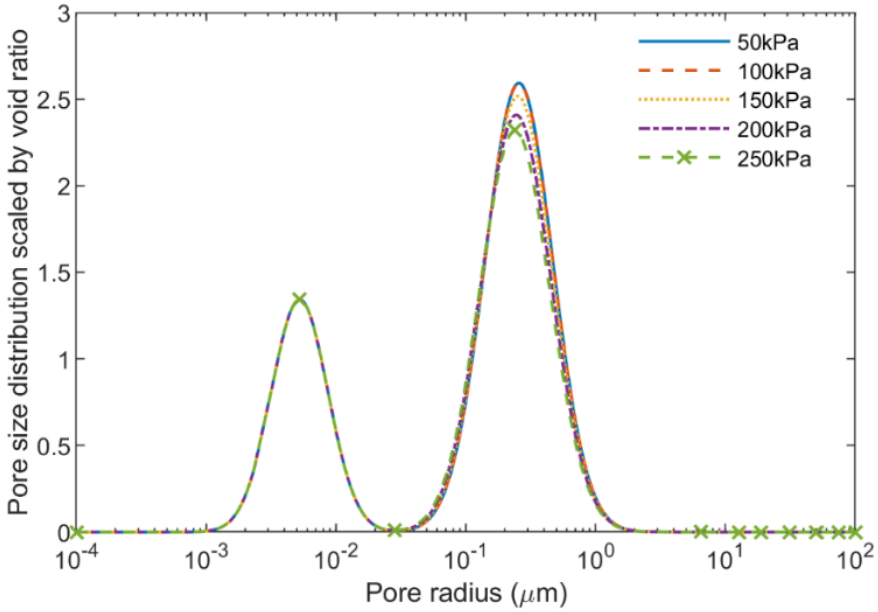

Figure 7.1 Initial pore size distribution (50 kPa) and its evolution under isotropic loading

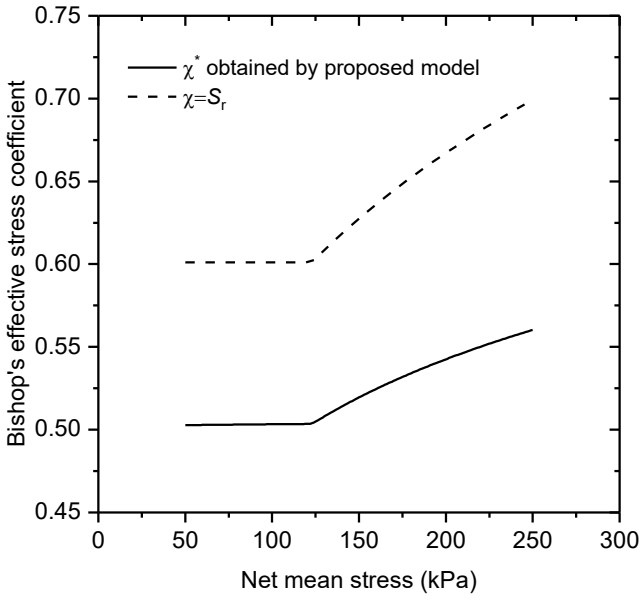
0.75
0.70
0.65
0.60
0.55
0.50
0.45
Bishop's effective stress coefficient
χ* obtained by proposed model
χ=Sr
0
50
100
150
200
250
300
Net mean stress (kPa)

(a)

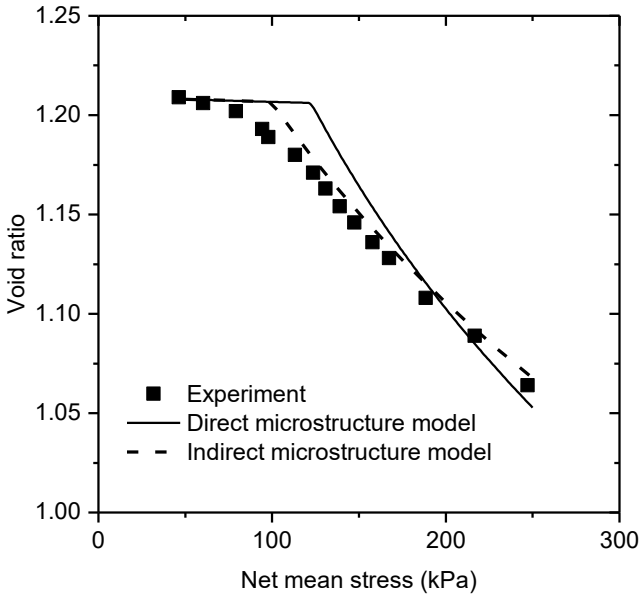
1.25
1.20
1.15
1.10
1.05
1.00
Void ratio
Experiment
Direct microstructure model
Indirect microstructure model
0
100
200
300
Net mean stress (kPa)

(b)

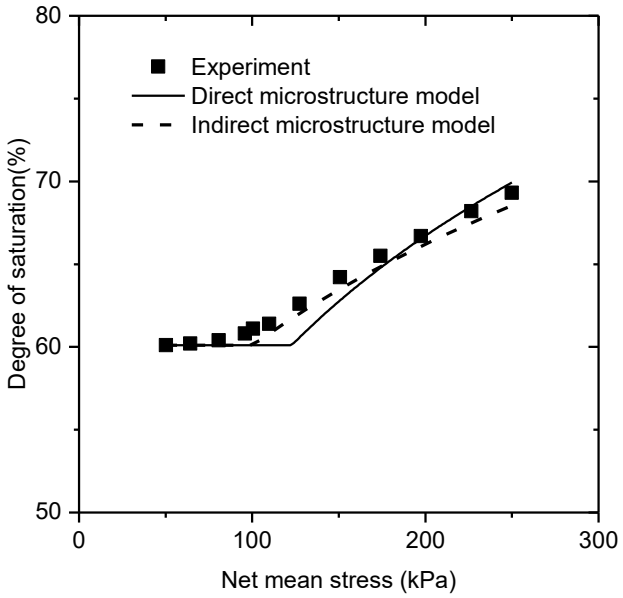

(c)

Figure 7.2 Comparison between modelling and experimental results: (a) Bishop's effective stress coefficient; (b) Void ratio; (c) Degree of saturation

7.3 Sensitivity analysis

Compared with using degree of saturation as the Bishop's effective stress coefficient, the PSD-dependent χ is significantly more complex. Firstly, because of the limitation of MIP in typical testing ranges (Tanaka et al. 2003; Li and Zhang 2009; Gramegna 2022), the PSDs obtained from MIP should not be considered as fully representative of the actual PSDs of soils, which may lead to inaccuracy in calculating χ . Secondly, due to the heterogeneity of soils and the irregularity of experimental PSDs, it is possible that the shape-fitting parameters for PSDs and evolutional parameters can be of variation for the same soil sample. Therefore, it is necessary to carry out model sensitivity analysis of the PSD-related parameters to evaluate the reliability of using MIP as the source of obtaining PSDs. In the following sections the sensitivity of the model to the various parameters used in the adopted PSD relationship is considered.

7.3.1 Sensitivity analysis (a_2)

The parameter a_2 represents the volumetric proportion of intra-aggregate pores. Since the summation of a_1 and a_2 is equal to the void ratio, the increase of a_2 will lead to a higher proportion of intra-aggregate pores compared to inter-aggregate pores. A_2 values of 0.001, 0.01, 0.1 and 0.5 are considered (the other parameters remain the same as indicated in Table 7.2), the resulting PSDs and their evolution are shown in Figure 7.3. Due to the zero value of evolutional parameters, the intra-aggregate PSDs remain constant regardless of each proportion. For inter-aggregate PSDs, it can be seen that there is still a similar downward movement of the peak

densities. Figure 7.4 presents the simulated hydro-mechanical behaviour and its comparison with the experimental results. In terms of χ, a significant increase can be witnessed with the increase of a_2. χ still has a similar changing tendency as the degree of saturation but χ is always smaller than the degree of saturation at each net mean stress. Despite the significant variation of χ, the change of a_2 does not have a profound impact on the hydro-mechanical behaviour. The difference in the void ratio and the degree of saturation is low compared to the large disparity among the parameters a_2. Therefore, the newly introduced model is not particularly sensitive to the proportion of intra-aggregate PSDs.

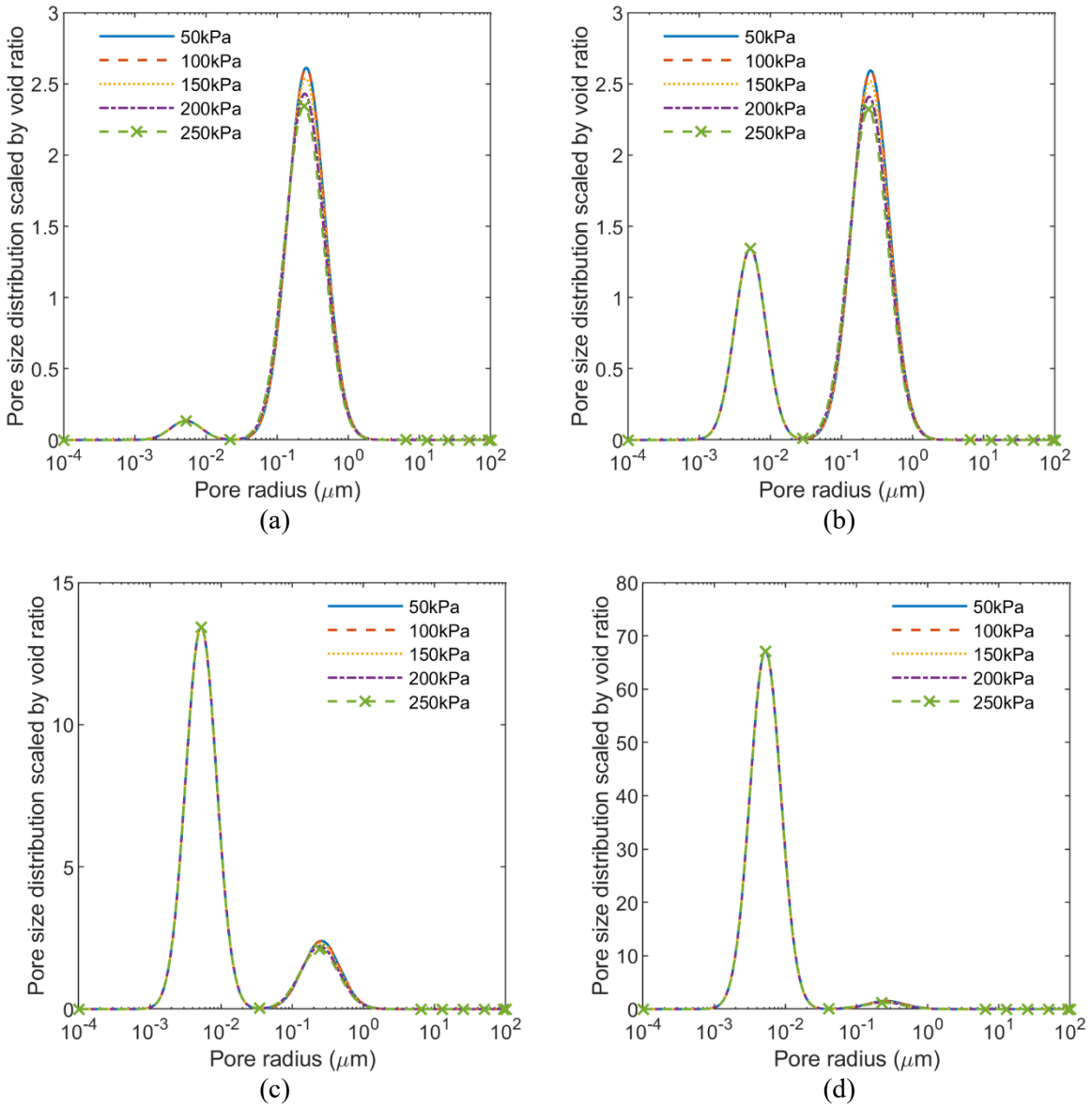

Figure 7.3 Evolution of pore size distributions under various a_2: (a) a_2=0.001; (b) a_2=0.01; (c) a_2=0.1; (d) a_2=0.5

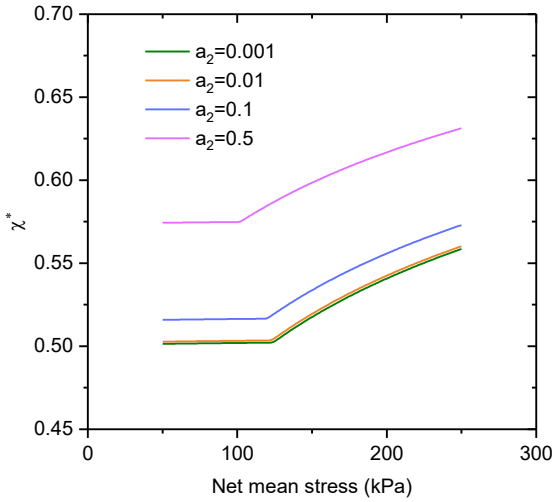

(a)

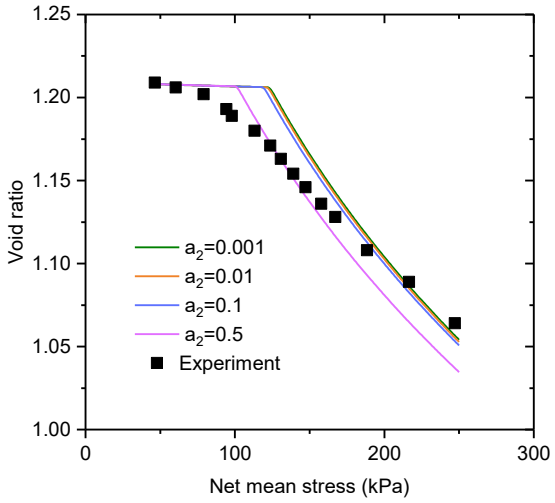

(b)

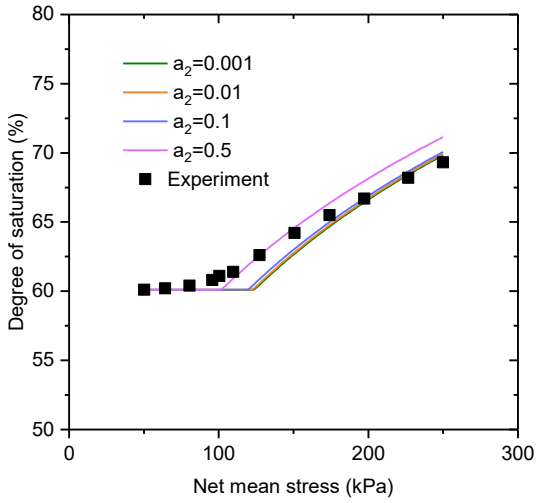

(c)

Figure 7.4 Model sensitivity to a_2: (a) Bishop's effective stress coefficient; (b) Void ratio; (c) Degree of saturation

7.3.2 Sensitivity analysis (σ_1)

The parameter σ_1 is the standard deviation of a log-normal distribution. σ_1 can affect the width and the pore size at peak density of the inter-aggregate PSD. Figure 7.5 presents the PSDs and their evolution at various values of σ_1 (0.3,0.6,1.2 and 2.4) (the other parameters remain the same as indicated in Table 7.2). The PSDs show less bimodality when σ_1 increases tending towards a unimodal form. During loading, the inter-aggregate peaks in the PSDs reduce. As shown in Figure 7.6, there is a slight impact on χ (the larger the σ_1 is, the smaller the χ will be), the void ratio and the degree of saturation when the σ_1 decreases from 2.4 to 0.6. When the σ_1 is 0.3, a sharp increase of χ can be seen, which can lead to a much larger effective stress

at a specific net mean stress. Therefore, the difference among simulated results increases and the yielding on both LC and SD yield surfaces occurs at a lower net mean stress.

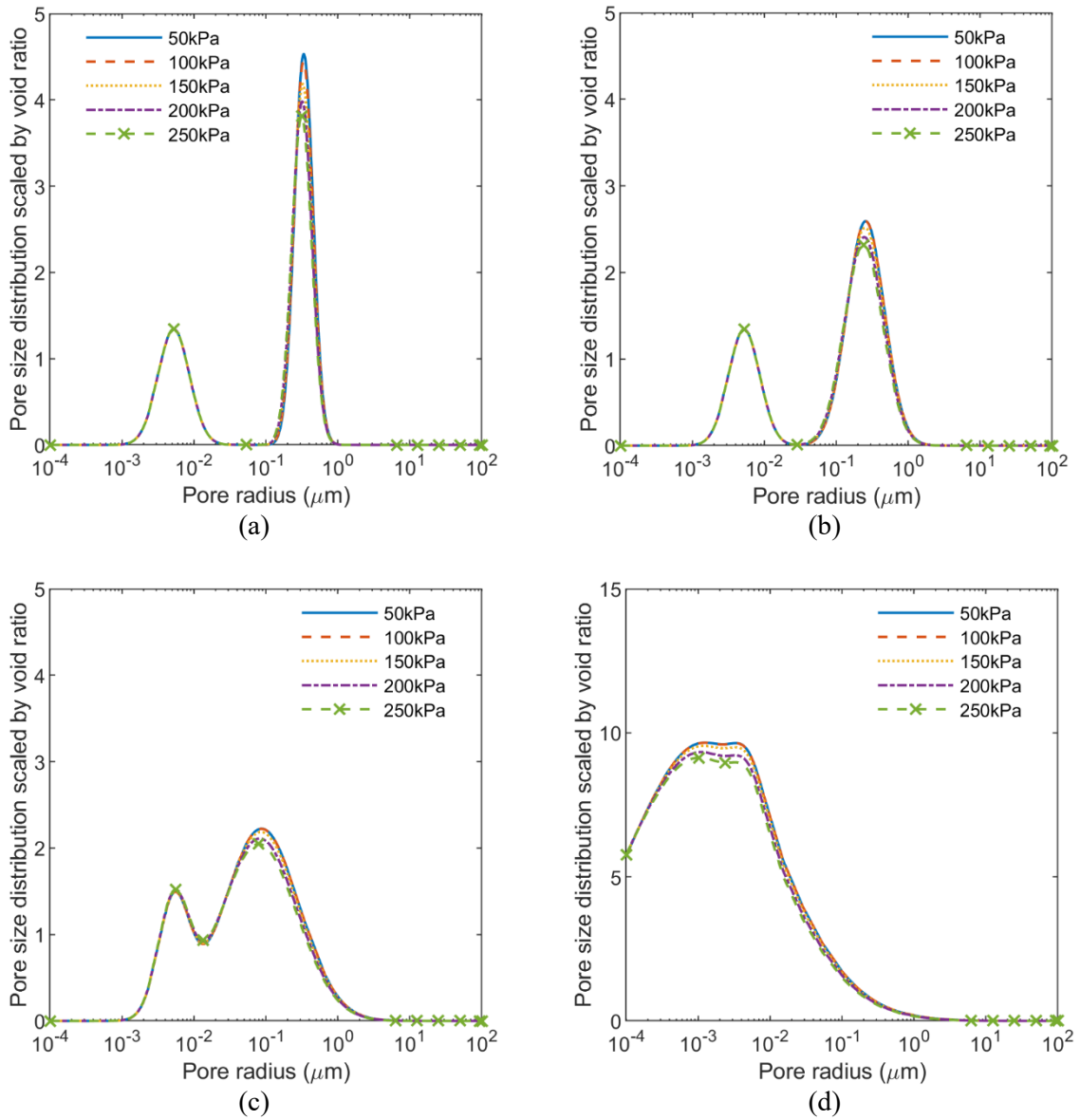

Figure 7.5 Evolution of pore size distributions under various σ_1: (a) σ_1=0.3; (b) σ_1=0.6; (c) σ_1=1.2; (d) σ_1=2.4

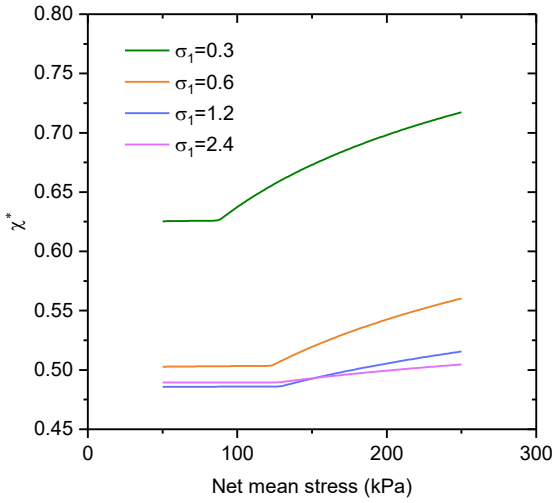

(a)

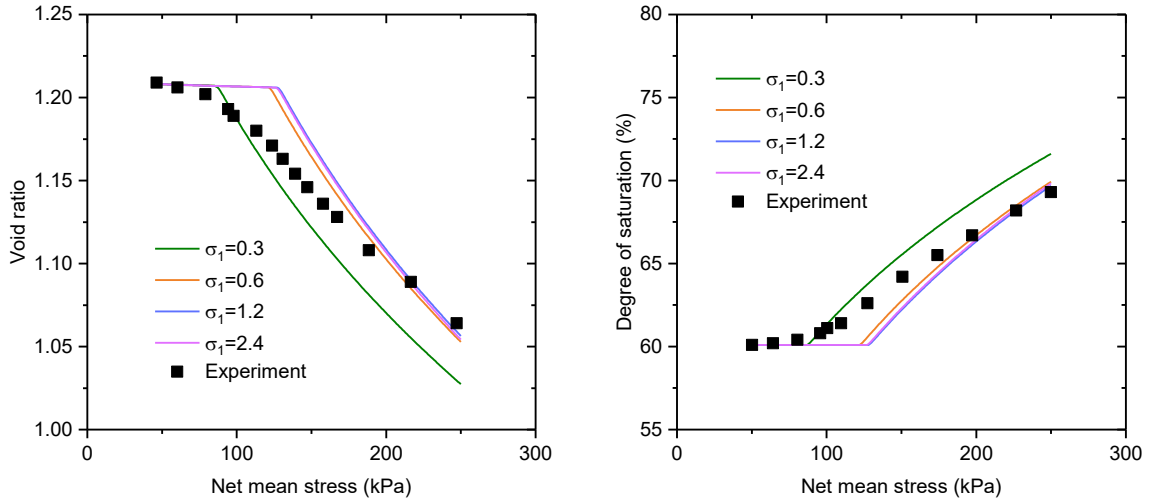

(b) (c)

Figure 7.6 Model sensitivity to σ_1: (a) Bishop's effective stress coefficient; (b) Void ratio; (c) Degree of saturation

7.3.3 Sensitivity analysis (μ_1)

The parameter μ_1 affects the peak density and the position of pore size at peak density for inter-aggregate PSDs. The PSDs under various values of μ_1 (-2, -1, -0.5 and -0.25) are presented in Figure 7.7. The other parameters remain the same as indicated in Table 7.2. It can be seen that the PSDs which have a higher μ_1 will have a lower peak density while its position moves to the right. The decrease of peak density is due to the compression of macropores. However, the evolution of PSDs become less significant with the increase of the parameter μ_1, especially when μ_1 is higher than -1. This is because χ is at a very low level (see Figure 7.8(a)) and the effective stress is not large enough to generate plastic deformation. Especially when μ_1 is -0.25, negative and unreasonable χ occurs (the contribution of suction to effective stress is 0

or positive (Wheeler et al. 2003)). According to Figure 7.8, the model shows great sensitivity to the parameter μ_1. Significant disparity between experimental results and simulated results can be seen when μ_1 varies from -2. A higher μ_1 will bring about a much lower χ, an obvious delay in yielding, and a less change in the void ratio and the degree of saturation.

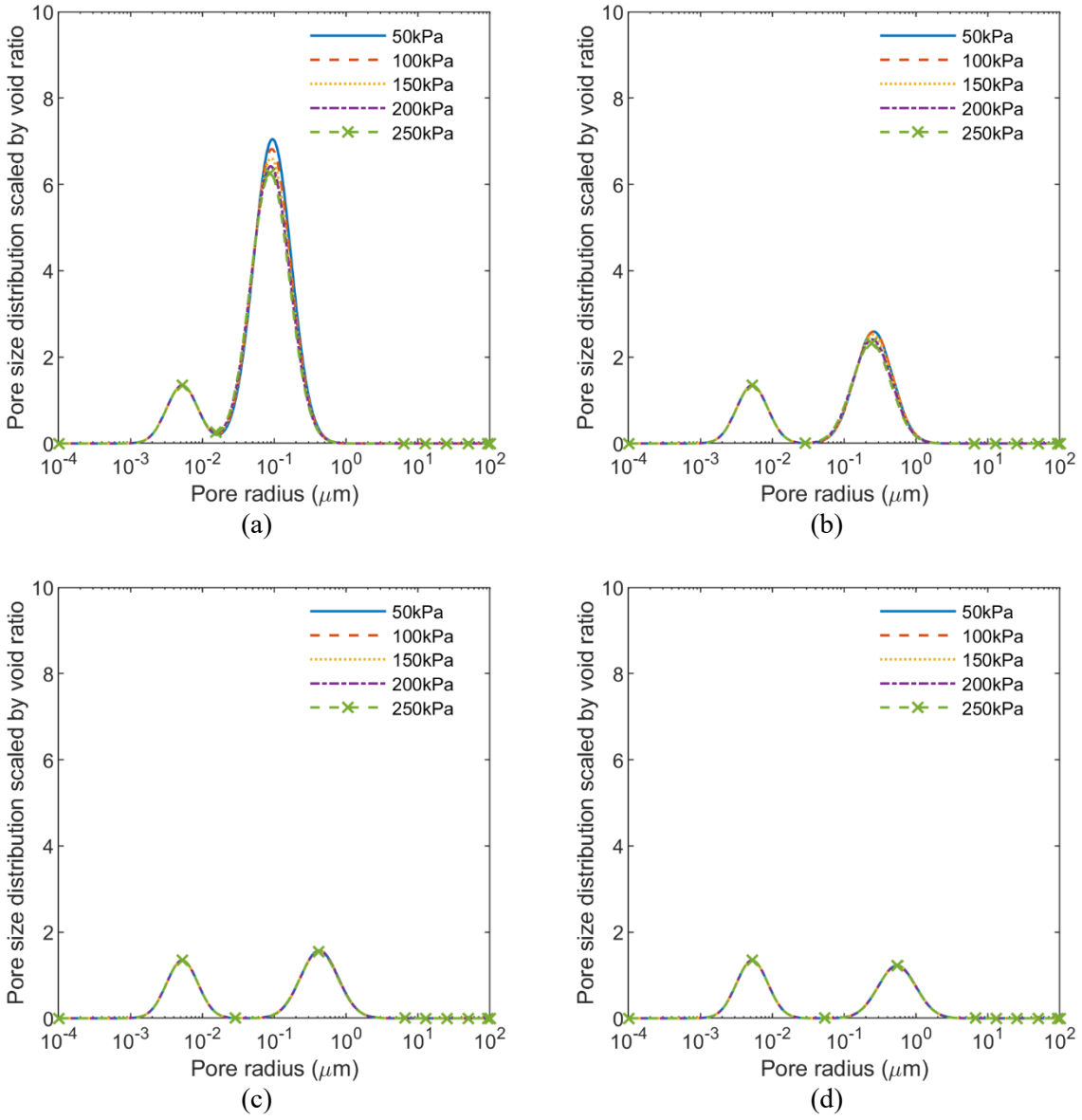

Figure 7.7 Evolution of pore size distributions under various μ_1: (a) μ_1=-2; (b) μ_1=-1; (c) μ_1=-0.5; (d) μ_1=-0.25

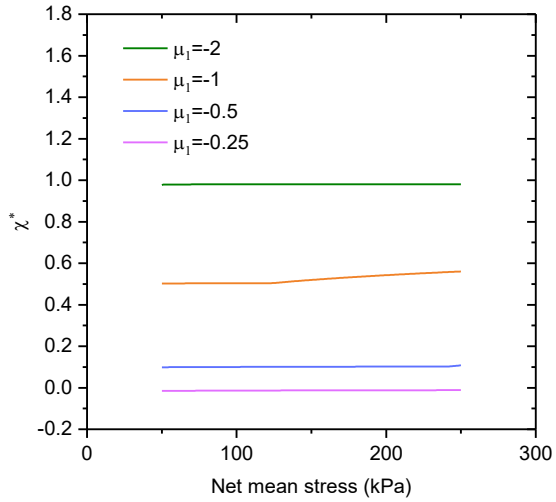

(a)

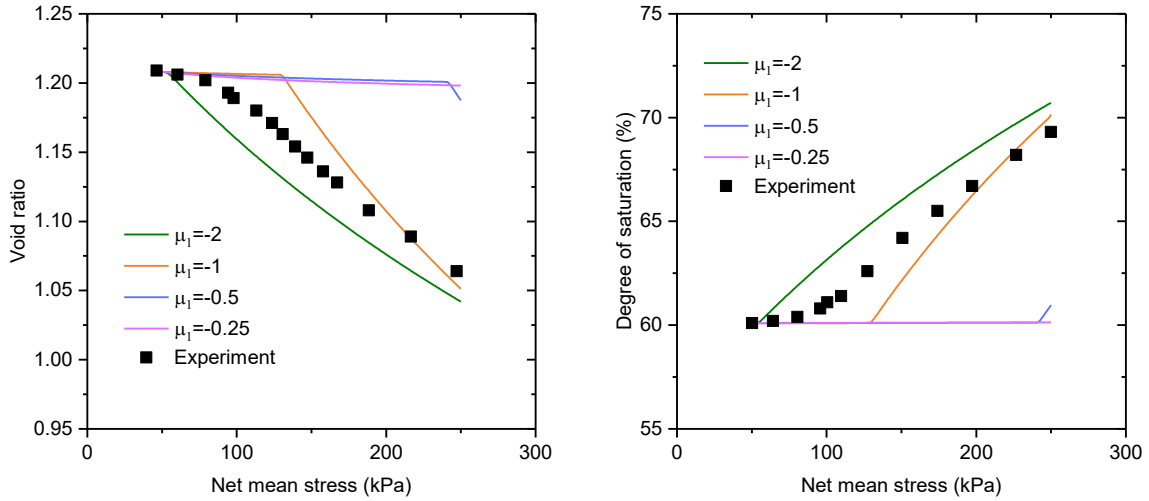

(b) (c)

Figure 7.8 Model sensitivity to μ_1: (a) Bishop's effective stress coefficient; (b) Void ratio; (c) Degree of saturation

7.3.4 Sensitivity analysis (K_2^1)

The parameter K_2^1 controls the evolution of the μ_1 with changes in void ratio. Since the void ratio always decreases during an isotropic loading path, the μ_1 will increase in this path when K_2^1 is negative but will decrease if K_2^1 is positive. In this sensitivity analysis, K_2^1 is selected as 0.15, 0.3, 0.6 and 1.2. As shown in Figure 7.9, it still can be observed that the peak density drops down but the difference at each K_2^1 among PSDs narrows with the increase of K_2^1. From Figure 7.10, the model, as expected, is also sensitive to the parameter K_2^1. With the increase of K_2^1, there is less volumetric change and less degree of saturation change due to the sharp decrease in χ.

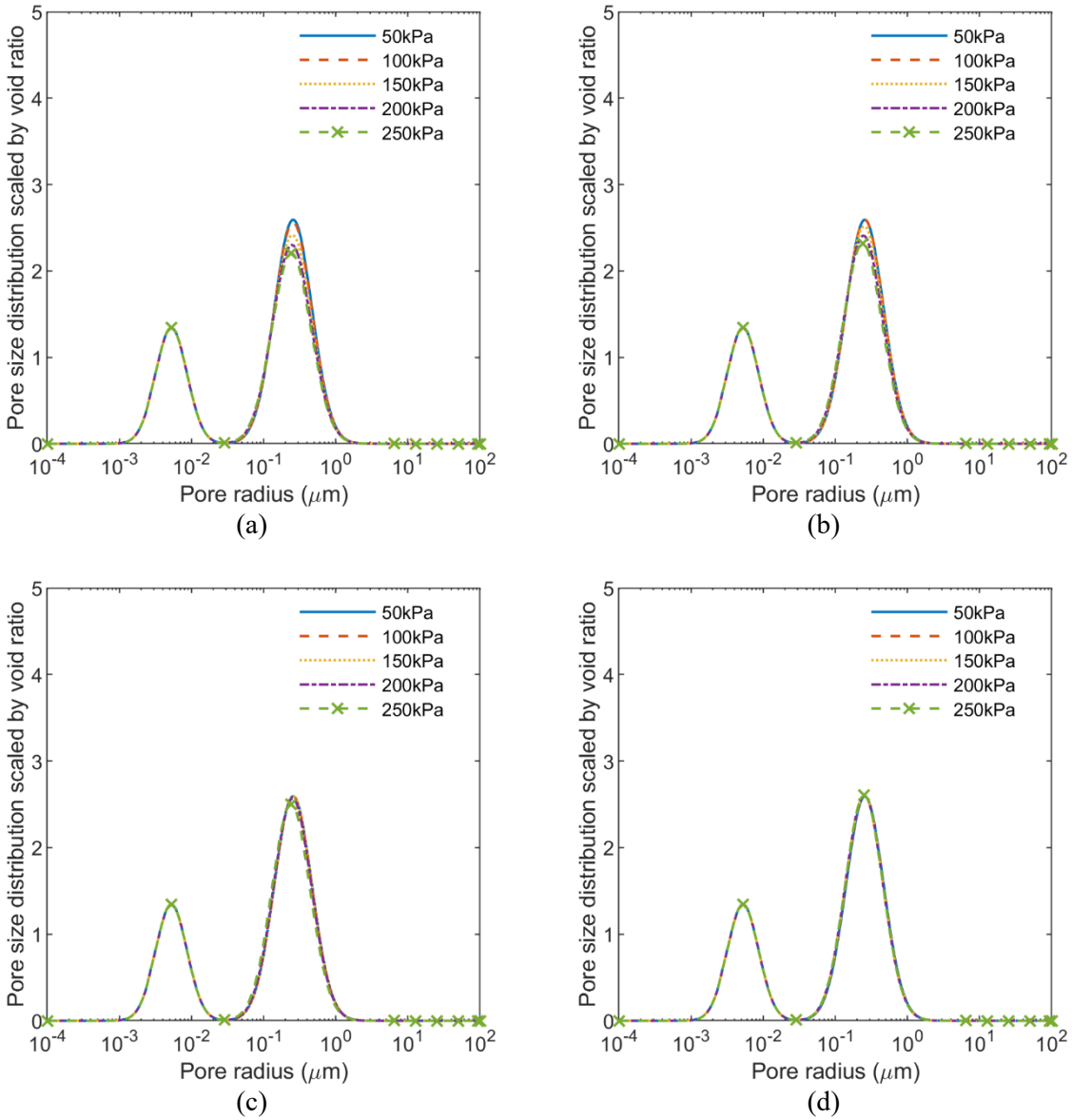

Figure 7.9 Evolution of pore size distributions under various K_2^1: (a) K_2^1=0.15; (b) K_2^1=0.3; (c) K_2^1=0.6; (d) K_2^1=1.2

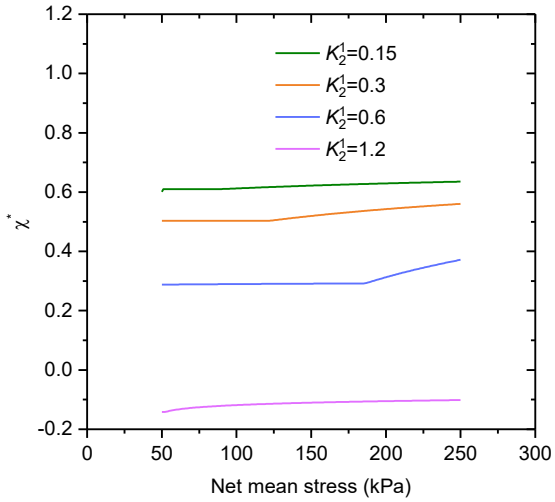

(a)

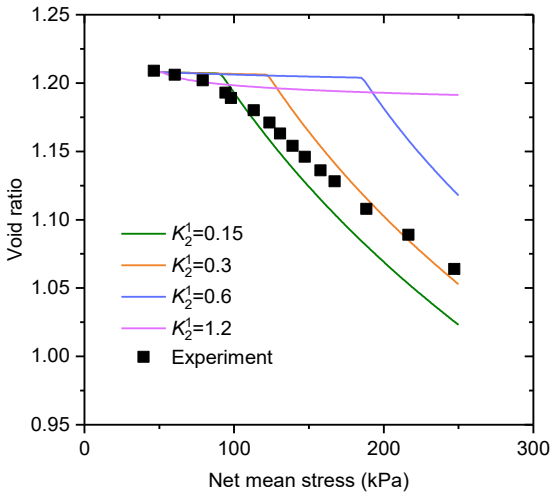

(b)

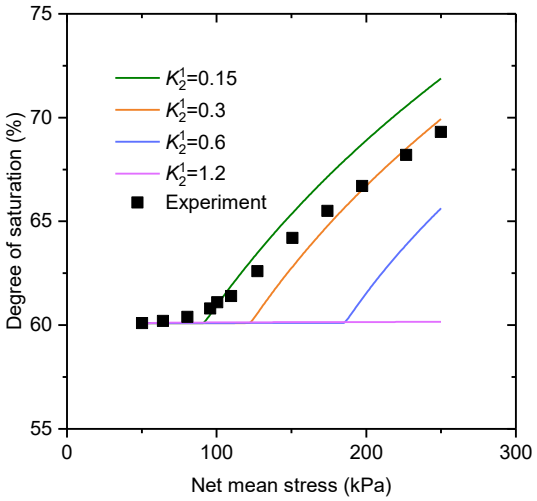

(c)

Figure 7.10 Model sensitivity to K_2^1: (a) Bishop's effective stress coefficient; (b) Void ratio; (c) Degree of saturation

7.3.5 Sensitivity analysis (K_3^1)

The parameter K_3^1 has an impact on the evolution of the standard deviation. A negative K_3^1 will lead to the increase of standard deviation during the loading while a positive K_3^1 will induce the decrease of the standard deviation. The movement of the PSDs under various K_3^1 (-0.24, -0.12, 0, 0.12) is similar to the movement previously stated (see Figure 7.11). As shown in Figure 7.12, the change of K_3^1 will moderately affect the simulated hydro-mechanical behaviour. At K_3^1 of -0.24, the effective stress coefficient χ is at the highest level and there is larger change in the void ratio and the degree of saturation compared with experimental result. With the increase of K_3^1, a smaller χ can be seen during isotropic loading, as a result of which the changes of void ratio and degree of saturation slow down. In general, the model shows some moderate sensitivity to K_3^1.

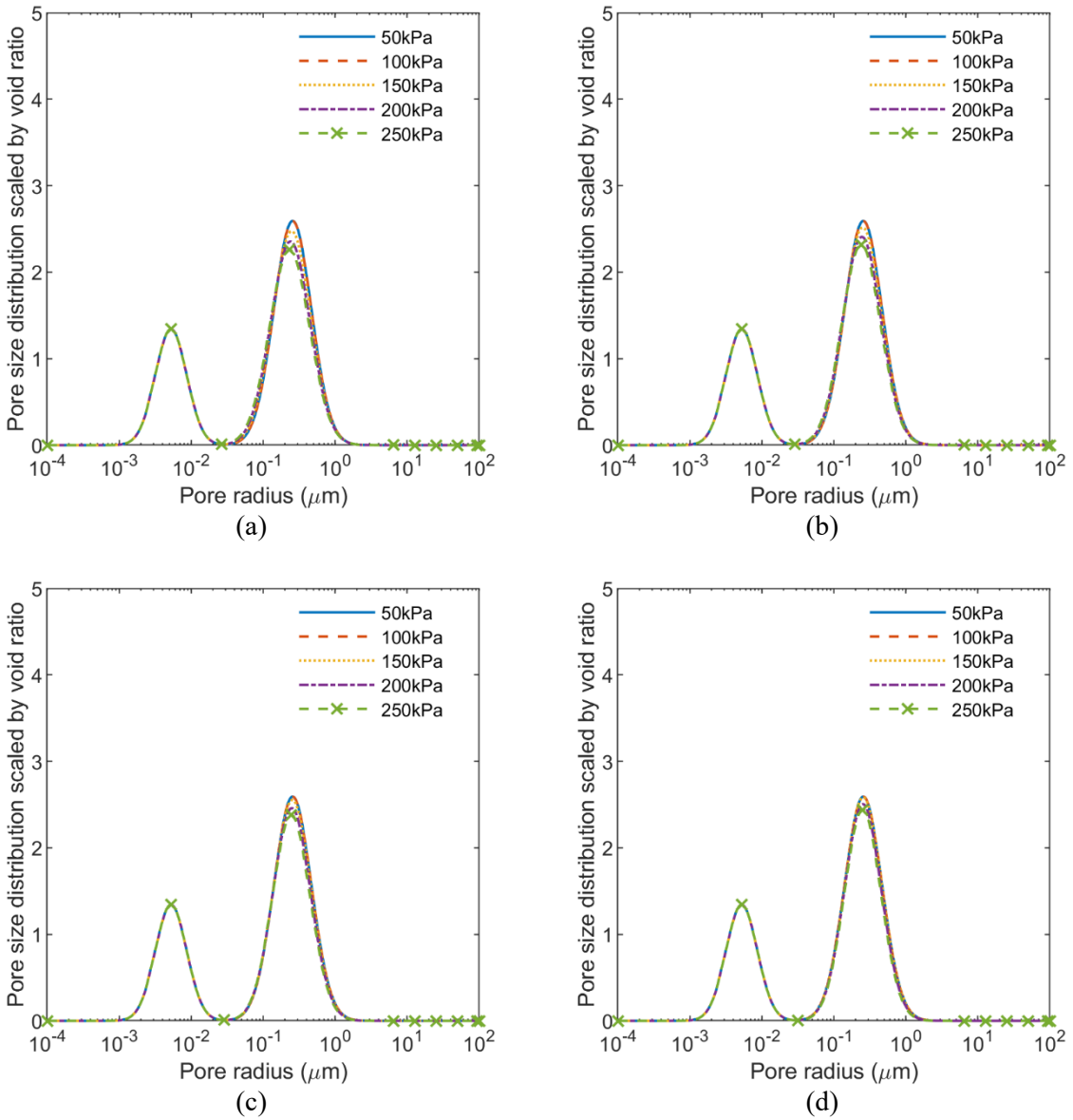

Figure 7.11 Evolution of pore size distributions under various K_3^1: (a) K_3^1=-0.24; (b) K_3^1=-0.12; (c) K_3^1=0; (d) K_3^1=0.12

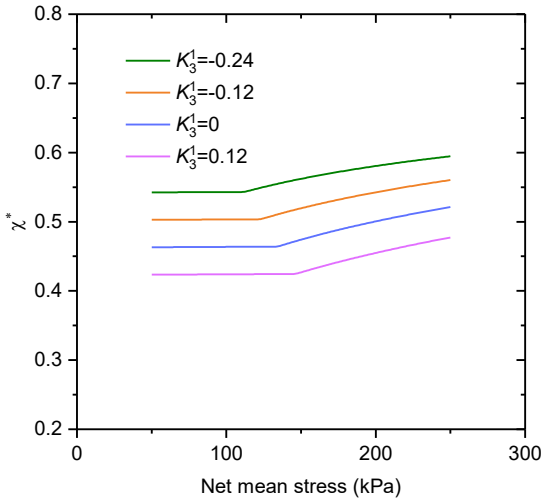

(a)

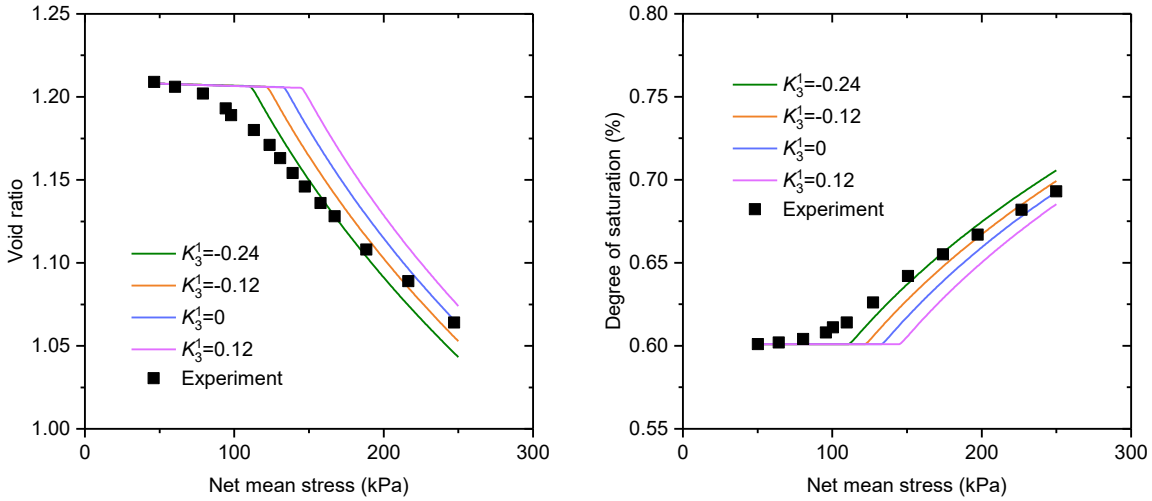

(b) (c)

Figure 7.12 Model sensitivity to K_3^1: (a) Bishop's effective stress coefficient; (b) Void ratio; (c) Degree of saturation

7.4 Concluding remarks

Model response and sensitivity analysis based on the published experiments on Speswhite kaolin (isotropic loading) and idealized assumptions on pore size distributions were undertaken to evaluate the performance of the direct microstructure model and the reliability of using PSDs obtained from MIP. According to the simulated results, the following conclusions can be drawn:

(1) According to the result from the model response, the model is able to reproduce the hydro-mechanical behaviour of unsaturated soils based on published hydro-mechanical parameters and assumed pore size distribution parameters of Speswhite kaolin. This also indicates the potential of this model to be applied to predicting the behaviour of other soils.

(2) According to the sensitivity analysis, the model is not sensitive to the volume proportion of the intra-aggregate pores (micropores) but is sensitive to the properties of the inter-aggregate pores (macropores) and the evolutional parameters. However, the degree of sensitivity to inter-aggregate pores properties is not excessively high as the difference between two adjacent curves is smaller than 10% in most cases. Under this circumstance, traditional methods for obtaining PSDs such as Mercury Intrusion Porosimetry (MIP) can be used to provide PSD-related parameters for this model.

This study is limited to the consideration of isotropic loading paths based on a combination of both experimentally obtained and assumed parameters (due to the lack of some detailed experimental evidence such as evolution of PSDs during loading). Despite this, model performance suggests that use of a PSD-dependent χ warrants further study. This future work should include MIP tests on triaxial samples that have experienced shearing load paths to different axial strains under controlled conditions, so as to allow fuller validation of the model.

CHAPTER 8

Model validation and application

8.1 Introduction

The validation and application of the proposed direct microstructural model is presented in this chapter. The model is validated by comparing the simulated microstructural-hydro-mechanical coupled behaviour to the experimental results presented in Chapter 4. The model is also applied to predict the evolution of SWCC under various loading conditions. The objectives of this chapter include: (1) evaluate the performance of the proposed model in reproducing the hydro-mechanical behaviour and PSD evolution of Dundee silt; (2) analyse the potential of the proposed in predicting the evolution of SWCC during loading. This chapter is organized as follows. The parameters and initial states for modelling are summarized in Section 8.2. The simulated loading paths are presented in Section 8.3. The comparison between modelling results and experiment results are analysed in Section 8.4. The application of the proposed model in SWCC is illustrated in Section 8.5.

8.2 Model parameters and initial states

Model parameters and initial states for modelling are obtained based on experimental results from Chapter 4 and are presented in this section.

8.2.1.1 Parameters for hydro-mechanical behaviour

In the model, there are 9 parameters required for modelling hydro-mechanical behaviour. λ and κ are the slope of normal consolidation line and the slope of rebound curve under saturated condition respectively and are obtained from the saturated isotropic loading and reloading tests. Parameters M and μ are the slope of critical state line and Poisson's ratio respectively. Parameters k_1 and k_2 describes the coupled movement of yielding surfaces during loading and can be acquired by experimental results of shearing when the stress path is yielding on two yield surfaces (as shown in Figure 8.1). G_s is the specific gravity. Parameters λ_s and κ_s are the slope of the main curve and the slope of the scanning curve when the SWCC is simplified and represented by three straight lines. In this study, the SWCCs of Dundee silt are obtained from the pore size distribution of Specimen M2 based on the relationship between PSD and SWCC (Simms and Yanful 2004b; Li and Vanapalli 2021), as shown in Figure 8.2. The parameters are presented in Table 8.1.

Table 8.1 Hydro-mechanical parameters of Dundee silt in modelling

Hydro-mechanical parameters	Value	Methods for parameter determination
λ	0.016	From the normal consolidation line in Section 4.3.6.1
κ	0.006	From the rebound curve in Section 4.3.6.1
λ_s	0.013	From Figure 8.2
κ_s	0.0013	From Figure 8.2
k_1	0.870	Determined based on simulating the saturated shearing of Specimen C (see Figure 8.1)
k_2	0.920	Determined with k_1
M	1.38	From the critical state line in Section 4.3.6.3
μ	0.3	This value is commonly adopted by other researchers (Kokusho 2000; Lloret-Cabot et al. 2013; Kumar Thota et al. 2021)
G_s	2.61	From pycnometer method (BS 1377-2 1990) in Section 3.2.2.2

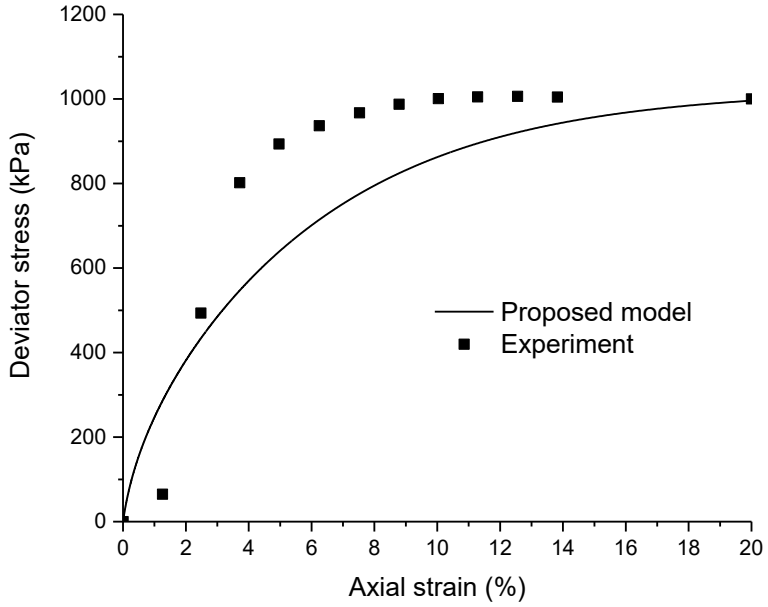

Figure 8.1 Reproducing stress-strain behaviour of Specimen C based on $k_1 = 0.870$ and $k_2 = 0.920$

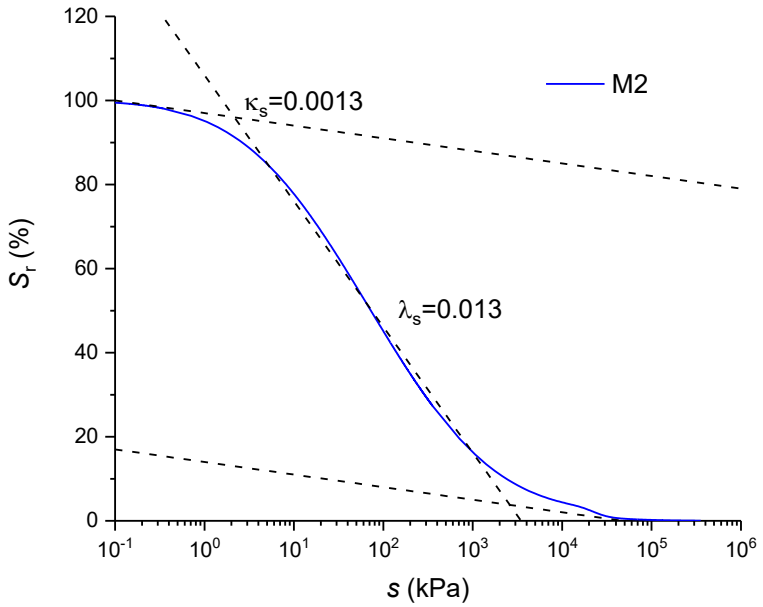

Figure 8.2 SWCC obtained from the PSD of Specimen M2

8.2.1.2 Parameters for PSDs

The differential PSD scaled by void ratio is defined as below:

$$f(D)=\frac{\mathrm{d}V}{V_s\mathrm{d}D} \tag{8-1}$$

where V is the total pore volume, V_s is the total solid volume and D is the pore diameter. Differential pore size distributions scaled by void ratio come from MIP tests and need to be fitted by Log-normal distribution (see Section 6.2.3) before being used in modelling. Since MIP results cannot fully represent soil microstructure and the intruded void ratio obtained by MIP can be different from the void ratio obtained by triaxial tests (discussed in Section 4.3.5), to ensure the consistency between modelling and experiment, the void ratio calculated by fitted PSDs must be the same as the void ratio obtained from triaxial tests (as described in Chapter 4). Therefore, the fitting parameters must meet the following requirement due to the feature of Log-normal Distribution:

$$\int_0^{+\infty} f(D)dD = a_1 + a_2 = e \tag{8-2}$$

Examples of fitting and fitting results are presented in Figure 8.3 and Table 8.2, respectively.

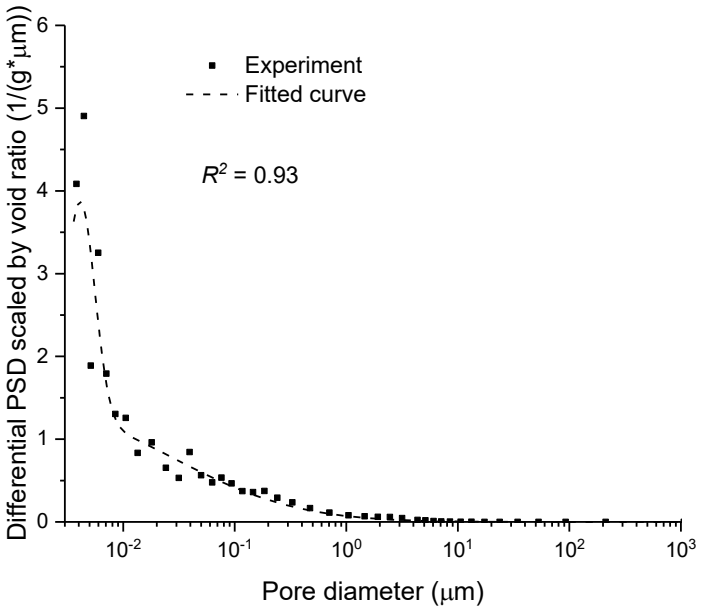

(a) Saturated Specimen M2

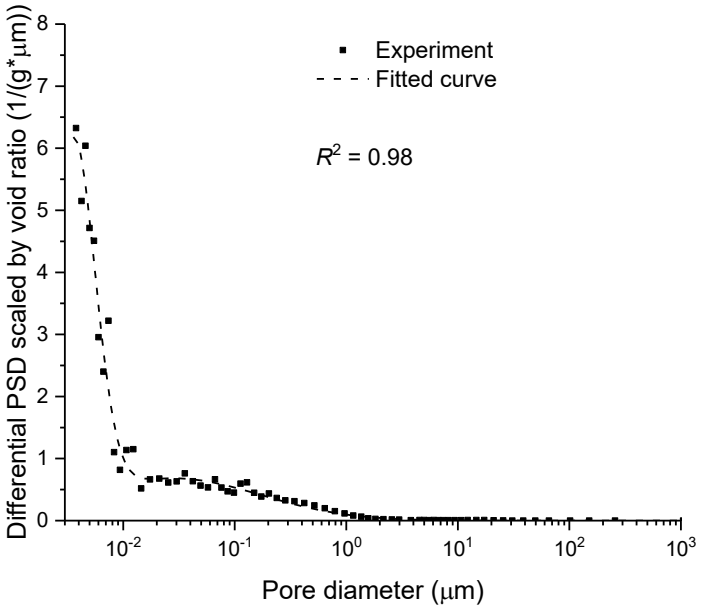

(b) Unsaturated Specimen M7

Figure 8.3 Examples of Pore size distributions scaled by void ratio and their fitted curves

Table 8.2 Fitting parameters of PSD

Specimen No.	a_1	a_2	μ_1	μ_2	σ_1	σ_2
M2 (20%)	0.467	0.009	0.414	-5.400	2.560	0.299
M3 (10%)	0.529	0.004	0.949	-5.383	3.118	0.157
M5 (5%)	0.517	0.005	0.940	-5.448	2.808	0.246
M6 (20%)	0.432	0.004	0.361	-5.317	2.301	0.031
M13 (10%)	0.459	0.017	0.182	-5.253	2.182	0.166
M14 (5%)	0.481	0.011	0.156	-5.405	1.979	0.309
M15 (20%)	0.511	0.037	-10.654	-6.821	3.651	0.057
M18 (10%)	0.511	0.050	-0.05	-5.570	1.640	0.949
M19 (5%)	0.463	0.115	0.289	-8.494	1.958	4.985
M7 (10%)	0.451	0.026	-0.279	-5.431	1.817	0.451
M12 (5%)	0.501	0.010	0.388	-5.340	2.113	0.267
M20 (10%)	0.470	0.023	-0.081	-5.562	2.140	0.462
M21 (15%)	0.478	0.012	0.196	-5.884	2.064	0.561

8.2.1.3 Parameters for PSDs evolution

The evolution of PSD is assumed to a function of the change of void ratio for a specific loading path (Li and Zhang 2009). This assumption was adopted because the evolution of PSD and the change of void ratio are strongly correlated. No matter what stress path the soil is undergoing, the change in PSD represents the increase and decrease of pore volumes at different pore diameter, which can be reflected from the change of void ratio. When there is a change of void ratio, the change in total pore volume will also be captured by the change of PSD such as the decrease of larger pores during compaction. Therefore, there is tight connection between the changes of PSD and void ratio, and so the evolution of PSD can be assumed to be related to the change of void ratio in modelling. Here the evolution parameters of the PSD for modelling of both the saturated and unsaturated tests are established based on the 200 kPa confining stress triaxial test. The relationship between void ratio and PSD parameters is presented in Figure 8.4, with the values of the parameters given in Table 8.3.

Table 8.3 Evolution parameters for saturated and unsaturated tests

Confining stresses	Suctions	K_1^1	K_2^1	K_3^1	K_1^2	K_2^2	K_3^2
100/200/400 kPa	0 kPa	1.086	9.908	8.253	-0.086	-0.133	-2.030
200 kPa	25/100 kPa						

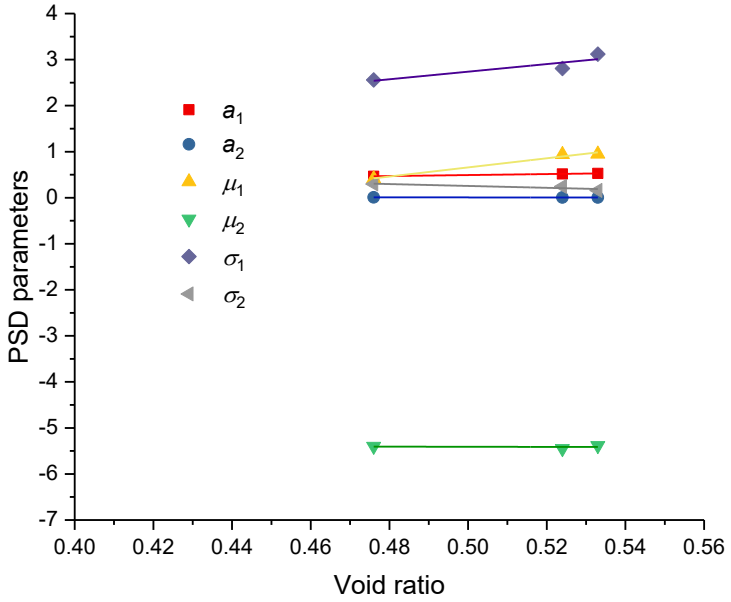

Figure 8.4 The relationship between void ratio and PSD parameters for saturated shearing under 200 kPa confining stress and fitting results

8.2.1.4 Initial states for modelling

Initial states including the parameters for the initial PSD at 0% axial strain are presented in Table 8.4 and Table 8.5 for saturated and unsaturated tests respectively. For saturated tests, the initial PSDs at 0% axial strain were estimated based on the initial void ratio, evolution parameters and the PSD of the saturated specimen M2. For unsaturated tests, the initial PSDs were based on the PSD of the unsaturated specimen M21, as unsaturated samples usually have a different shape (bimodal) while saturated ones have a unimodal shape even if they are at the same void ratio. The different values of a_1, a_2, μ_1, μ_2, σ_1 and σ_2 reflect the different initial void ratio at the start of the modelled shearing stage.

Table 8.4 Initial states for saturated tests

Initial states	Value	Initial states	Value	Initial states	Value
p_{net}/kPa	100	p_{net}/kPa	200	p_{net}/kPa	400
s/kPa	0	s/kPa	0	s/kPa	0
e	0.587	e	0.549	e	0.526
S_r/%	100.0	S_r/%	100.0	S_r/%	100.0
p_0^*/kPa	100	p_0^*/kPa	200	p_0^*/kPa	400
a_1	0.587	a_1	0.546	a_1	0.521
μ_1	1.514	μ_1	1.137	μ_1	0.909
σ_1	3.476	σ_1	3.162	σ_1	2.972
a_2	0.000	a_2	0.003	a_2	0.005
μ_2	-5.415	μ_2	-5.410	μ_2	-5.407
σ_2	0.074	σ_2	0.151	σ_2	0.198

Table 8.5 Initial states for unsaturated tests

Initial states	Value	Initial states	Value
p_{net}/kPa	200	p_{net}/kPa	200
s/kPa	25	s/kPa	100
e	0.531	e	0.533
S_r/%	74.54	S_r/%	72.70
p_0^*/kPa	200	p_0^*/kPa	200
a_1	0.523	a_1	0.525
μ_1	0.602	μ_1	0.622
σ_1	2.402	σ_1	2.419
a_2	0.008	a_2	0.008
μ_2	-5.889	μ_2	-5.890
σ_2	0.478	σ_2	0.474

8.3 Stress path for modelling

Three stress paths are considered for saturated tests with shearing under constant confining stresses of 100, 200 and 400 kPa. For unsaturated tests, two stress paths are considered with shearing under constant net confining stress of 200 kPa at two different suctions (25 kPa and 100 kPa).

8.4 Model validation

In the following sections, the proposed model is validated by comparing the modelling results with experimental results including saturated triaxial tests (confining stresses: 100, 200 and 400 kPa, respectively) and unsaturated triaxial tests (suctions: 25 and 100 kPa, respectively).

8.4.1.1 Saturated triaxial tests

8.4.1.1.1 Shearing at constant confining stress of 100 kPa

A saturated shearing path under a constant confining stress of 100 kPa from 0% to 20% axial strain for Specimen M15, M18 and M19 was modelled and compared with experimental results. As can be seen in Figure 8.5(a), the proposed model has a good performance in reproducing the changing tendency of deviatoric stress with axial strain despite that the model did not capture the peak of deviatoric stress and also overestimated the volumetric strain as indicated by the experimental results (see Figure 8.5(b) and (c)). As expected, the Bishop's effective stress coefficient remains 1 during shearing due to the saturated condition.

Figure 8.6 presents the comparison in PSDs among the modelling results, fitted curves and experimental results at 5%, 10% and 20% axial strain. The fitted curves are the ones presented in Table 8.2. At 5% axial strain, both the modelling result and the fitted curve align with the experimental result despite small difference for pores smaller than 0.01 μm in diameter. At 10% axial strain, the modelling result is consistent with the experimental result in the pore size range from 0.02 to 1000 μm but is less better than the fitted curve in the pore size range smaller than 0.02 μm. At 20% axial stain, the modelling result is better than the fitted curve in the pore size range from 0.02 to 1 μm despite a slight difference with the experimental result and fitted curve for pore size smaller than 0.02 μm.

Generally, it can be concluded that the proposed model satisfactorily predicted the evolution of pore size distribution at each axial strain despite small differences for smaller pores. For saturated triaxial tests, since the suction is always zero and Bishop's parameter is invariably 1. The effective stress is always equal to the net mean stress no matter it is a direct microstructure model or an indirect microstructure model. Therefore, the predicted stress-strain behaviour will be the same for both models. That is also the merit of the direct microstructure model because it can not only present the stress-strain behaviour as reliable as a normal model but also can give the evolution of PSD.

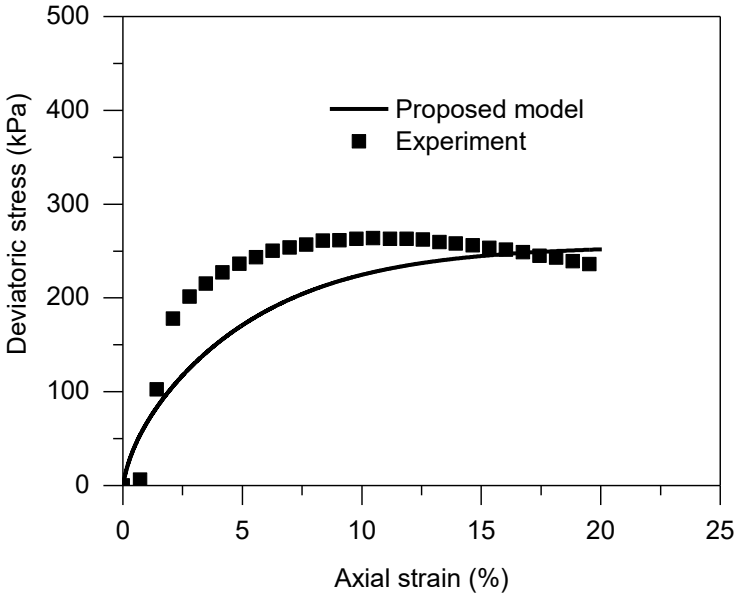

(a) Axial strain – Deviatoric stress

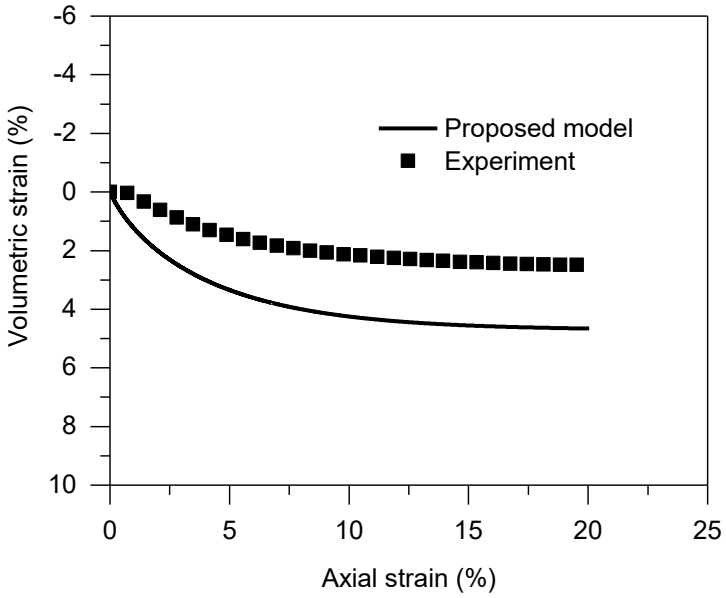

(b) Axial strain – Volumetric strain

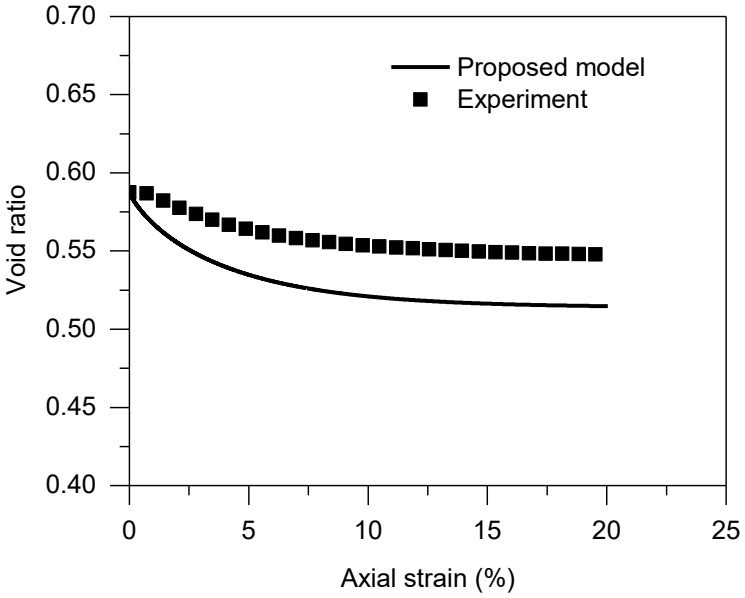

(c) Axial strain – Void ratio

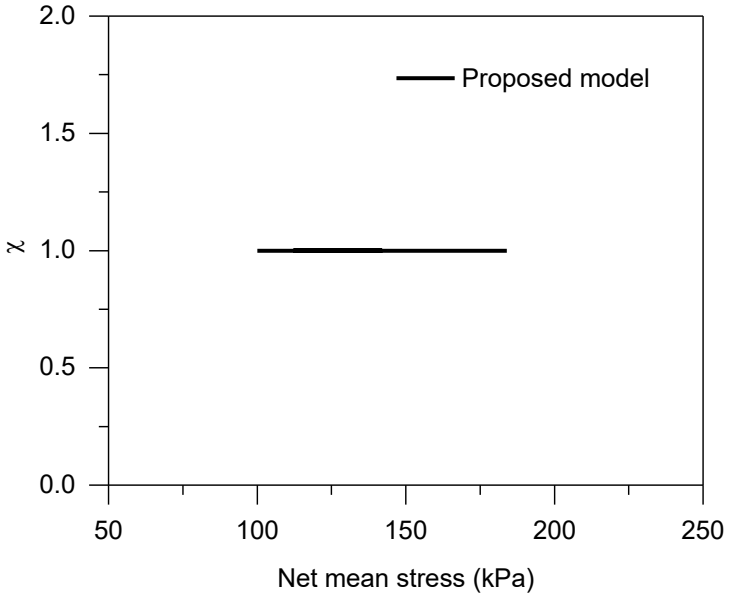

(d) Net mean stress – χ

Figure 8.5 Comparison in stress-strain behaviour between experimental and modelling results of saturated shearing under a constant confining stress of 100 kPa

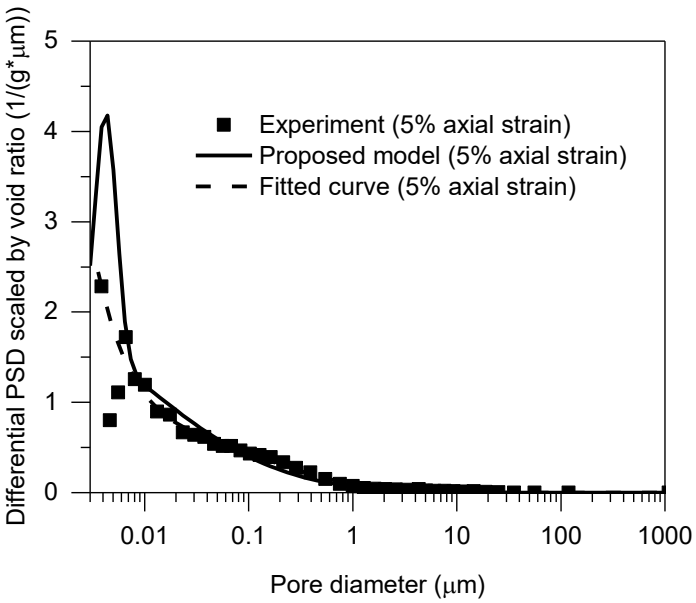

(a) PSDs at 5% axial strain

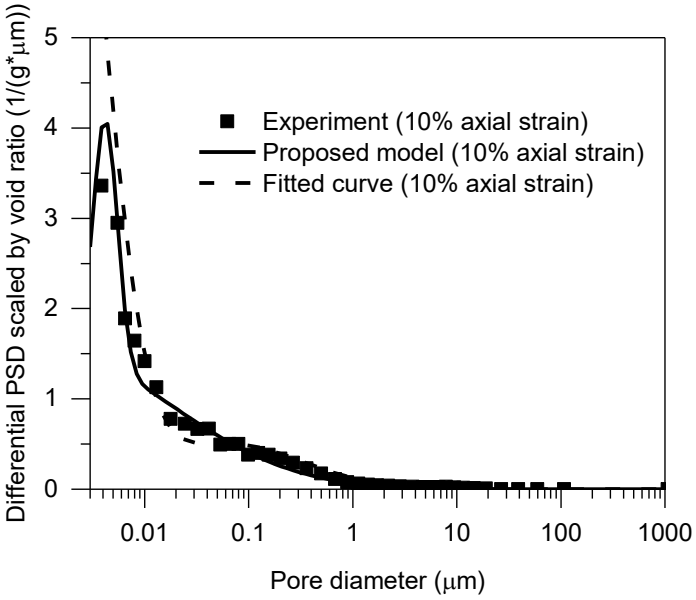

(b) PSDs at 10% axial strain

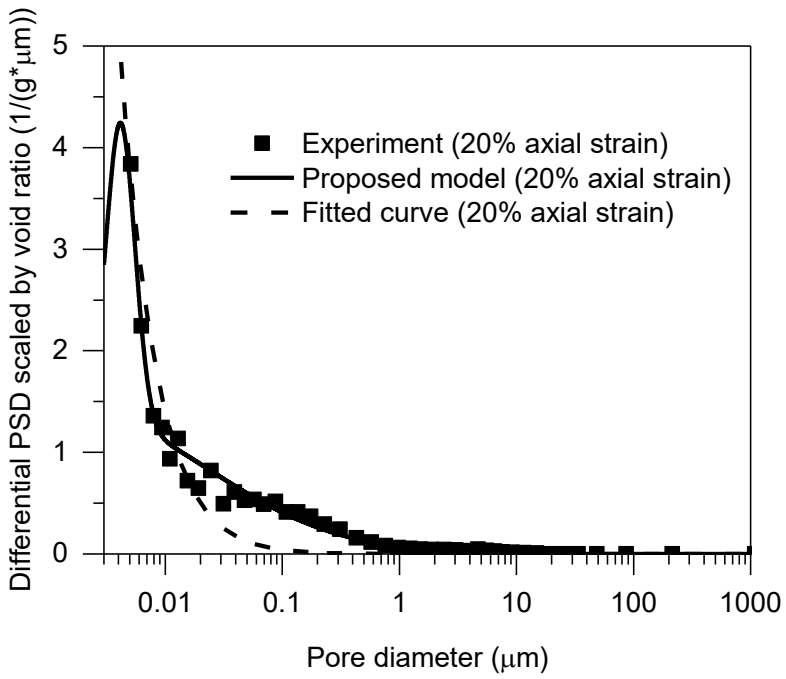

(c) PSDs at 20% axial strain

Figure 8.6 Comparison in PSDs and their evolution between experimental and modelling results of saturated shearing under a constant confining stress of 100 kPa

8.4.1.1.2 Shearing at constant confining stress of 200 kPa

A saturated shearing path was modelled under a constant confining stress of 200 kPa and compared to the experimental results of Specimen M2, M3 and M5. As shown in Figure 8.7, the proposed model has a very satisfactory performance in reproducing the stress-strain behaviour during the saturated shearing despise nuanced differences between experimental and modelling results. As expected, the χ predicted by this model is invariably 1 during shearing (see Figure 8.7(d)), which is consistent to the results of other models where degree of saturation is adopted as χ (Wheeler et al. 2003; Laloui and Nuth 2009; Lloret-Cabot et al. 2013). The model also succeeds in predicting the pore size distribution at each axial strain, as shown in Figure 8.8. There is little difference among the modelling results, fitted curve (presented in Table 8.2) and experimental results. This is not only because of the model's well-established consideration of microstructure, but also because the pore size distribution changes very little during shearing when it is scaled by void ratio.

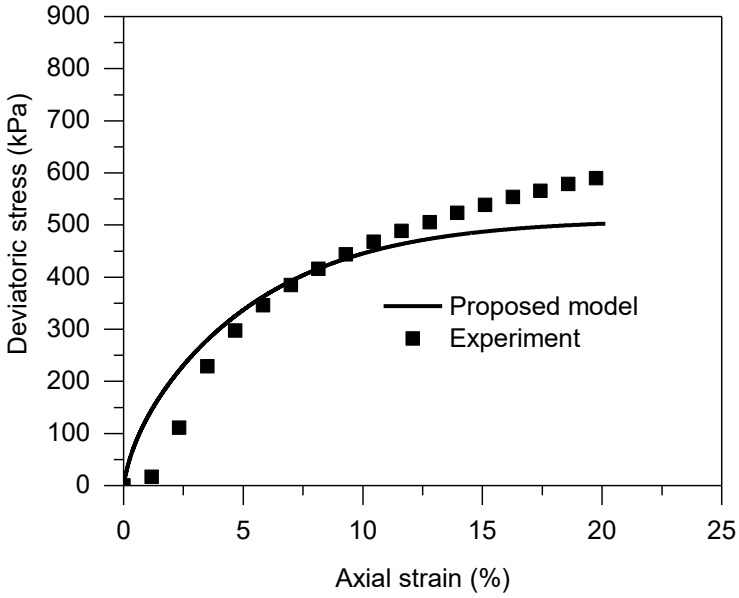

(a) Axial strain – Deviatoric stress

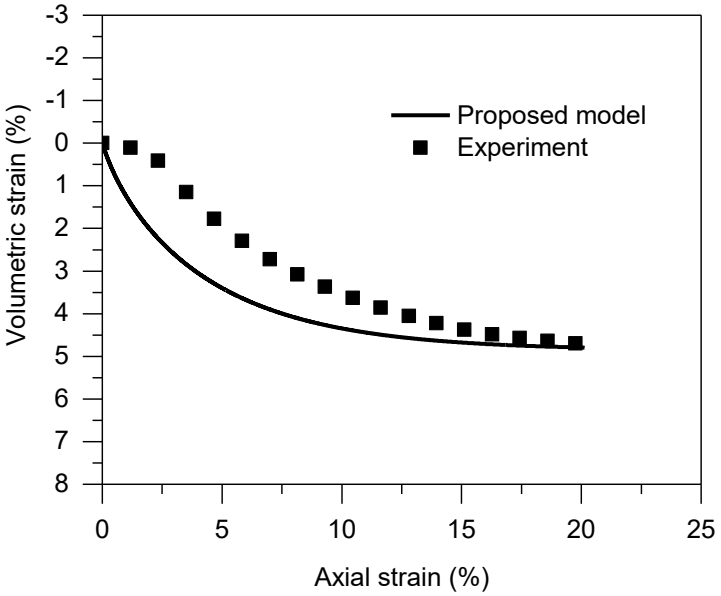

(b) Axial strain – Volumetric strain

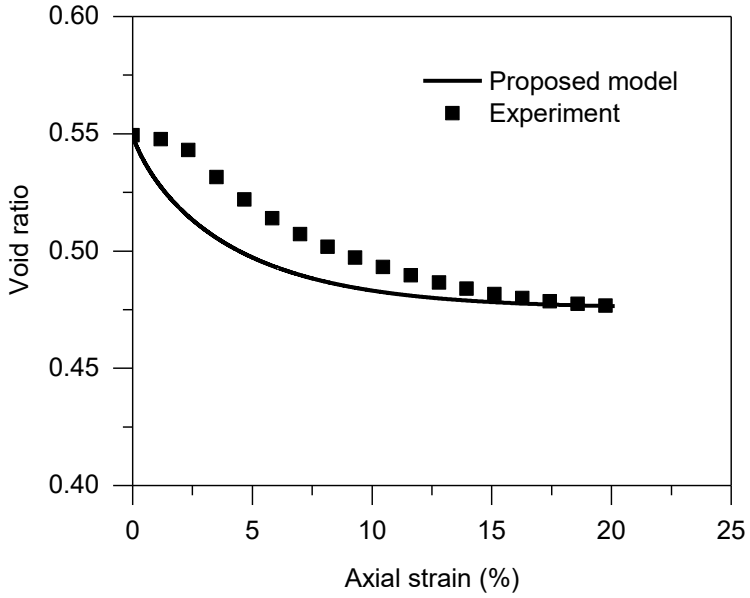

(c) Axial strain – Void ratio

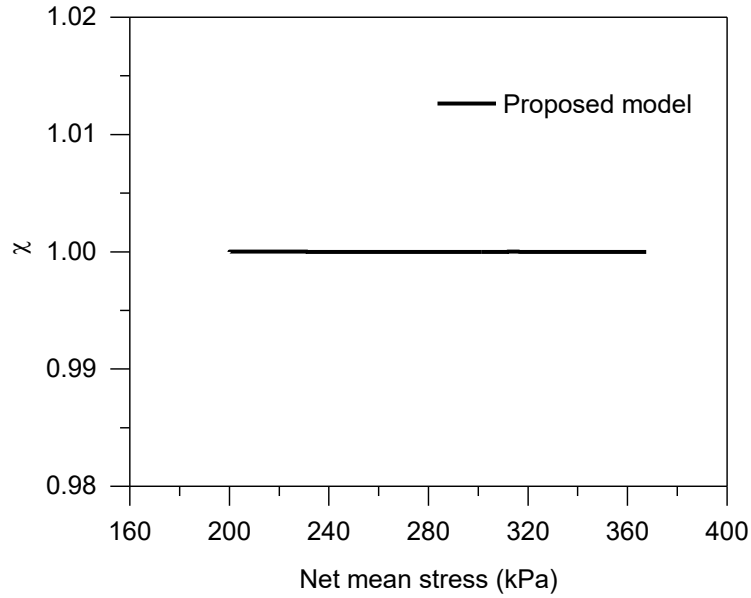

(d) Net mean stress – χ

Figure 8.7 Comparison in stress-strain behaviour between experimental and modelling results of saturated shearing under a constant confining stress of 200 kPa

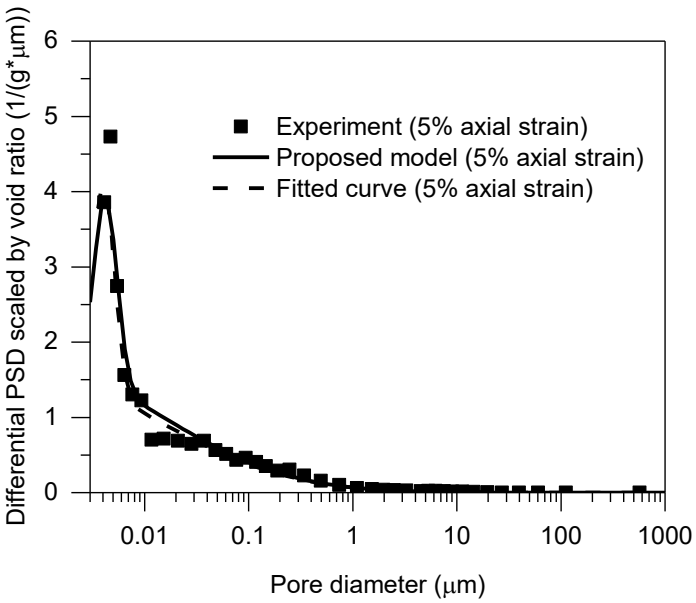

(a) PSDs at 5% axial strain

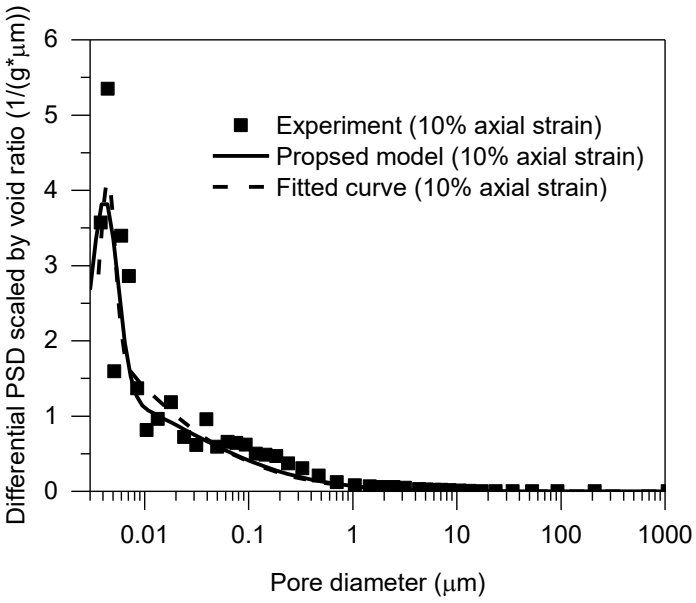

(b) PSDs at 10% axial strain

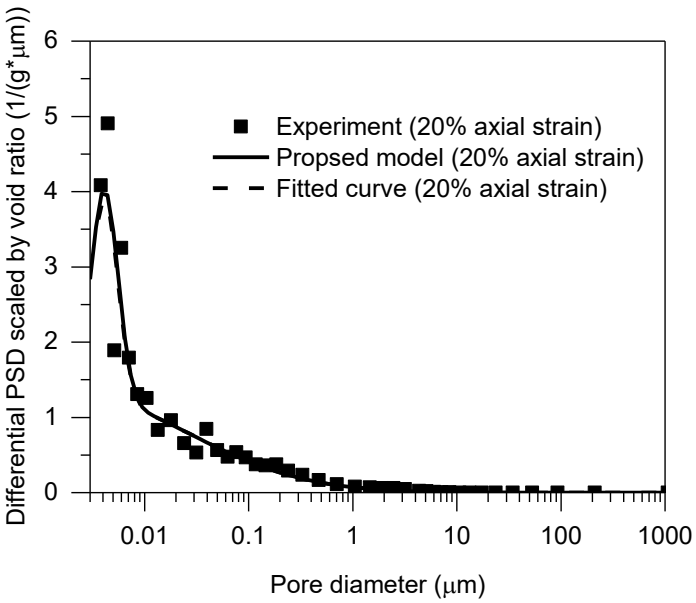

(c) PSDs at 20% axial strain

Figure 8.8 Comparison in PSDs and their evolution between experimental and modelling results of saturated shearing under a constant confining stress of 200 kPa

8.4.1.1.3 Shearing at constant confining stress of 400 kPa

Figure 8.9 presents the comparison in stress-strain behaviour between experimental and modelling results of saturated shearing under a constant confining stress of 400 kPa (Specimen M6, M13 and M14) and Figure 8.10 presents the comparison in PSDs and their evolution between experimental and modelling results. Under 400 kPa confining stress, the proposed model still has satisfactory performance in reproducing the hydro-mechanical behaviour of Dundee silt and the evolution of PSDs despite the difference for pores smaller than 0.01 μm.

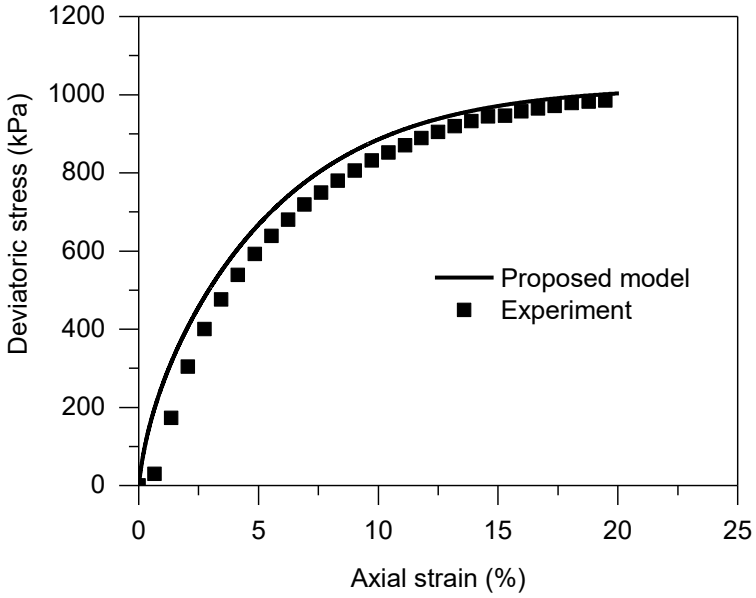

(a) Axial strain – Deviatoric stress

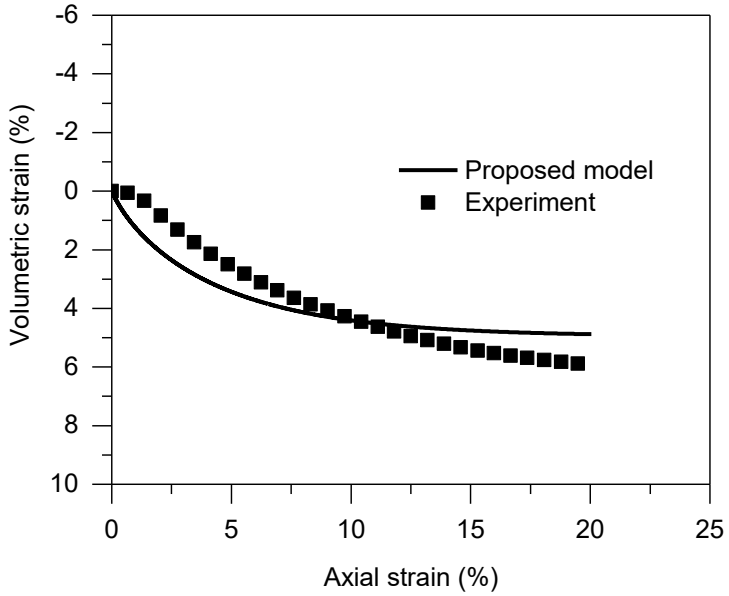

(b) Axial strain – Volumetric strain

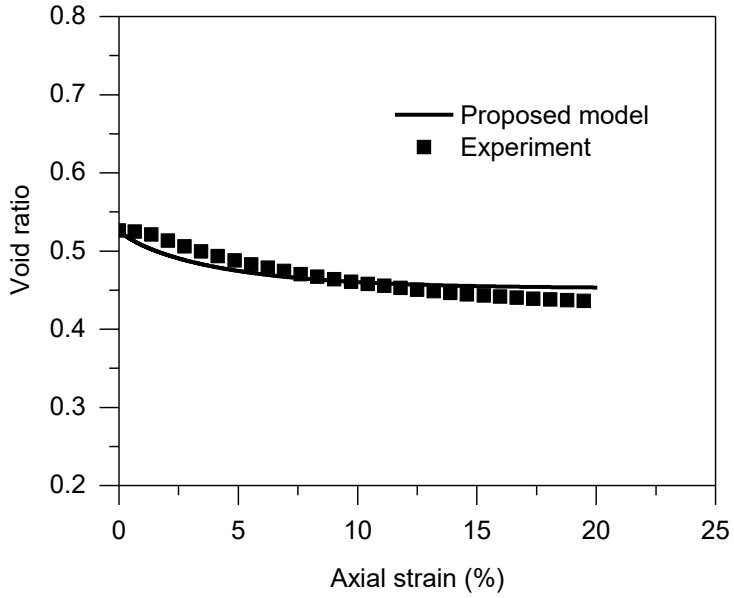

(c) Axial strain – Void ratio

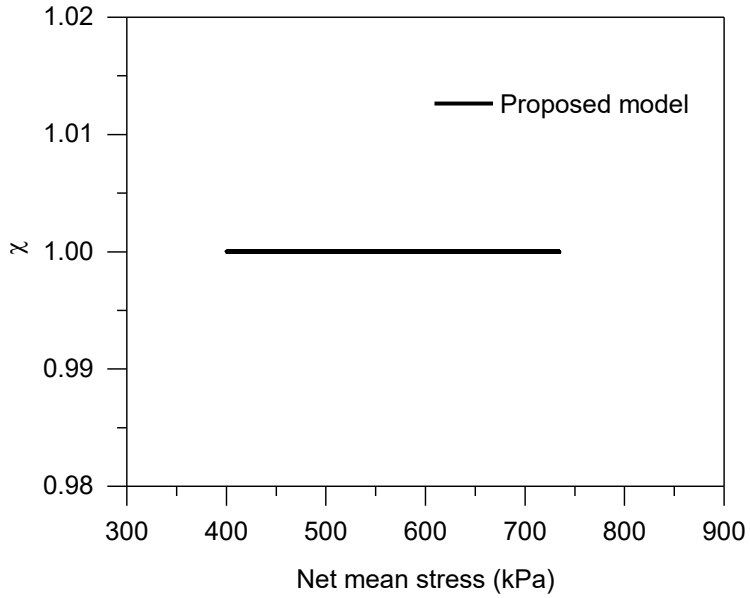

(d) Net mean stress – χ

Figure 8.9 Comparison in stress-strain behaviour between experimental and modelling results of saturated shearing under a constant confining stress of 400 kPa

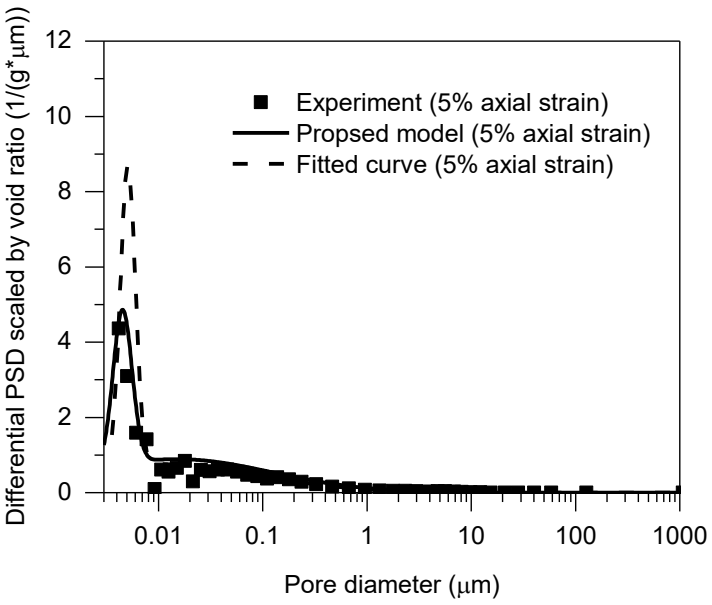

(a) PSDs at 5% axial strain

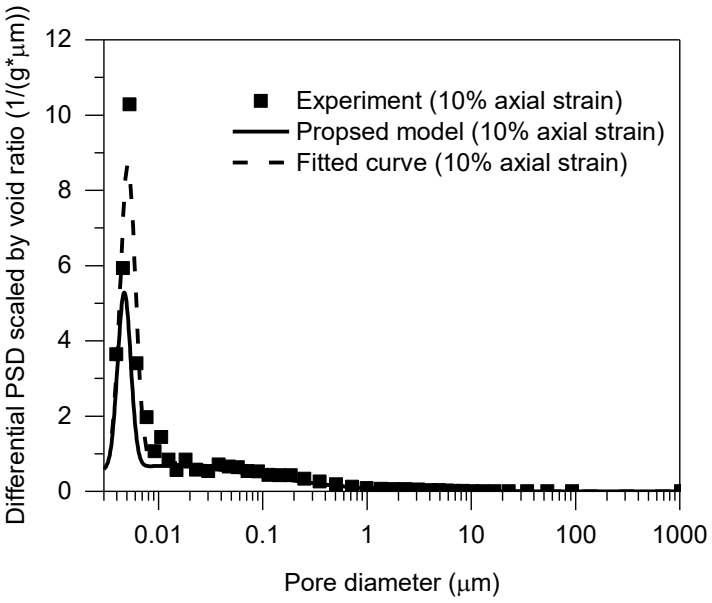

(b) PSDs at 10% axial strain

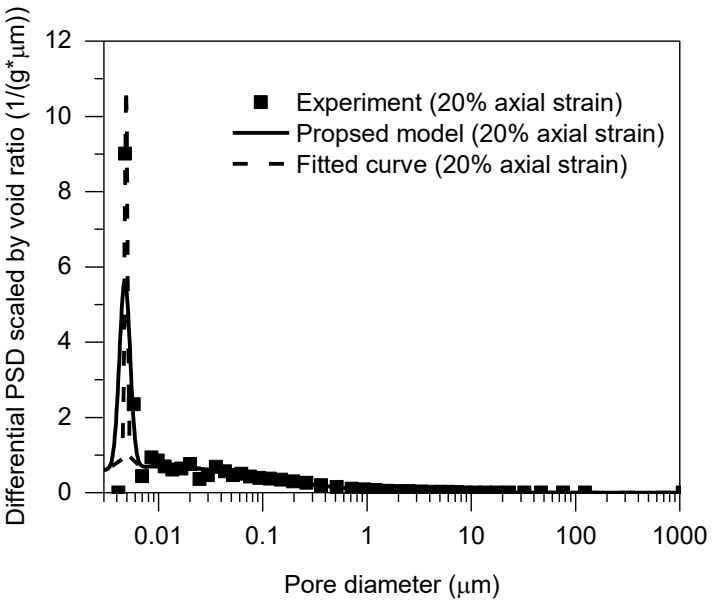

(c) PSDs at 20% axial strain

Figure 8.10 Comparison in PSDs and their evolution between experimental and modelling results of saturated shearing under a constant confining stress of 400 kPa

8.4.1.2 Unsaturated triaxial tests

The model validation for unsaturated triaxial tests under two different suctions (25 and 100 kPa) is presented in the sections below.

8.4.1.2.1 25 kPa suction

Figure 8.11 presents the model validation for the unsaturated triaxial tests conducted at a constant net mean stress of 200 kPa and at a constant suction of 25 kPa to 15% axial strain. As shown in Figure 8.11(a), the proposed model has a satisfactory performance in predicting the change of deviatoric stress with increasing axial strain. The proposed model overestimates the volumetric strain which leads to a lower void ratio compared with the experimental result (see Figure 8.11(b) and (c)). This can be attributed to the volumetric strain-related parameter λ. This parameter was selected only for saturated condition and ignored its change under unsaturated conditions. In terms of degree of saturation, the proposed model still performs well compared to the experimental result, as shown in Figure 8.11(d). According to the modelling result, based on the chosen evolutional parameters for PSD, the Bishop's effective stress coefficient χ remains 0 during the early stage of this shearing and then starts to increase to a value of 0.15 (see Figure 8.11(e)).

Figure 8.12 presents the comparison in PSDs between the modelling results and experimental results. In general, the proposed model succeeds in predicting the evolution of PSD during shearing despite small difference for very small pores.

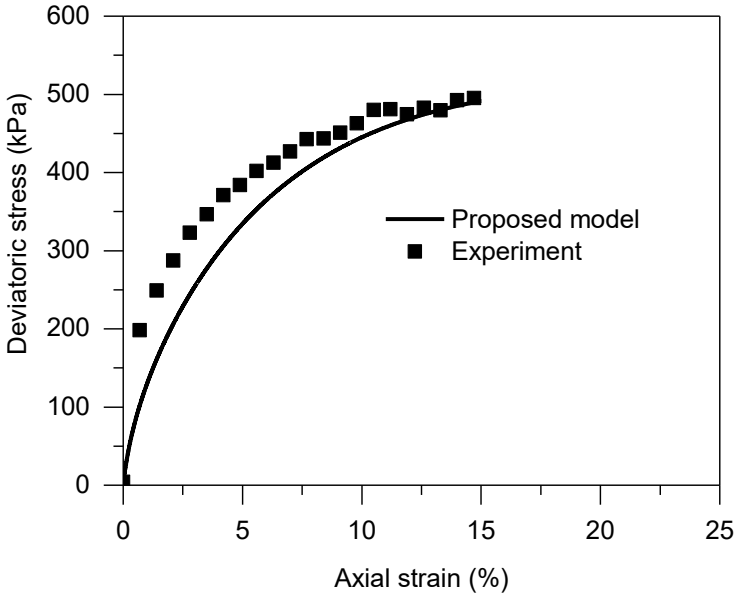

(a) Axial strain – Deviatoric stress

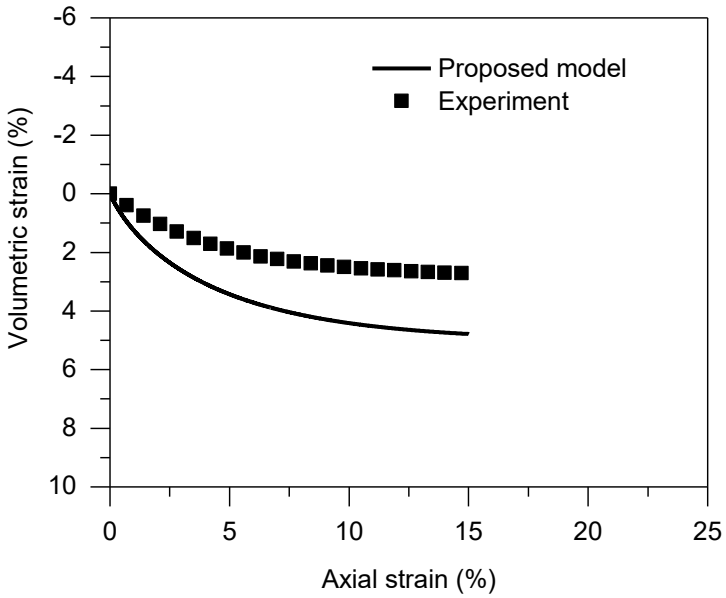

(b) Axial strain – Volumetric strain

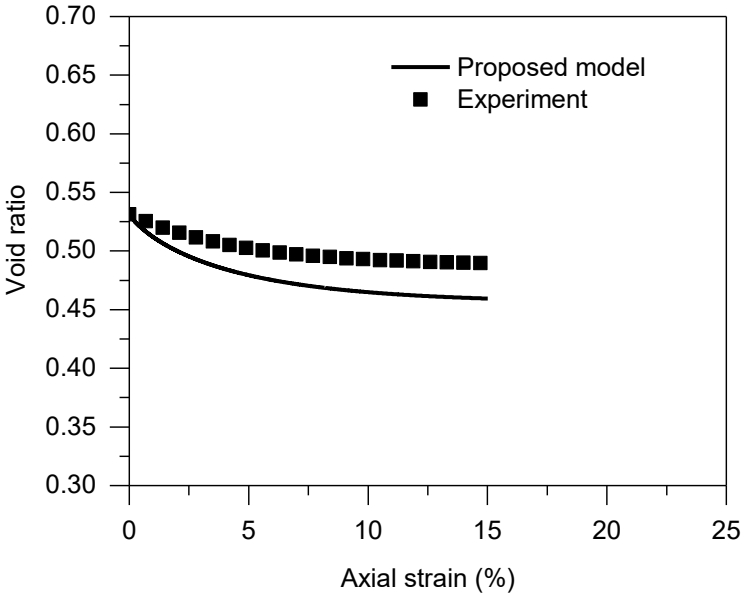

(c) Axial strain – Void ratio

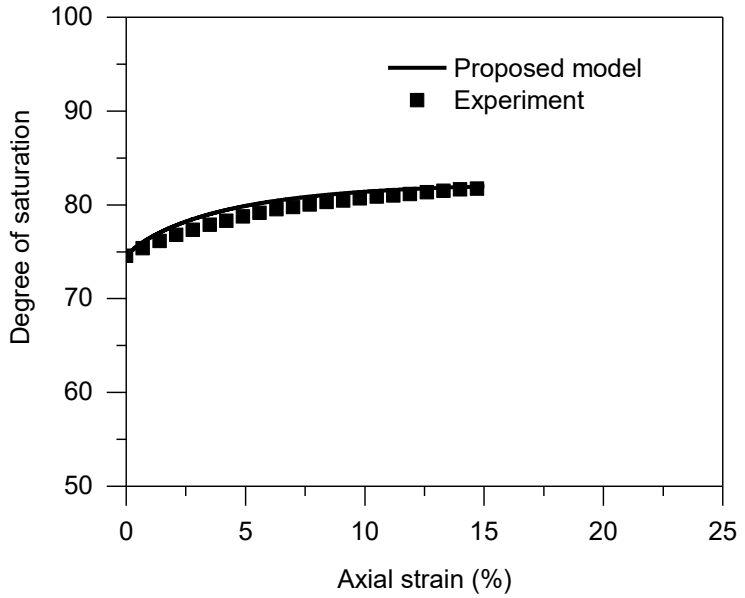

(d) Axial strain – Degree of saturation

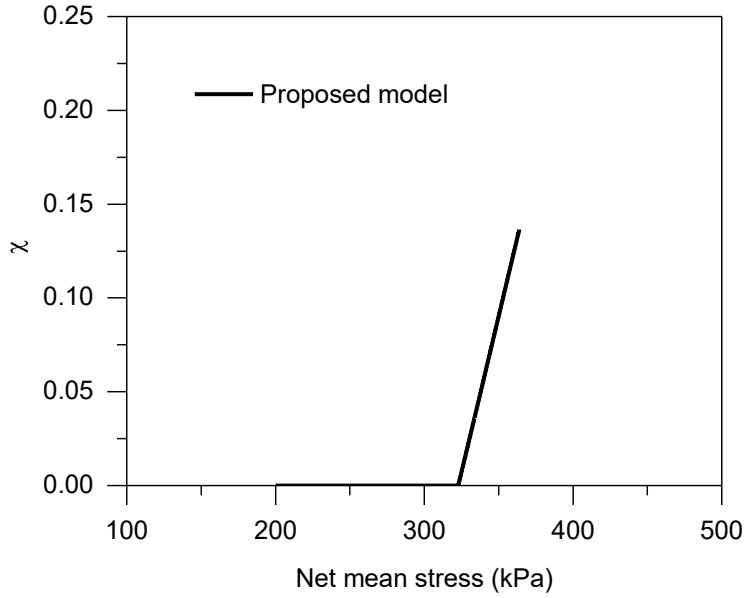

(e) Net mean stress – χ

Figure 8.11 Comparison in hydro-mechanical behaviour between experimental and modelling results of unsaturated shearing under a constant net confining stress of 200 kPa and a constant suction of 25 kPa

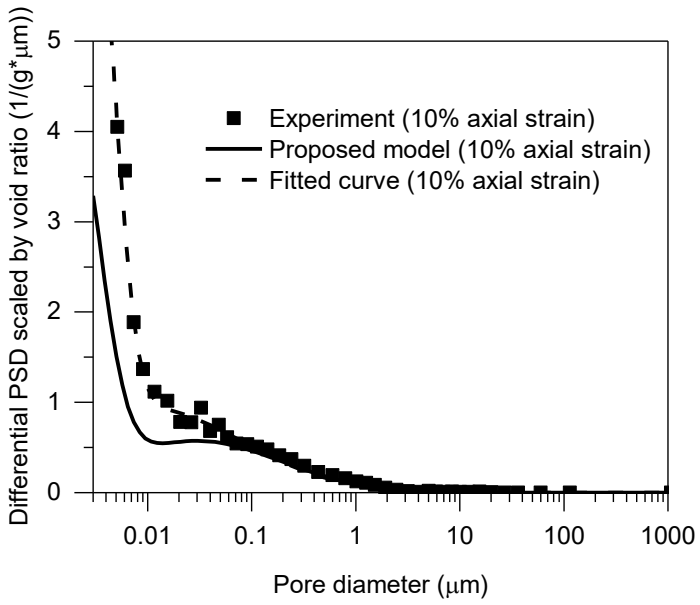

(a) PSDs at 10% axial strain

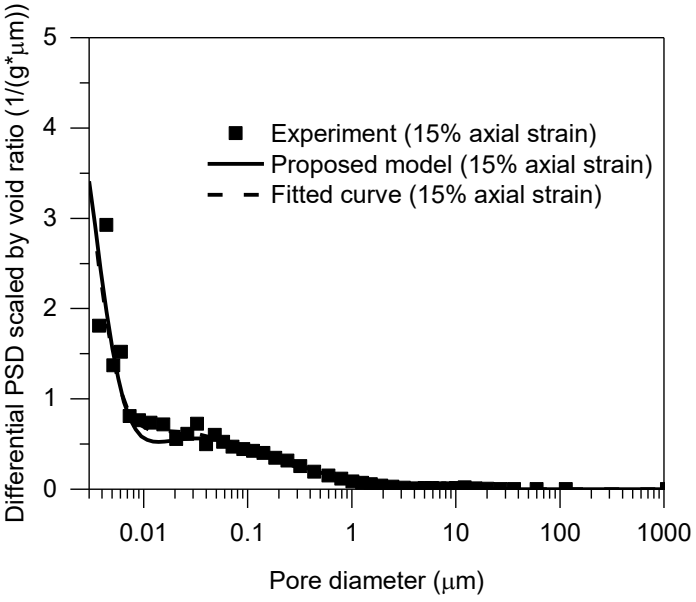

(b) PSDs at 15% axial strain

Figure 8.12 Comparison in PSDs between experimental and modelling results of unsaturated shearing under a constant net confining stress of 200 kPa and a constant suction of 25 kPa

8.4.1.2.2 100 kPa suction

Figure 8.13 presents the comparison in hydro-mechanical behaviour between experimental and modelling results of unsaturated shearing under a constant net confining stress of 200 kPa and a constant suction of 100 kPa. The model still succeeds in reproducing

the changing tendency of deviatoric stress, volumetric strain, void ratio and degree of saturation despite the overestimation of volumetric strain change and void ratio change (see Figure 8.13 (c) and (d)) which may be attribute to that the hydro-mechanical parameters in unsaturated modelling come from saturated tests. The Bishop's effective stress coefficient χ remains 0 during shearing according to the modelling result (see Figure 8.13 (e)) even though the degree of saturation is over 70%. This is very different from using degree of saturation as the χ which provides at least 70 kPa more effective stress while in this model the 100 kPa suction has 0 contribution to the effective stress due to the 0 χ. This phenomenon will be discussed later in this section. As shown in Figure 8.14, the model also has a satisfactory performance in reproducing the evolution of PSDs during shearing compared with both experimental results and fitted curves despite difference in small pores.

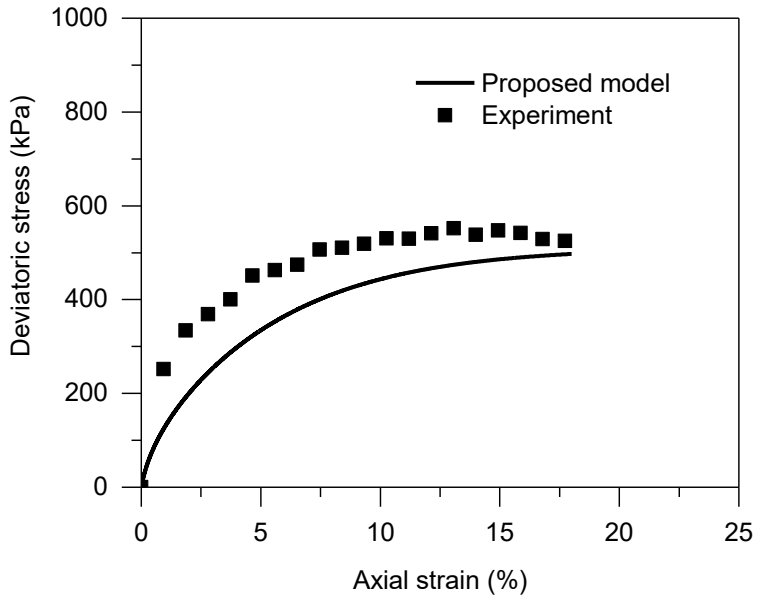

(a) Axial strain – Deviatoric stress

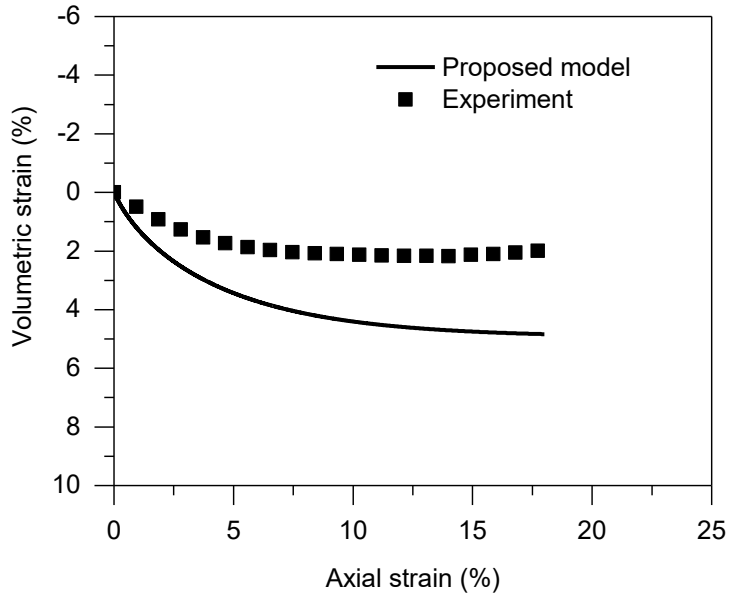

(b) Axial strain – Volumetric strain

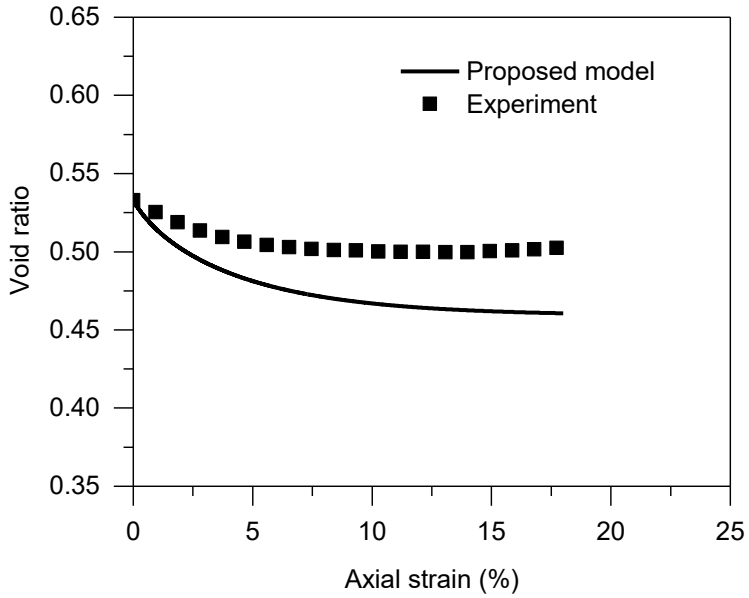

(c) Axial strain – Void ratio

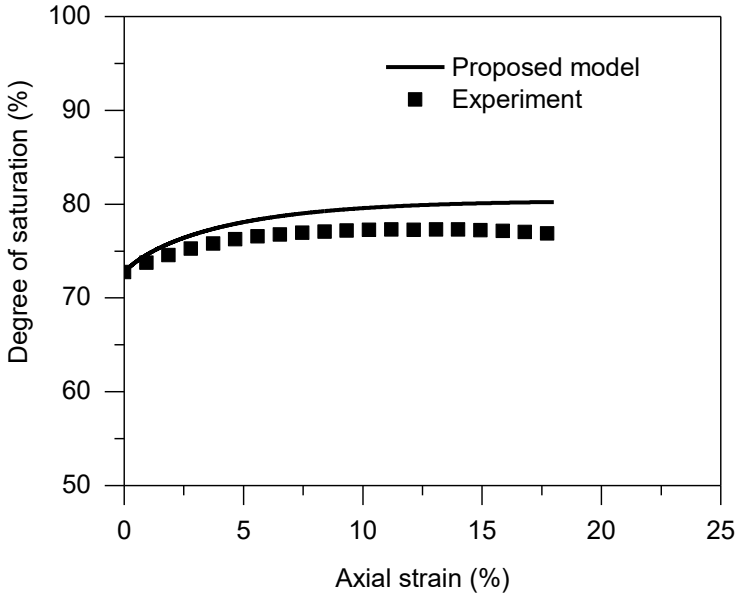

(d) Axial strain – Degree of saturation

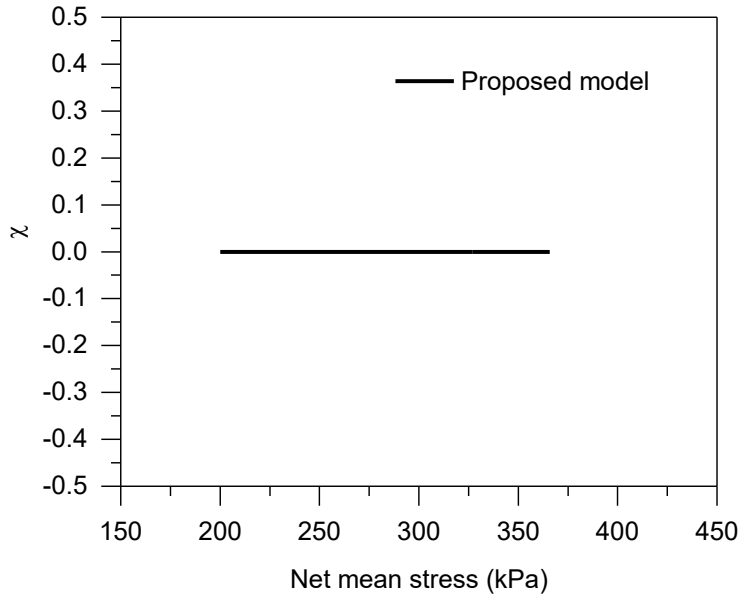

(e) Net mean stress – χ

Figure 8.13 Comparison in hydro-mechanical behaviour between experimental and modelling results of unsaturated shearing under a constant net confining stress of 200 kPa and a constant suction of 100 kPa

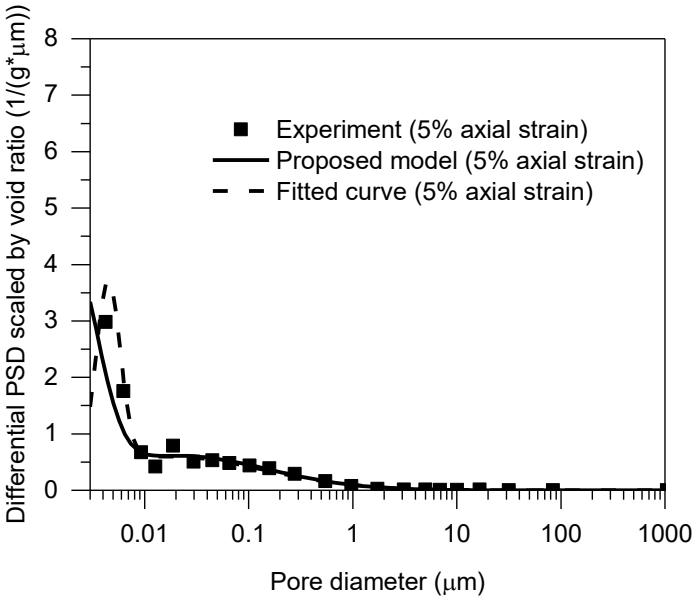

(a) PSDs at 5% axial strain

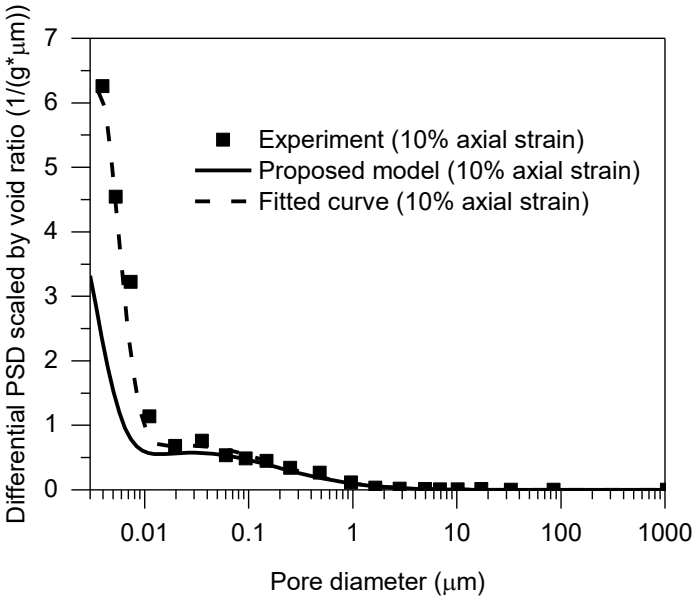

(b) PSDs at 10% axial strain

Figure 8.14 Comparison in PSDs between experimental and modelling results of unsaturated shearing under a constant net confining stress of 200 kPa and a constant suction of 100 kPa

In this study, the Bishop's effective stress coefficient χ is represented by the ratio of water ratio change and void ratio change which is related to the evolution of pore size distribution. Compared with the commonly used degree of saturation, this definition of χ will not only be different to the degree of saturation in value but also can provide some interesting findings. A modelling example is considered here based on the two fitted PSDs of Specimen M7 and M12.

Considering a range of suctions between 0.001 to 201001 kPa (equivalent pore entrance diameter at these suctions are 0.0014 to 291200 μm), the degree of saturation at each suction and χ at each degree of saturation can be calculated. This example allows the illustration of how χ changes with the degree of saturation based on two constant PSDs. As shown in Figure 8.15, χ calculated from PSDs is only the same as the degree of saturation at 0% and 100% saturation. The χ calculated from PSD is always smaller than the degree of saturation between 0% and 100%. At 90% saturation, the gap reaches the maximum where the χ calculated from PSD is still zero while that from degree of saturation is 0.90. After 90% saturation, the χ calculated from PSD starts to become nonzero and increase with degree of saturation. This result explains why the χ is always zero when modelling the shearing of Specimen M4, M7 and M12. The degree of saturation during shearing is always smaller than 90% so that χ remains zero. A similar finding has also been presented by Vaunat and Casini who noted that χ can maintain zero at a high degree of saturation even though the suction is not extremely large. This is the theoretical explanation for the zero χ.

The suction for these samples is 100 kPa but due to the zero χ, the suction contributes little to the effective stress. Therefore, the result of unsaturated shearing (Specimen M4) under a constant net confining stress of 200 kPa and a constant suction of 100 kPa should theoretically be identical to that of saturated shearing (Specimen M2) under a constant confining stress of 200 kPa. As presented in Figure 8.16, despite the small difference that might be attributed to the nuance in initial water contents and initial dry densities of these two samples, the increases of deviatoric stress during shearing for these two samples are almost consistent with each other and approaches the same value at 18% axial strain. This provides some experimental evidence that the 100 kPa suction does not make a significant contribution to the effective stress (χ is zero). Alternatively, if the definition of $\chi=S_r$ was used then χ is in the range 0.72 to 0.77 in the unsaturated test, and so the suction should increase the effective stress by 72 to 77 kPa which would be expected to result in a much higher deviatoric stress during shearing compared with the saturation test.

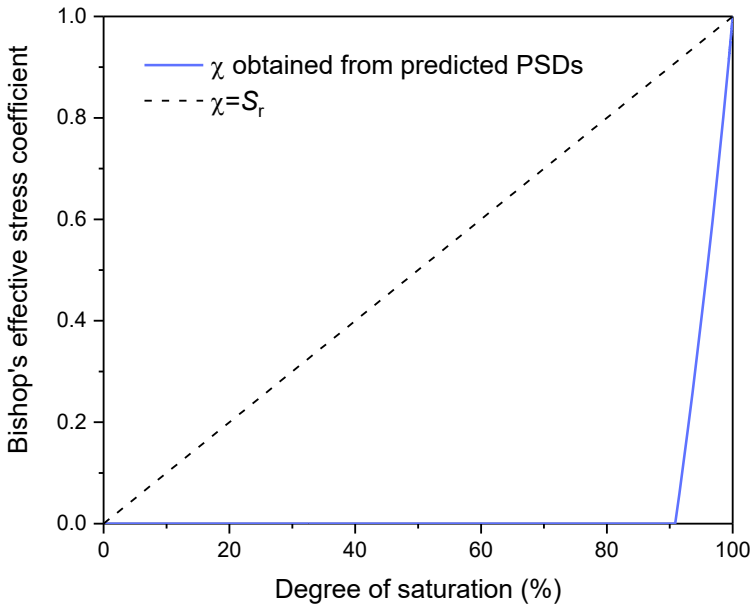

Figure 8.15 Comparison in χ calculated by two different methods

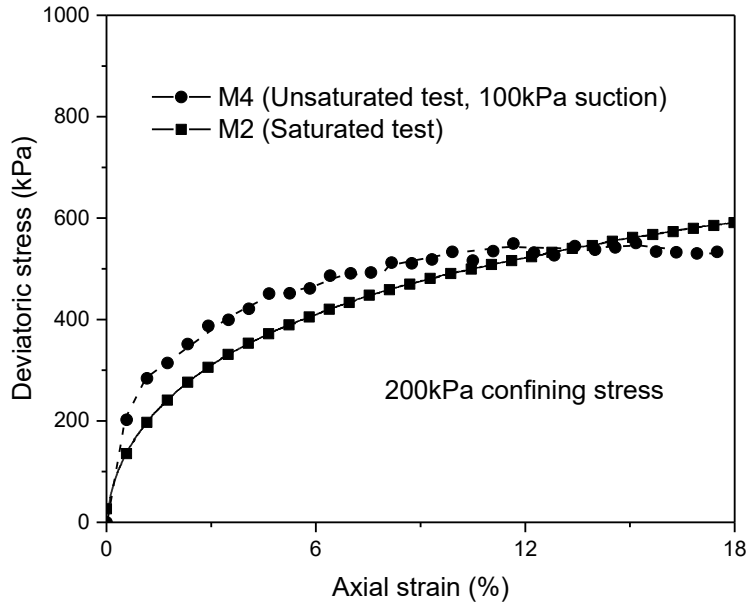

Figure 8.16 Comparison in deviatoric stress between Specimen M4 and M2

8.5 Model application in SWCC

Based on the relationship between pore volume and pore water content, the soil-water characteristic curve (SWCC) can be estimated from pore size distribution (Fredlund and Xing 1994; Simms and Yanful 2004b). Since the adopted model can reproduce the evolution of pore size distribution during loading, it can also be applied to predict the SWCC at a specific dry density (void ratio). Figure 8.17 presents the comparison in SWCCs between the modelling results and experimental results obtained by various methods. By comparing the results at dry

density of 1.62 Mg/m^3, it can be seen that the modelling results have a good performance in reproducing the changing tendency of water content (degree of saturation). The modelling result of M11 also has a good agreement with the experimental results obtained by GDS seems to agree with the modelling results at dry density of 1.77 Mg/m^3. However, differences can still be seen among these results. The SWCCs obtained by WP4C tend to decrease more sharply with increasing suction when compared to corresponding modelling results. This might be attributed to the difference in microstructure generated by different preparation methods. As reported by some researchers (Li and Zhang 2009; Wang et al. 2020), samples prepared to the same void ratio (dry density) by different methods will not necessarily have the same pore size distribution. For example, M9 and M11 both have a dry density of 1.62 Mg/m^3, but they have different pore size distributions and SWCCs because M9 was prepared under saturated condition while M11 was unsaturated. In this study, the modelling results are all based on the PSDs of samples prepared by triaxial tests while the experimental results are for compacted samples or original samples, which can account for the differences in SWCCs.

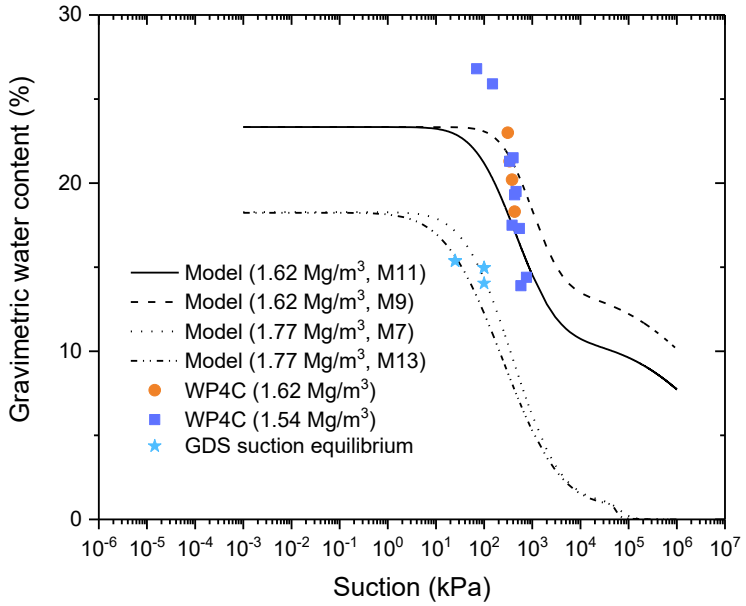

(a) Suction – Gravimetric water content

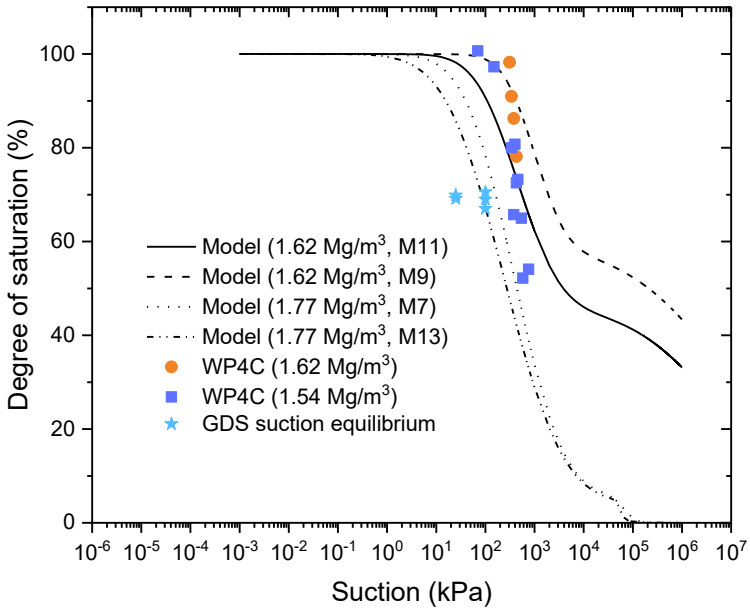

(b) Suction – degree of saturation

Figure 8.17 Comparison in SWCCs between modelling results and experimental results

8.6 Concluding remarks

The proposed model that considers the interaction between hydro-mechanical behaviour and microstructure is validated in this chapter by comparing the modelling results with the experimental results of Dundee silt. All model parameters and initial conditions were chosen based on the experimental results. Based on the comparison between both the experimental and modelling results, the following conclusions can be drawn:

(1) According to the modelling results, the direct microstructure model can satisfactorily reproduce both the hydro-mechanical behaviour and the PSD evolution of Dundee silt during shearing. The Bishop's effective stress coefficient χ remains 0 (the 100 kPa suction has no contribution to the effective stress) when modelling the unsaturated shearing, even though the degree of saturation is over 70%. This is significantly different from the χ represented by the degree of saturation. The theory of using PSD to calculate χ has already proved the possibility of having a low χ even at a high degree of saturation. It is also experimentally validated by the comparison with the results of saturated shearing under a constant net confining stress of 200 kPa. Despite small difference, the deviatoric stress towards critical state of saturated shearing is almost the same as that of this unsaturated shearing. This means that the suction did not contribute to the effective stress, otherwise a higher deviatoric stress should be witnessed. Since the suction is 100kPa, the only possibility is that χ is 0. However, this is only validated based on the shearing of Dundee silt under 200 kPa confining stress and 100 kPa suction. More evidence from other soils and loading conditions should be carried out for further validation.

(2) According to the relationship between PSD and SWCC, the direct microstructure model can also be used to reproduce the SWCC at each dry density based on the PSD at the same dry density. The SWCCs predicted by the model generally reproduced the changing tendency of water content (or degree of saturation) with suctions. However, differences can still be seen among these results. The SWCCs obtained by WP4C tend to decrease more sharply with increasing suction when compared to corresponding modelling results. This might be attributed to the difference in microstructure generated by different preparation methods.

CHAPTER 9

Conclusions and recommended further research

9.1 Conclusions

The microstructural-hydro-mechanical coupled behaviour of saturated and unsaturated soils has been studied in terms of both experimental behaviour and modelling. In this study, the interaction between the evolution of pore size distribution (PSD) and the hydro-mechanical behaviour has been investigated. Subsequently the stress-strain behaviour in triaxial conditions and water retention behaviour can be considered from the perspective of microstructure, which is beneficial to the future study of many engineering problems such as rainfall-induced landslide, contaminant transport and soil barrier.

For experiments, a natural low-plastic soil, has been studied via a programme of triaxial, MIP and SWCC tests. Compacted samples were prepared at an initial water content of 15% and initial dry densities of ~1.76 Mg/m^3 and ~1.62 Mg/m^3. These samples were then saturated or subjected to a specific suction, consolidated and taken to isotropic loading or shearing under various conditions. After triaxial tests were finished, samples were broken down into lumps before being freeze or oven dried. Afterwards, since PSD was employed as an indicator of soil microstructure, MIP tests were conducted on these dried samples to obtain PSDs under various loading conditions, based on which the interaction between microstructure and the hydro-mechanical behaviour of Dundee silt can be analysed. SWCC tests were also conducted using the chilled mirror dew point technique to obtain the water retention behaviour of Dundee silt with different dry densities.

For modelling, the performance of an existing model with indirect consideration of soil microstructure (indirect microstructure model) was evaluated and the indirect model's limitations analysed. Afterwards, to directly consider soil microstructure, a constitutive model allowing for the interaction between evolution of microstructure and hydro-mechanical behaviour of unsaturated soils (direct microstructure model) was proposed and evaluated. The direct microstructure model for the first time adopts a PSD-dependent Bishop's effective stress coefficient in an existing hydro-mechanical coupled model. The direct microstructure model is able to represent the hydro-mechanical behaviour and microstructural evolution within the same framework and has the potential of studying SWCC and the effects of microstructure in other multi-coupling behaviour of soils. Model response and sensitivity analysis based on the published experiments on Speswhite kaolin (isotropic loading) and idealized assumptions on pore size distributions were undertaken to evaluate the performance of the model and the reliability of using PSDs obtained from MIP. The proposed model was also validated by reproducing both the hydro-mechanical behaviour and the evolution of PSDs under various loading conditions as indicated by experimental results. All model parameters and initial

conditions were chosen based on the experimental results. The possibility of using this model to predict the evolution of SWCC is also explored in the study.

Based on both the experimental and modelling results, the following conclusions can be drawn:

(1) The hydro-mechanical behaviour of the low-plastic silt is similar to that of other fine-grained soils reported in other research. A higher confining stress can lead to the increase of deviatoric stress at critical state and reduce the possibility of strain softening. A higher displacement rate can result in a lower shear strength and a larger axial strain is required to reach the peak deviatoric stress. An increasing initial dry density can bring about an increase in shear strength, cohesion and friction angle.

(2) A synchronous evolution of soil microstructure (pore size distribution) along with the changes of axial strain, confining stress, suction, void ratio and water content was observed during different loading paths (compaction, saturation and triaxial paths), helping to reveal the interaction between the soil microstructure and the hydro-mechanical behaviour. The pore size distribution of Dundee silt compacted at the dry side of the compaction curve or subjected to a suction has a bimodal shape with two significant peaks. One is related to the inter-aggregate pores (macropores with relatively larger pore sizes) and the other is related to the intra-aggregate pores (micropores with relatively smaller pore sizes). These two kinds of pores manifest different behaviour during loading. For inter-aggregate pores, an obvious downward and leftward movement of inter-aggregate PSD can be witnessed during unsaturated shearing which represents the compression of larger pores. However, for intra-aggregate pores, the movement of corresponding PSD is much less significant, but an upward movement can be seen which indicates the increase of small pores. Since samples' void ratios decrease during unsaturated shearing, it can be concluded that the main source of sample compression comes from the decrease of inter-aggregate pores. Besides, even though the saturated shearing will to some extent make the bimodality of PSD less significant, it will not be eliminated to unimodality even at 20% axial strain. Since the evolution of PSD follows a clear and regular principle, the microstructural-hydro-mechanical coupled behaviour can be simulated by constitutive modelling given the close correlation between the void ratio change and the evolution of pore size distribution.

(3) A higher initial dry density and confining stress lead to the left movement of pore size distribution due to the compression of larger pores while the decrease of suction can turn the bimodal PSD to unimodal PSD.

(4) Aside from initial dry density, confining stress and suction, there are many other factors that can affect PSDs, including heterogeneity, drying methods and samples sizes. Void ratios provided by GDS usually represent the average void ratio inside of a triaxial sample. However, due to the heterogeneity, the void ratio in the centre layer might be larger than that in the edge layer because the edge layer is closer to the loading piston and can be more

compressed. Different drying methods can also have an impact on the PSD that oven drying tends to bring about the shrinkage of samples while freeze drying can preserve more smaller pores and no volume change will happen when the water turns into ice due to the rapid freezing in liquid nitrogen. Besides, open voids generated during cutting samples to smaller lumps will occur on the surface of cutting edge. Therefore, a smaller size of lump, which has a higher specific surface area, will be more severely affected by unexpected large voids, which leads to a higher intruded void ratio. Even though there are many factors that can affect the representativeness of PSDs obtained by MIP, those PSDs are still generally informative and able to represent the evolution of PSDs during loading because of the relatively high reliability of providing PSD shapes, peak positions and evolutional features.

(5) According to the result from the model response, the direct model is able to reproduce the hydro-mechanical behaviour of unsaturated soils based on published hydro-mechanical parameters and assumed pore size distribution parameters of Speswhite kaolin. This also indicates the potential of this model to be applied to predicting the behaviour of other soils. According to the sensitivity analysis, the model is not sensitive to the volume proportion of the intra-aggregate pores (micropores) but is sensitive to the properties of the inter-aggregate pores (macropores) and the evolutional parameters. However, as the degree of sensitivity to inter-aggregate pores properties is not excessively high, traditional methods for obtaining PSDs such as Mercury Intrusion Porosimetry (MIP) can be used to provide PSD-related parameters for this model.

(6) According to the modelling results, the direct microstructure model can satisfactorily reproduce both the hydro-mechanical behaviour and the PSD evolution of Dundee silt during shearing. Under the suction of 100 kPa, the Bishop's effective stress coefficient χ remains 0 when modelling the unsaturated shearing, even though the degree of saturation is over 70%. This is significantly different from the χ represented by the degree of saturation. The theory of using PSD to calculate χ has already proved the possibility of having a low χ even at a high degree of saturation. It is also experimentally validated by the comparison with the results of saturated shearing under a constant net confining stress of 200 kPa. Despite small difference, the deviatoric stress towards critical state of saturated shearing is almost the same as that of this unsaturated shearing. This means that the suction did not contribute to the effective stress, otherwise a higher deviatoric stress should be witnessed. Since the suction is 100 kPa, the only possibility is that χ is 0. This explanation can also be applied to the result of shearing under 25 kPa suction.

(7) According to the relationship between PSD and SWCC, the direct microstructure model can also be used to reproduce the SWCC at each dry density based on the PSD at the same dry density. The SWCCs predicted by the model generally reproduced the changing tendency of water content (or degree of saturation) with suctions. However, differences can still be seen among these results. The SWCCs obtained by WP4C tend to decrease more sharply with increasing suction when compared to corresponding modelling results. This might be attributed to the difference in microstructure generated by different preparation methods.

9.2 Recommended further research

The following work can be done as further research:

(1) The experimental and modelled microstructural-hydro-mechanical behaviour of soils is only investigated based on Dundee silt in this study. This behaviour can be further studied with various kinds of soils such as London clay, Speswhite kaolin and betonite.

(2) Soil microstructure is represented by the pore size distribution in this study. A more detailed description of microstructure which includes the morphologic features can be considered in both modelling and experiments.

(3) The pore size distribution is only obtained by MIP tests in this study. More developed methods can be used to explore and quantify the soil microstructure.

(4) More SWCC tests under various conditions can be done and SWCC samples can be directly taken to microstructure detection tests to study the interaction between the soil microstructure and the water retention behaviour.

(5) The possibility of using a microstructure related model to predict the SWCC has been explored in this study. The application of the model can be further studied in terms of permeability, waste transportation, and thermal and chemical effects on soil microstructure.

REFERENCES

Abu-Farsakh, M., Coronel, J. and Tao, M. 2007. Effect of Soil Moisture Content and Dry Density on Cohesive Soil–Geosynthetic Interactions Using Large Direct Shear Tests. *Journal of Materials in Civil Engineering* 19(7), pp. 540–549. doi: 10.1061/(asce)0899-1561(2007)19:7(540).

Ahmed, S., Lovell, C.W. and Diamond, S. 1974. Pore Sizes and Strength of a Compacted Clay : Technical Paper. Available at: https://docs.lib.purdue.edu/jtrp/1408.

Alazaiza, M.Y.D., Ngien, S.K., Bob, M.M., Kamaruddin, S.A. and Ishak, W.M.F. 2017. Influence of Macro-pores on DNAPL Migration in Double-Porosity Soil Using Light Transmission Visualization Method. *Transport in Porous Media* 117(1), pp. 103–123. doi: 10.1007/s11242-017-0822-3.

Alekseeva, T.V. 2007. Soil microstructure and factors of its formation. *Eurasian Soil Science* 40(6), pp. 649–659. doi: 10.1134/S1064229307060063.

Almahbobi, S.A. 2018. *Experimental study of volume change and shear strength behaviour of statically compacted collapsible soil*. UK: Cardiff University.

Al-Mukhtar, M., Khattab, S. and Alcover, J.-F. 2012. Microstructure and geotechnical properties of lime-treated expansive clayey soil. *Engineering geology* 139, pp. 17–27. doi: https://doi.org/10.1016/j.enggeo.2012.04.004.

Alonso, E.E., Gens, A. and Josa, A. 1990. A constitutive model for partially saturated soils. *Géotechnique* 40(3), pp. 405–430. doi: 10.1680/geot.1990.40.3.405.

Alonso, E.E., Pereira, J.-M., Vaunat, J. and Olivella, S. 2010. A microstructurally based effective stress for unsaturated soils. *Géotechnique* 60(12), pp. 913–925. doi: 10.1680/geot.8.P.002.

Alonso, E.E., Pinyol, N.M. and Gens, A. 2013. Compacted soil behaviour: initial state, structure and constitutive modelling. *Géotechnique* 63(6), p. 463. doi: https://doi.org/10.1680/geot.11.P.134.

Anantanasakul, P., Yamamuro, J.A. and Kaliakin, V.N. 2012. Stress-Strain and Strength Characteristics of Silt-Clay Transition Soils. *Journal of Geotechnical and Geoenvironmental Engineering* 138(10), pp. 1257–1265. doi: 10.1061/(ASCE)GT.1943-5606.0000692.

Andersen, K.H. and Schjetne, K. 2013. Database of Friction Angles of Sand and Consolidation Characteristics of Sand, Silt, and Clay. *Journal of Geotechnical and Geoenvironmental Engineering* 139(7), pp. 1140–1155. doi: 10.1061/(ASCE)GT.1943-5606.0000839.

Arroyo, H., Rojas, E., P&#233, rez-Rea, M., Luz, A.D.L., Horta, J. and Arroyo, J. 2015. Coupling pore-size distribution and volumetric strains to predict soil-water characteristic curves. *From Fundamentals to Applications in Geotechnics*, pp. 2078–2085. doi: 10.3233/978-1-61499-603-3-2078.

Bagherieh, A.R., Khalili, N., Habibagahi, G. and Ghahramani, A. 2009. Drying response and effective stress in a double porosity aggregated soil. *Engineering Geology* 105(1), pp. 44–50. doi: 10.1016/j.enggeo.2008.12.009.

Baille, W., Tripathy, S. and Schanz, T. 2014. Effective Stress in Clays of Various Mineralogy. *Vadose Zone Journal*, p. 10.

Baker, R. and Frydman, S. 2009. Unsaturated soil mechanics: Critical review of physical foundations. *Engineering Geology* 106(1), pp. 26–39. doi: 10.1016/j.enggeo.2009.02.010.

Barbour, S.L. 1998. Nineteenth Canadian Geotechnical Colloquium: The soil-water characteristic curve: a historical perspective. *Canadian Geotechnical Journal* 35(5), pp. 873–894.

Barden, L., Madedor, A.O. and Sides, G.R. 1969. Volume change characteristics of unsaturated clay. *Journal of Soil Mechanics & Foundations Div*.

Belnap, J. and Gardner, J.S. 1993. Soil microstructure in soils of the Colorado Plateau: the role of the cyanobacterium Microcoleus vaginatus. *Great Basin Naturalist* 53(1), p. 6.

Beren, M., Çobanoglu, I., Çelik, S.B. and Ündül, Ö. 2020. Shear Rate Effect on Strength Characteristics of Sandy Soils. *Soil Mechanics and Foundation Engineering* 57(4), pp. 281–287. doi: 10.1007/s11204-020-09667-y.

Bishop, A.W. 1959. The Principle of Effective Stress. *Teknisk ukeblad* 39, pp. 859–863.

Bishop, A.W. and Wesley, L.D. 1975. A hydraulic triaxial apparatus for controlled stress path testing. *Géotechnique* 25(4), pp. 657–670. doi: 10.1680/geot.1975.25.4.657.

Bol, E., Önalp, A., Özocak, A. and Sert, S. 2019. Estimation of the undrained shear strength of Adapazari fine grained soils by cone penetration test. *Engineering Geology* 261, p. 105277. doi: 10.1016/j.enggeo.2019.105277.

Brooks, R. and Corey, T. 1964. HYDRAU uc properties of porous media. *Hydrology Papers, Colorado State University* 24, p. 37.

Bulut, R., Lytton, R.L. and Wray, W.K. 2012. Soil Suction Measurements by Filter Paper. *Expansive Clay Soils and Vegetative Influence on Shallow Foundations*, pp. 243–261. doi: 10.1061/40592(270)14.

Burton, G.J., Sheng, D. and Campbell, C. 2014. Bimodal pore size distribution of a high-plasticity compacted clay. *Géotechnique Letters* 4(2), pp. 88–93. doi: 10.1680/geolett.14.00003.

Cai, G., Li, M., Han, B., Di, K., Liu, Q. and Li, J. 2020a. Numerical Analysis of Unsaturated Soil Slopes under Rainfall Infiltration Based on the Modified Glasgow Coupled Model. *Advances in Civil Engineering* 2020. Available at: https://www.hindawi.com/journals/ace/2020/8865179/.

Cai, G., Zhou, A., Liu, Y., Xu, R. and Zhao, C. 2020b. Soil water retention behavior and microstructure evolution of lateritic soil in the suction range of 0–286.7MPa. *Acta Geotechnica* 15, pp. 3327–3341. doi: 10.1007/s11440-020-01011-w.

Cai, G.Q., Wang, Y.N., Zhou, A.N. and Zhao, C.G. 2018. A microstructure-dependent hydro-mechanical coupled constitutive model for unsaturated soils. *Chinese Journal of Geotechnical Engineering* 40(04), pp. 618–624. doi: 10.11779/CJGE201804005.

Casey, B., Germaine, J.T., Abdulhadi, N.O., Kontopoulos, N.S. and Jones, C.A. 2016. Undrained Young's Modulus of Fine-Grained Soils. *Journal of Geotechnical and Geoenvironmental Engineering* 142(2), p. 04015070. doi: 10.1061/(ASCE)GT.1943-5606.0001382.

Casini, F. 2008. *Numerical modelling of coupled behaviour in unsaturated soils*. Italy: Universitá degli Studi di Roma 'La Sapienza'.

Casini, F., Vaunat, J., Romero, E. and Desideri, A. 2012. Consequences on water retention properties of double-porosity features in a compacted silt. *Acta Geotechnica* 7(2), pp. 139–150. doi: 10.1007/s11440-012-0159-6.

Chen, K., He, X., Liang, F. and Sheng, D. 2024. Influences of ink-bottle effect evolution on water retention hysteresis of unsaturated soils: An experimental investigation. *Engineering Geology* 330, p. 107409. doi: 10.1016/j.enggeo.2024.107409.

Chen, Y. and Banin, A. 1975. Scanning electron microscope (SEM) observations of soil structure changes induced by sodium-calcium exchange in relation to hydraulic conductivity. *Soil Science* 120(6), pp. 428–436.

Chen, Y. and Kulhawy, F.H. 1993. Undrained Strength Interrelationships among CIUC, UU, and UC Tests. *Journal of Geotechnical Engineering* 119(11), pp. 1732–1750. doi: 10.1061/(ASCE)0733-9410(1993)119:11(1732).

Chu, J., Lo, S. -C. R. and Lee, I.K. 1992. Strain-Softening Behavior of Granular Soil in Strain-Path Testing. *Journal of Geotechnical Engineering* 118(2), pp. 191–208. doi: 10.1061/(ASCE)0733-9410(1992)118:2(191).

Collins, B.D. and Znidarcic, D. 2004. Stability analyses of rainfall induced landslides. *Journal of geotechnical and geoenvironmental engineering* 130(4), pp. 362–372.

Cui, Y.J. and Delage, P. 1996. Yielding and plastic behaviour of an unsaturated compacted silt. *Géotechnique* 46(2), pp. 291–311. doi: 10.1680/geot.1996.46.2.291.

Cuisinier, O., Auriol, J.-C., Le Borgne, T. and Deneele, D. 2011. Microstructure and hydraulic conductivity of a compacted lime-treated soil. *Engineering geology* 123(3), pp. 187–193. doi: 10.1016/j.enggeo.2011.07.010.

Davies, M.C.R. and Newson, T.A. 1992. A critical state constitutive model for anisotropic soil. In: *Predictive soil mechanics*. Thomas Telford Publishing, pp. 219–229. Available at: https://www.icevirtuallibrary.com/doi/abs/10.1680/psm.19164.0014.

Delage, P. 2007. Microstructure Features in the Behaviour of Engineered Barriers for Nuclear Waste Disposal. In: Schanz, T. ed. *Experimental Unsaturated Soil Mechanics*. Berlin, Heidelberg: Springer, pp. 11–32. doi: 10.1007/3-540-69873-6_2.

Delage, P., Audiguier, M., Cui, Y.-J. and Howat, M.D. 1996. Microstructure of a compacted silt. *Canadian Geotechnical Journal* 33(1), pp. 150–158. doi: 10.1139/t96-030.

Delage, P., Marcial, D., Cui, Y.J. and Ruiz, X. 2006. Ageing effects in a compacted bentonite: a microstructure approach. *Géotechnique* 56(5), pp. 291–304. doi: 10.1680/geot.2006.56.5.291.

Della Vecchia, G., Dieudonné, A.-C., Jommi, C. and Charlier, R. 2015. Accounting for evolving pore size distribution in water retention models for compacted clays. *International Journal for Numerical and Analytical Methods in Geomechanics* 39(7), pp. 702–723. doi: 10.1002/nag.2326.

Eral, H.B., 't Mannetje, D.J.C.M. and Oh, J.M. 2013. Contact angle hysteresis: a review of fundamentals and applications. *Colloid and Polymer Science* 291(2), pp. 247–260. doi: 10.1007/s00396-012-2796-6.

Estabragh, A.R. and Javadi, A.A. 2008. Critical state for overconsolidated unsaturated silty soil. *Canadian Geotechnical Journal* 45(3), pp. 408–420. doi: 10.1139/T07-105.

Finn, R. 1999. Capillary Surface Interfaces. 46(7).

Fredlund, D.G. and Morgenstern, N.R. 1977. Stress State Variables for Unsaturated Soils. *Journal of the Geotechnical Engineering Division* 103(5), pp. 447–466. doi: 10.1061/AJGEB6.0000423.

Fredlund, D.G., Morgenstern, N.R. and Widger, R.A. 1978. The shear strength of unsaturated soils. *Canadian Geotechnical Journal* 15(3), pp. 313–321. doi: 10.1139/t78-029.

Fredlund, D.G. and Rahardjo, H. 1993. *Soil mechanics for unsaturated soils*. John Wiley & Sons.

Fredlund, D.G. and Xing, A. 1994. Equations for the soil-water characteristic curve. *Canadian Geotechnical Journal* 31(4), pp. 521–532. doi: 10.1139/t94-061.

Galle, C. 2001. Effect of drying on cement-based materials pore structure as identified by mercury intrusion porosimetry A comparative study between oven-, vacuum-, and freeze-drying. *Cement and Concrete Research*.

Gao, Q.-F., Jrad, M., Hattab, M., Fleureau, J.-M. and Ameur, L.I. 2020a. Pore Morphology, Porosity, and Pore Size Distribution in Kaolinitic Remolded Clays under Triaxial Loading. *International Journal of Geomechanics* 20(6), p. 04020057. doi: 10.1061/(ASCE)GM.1943-5622.0001682.

Gao, Y., Sun, D., Zhou, A. and Li, J. 2020b. Predicting Shear Strength of Unsaturated Soils over Wide Suction Range. *International Journal of Geomechanics* 20(2), p. 04019175. doi: 10.1061/(ASCE)GM.1943-5622.0001555.

Garakani, A.A., Haeri, S.M., Khosravi, A. and Habibagahi, G. 2015. Hydro-mechanical behavior of undisturbed collapsible loessial soils under different stress state conditions. *Engineering geology* 195, pp. 28–41.

Gardner, W.R. 1958. Mathematics of Isothermal Water Conduction Unsaturated Soil. *Highway Research Board Special Report*. Available at: https://www.semanticscholar.org/paper/MATHEMATICS-OF-ISOTHERMAL-WATER-CONDUCTION-IN-SOIL-Gardner/afa446b201cc5b38806a04d9f6909f781ded7c95.

Gee, G.W., Campbell, M.D., Campbell, G.S. and Campbell, J.H. 1992. Rapid Measurement of Low Soil Water Potentials Using a Water Activity Meter. *Soil Science Society of America Journal* 56(4), pp. 1068–1070. doi: 10.2136/sssaj1992.03615995005600040010x.

Gens, A., Sánchez, M. and Sheng, D. 2006. On constitutive modelling of unsaturated soils. *Acta Geotechnica* 1(3), pp. 137–147. doi: 10.1007/s11440-006-0013-9.

Ghiadistri, G., Zdravković, L., Potts, D.M. and Tsiampousi, A. 2019. Calibration of a double structure constitutive model for unsaturated compacted soils. Tarantino, A. and Ibraim, E. eds. *E3S Web of Conferences* 92, p. 15002. doi: 10.1051/e3sconf/20199215002.

Ghiadistri, G.M., Potts, D.M., Zdravković, L. and Tsiampousi, A. 2018. A new double structure model for expansive clays. Available at: https://api.semanticscholar.org/CorpusID:259933558.

Godt, J., Lu, N. and Baum, R.L. 2013. A hydro-mechanical framework for early warning of rainfall-induced landslides (Invited). 2013, pp. NH13D-01.

Gramegna, L. 2022. Pore size distribution evolution in pellets based bentonite hydration: Comparison between experimental and numerical results. *Engineering Geology* 304, p. 106700. doi: https://doi.org/10.1016/j.enggeo.2022.106700.

Groffman, P.M. and Tiedje, J.M. 1988. Denitrification hysteresis during wetting and drying cycles in soil. *Soil Science Society of America Journal* 52(6), pp. 1626–1629.

Gruber, S. and Haeberli, W. 2007. Permafrost in steep bedrock slopes and its temperature-related destabilization following climate change. *Journal of Geophysical Research: Earth Surface* 112(F2). Available at: https://onlinelibrary.wiley.com/doi/abs/10.1029/2006JF000547.

Guan, Y. and Fredlund, D.G. 1997. Use of the tensile strength of water for the direct measurement of high soil suction. 34.

Guo-qing C. a. I., Ce Z., Jian L.I. and Cheng-gang Z. 2018. Prediction method for SWCC considering initial dry density. *Chinese Journal of Geotechnical Engineering* 40(S2), pp. 27–31. doi: 10.11779/CJGE2018S2006.

Guoqing, C., Tianchi, W., Hao, L., Chenggang, Z., Jingjing, T. and Jian, L. 2020. A deformation-dependent soil-water characteristic surface model considering hysteresis. *E3S Web of Conferences* 195, p. 02014. doi: 10.1051/e3sconf/202019502014.

Guo-Quan, D., Xia, B., Jun-Ping, Y. and Jun-Gao, Z. 2022. Bimodal SWCC and Bimodal PSD of Soils with Dual-Porosity Structure. *Mathematical Problems in Engineering* 2022. Available at: https://www.hindawi.com/journals/mpe/2022/4052956/.

Hensley, P.J. and Savvidou, C. 1993. Modelling coupled heat and contaminant transport in groundwater. *International journal for numerical and analytical methods in geomechanics* 17(7), pp. 493–527.

Higo, Y. and Kido, R. 2024. A microscopic interpretation of hysteresis in the water retention curve of sand. *Géotechnique*, pp. 1–9. doi: 10.1680/jgeot.23.00084.

Hilf, J.W. 1956. An Investigation of Pore Water Pressure in Compacted Cohesive Soils. Available at: https://trid.trb.org/View/124792.

Ho, D.Y. and Fredlund, D.G. 1982. Strain rates for unsaturated soil shear strength testing. In: *Proceedings of the Seventh Southeast Asian Geotechnical Conference*. Southeast Asian Geotechnical Society (SEAGS), Pathumthani, Thailand, pp. 787–803.

Houlsby, G.T. 1997. The work input to an unsaturated granular material. *Geotechnique* 47(1), pp. 193–196. doi: 10.1680/geot.1997.47.1.193.

Houston, S.L., Perez-Garcia, N. and Houston, W.N. 2008. Shear Strength and Shear-Induced Volume Change Behavior of Unsaturated Soils from a Triaxial Test Program. *Journal of Geotechnical and Geoenvironmental Engineering* 134(11), pp. 1619–1632. doi: 10.1061/(ASCE)1090-0241(2008)134:11(1619).

Hu, R.L., Yeung, M.R., Lee, C.F. and Wang, S.J. 2001. Mechanical behavior and microstructural variation of loess under dynamic compaction. *Engineering Geology* 59(3–4), pp. 203–217. doi: https://doi.org/10.1016/S0013-7952(00)00074-0.

Izdebska-Mucha, D., TrzcińSk, J., Żbik, M.S. and Frost, R.L. 2011. Influence of hydrocarbon contamination on clay soil microstructure. *Clay Minerals* 46(1), pp. 47–58. doi: 10.1180/claymin.2011.046.1.47.

Izdebska-Mucha, D. and Trzciński, J. 2008. Effects of petroleum pollution on clay soil microstructure. Available at: https://depot.ceon.pl/handle/123456789/15879.

Jia, R., Lei, H. and Li, K. 2020. Compressibility and Microstructure Evolution of Different Reconstituted Clays during 1D Compression. *International Journal of Geomechanics* 20(10), p. 04020181. doi: 10.1061/(ASCE)GM.1943-5622.0001830.

Jiang, Y., Einav, I. and Liu, M. 2017. A thermodynamic treatment of partially saturated soils revealing the structure of effective stress. *Journal of the Mechanics and Physics of Solids* 100, pp. 131–146. doi: 10.1016/j.jmps.2016.11.018.

Joy, D.C. and Pawley, J.B. 1992. High-resolution scanning electron microscopy. *Ultramicroscopy* 47(1), pp. 80–100. doi: 10.1016/0304-3991(92)90186-N.

Juang, C.H. and Holtz, R.D. 1986. Fabric, Pore Size Distribution, and Permeability of Sandy Soils. *Journal of Geotechnical Engineering* 112(9), pp. 855–868. doi: 10.1061/(ASCE)0733-9410(1986)112:9(855).

Kan, J., Li, G., Zhang, N., Wang, P., Han, C. and Wang, S. 2021. Changing Characteristics of Sandstone Pore Size under Cyclic Loading. *Geofluids* 2021, p. e6664925. doi: 10.1155/2021/6664925.

Kokusho, T. 2000. Correlation of Pore-Pressure B-Value with P-Wave Velocity and Poisson's Ratio for Imperfectly Saturated Sand or Gravel. *Soils and Foundations* 40(4), pp. 95–102. doi: 10.3208/sandf.40.4_95.

Koliji, A., Vulliet, L. and Laloui, L. 2010. Structural characterization of unsaturated aggregated soil. *Canadian Geotechnical Journal* 47(3), pp. 297–311. doi: 10.1139/T09-089.

Kumar Thota, S., Duc Cao, T. and Vahedifard, F. 2021. Poisson's Ratio Characteristic Curve of Unsaturated Soils. *Journal of Geotechnical and Geoenvironmental Engineering* 147(1), p. 04020149. doi: 10.1061/(ASCE)GT.1943-5606.0002424.

Laloui, L. and Nuth, M. 2009. On the use of the generalised effective stress in the constitutive modelling of unsaturated soils. *Computers and Geotechnics* 36(1), pp. 20–23. doi: 10.1016/j.compgeo.2008.03.002.

Lawrence, G.P., Payne, D. and Greenland, D.J. 1979. Pore Size Distribution in Critical Point and Freeze Dried Aggregates from Clay Subsoils. *Journal of Soil Science* 30(3), pp. 499–516. doi: 10.1111/j.1365-2389.1979.tb01004.x.

Lee, S.Y. and Tank, R.W. 1985. Role of clays in the disposal of nuclear waste: A review. *Applied Clay Science* 1(1), pp. 145–162. doi: 10.1016/0169-1317(85)90570-8.

Leong, E.C. and Cheng, Z.Y. 2016. Effects of Confining Pressure and Degree of Saturation on Wave Velocities of Soils. *International Journal of Geomechanics* 16(6), p. D4016013. doi: 10.1061/(ASCE)GM.1943-5622.0000727.

Leong, E.C. and Rahardjo, H. 1997. Review of soil-water characteristic curve equations. *Journal of geotechnical and geoenvironmental engineering* 123(12), pp. 1106–1117.

Letey, J., Osborn, J. and Pelishek, R.E. 1962. The influence of the water-solid contact angle on water movement in soil. *International Association of Scientific Hydrology. Bulletin* 7(3), pp. 75–81. doi: 10.1080/02626666209493272.

Li, J. et al. 2015. A comparison of experimental methods for describing shale pore features — A case study in the Bohai Bay Basin of eastern China. *International Journal of Coal Geology* 152, pp. 39–49. doi: 10.1016/j.coal.2015.10.009.

Li, J., Yin, Z.-Y., Cui, Y.-J., Liu, K. and Yin, J.-H. 2019. An elasto-plastic model of unsaturated soil with an explicit degree of saturation-dependent CSL. *Engineering Geology* 260, p. 105240. doi: 10.1016/j.enggeo.2019.105240.

Li, J., Zhao, C., Cai, G., Asreazad, S., Xu, X.F. and Huang, Q. 2013. The input work expression and the thermodynamics-based modelling framework for unsaturated expansive soils with double porosity. *Chinese Science Bulletin* 58(27), pp. 3422–3429. doi: 10.1007/s11434-013-5828-9.

Li, P., Shao, S. and Vanapalli, S.K. 2020. Characterizing and modeling the pore-size distribution evolution of a compacted loess during consolidation and shearing. *Journal of Soils and Sediments* 20(7), pp. 2855–2867. doi: 10.1007/s11368-020-02621-3.

Li, P., Shao, S., Xiao, T. and Zhu, D. 2021. Pore-Size Distribution Evolution of Intact, Compacted, and Saturated Loess from China during Consolidation and Shearing. *Advances in Civil Engineering* 2021, p. e6644471. doi: 10.1155/2021/6644471.

Li, X. and Zhang, L.M. 2009. Characterization of dual-structure pore-size distribution of soil. *Canadian Geotechnical Journal* 46(2), pp. 129–141. doi: 10.1139/T08-110.

Li, X.S. 2003. Effective stress in unsaturated soil: a microstructural analysis. *Géotechnique* 53(2), pp. 273–277. doi: 10.1680/geot.2003.53.2.273.

Li, Y. and Vanapalli, S.K. 2021. A novel modeling method for the bimodal soil-water characteristic curve. *Computers and Geotechnics* 138, p. 104318. doi: 10.1016/j.compgeo.2021.104318.

Likos, W.J. and Lu, N. 2002. Filter Paper Technique for Measuring Total Soil Suction. *Transportation Research Record* 1786(1), pp. 120–128. doi: 10.3141/1786-14.

Likos, W.J. and Lu, N. 2004. Hysteresis of capillary stress in unsaturated granular soil. *Journal of Engineering mechanics* 130(6), pp. 646–655.

Likos, W.J., Wayllace, A., Godt, J. and Lu, N. 2010. Modified Direct Shear Apparatus for Unsaturated Sands at Low Suction and Stress. *Geotechnical Testing Journal* 33(4), pp. 286–298. doi: 10.1520/GTJ102927.

Liu, K., Yin, J.-H., Chen, W.-B., Feng, W.-Q. and Zhou, C. 2020a. The stress–strain behaviour and critical state parameters of an unsaturated granular fill material under different suctions. *Acta Geotechnica* 15(12), pp. 3383–3398. doi: 10.1007/s11440-020-00973-1.

Liu, K., Yuan, K. and Wu, K. 2020b. Effect of Water Content and Dry Density on Mechanical Properties of Compaction Loess. *IOP Conference Series: Earth and Environmental Science* 598(1), p. 012063. doi: 10.1088/1755-1315/598/1/012063.

Liu, X.F., de Carteret, R., Buzzi, O.P. and Fityus, S.G. 2016. Microstructural effects of environmental salinity on unbound granular road pavement material upon drying. *Acta Geotechnica* 11(2), pp. 445–451. doi: 10.1007/s11440-015-0393-9.

Lloret, A., Villar, M.V., Sánchez, M., Gens, A., Pintado, X. and Alonso, E.E. 2003. Mechanical behaviour of heavily compacted bentonite under high suction changes. *Géotechnique* 53(1), pp. 27–40. doi: 10.1680/geot.2003.53.1.27.

Lloret-Cabot, M., Sánchez, M. and Wheeler, S.J. 2013. Formulation of a three-dimensional constitutive model for unsaturated soils incorporating mechanical-water retention couplings. *International Journal for Numerical and Analytical Methods in Geomechanics* 37(17), pp. 3008–3035. doi: 10.1002/nag.2176.

Low, H.-E., Phoon, K.-K., Tan, T.-S. and Leroueil, S. 2008. Effect of soil microstructure on the compressibility of natural Singapore marine clay. *Canadian Geotechnical Journal* 45(2), pp. 161–176. doi: 10.1139/T07-075.

Lu, N. and Likos, W.J. 2004. *Unsaturated soil mechanics*. Wiley.

Luo, S., Zhou, B., Likos, W.J. and Lu, N. 2024. Determining Capillary Pore–Size Distribution of Soil from Soil–Water Retention Curve. *Journal of Geotechnical and Geoenvironmental Engineering* 150(2), p. 04023138. doi: 10.1061/JGGEFK.GTENG-11647.

Ma, S., Huang, X., Duan, Z., Ma, M. and Shao, Y. 2021. New Prediction Model for SWCC of Expansive Soil Considering Drying and Wetting Cycles. *Journal of Mining Science* 57(3), pp. 393–404. doi: 10.1134/S1062739121030054.

Ma, T., Wei, C., Yao, C. and Yi, P. 2020. Microstructural evolution of expansive clay during drying–wetting cycle. *Acta Geotechnica* 15(8), pp. 2355–2366. doi: 10.1007/s11440-020-00938-4.

Malaya, C. and Sreedeep, S. 2012. Critical Review on the Parameters Influencing Soil-Water Characteristic Curve. *Journal of Irrigation and Drainage Engineering* 138(1), pp. 55–62. doi: 10.1061/(ASCE)IR.1943-4774.0000371.

Maleki, M. and Bayat, M. 2012. Experimental evaluation of mechanical behavior of unsaturated silty sand under constant water content condition. *Engineering Geology* 141–142, pp. 45–56. doi: 10.1016/j.enggeo.2012.04.014.

Marshall, T.J. 1958. A Relation Between Permeability and Size Distribution of Pores. *Journal of Soil Science* 9(1), pp. 1–8. doi: 10.1111/j.1365-2389.1958.tb01892.x.

Marshall, T.J., Holmes, J.W. and Rose, C.W. 1996. *Soil Physics*. Cambridge University Press.

Mašín, D. 2010. Predicting the dependency of a degree of saturation on void ratio and suction using effective stress principle for unsaturated soils. *International Journal for Numerical and Analytical Methods in Geomechanics* 34(1), pp. 73–90. doi: 10.1002/nag.808.

Mašín, D. 2013. Double structure hydromechanical coupling formalism and a model for unsaturated expansive clays. *Engineering Geology* 165, pp. 73–88. doi: 10.1016/j.enggeo.2013.05.026.

Mašín, D., Herbstová, V. and Boháč, J. 2005. Properties of double porosity clayfills and suitable constitutive models. *Proceedings of the 16th International Conference on Soil Mechanics and Geotechnical Engineering*, pp. 827–830. doi: 10.3233/978-1-61499-656-9-827.

Matsuoka, H. 1974. Dilatancy Characteristics of Soil. *Soils and Foundations* 14(3), pp. 13–24. doi: 10.3208/sandf1972.14.3_13.

Miguel, M.G. and Bonder, B.H. 2012. Soil–Water Characteristic Curves Obtained for a Colluvial and Lateritic Soil Profile Considering the Macro and Micro Porosity. *Geotechnical and Geological Engineering* 30(6), pp. 1405–1420. doi: 10.1007/s10706-012-9545-y.

Musso, G., Azizi, A. and Jommi, C. 2020. A microstructure-based elastoplastic model to describe the behaviour of a compacted clayey silt in isotropic and triaxial compression. *Canadian Geotechnical Journal* 57(7), pp. 1025–1043. doi: 10.1139/cgj-2019-0176.

Musso, G., Romero, E. and Vecchia, G.D. 2013. Double-structure effects on the chemo-hydro-mechanical behaviour of a compacted active clay. *Géotechnique* 63(3), pp. 206–220. doi: 10.1680/geot.SIP13.P.011.

Nagpal, N.K., Boersma, L. and Debacker, L.W. 1972. Pore Size Distributions of Soils From Mercury Intrusion Porosimeter Data. *Soil Science Society of America Journal*, p. 4. doi: https://doi.org/10.2136/sssaj1972.03615995003600020019x.

Navarro, V., Asensio, L., De la Morena, G., Gharbieh, H., Alonso, J. and Pulkkanen, V.-M. 2020a. From double to triple porosity modelling of bentonite pellet mixtures. *Engineering Geology* 274, p. 105714. doi: 10.1016/j.enggeo.2020.105714.

Navarro, V., Asensio, L., Gharbieh, H., De la Morena, G. and Pulkkanen, V.-M. 2020b. A triple porosity hydro-mechanical model for MX-80 bentonite pellet mixtures. *Engineering Geology* 265, p. 105311. doi: 10.1016/j.enggeo.2019.105311.

Ng, C.W.W. and Chiu, A.C.F. 2001. Behavior of a Loosely Compacted Unsaturated Volcanic Soil. *Journal of Geotechnical and Geoenvironmental Engineering* 127(12), pp. 1027–1036. doi: 10.1061/(ASCE)1090-0241(2001)127:12(1027).

Ng, C.W.W., Lai, C.H. and Chiu, C.F. 2012. A Modified Triaxial Apparatus for Measuring the Stress Path-Dependent Water Retention Curve. *Geotechnical Testing Journal* 35(3), pp. 490–495. doi: 10.1520/GTJ104203.

Ng, C.W.W., Sadeghi, H. and Jafarzadeh, F. 2017. Compression and shear strength characteristics of compacted loess at high suctions. *Canadian Geotechnical Journal* 54(5), pp. 690–699. doi: 10.1139/cgj-2016-0347.

Ng, C.W.W., Sadeghi, H., Jafarzadeh, F., Sadeghi, M., Zhou, C. and Baghbanrezvan, S. 2019. Effect of microstructure on shear strength and dilatancy of unsaturated loess at high suctions. *Canadian Geotechnical Journal*. Available at: https://cdnsciencepub.com/doi/abs/10.1139/cgj-2018-0592.

Nikooee, E., Habibagahi, G., Hassanizadeh, S.M. and Ghahramani, A. 2013. Effective Stress in Unsaturated Soils: A Thermodynamic Approach Based on the Interfacial Energy and Hydromechanical Coupling. *Transport in Porous Media* 96(2), pp. 369–396. doi: 10.1007/s11242-012-0093-y.

Nimmo, J.R. 2013. Porosity and Pore Size Distribution. *Reference Module in Earth Systems and Environmental Sciences*.

Niu, F., Luo, J., Lin, Z., Fang, J. and Liu, M. 2016. Thaw-induced slope failures and stability analyses in permafrost regions of the Qinghai-Tibet Plateau, China. *Landslides* 13(1), pp. 55–65. doi: 10.1007/s10346-014-0545-2.

Niu, G., Cui, Y.-J., Pereira, J.-M., Shao, L. and Sun, D. 2021. Determining Bishop's parameter χ based on pore-size distribution. *Géotechnique Letters* 11(1), pp. 74–79. doi: 10.1680/jgele.20.00095.

NIU, G., SHAO, L., SUN, D., WEI, C., GUO, X. and XU, H. 2020. Evolution law of pore-size distribution in soil-water retention test. *Rock and Soil Mechanics* 41(4). Available at: https://rocksoilmech.researchcommons.org/journal/vol41/iss4/3.

Nuth, M. and Laloui, L. 2008. Effective stress concept in unsaturated soils: Clarification and validation of a unified framework. *International Journal for Numerical and Analytical Methods in Geomechanics* 32(7), pp. 771–801. doi: 10.1002/nag.645.

Oda, M., Takemura, T. and Takahashi, M. 2004. Microstructure in shear band observed by microfocus X-ray computed tomography. *Géotechnique* 54(8), pp. 539–542. doi: 10.1680/geot.2004.54.8.539.

Oualmakran, M., Mercatoris, B.C.N. and François, B. 2016. Pore-size distribution of a compacted silty soil after compaction, saturation, and loading. *Canadian Geotechnical Journal* 53(12), pp. 1902–1909. doi: 10.1139/cgj-2016-0184.

Pasha, A.Y., Khoshghalb, A. and Khalili, N. 2017. Hysteretic Model for the Evolution of Water Retention Curve with Void Ratio. *Journal of Engineering Mechanics* 143(7), p. 04017030. doi: 10.1061/(ASCE)EM.1943-7889.0001238.

Penumadu, D. and Dean, J. 2000. Compressibility effect in evaluating the pore-size distribution of kaolin clay using mercury intrusion porosimetry. 37.

Pham, H.Q., Fredlund, D.G. and Barbour, S.L. 2005. A study of hysteresis models for soil-water characteristic curves. *Canadian Geotechnical Journal* 42(6), pp. 1548–1568.

Pham, T.A. and Sutman, M. 2023. Modeling the combined effect of initial density and temperature on the soil–water characteristic curve of unsaturated soils. *Acta Geotechnica* 18(12), pp. 6427–6455. doi: 10.1007/s11440-023-01920-6.

Qian, J., Lin, Z. and Shi, Z. 2022. Experimental and modeling study of water-retention behavior of fine-grained soils with dual-porosity structures. *Acta Geotechnica*. Available at: https://doi.org/10.1007/s11440-022-01483-y.

Rabot, E., Wiesmeier, M., Schlüter, S. and Vogel, H.-J. 2018. Soil structure as an indicator of soil functions: A review. *Geoderma* 314, pp. 122–137. doi: 10.1016/j.geoderma.2017.11.009.

Rahardjo, H., Cong Thang, N., Kim, Y. and Leong, E.-C. 2018. Unsaturated elasto-plastic constitutive equations for compacted kaolin under consolidated drained and shearing-infiltration conditions. *Soils and Foundations* 58(3), pp. 534–546. doi: 10.1016/j.sandf.2018.02.019.

Rahardjo, H., Heng, O.B. and Choon, L.E. 2004. Shear strength of a compacted residual soil from consolidated drained and constant water content triaxial tests. *Canadian Geotechnical Journal* 41(3), pp. 421–436. doi: 10.1139/t03-093.

Rahardjo, H., Satyanaga, A., Mohamed, H., Yee Ip, S.C. and Shah, R.S. 2019. Comparison of Soil–Water Characteristic Curves from Conventional Testing and Combination of Small-Scale Centrifuge and Dew Point Methods. *Geotechnical and Geological Engineering* 37(2), pp. 659–672. doi: 10.1007/s10706-018-0636-2.

Rajesh, S. and Viswanadham, B.V.S. 2011. Hydro-mechanical behavior of geogrid reinforced soil barriers of landfill cover systems. *Geotextiles and Geomembranes* 29(1), pp. 51–64.

Rasheed, M.W. et al. 2022. Soil Moisture Measuring Techniques and Factors Affecting the Moisture Dynamics: A Comprehensive Review. *Sustainability* 14(18), p. 11538. doi: 10.3390/su141811538.

Read, H.E. and Hegemier, G.A. 1984. Strain softening of rock, soil and concrete — a review article. *Mechanics of Materials* 3(4), pp. 271–294. doi: 10.1016/0167-6636(84)90028-0.

Rees, S. 2013. Introduction to triaxial testing: Part 1.

Ringrose-Voase, A.J. 1991. Micromorphology of soil structure - Description, quantification, application. *Soil Research* 29(6), pp. 777–813. doi: 10.1071/sr9910777.

Romero, E., Gens, A. and Lloret, A. 1999. Water permeability, water retention and microstructure of unsaturated compacted Boom clay. *Engineering Geology* 54(1), pp. 117–127. doi: 10.1016/S0013-7952(99)00067-8.

Romero, E. and Simms, P.H. 2008. Microstructure investigation in unsaturated soils: a review with special attention to contribution of mercury intrusion porosimetry and environmental scanning electron microscopy. *Geotechnical and Geological Engineering* 26(6), pp. 705–727. doi: 10.1007/s10706-008-9204-5.

Russell, A. r. and Buzzi, O. 2012. A fractal basis for soil-water characteristics curves with hydraulic hysteresis. *Géotechnique* 62(3), pp. 269–274. doi: 10.1680/geot.10.P.119.

Russell, A.R. 2010. Water retention characteristics of soils with double porosity. *European Journal of Soil Science* 61(3), pp. 412–424. doi: 10.1111/j.1365-2389.2010.01237.x.

Sabetamal, H., Sheng, D. and Carter, J.P. 2022. Coupled hydro-mechanical modelling of unsaturated soils; numerical implementation and application to large deformation problems. *Computers and Geotechnics* 152, p. 105044. doi: 10.1016/j.compgeo.2022.105044.

Sánchez, M., Gens, A., Guimarães, L. do N. and Olivella, S. 2005. A double structure generalized plasticity model for expansive materials. *International Journal for Numerical and Analytical Methods in Geomechanics* 29(8), pp. 751–787. doi: 10.1002/nag.434.

Sánchez, M., Gens, A., Guimaraes, L. and Olivella, S. 2001. Generalized plasticity model for THM simulations involving expansive clays. In: *Proceedings of the 6th Int. Workshop on Key Issues in Waste Isolation Research*. pp. 28–30.

Scaringi, G. and Di Maio, C. 2016. Influence of Displacement Rate on Residual Shear Strength of Clays. *Procedia Earth and Planetary Science* 16, pp. 137–145. doi: 10.1016/j.proeps.2016.10.015.

Schlüter, S., Sammartino, S. and Koestel, J. 2020. Exploring the relationship between soil structure and soil functions via pore-scale imaging. *Geoderma* 370, p. 114370. doi: 10.1016/j.geoderma.2020.114370.

Sellin, P. and Leupin, O.X. 2013. The Use of Clay as an Engineered Barrier in Radioactive-Waste Management a Review. *Clays and Clay Minerals* 61(6), pp. 477–498. doi: 10.1346/CCMN.2013.0610601.

Shear strength characteristics of Shiraz unsaturated silty clay. 2009. *Iranian Journal of Science and Technology Transactions of Civil Engineering* 33(4), pp. 327–341. doi: 10.22099/ijstc.2009.710.

Shen, C.N., Fang, X., Wang, H.W., Sun, S.G. and Guo, J.F. 2009. Research on Effects of Suction, Water Content and Dry Density on Shear Strength of Remolded Unsaturated Soils. *Yantu Lixue/Rock and Soil Mechanics* 30(5), p. 1347.

Sheng, D. 2011. Review of fundamental principles in modelling unsaturated soil behaviour. *Computers and Geotechnics* 38(6), pp. 757–776.

Sheng, D., Fredlund, D.G. and Gens, A. 2008. A new modelling approach for unsaturated soils using independent stress variables. *Canadian Geotechnical Journal* 45(4), pp. 511–534. doi: 10.1139/T07-112.

Sheng, D., Sloan, S.W. and Gens, A. 2004. A constitutive model for unsaturated soils: thermomechanical and computational aspects. *Computational Mechanics* 33(6), pp. 453–465.

Simms, P.H. and Yanful, E.K. 2002. Predicting soil—water characteristic curves of compacted plastic soils from measured pore-size distributions.

Simms, P.H. and Yanful, E.K. 2004a. A discussion of the application of mercury intrusion porosimetry for the investigation of soils, including an evaluation of its use to estimate volume change in compacted clayey soils. *Geotechnique* 54(6), pp. 421–426.

Simms, P.H. and Yanful, E.K. 2004b. Estimation of Soil–Water Characteristic Curve of Clayey Till Using Measured Pore-Size Distributions. *Journal of Environmental Engineering* 130(8), pp. 847–854. doi: 10.1061/(ASCE)0733-9372(2004)130:8(847).

Sivakumar, V. 1993. *A critical state framework for unsaturated soil.* phd, University of Sheffield. Available at: https://etheses.whiterose.ac.uk/21744/.

Sivakumar, V., Sivakumar, R., Boyd, J. and Mackinnon, P. 2010. Mechanical behaviour of unsaturated kaolin (with isotropic and anisotropic stress history). Part 2: performance under shear loading. *Géotechnique* 60(8), pp. 595–609. doi: 10.1680/geot.8.P.008.

Skempton, A.W. 1954. The Pore-Pressure Coefficients A and B. *Géotechnique* 4(4), pp. 143–147. doi: 10.1680/geot.1954.4.4.143.

Sleutel, S. et al. 2008. Comparison of different nano- and micro-focus X-ray computed tomography set-ups for the visualization of the soil microstructure and soil organic matter. *Computers & Geosciences* 34(8), pp. 931–938. doi: 10.1016/j.cageo.2007.10.006.

Song, Z., Zhao, K. and Zhou, F. 2020. Analytical extension of double-porosity solutions under three-dimensional axisymmetric loadings. *Computers and Geotechnics* 119, p. 103373. doi: 10.1016/j.compgeo.2019.103373.

Sorbino, G. and Nicotera, M.V. 2013. Unsaturated soil mechanics in rainfall-induced flow landslides. *Engineering Geology* 165, pp. 105–132.

Sridharan, A., Altschaeffl, A.G. and Diamond, S. 1971. Pore Size Distribution Studies. *Journal of the Soil Mechanics and Foundations Division* 97(5), pp. 771–787. doi: 10.1061/JSFEAQ.0001595.

Stannard, D. 1992. Tensiometers—Theory, Construction, and Use. *Geotechnical Testing Journal* 15(1), pp. 48–58. doi: 10.1520/GTJ10224J.

Stone, K.J.L. and Wood, D.M. 1992. Effects of Dilatancy and Particle Size Observed in Model Tests on Sand. *Soils and Foundations* 32(4), pp. 43–57. doi: 10.3208/sandf1972.32.4_43.

Stróżyk, J. and Tankiewicz, M. 2014. The Undrained Shear Strength of Overconsolidated Clays. *Procedia Engineering* 91, pp. 317–321. doi: 10.1016/j.proeng.2014.12.067.

Sun, D., Matsuoka, H. and Xu, Y. 2004. Collapse Behavior of Compacted Clays in Suction-Controlled Triaxial Tests. *Geotechnical Testing Journal* 27(4), pp. 362–370. doi: 10.1520/GTJ11418.

Sun, D., You, G., Annan, Z. and Daichao, S. 2016a. Soil–water retention curves and microstructures of undisturbed and compacted Guilin lateritic clay. *Bulletin of Engineering Geology and the Environment* 75(2), pp. 781–791. doi: 10.1007/s10064-015-0765-2.

Sun, D., Zhang, J., Gao, Y. and Sheng, D. 2016b. Influence of Suction History on Hydraulic and Stress-Strain Behavior of Unsaturated Soils. *International Journal of Geomechanics* 16(6), p. D4015001. doi: 10.1061/(ASCE)GM.1943-5622.0000602.

Taina, I.A., Heck, R.J. and Elliot, T.R. 2008. Application of X-ray computed tomography to soil science: A literature review. *Canadian Journal of Soil Science* 88(1), pp. 1–19.

Tanaka, H., Shiwakoti, D.R., Omukai, N., Rito, F., Locat, J. and Tanaka, M. 2003. Pore size distribution of clayey soils measured by mercury intrusion porosimetry and its relation to hydraulic conductivity. *Soils and Foundations* 43(6), pp. 63–73. doi: https://doi.org/10.3208/sandf.43.6_63.

Tang, C.-S., Lin, L., Cheng, Q., Zhu, C., Wang, D.-W., Lin, Z.-Y. and Shi, B. 2020. Quantification and characterizing of soil microstructure features by image processing technique. *Computers and Geotechnics* 128, p. 103817. doi: 10.1016/j.compgeo.2020.103817.

Tarantino, A. 2009. A water retention model for deformable soils. *Géotechnique* 59(9), pp. 751–762. doi: 10.1680/geot.7.00118.

Tarantino, A. and Mongiovì, L. 2001. Experimental procedures and cavitation mechanisms in tensiometer measurements. In: Toll, D. G. ed. *Unsaturated Soil Concepts and Their Application in Geotechnical Practice*. Dordrecht: Springer Netherlands, pp. 189–210. Available at: https://doi.org/10.1007/978-94-015-9775-3_1.

Terzaghi, K. 1925. Modern conceptions concerning foundation engineering. *Journal of the Boston Society of Civil Engineers* 12(10), pp. 397–439.

Terzaghi, K. von. 1936. The shearing resistance of saturated soils and the angle between the planes of shear. *First international conference on soil Mechanics, 1936* 1, pp. 54–59.

Thom, R., Sivakumar, R., Sivakumar, V., Murray, E.J. and Mackinnon, P. 2007. Pore size distribution of unsaturated compacted kaolin: the initial states and final states following saturation. *Géotechnique* 57(5), pp. 469–474. doi: 10.1680/geot.2007.57.5.469.

Tian, H., Wei, C., Lai, Y. and Chen, P. 2018. Quantification of Water Content during Freeze–Thaw Cycles: A Nuclear Magnetic Resonance Based Method. *Vadose Zone Journal* 17(1), p. 160124. doi: 10.2136/vzj2016.12.0124.

Toll, D.G. and Ong, B.H. 2003. Critical-state parameters for an unsaturated residual sandy clay. *Géotechnique* 53(1), pp. 93–103. doi: 10.1680/geot.2003.53.1.93.

Tripathy, S., Elgabu, H. and Thomas, H.R. 2014a. Soil-water characteristic curves from various laboratory techniques. p. 7.

Tripathy, S., Tadza, M.Y.M. and Thomas, H.R. 2014b. Soil-water characteristic curves of clays. *Canadian Geotechnical Journal* 51, pp. 869–883. doi: https://doi.org/10.1139/cgj-2013-0089.

Troncone, A. 2005. Numerical analysis of a landslide in soils with strain-softening behaviour. *Géotechnique* 55(8), pp. 585–596. doi: 10.1680/geot.2005.55.8.585.

Tsiampousi, A., Day, C. and Petalas, A. 2024. Engineering soil barriers to minimise annual shrinkage/swelling in plastic clays. *Geomechanics for Energy and the Environment* 38, p. 100540. doi: 10.1016/j.gete.2024.100540.

Tsiampousi, A., ZDRAVKOVIć, L. and Potts, D. m. 2013. A three-dimensional hysteretic soil-water retention curve. *Géotechnique* 63(2), pp. 155–164. doi: 10.1680/geot.11.P.074.

Tsuji, G.Y., Watanabe, R.T. and Sakai, W.S. 1975. Influence of Soil Microstructure on Water Characteristics of Selected Hawaiian Soils 1. *Soil Science Society of America Journal* 39(1), pp. 28–33. doi: https://doi.org/10.2136/sssaj1975.03615995003900010011x.

Uchaipichat, A. and Khalili, N. 2009. Experimental investigation of thermo-hydro-mechanical behaviour of an unsaturated silt. *Géotechnique* 59(4), pp. 339–353. doi: 10.1680/geot.2009.59.4.339.

Van Genuchten, M.T. 1980. A closed-form equation for predicting the hydraulic conductivity of unsaturated soils 1. *Soil science society of America journal* 44(5), pp. 892–898.

Vanapalli, S.K., Fredlund, D.G., Pufahl, D.E. and Clifton, A.W. 1996. Model for the prediction of shear strength with respect to soil suction. *Canadian Geotechnical Journal* 33(3), pp. 379–392. doi: 10.1139/t96-060.

Vanapalli, S.K., Salinas, L.M., Avila, D. and Karube, D. 2002. Suction and storage characteristics of unsaturated soils.

Vaunat, J. and Casini, F. 2017. A procedure for the direct determination of Bishop's χ parameter from changes in pore size distribution. *Géotechnique* 67(7), pp. 631–636. doi: 10.1680/jgeot.15.T.016.

Wanatowski, D., Chu, J. and Lo, R.S.-C. 2008. Strain-softening behaviour of sand in strain path testing under plane-strain conditions. *Acta Geotechnica* 3(2), pp. 99–114. doi: 10.1007/s11440-008-0064-1.

Wang, H., Cui, Y.-J., Vu, M.N., Zhang, F. and Talandier, J. 2023. On the hydro-mechanical behaviour of unsaturated damaged Callovo-Oxfordian claystone. *Engineering Geology* 319, p. 107107. doi: 10.1016/j.enggeo.2023.107107.

Wang, J.-D., Li, P., Ma, Y. and Vanapalli, S.K. 2019. Evolution of pore-size distribution of intact loess and remolded loess due to consolidation. *Journal of Soils and Sediments* 19(3), pp. 1226–1238. doi: 10.1007/s11368-018-2136-7.

Wang, J.-D., Li, P., Ma, Y., Vanapalli, S.K. and Wang, X.-G. 2020. Change in pore-size distribution of collapsible loess due to loading and inundating. *Acta Geotechnica* 15(5), pp. 1081–1094. doi: 10.1007/s11440-019-00815-9.

Wang, M. and Bai, X. 2012. Collapse Property and Microstructure of Loess. *Advances in Unsaturated Soil, Seepage, and Environmental Geotechnics*, pp. 111–118. doi: 10.1061/40860(192)10.

Wang, Y., Yang, H. and Jing, X. 2021. Structural Characteristics of Natural Loess in Northwest China and its Effect on Shear Behavior. *Geotechnical and Geological Engineering* 39(1), pp. 65–78. doi: 10.1007/s10706-020-01420-4.

Washburn, E.W. 1921. The Dynamics of Capillary Flow. *Physical Review* 17(3), pp. 273–283. doi: 10.1103/PhysRev.17.273.

Wheeler, S.J., Gallipoli, D. and Karstunen, M. 2002. Comments on use of the Barcelona Basic Model for unsaturated soils. *International Journal for Numerical and Analytical Methods in Geomechanics* 26(15), pp. 1561–1571. doi: 10.1002/nag.259.

Wheeler, S.J., Sharma, R.S. and Buisson, M.S.R. 2003. Coupling of hydraulic hysteresis and stress–strain behaviour in unsaturated soils. *Géotechnique* 53(1), pp. 41–54. doi: https://doi.org/10.1680/geot.2003.53.1.41.

Wheeler, S.J. and Sivakumar, V. 1995. An elasto-plastic critical state framework for unsaturated soil. *Géotechnique* 45(1), pp. 35–53.

Wijaya, M. and Leong, E.C. 2016. Equation for unimodal and bimodal soil–water characteristic curves. *Soils and Foundations* 56(2), pp. 291–300. doi: 10.1016/j.sandf.2016.02.011.

Woignier, T., Morell, M., Morell, O., Duffours, L. and Soler, A. 2011. Low water transport in fractal microstructure of tropical soils: application to chlordecone pesticide trapping. *Ecohydrology & Hydrobiology* 11(1), pp. 121–127. doi: 10.2478/v10104-011-0035-2.

Wood, D.M. and Belkheir, K. 1994. Strain softening and state parameter for sand modelling. *Géotechnique* 44(2), pp. 335–339. doi: 10.1680/geot.1994.44.2.335.

WP4C Manual. 2019

Wu, T. 2020. *A Coupled Hydro-mechanical Constitutive Model for Unsaturated Soils with Double Pore Structure*. China: Beijing Jiaotong University. Available at: 10.26944/d.cnki.gbfju.2020.003320.

Wu, T., Cai, G., Cleall, P. and Tripathy, S. 2022. Microstructurally Related Model for Predicting Behavior of Unsaturated Soils with Double Porosity in Triaxial Space. *International Journal of Geomechanics* 22(12), p. 04022216. doi: 10.1061/(ASCE)GM.1943-5622.0002569.

Wu, T., Cleall, P., Tripathy, S. and Cai, G. 2023. Consideration of microstructure in modelling the hydro-mechanical behaviour of unsaturated soils. *E3S Web of Conferences* 382, p. 11005. doi: 10.1051/e3sconf/202338211005.

Wu, T., Cleall, P.J. and Tripathy, S. 2024. A constitutive model considering the interaction between evolution of microstructure and hydro-mechanical behaviour of unsaturated soils. *Computers and Geotechnics* 176, p. 106775. doi: 10.1016/j.compgeo.2024.106775.

Yan, W., Birle, E. and Cudmani, R. 2021. A simple approach for predicting soil water characteristic curve of clayey soils using pore size distribution data. *MATEC Web of Conferences* 337, p. 02012. doi: 10.1051/matecconf/202133702012.

Ying, Z., Cui, Y.-J., Benahmed, N. and Duc, M. 2023. Drying effect on the microstructure of compacted salted silt. *Géotechnique* 73(1), pp. 62–70. doi: 10.1680/jgeot.20.P.319.

Yong, R.N. 2003. Influence of microstructural features on water, ion diffusion and transport in clay soils. *Applied Clay Science* 23(1), pp. 3–13. doi: 10.1016/S0169-1317(03)00081-4.

You G. a. O. and De-an S.U.N. 2017. Determination of basic parameters of unimodal and bimodal soil water characteristic curves. *Chinese Journal of Geotechnical Engineering* 39(10), pp. 1884–1891. doi: 10.11779/CJGE201710017.

You G. a. O., De-an S.U.N., Jun-ran Z. and Ting L.U.O. 2019. Soil-water characteristics of unsaturated soils considering initial void ratio and hydraulic path. *Chinese Journal of Geotechnical Engineering* 41(12), pp. 2191–2196. doi: 10.11779/CJGE201912003.

Yu, C.Y., Chow, J.K. and Wang, Y.-H. 2016. Pore-size changes and responses of kaolinite with different structures subject to consolidation and shearing. *Engineering Geology* 202, pp. 122–131. doi: 10.1016/j.enggeo.2016.01.007.

Zhai, Q. et al. 2023. Prediction of the soil–water characteristic curves for the fine-grained soils with different initial void ratios. *Acta Geotechnica* 18(10), pp. 5359–5368. doi: 10.1007/s11440-023-01833-4.

Zhai, Q. and Rahardjo, H. 2015. Estimation of permeability function from the soil–water characteristic curve. *Engineering Geology* 199, pp. 148–156. doi: 10.1016/j.enggeo.2015.11.001.

Zhai, Q., Rahardjo, H., Satyanaga, A., Dai, G. and Zhuang, Y. 2020. Framework to estimate the soil-water characteristic curve for soils with different void ratios. *Bulletin of Engineering Geology and the Environment* 79(8), pp. 4399–4409. doi: 10.1007/s10064-020-01825-8.

Zhang, C., Li, J.-Z. and He, Y. 2020. Experimental Study on Viscoplastic Property of Unsaturated Reticulate Red Clay Used as an Engineered Barrier. *Geofluids* 2020, pp. 1–13. doi: 10.1155/2020/1523659.

Zhang, C. and Lu, N. 2020. Unified Effective Stress Equation for Soil. *Journal of Engineering Mechanics* 146(2), p. 04019135. doi: 10.1061/(ASCE)EM.1943-7889.0001718.

Zhang, J., Sun, D., Zhou, A. and Jiang, T. 2016. Hydromechanical behaviour of expansive soils with different suctions and suction histories. *Canadian Geotechnical Journal* 53(1), pp. 1–13. doi: 10.1139/cgj-2014-0366.

Zhang, L. and Chen, Q. 2005. Predicting Bimodal Soil–Water Characteristic Curves. *Journal of Geotechnical and Geoenvironmental Engineering* 131(5), pp. 666–670. doi: 10.1061/(ASCE)1090-0241(2005)131:5(666).

Zhang, L.M. and Li, X. 2010. Microporosity structure of coarse granular soils. *Journal of Geotechnical and Geoenvironmental Engineering* 136(10), pp. 1425–1436.

Zhang, Y. 2005. The microstructure and formation of biological soil crusts in their early developmental stage. *Chinese Science Bulletin* 50(2), pp. 117–121. doi: 10.1007/BF02897513.

Zhao, H.F. and Zhang, L.M. 2014. Effect of coarse content on shear behavior of unsaturated coarse granular soils. *Canadian Geotechnical Journal* 51(12), pp. 1371–1383. doi: 10.1139/cgj-2012-0292.

Zhao, H.F., Zhang, L.M. and Fredlund, D.G. 2013. Bimodal Shear-Strength Behavior of Unsaturated Coarse-Grained Soils. *Journal of Geotechnical and Geoenvironmental Engineering* 139(12), pp. 2070–2081. doi: 10.1061/(ASCE)GT.1943-5606.0000937.

Zhou, Y., Su, K. and Wu, H. 2015. Hydro-mechanical interaction analysis of high pressure hydraulic tunnel. *Tunnelling and Underground Space Technology* 47, pp. 28–34. doi: 10.1016/j.tust.2014.12.004.

Zou, L. 2018. *Effects of grain-size distribution and hysteresis on soil-water characteristic curve (SWCC)*. Nanyang Technological University. Available at: http://hdl.handle.net/10220/47603.